Role of mitochondrial dynamics and function in *Drosophila* embryo morphogenesis

A thesis

Submitted in partial fulfilment of the requirements

of the degree of

DOCTOR OF PHILOSOPHY

by

SAYALI CHOWDHARY

20112001

INDIAN INSTITUTE OF SCIENCE EDUCATION AND RESEARCH

PUNE

Dedicated to my beloved Aai, Baba and Aaji

Certificate

It is certified that the work incorporated in the thesis entitled ("**Role of mitochondrial dynamics and function in *Drosophila* embryo morphogenesis**") submitted by Sayali Chowdhary was carried out by the candidate, under my supervision. The work presented here or any part of it has not been included in any other thesis submitted previously for the award of any degree or diploma from any other University or institution.

Date: 19/03/2019

Dr. Richa Rikhy

(Supervisor)

Declaration

I declare that this written submission represents my research work in my own words and where others' ideas or works have been included, I have adequately cited and referenced the original sources. I also declare that I have adhered to all principles of academic honesty and integrity and have not misrepresented or fabricated or falsified any idea/data/fact/source in my submission. I understand that violation of the above will be the cause for disciplinary action by the Institute and can also evoke penal action from the sources which have thus not been properly cited or from whom proper permission has not been taken when needed.

Date:

Sayali Chowdhary

Reg. No: 20112001

Acknowledgements

It has been a great learning experience since I joined IISER, Pune for Integrated PhD program. It would not have been possible for me without the support I received from many people during this journey.

I am extremely grateful to my PhD thesis advisor Dr. Richa Rikhy for giving me an opportunity to work with her. She has always been enthusiastic about new ideas, encouraged me to come up with "*jugaads*" and helped me grow professionally and personally. She has always given her sincere word of advice, whether about science or otherwise. I thank her for sharing her immense expertise in genetics and imaging throughout. She has always encouraged me to attend relevant meetings and discuss ideas with eminent scientists.

Thanks to my RAC members Dr. Aurnab Ghose, Dr. Nagaraj Balasubramanian and Dr. Deepa Subramanyam for their criticism and experimental suggestions during the RAC meetings. I would also like to thank Dr. Girsh Ratnaparkhi for questions and suggestions during the lab meetings. His questions and wisdom about the experimental basics helped in revisiting the project in different angles.

Dr. Nagaraj Balasubramanian was my mentor for the first two years of integrated PhD. He helped me a lot in getting adjusted to the system and was patient in answering my questions about the coursework and overall PhD structure.

I thank Rachel Cox, Thomas Lecuit, Leo Pallanck, Krishanu Ray, Siegfried Roth, Anuradha Ratnaparkhi and Girish Ratnaparkhi for Antibody and fly reagents used in the project. I also thank BDSC, VDRC and NCBS stock centres for fly stocks.

IISER, Pune provides state of the art infrastructure with incredible facilities. I would like to thank fly facility (Snehal, Yashwant and others) for maintaining stocks and providing fly media, microscopy facility (Vijay, Santosh, Rahul and Aditi) and administration (Mrinalini, Piyush, Kalpesh, Shabnam, Roopali, Mahesh, Nayana and Tushar). I am grateful to Vijay Vittal for teaching microscopy basics and help with imaging troubleshooting.

Special thanks to University Grants Commission for my graduate fellowship. Additionally, I thank Infosys Foundation and Department of Biotechnology, India for funding conference travel expenses.

I would like to thank Bhavin, Somya, Bilwa, Dnyanesh, Debasmita and Akshada for their help in weeding out errors and typos in some of the thesis chapters.

RR lab members is a super crazy bunch of people who appropriately match to the lab acronym M.A.D. lab. All of my labmates have been extremely helpful, especially in changing fly cage plates many times for me. Lab seniors Aparna and Darshika taught experimental techniques during lab rotation. Bipasha has always offered her selfless help during any experiment. Sameer's technical queries durin g lab meetings helped in improving analysis. Dnyanesh and Bhavin's suggestions about various experiments were useful. Swati has always given an ear to my random rants and shared her life philosophy whenever I needed to get focused. I am thankful to Darshika and Dnyanesh for their help with the manuscript. Thanks to Devashree for cloning Mito-PA-GFP line. I would like to thank previous lab members: Tirthasree, Vishnu, Radhika, Rohan, Prachi, Gayatri and Prachiti for their suggestions and help. It was a great experience working with Arijit, Abhijeet, Bhagyashree D. and Somya. Bhagyashree helped with analysis of *drp1*^{SG}; *opa1*^{i} data during her lab rotation. Somya helped in setting up experiments for Toll-Dorsal pathway modifications. I thank all the lab members and Richa for maintaining a cheerful and optimistic work environment in the lab.

I am sure to have found friends here at IISER during these years of integrated PhD. I would like to thank my batchmates for being “co-sufferers”. Thanks to Libi, Bhagyshree, Rupa and Manawa for their support and words of wisdom. Ketakee, Chaitanya, Sampada, Shubhankar, Aditi, Niraja, Devika, Sanket, Shraddha and Manasi were greatly successful in distracting me from work. Thanks to annoying little kids: Gayatri and Prachiti for putting up with my craziness. I have found sisters for life in these two. Evening coffee sessions with Ketakee, Chaitanya, Sampada and Aditi would turn a 10 mins break into an hour long discussion session over any given topic ranging from science to philosophy and comics to real world issues. I have shared numerous crazy moments with Aditi, Sampada and Ketakee which I will cherish forever.

Thanks to coffee, coffee and some more coffee from G1 canteen and CCD for keeping me awake during long sessions. I also thank G1 canteen Anna, for providing evening snacks and a humorous statement for free with the food.

I am thankful to my non-IISER friends for their constant support and boost. Spontaneous gossip and discussion sessions with Bilwa, Radhika, Loukik, Tanvee, Prashant, Akshada, Mugdha and Achintya have helped in reliving the work stress.

I am lucky to have an incredibly supportive family. Thanks to aai, baba and aaji who have encouraged and nurtured my dream to become a scientist and being strong pillars of support throughout. No words can express my gratitude for them.

Table of Contents

List of Figures

List of Tables

Abbreviations

2-DG	2-deoxy-D-glucose
AMPK	5' adenosine monophosphate-activated protein kinase
ATP	Adenosine Tri Phosphate
Bcl-2	B-cell lymphoma 2
CoVa	Cytochrome C oxidase subunit Va
Cta	Concertina
Dhc64C	Dynein Heavy Chain 64C subunit
Dhc	Dynein Heavy chain
DHE	dihydroethidium
Drp1	Dynamin related protein 1
EGFR	Epidermal Growth factor receptor
EM	Electron microscopy
ER	Endoplasmic Reticulum
ERK	Extracellular signal regulated kinases
ESCs	Embryonic Stem Cells
ETC	Electron Transport Chain
FCCP	Carbonyl cyanide-4-(trifluoromethoxy) phenylhydrazone
FRAP	Fluorescence Recovery after Photobleaching
FLIP	Fluorescence Loss in Photobleaching
FAD	Flavin adenine dinucleotide
Fog	Folded Gastrulation
FOXO1	Forkhead box, sub-group O
Fzo	Fuzzy Onions
GSK3	Glycogen Synthase Kinase 3
HIF-α	Hypoxia induced factor α
JNK	c-Jun N-terminal kinase
Khc	Kinesin Heavy Chain
LH	Limonene:Heptane (1:1)
Lkb1	Liver kinase B1

MAM	Mitochondria Associated ER Membrane
Marf	Mitochondrial assembly regulatory factor
Mff	Mitochondrial fission factor
Mfn	Mitofusin
Mdv1	Mitochondrial division protein 1
MRLC	Myosin Regulatory Light Chain
Miro	Mitochondrial RhoGTPase
mtDNA	Mitochondrial DNA
mtlrRNA	Mitochondrially encoded large ribosomal RNA
mTOR	mammalian target of rapamycin
NADH	Nicotinamide adenine dinucleotide
NC	Nuclear division cycle
NF-κB	Nuclear factor-kappaB
PA	Photo Activation
PBS	Phosphate buffered saline
PDSW	NADH dehydrogenase (ubiquinone) PDSW subunit
PFA	para-formaldehyde
PGC	Posterior Germ Cells
OMM	Outer mitochondrial membrane
Opa1	Optic atrophy 1
ROI	Region of Interest
ROS	Reactive Oxygen Species
SEM	Standard error of mean
SOD	Superoxide dismutase
TAG	Triacyl Glycerides
TCA	Tricarboxylic Acid Cycle
TMRE	tetramethylrhodamine, ethyl ester
wntD	wnt inhibitor of Dorsal
WT	Wild Type

Abstract

Mitochondria, in addition to their well-known function of ATP synthesis, are also involved in a wide variety of cellular processes, such as apoptosis, calcium homeostasis and signalling. Mitochondria are structured by dedicated fusion and fission machinery that consists of well characterized GTPase proteins. The mitochondrial morphology is modified based on cell type and physiological requirements and is linked with a wide range of signalling pathways. Embryogenesis involves complex cascades of signalling that occur at specific milestones of the development. Hints from the literature suggest a temporal regulation of mitochondrial function and localization in ascidian and mammalian embryos. Mislocalization and deregulation of mitochondrial structure lead to cellular and embryonic lethality. However, a systematic analysis of mitochondrial shape and localization with respect to functional regulation and signalling during embryogenesis has not been carried out so far. We characterized mitochondria in early *Drosophila* embryogenesis using mitochondrially localized GFP and found that mitochondria are small and dispersed around nuclei in syncytial, cellular blastoderm, and gastrulating embryos. Mitochondria are basally enriched during syncytial stage and are actively re-distributed to the apical side during cellularization. Apical migration of mitochondria is specifically enhanced in the ventral furrow cells during gastrulation. This re-localization of mitochondria is microtubule dependent. This apical redistribution of mitochondria is abolished in embryos mutant for mitochondrial fission protein Drp1. Myosin II levels are reduced in *drp1* mutant embryos and the cells formed during cellularization in embryos are shorter and have wider contractile rings at their basal regions. The misaligned ventral furrow cells also have lowered Myosin II accumulation at their apical regions in *drp1* mutant embryos. This is likely due to reduced levels of reactive oxygen species (ROS) in these embryos. We find that apical mitochondrial transport in ventral furrow cells is regulated by the Toll-Dorsal pathway. Upregulation of Dorsal enhances the ventral signalling and apical accumulation of mitochondria whereas *fog* loss of function shows reduced mitochondrial apical transport in the ventral furrow cells. Thus, we demonstrate that mitochondrial localization is regulated by the Toll-Dorsal pathway and propose that their function is essential for functioning of Toll-Dorsal pathway. We are further examining the functional role of mitochondria in regulation of this pathway.

Synopsis

Name of the Student: Sayali Chowdhary

Registration number: 20112001

Name of Thesis advisor: Dr. Richa Rikhy

Date of Registration: 1st August 2011

Place: Indian Institute of Science Education and Research, Pune

Title: **Role of mitochondrial dynamics and function in *Drosophila* embryo morphogenesis**

1. Introduction

Mitochondria are primarily known for their function in ATP synthesis and thereby called "Power house of the Cell". In addition to this prime function, they are also involved in regulation of a number of physiological processes such as calcium signalling and ROS production. Mitochondrial shape is dynamic in the eukaryotic cells and they can exist as an intricate reticular network or small punctate form (Bereiter-Hahn and Vöth, 1994). The mitochondrial structure is often correlated with their function and metabolic output (Mishra and Chan, 2016). Larger mitochondria have a complex cristae organization which helps harbouring more electron transport chain (ETC) components (Cogliati et al., 2013) thereby enhancing the ATP output in differentiated cells such as muscles, neurons, pancreatic cells and cardiomyocytes (Kuznetsov et al., 2009). On the other hand small mitochondria are considered to be poor ATP producers in the literature and are present in stem cells and embryonic cells (Lees et al., 2017; Motta et al., 2000; Sathananthan and Trounson, 2000). Mitochondrial shape is regulated by fission and fusion proteins with aid from the cytoskeleton. These proteins are dynamin family GTPases which can actively modify mitochondrial membrane architecture (Chan, 2006). Different mitochondrial shapes are associated with a variety of signalling pathways. Mitochondrial fragmentation by EGFR pathway is essential for cellular differentiation (Mitra et al., 2012; Tomer et al., 2018). Regulation of mitochondrial fusion by Hippo/Yorkie pathway is implicated in cell growth and cancers (Nagaraj et al., 2012). Mitochondrial interaction with Bcl-2 family proteins is essential for apoptosis (Dewson and Kluck, 2009). Mitochondrial size is regulated during cell cycle to provide for increase energy demands (Mitra et al., 2009). More such emerging

studies indicate involvement and regulation of mitochondria in a number of key signalling pathways of cell fate determination and patterning based on their structure and dynamics.

Embryogenesis consists of cascades of complex signalling that are spatio-temporally regulated as the embryonic stem cells specialize to attain a peculiar fate. They are maternally inherited in the embryos and therefore implicated in diseases related to mitochondrial DNA (mtDNA) mutations (Giles et al., 1980; May-Panloup et al., 2016). Mitochondria are small and dispersed in the early blastoderm embryos (Acton et al., 2004; Van Blerkom et al., 2000; Motta et al., 2000; Sathananthan and Trounson, 2000) and their ATP synthesis is initiated by Calcium signalling during fertilization of the eggs (Dumollard et al., 2003; Roegiers et al., 1995). Although they are abundant around the nuclei, the active mitochondria are localized cortically in the mammalian embryos (Acton et al., 2004; Van Blerkom et al., 2003). Mitochondrial distribution is asymmetric in *Xenopus* and sea urchin embryos (Roegiers et al., 1995). Mitochondrial asymmetric distribution and activity define the oral-arboral axis in the sea urchin embryos (Coffman et al., 2004). Another study postulates increased mitochondrial localization and function at the prospective gastrulation site in *Xenopus* embryos (Yost et al., 1995). A thorough analysis of how mitochondria may regulate processes during embryogenesis is absent in the field. This led us to perform a systematic analysis of mitochondrial morphology and function in the embryonic development.

We characterized mitochondrial morphology and distribution in the early *Drosophila* embryogenesis and attempted to understand the effects of mitochondrial morphology alteration at the cellular level. The key findings are as follows:

2. Results

2.1 Mitochondria are enriched basally and are compartmentalized in the syncytial cells

Nuclei in the syncytial embryo are partially covered with plasma membrane on the apical regions. Despite the presence of free cytoplasm at the basal regions, organelles such as ER and Golgi and plasma membrane associated proteins localize within one nuclear-cytoplasmic territory (Frescas et al., 2006; Mavrakis et al., 2009). We visualized mitochondria using maternally expressed mitochondrially localized GFP (Mito-GFP) in the

syncytial embryos and found that they occurred as small discrete structures enriched at the basal regions of syncytial cells. The basal enrichment of mitochondria is determined by microtubule motor Kinesin-1. We monitored their movement using photobleaching and photoactivation. The mitochondria did not have significant lateral movement, leading to their restricted localization within a syncytial cell.

2.2 Mitochondrial metabolism is required for metaphase furrow elongation.

First, to test the mode of metabolism in the *Drosophila* embryos, we inhibited either glycolysis or ETC using pharmacological inhibitor drugs and measured the levels of ATP sensor activated AMPK (pAMPK) in the syncytial cells. AMPK is activated by phosphorylation by upstream kinases upon ATP depletion (Hardie et al., 2006; Sakamoto et al., 2005). pAMPK signal in the syncytial cells did not change upon inhibition of glycolysis and was significantly elevated in the treatments with ETC drug inhibitors. Similar results were obtained when we knocked down components of ETC: PDSW subunit of NADH dehydrogenase complex (Complex I, *pdsw*) and cytochrome C oxidase subunit Va (Complex IV, *cova*), using RNAi based approach. Thus these data established that mitochondrial ETC is the ATP source in the syncytial embryos.

We then explored the implications of ATP depletion. The short membrane structures covering the syncytial nuclei extend basally during metaphase forming furrows with the help of rapid actin assembly and may require abundant energy supply. The treatment with ETC inhibitor drugs and knockdown of *pdsw* and *cova* led to shortening of these metaphase furrows. Therefore despite the small shape, mitochondria produce ATP, which may be locally delivered to the growing membranes for rapid actin dynamics. It also possible that the phenotype of shorter furrows is due to interaction of AMPK signalling with cytoskeletal components (Cook et al., 2014; Lee et al., 2007).

2.3 Mitochondria are transported apically during cellularization and gastrulation

During cellularization the short membranes extend towards basal regions and enclose the nuclei to form tall epithelial cells (Mazumdar and Mazumdar, 2002; Warn and Robert-Nicoud, 1990). We imaged mitochondria during cellularization using the Mito-GFP tag and observed their increased accumulation at the apical regions of cells. Using photoactivation

we showed that they migrate apically from basal regions. The apical migration is assisted by microtubule motors. Knockdown of Kinesin-1 (*khc*) resulted in premature mitochondrial transport toward the apical regions whereas they clustered at the basal regions in Dynein (*dhc*) knockdown embryos. Thus Dynein motors transport mitochondria apically during cellularization.

To observe mitochondrial dynamics during gastrulation, we aligned embryos vertically or end on, such that their dorso-ventral axis was visible. We observed that post cellularization, mitochondrial apical transport is enhanced only in the ventral furrow cells. Mitochondrial transport was not seen in the lateral region cells post cellularization. The data indicate that specific relocalization of mitochondria is likely to be by the virtue of Toll-Dorsal signalling in the ventral furrow region and there may be a distinctive functional relevance of apical mitochondria in the ventral furrow cells. We tested whether this pathway influenced mitochondrial transport further.

2.4 Mitochondrial shape is essential for their apical transport

It is known that maintenance of mitochondrial architecture is obligatory for embryonic survival (Chen et al., 2003; Ishihara et al., 2009; Moore et al., 2010). We maternally depleted the levels of fission protein Drp1 and fusion proteins Marf and Opa1 using RNAi or genomic mutations. We also employed a strategy of over-expressing mutant form of proteins. Optimum knockdown of these proteins was lethal. We found that mitochondria were clustered in *drp1* knockdown or mutations. The morphology did not change in Marf or Opa1 knockdown. We followed *drp1* mutant: $drp1^{SG}$ and *drp1* RNAi ($drp1^{i}$) based on the extent of phenotype and embryonic lethality. We were able to revert the mitochondrial shape from clustered to fragmented when we knocked down *opa1* in the background of $drp1^{SG}$ ($drp1^{SG}$; $opa1^{i}$). This indicated that both fission and fusion machinery are active in the embryos.

Mitochondria formed large clusters of mitochondria located at the basal regions in $drp1^{SG}$ and $drp1^{i}$. These large clusters of mitochondria failed to migrate apically during cellularization and gastrulation. We observed a rescue of this transport defect in $drp1^{SG}$; $opa1^{i}$ embryos. Therefore, mitochondrial morphology is essential for their apical transport.

2.5 Cellular morphology is altered in *drp1*^{SG} embryos.

We then analysed how *drp1* mutation may affect the process of cellularization. We visualized membrane extension dynamics during cellularization using tagged Myosin regulatory light chain (Sqh-mCherry). The cellularization ended abruptly and significantly shorter cells were formed in the *drp1*^{SG} embryos. The basal contractile rings of these cells did not completely constrict to enclose the cellular compartment. Myosin II localization and activity is required for membrane extension and constriction during cellularization (He et al., 2016; Wenzl et al., 2010; Young et al., 1991). *drp1*^{SG} embryos had lowered levels of Sqh, likely leading to membrane extension and constriction defects. Myosin activity is regulated by ROS levels during *Drosophila* embryo dorsal closure (Muliyil and Narasimha, 2014). In accordance with this study, we found that the level of ROS was reduced in *drp1*^{SG} embryos and is likely the cause of Sqh depletion.

2.6 *drp1*^{SG} embryos contain shallow ventral furrow with misaligned cells.

Pulsatile Myosin II helps in the apical constriction and invagination of ventral furrow cells (Martin et al., 2009). We found that ventral furrow in *drp1*^{SG} embryos was jagged and had misaligned cells. The furrow morphology appeared shallow in the end-on orientation. The furrow did not completely close. Similar to cellularization, Sqh levels were reduced at the apical regions of the ventral furrow cells. This suggests that mitochondrial localization and probably ROS based activity is required for ventral furrow morphogenesis.

2.7 Apical transport of mitochondria during gastrulation depends on Toll-Dorsal signalling

Ventral fate is regulated by Toll-Dorsal signalling through a number of transcription factors regulating Myosin II localization at the apical regions of ventral furrow cells (Dawes-Hoang, 2005; Martin et al., 2009; Morisato, 2001). We had observed that mitochondria localize specifically at the apical regions of ventral cells. Also, the lack of mitochondrial transport and activity in *drp1*^{SG} embryos led to decreased Myosin activity and distorted ventral furrow morphology. Over-expression of Dorsal in the *Drosophila* embryos extended the zone of mitochondrial apical transport to almost the entire embryo compared to a restricted ventral region in the WT. Knockdown of a downstream factor *fog* reduced mitochondrial transport

at the ventral furrow. Thus based on these experiments, mitochondria operate under the influence of Toll-Dorsal pathway and possibly aid in regulating Myosin II activity.

In summary, mitochondrial distribution is regulated at distinctive stages of embryonic development in *Drosophila*. Their shape and activity are essential for membrane ingression during syncytial stage and cellularization and ventral furrow ingression during gastrulation. The study partly demonstrates and proposes the regulation of mitochondria by axis determination Toll-Dorsal pathway in the *Drosophila* embryogenesis.

3. References

1. Acton, B.M., Jurisicova, A., Jurisica, I., and Casper, R.F. (2004). Alterations in mitochondrial membrane potential during preimplantation stages of mouse and human embryo development. 10, 23–32.
2. Bereiter-Hahn, J., and Vöth, M. (1994). Dynamics of mitochondria in living cells: shape changes, dislocations, fusion, and fission of mitochondria. Microsc. Res. Tech. 27, 198–219.
3. Van Blerkom, J., Davis, P., and Alexander, S. (2000). Differential mitochondrial distribution in human pronuclear embryos leads to disproportionate inheritance between blastomeres: Relationship to microtubular organization, ATP content and competence. Hum. Reprod. 15, 2621–2633.
4. Van Blerkom, J., Davis, P., and Alexander, S. (2003). Inner mitochondrial membrane potential (¥m), cytoplasmic ATP content and free Ca2+ levels in metaphase II mouse oocytes. Hum. Reprod. 18, 2429–2440.
5. Chan, D.C. (2006). Mitochondrial fusion and fission in mammals. Annu. Rev. Cell Dev. Biol. 22, 79–99.
6. Chen, H., Detmer, S.A., Ewald, A.J., Griffin, E.E., Fraser, S.E., and Chan, D.C. (2003). Mitofusins Mfn1 and Mfn2 coordinately regulate mitochondrial fusion and are essential for embryonic development. J. Cell Biol. 160, 189–200.
7. Coffman, J.A., McCarthy, J.J., Dickey-Sims, C., and Robertson, A.J. (2004). Oral-aboral axis specification in the sea urchin embryo: II. Mitochondrial distribution and redox state contribute to establishing polarity in *Strongylocentrotus purpuratus*. Dev. Biol. 273, 160–171.

8. Cogliati, S., Frezza, C., Soriano, M.E., Varanita, T., Quintana-cabrera, R., Corrado, M., Cipolat, S., Costa, V., Casarin, A., Gomes, L.C., et al. (2013). Mitochondrial Cristae Shape Determines Respiratory Chain Supercomplexes Assembly and Respiratory Efficiency. Cell 155, 160–171.
9. Cook, M., Bolkan, B.J., and Kretzschmar, D. (2014). Increased actin polymerization and stabilization interferes with neuronal function and survival in the AMPK - α mutant loechrig. PLoS One 9.
10. Dawes-Hoang, R.E. (2005). Folded Gastrulation, Cell Shape Change and the Control of Myosin Localization. Development 132, 4165–4178.
11. Dewson, G., and Kluck, R.M. (2009). Mechanisms by which Bak and Bax permeabilise mitochondria during apoptosis. J. Cell Sci. 122, 2801–2808.
12. Dumollard, R., Hammar, K., Porterfield, M., Smith, P.J., Cibert, C., Rouvière, C., and Sardet, C. (2003). Mitochondrial respiration and Ca2+ waves are linked during fertilization and meiosis completion. Development 130, 683–692.
13. Frescas, D., Mavrakis, M., Lorenz, H., DeLotto, R., and Lippincott-Schwartz, J. (2006). The secretory membrane system in the *Drosophila* syncytial blastoderm embryo exists as functionally compartmentalized units around individual nuclei. J. Cell Biol. 173, 219–230.
14. Giles, R.E., Blanc, H., Cann, H.M., and Wallace, D.C. (1980). Maternal inheritance of human mitochondrial DNA. Proc. Natl. Acad. Sci. U. S. A. 77, 6715–6719.
15. Hardie, D.G., Hawley, S.A., and Scott, J.W. (2006). AMP-activated protein kinase--development of the energy sensor concept. J. Physiol. 574, 7–15.
16. He, B., Martin, A., and Wieschaus, E. (2016). Flow-dependent myosin recruitment during *Drosophila* cellularization requires zygotic dunk activity. Development 143, 2417–2430.
17. Ishihara, N., Nomura, M., Jofuku, A., Kato, H., Suzuki, S.O., Masuda, K., Otera, H., Nakanishi, Y., Nonaka, I., Goto, Y., et al. (2009). Mitochondrial fission factor Drp1 is essential for embryonic development and synapse formation in mice. Nat. Publ. Gr. 11, 958–966.
18. Kuznetsov, A. V., Hermann, M., Saks, V., Hengster, P., and Margreiter, R. (2009). The cell-type specificity of mitochondrial dynamics. Int. J. Biochem. Cell Biol. 41, 1928–1939.

19. Lee, J.H., Koh, H., Kim, M., Kim, Y., Lee, S.Y., Karess, R.E., Lee, S.-H., Shong, M., Kim, J.-M., Kim, J., et al. (2007). Energy-dependent regulation of cell structure by AMP-activated protein kinase. Nature 447, 1017–1020.
20. Lees, J.G., Gardner, D.K., and Harvey, A.J. (2017). Pluripotent Stem Cell Metabolism and Mitochondria: Beyond ATP. Stem Cells Int. 2017, 1–17.
21. Martin, A.C., Kaschube, M., and Wieschaus, E.F. (2009). Pulsed contractions of an actin–myosin network drive apical constriction. Nature 457, 495–499.
22. Mavrakis, M., Rikhy, R., and Lippincott-Schwartz, J. (2009). Plasma Membrane Polarity and Compartmentalization Are Established before Cellularization in the Fly Embryo. Dev. Cell 16, 93–104.
23. May-Panloup, P., Boucret, L., Chao de la Barca, J.-M., Desquiret-Dumas, V., Ferré-L'Hotellier, V., Morinière, C., Descamps, P., Procaccio, V., and Reynier, P. (2016). Ovarian ageing: the role of mitochondria in oocytes and follicles. Hum. Reprod. Update 22, 725–743.
24. Mazumdar, A., and Mazumdar, M. (2002). How one becomes many: Blastoderm cellularization in *Drosophila* melanogaster. BioEssays 24, 1012–1022.
25. Mishra, P., and Chan, D.C. (2016). Metabolic regulation of mitochondrial dynamics. J. Cell Biol. 212, 379–387.
26. Mitra, K., Wunder, C., and Roysam, B. (2009). A hyperfused mitochondrial state achieved at G1–S regulates cyclin E buildup and entry into S phase. Proc. … 106.
27. Mitra, K., Rikhy, R., Lilly, M., and Lippincott-Schwartz, J. (2012). DRP1-dependent mitochondrial fission initiates follicle cell differentiation during *Drosophila* oogenesis. J. Cell Biol. 197, 487–497.
28. Moore, B.A., Gonzalez, G.D., and Caspary, T. (2010). Mitochondrial retention of Opa1 is required for mouse embryogenesis. Mamm. Genome 21, 350–360.
29. Morisato, D. (2001). Spätzle regulates the shape of the Dorsal gradient in the *Drosophila* embryo. Development 128, 2309–2319.
30. Motta, P.M., Nottola, S.A., Makabe, S., and Heyn, R. (2000). Mitochondrial morphology in human fetal and adult female germ cells. 15, 129–147.
31. Muliyil, S., and Narasimha, M. (2014). Mitochondrial ROS Regulates Cytoskeletal and Mitochondrial Remodeling to Tune Cell and Tissue Dynamics in a Model for Wound Healing. Dev. Cell 28, 239–252.

32. Nagaraj, R., Gururaja-rao, S., Jones, K.T., Slattery, M., Negre, N., Braas, D., Christofk, H., White, K.P., and Mann, R. (2012). Control of mitochondrial structure and function by the Yorkie / YAP oncogenic pathway. Genes Dev. 26, 2027–2037.
33. Roegiers, F., McDougall, A., and Sardet, C. (1995). The sperm entry point defines the orientation of the calcium-induced contraction wave that directs the first phase of cytoplasmic reorganization in the ascidian egg. Development 121, 3457–3466.
34. Sakamoto, K., McCarthy, A., Smith, D., Green, K.A., Grahame Hardie, D., Ashworth, A., and Alessi, D.R. (2005). Deficiency of LKB1 in skeletal muscle prevents AMPK activation and glucose uptake during contraction. EMBO J. 24, 1810–1820.
35. Sathananthan, A.H., and Trounson, A.O. (2000). Mitochondrial morphology during preimplantational human embryogenesis. Hum. Reprod. 15, 148–159.
36. Tomer, D., Chippalkatti, R., Mitra, K., and Rikhy, R. (2018). ERK regulates mitochondrial membrane potential in fission deficient *Drosophila* follicle cells during differentiation. Dev. Biol. 434, 48–62.
37. Warn, R.M., and Robert-Nicoud, M. (1990). F-actin organization during the cellularization of the *Drosophila* embryo as revealed with a confocal laser scanning microscope. J. Cell Sci. 96 (Pt 1), 35–42.
38. Wenzl, C., Yan, S., Laupsien, P., and Großhans, J. (2010). Localization of RhoGEF2 during *Drosophila* cellularization is developmentally controlled by slam. Mech. Dev. 127, 371–384.
39. Yost, H.J., Phillips, C.R., Boore, J.L., Bertman, J., Whalon, B., and Danilchik, M. V. (1995). Relocation of mitochondria to the prospective dorsal marginal zone during *Xenopus* embryogenesis. Dev. Biol. 170, 83–90.
40. Young, P.E., Pesacreta, T.C., and Kiehart, D.P. (1991). Dynamic changes in the distribution of cytoplasmic myosin during *Drosophila* embryogenesis. Development 111, 1–14.

Chapter 1

Introduction

1.1 Mitochondria are essential organelles of eukaryotic cells

It is thought that mitochondria have evolved from a symbiont α-proteobacteria species found inside eukaryotic host cells. Mitochondria are semi-autonomous organelles holding significance in aerobic metabolism and production of ATP in cells. They possess their own DNA, obtained from their bacterial form. Apart from the known function of ATP production, their shape and distribution suggest their role in regulating the essential signalling processes of cell. Transportation of mitochondria occurs via microtubules and their localization is necessary for survival and effective functioning of cell. Different kinds of cells demonstrate various shapes of mitochondria. Stem cells and embryos have comparatively smaller and lesser number while on the other hand, differentiated cells can show long shaped ones. Embryonic development depends on mitochondrial function. Also the literature indicates that any perturbations in the shape of mitochondria affects embryonic patterning and can lead to lethality. The regulation of mitochondrial morphology and its functions in the embryo still remains an information to be uncovered.

1.1.1 Mitochondria produce cellular ATP

As the primary function of mitochondria is ATP production, they are called “the powerhouse of the cell”. The mitochondria are semi-autonomous due to presence of its own DNA and ribosomes, that enable it to produce tRNAs and components of electron transport chain. The ATP generation occurs by redox cycles of electron transport chain (ETC) proteins which are found in in the inner mitochondrial membrane. This membrane folds to form numerous loops called cristae (Fig. 1.1) (Stroud and Ryan, 2013). Mitochondria play a role in oxidization of carbon compounds by a chain of redox reactions in ETC, called as the Kreb’s cycle or tricarboxylic acid (TCA) cycle. The ETC involves four protein complexes that transport electrons, acting as electron acceptors and donors. These complexes are NADH dehydrogenase (Complex I), succinate dehydrogenase (Complex II), cytochrome bc1 complex (Complex III) and Cytochrome oxidase (Complex IV). ETC complexes are coupled to ATP synthase complex utilizes the proton gradient across inner mitochondrial membrane to

hydrolyse ADP to ATP in the mitochondrial matrix (Fig. 1.2). Water molecules are produced as a result of reduction of oxygen during electron transfer. 34 ATP molecules are produced during the Kreb's cycle and oxidative phosphorylation (Ernster and Schatz, 1981). Respiratory chain complexes also form super-complexes that play a role in raising the efficiency of respiration. This was seen in yeast and mammalian cells (Lapuente-brun et al., 2013; SchaÈgger and Pfeiffer, 2000). Supercomplex assembly is controlled by inner membrane architecture, in turn by mitochondrial inner membrane fusion protein Opa1 (Cogliati et al., 2013). There is a close association of ATP production and cristae architecture. The intricate cristae structure brings about assembly of more super complexes and thus increasing ATP generation (Cogliati et al., 2013). The last component of ETC, i.e. ATPase is also central l for maintaining the structure (Saddar et al., 2008).

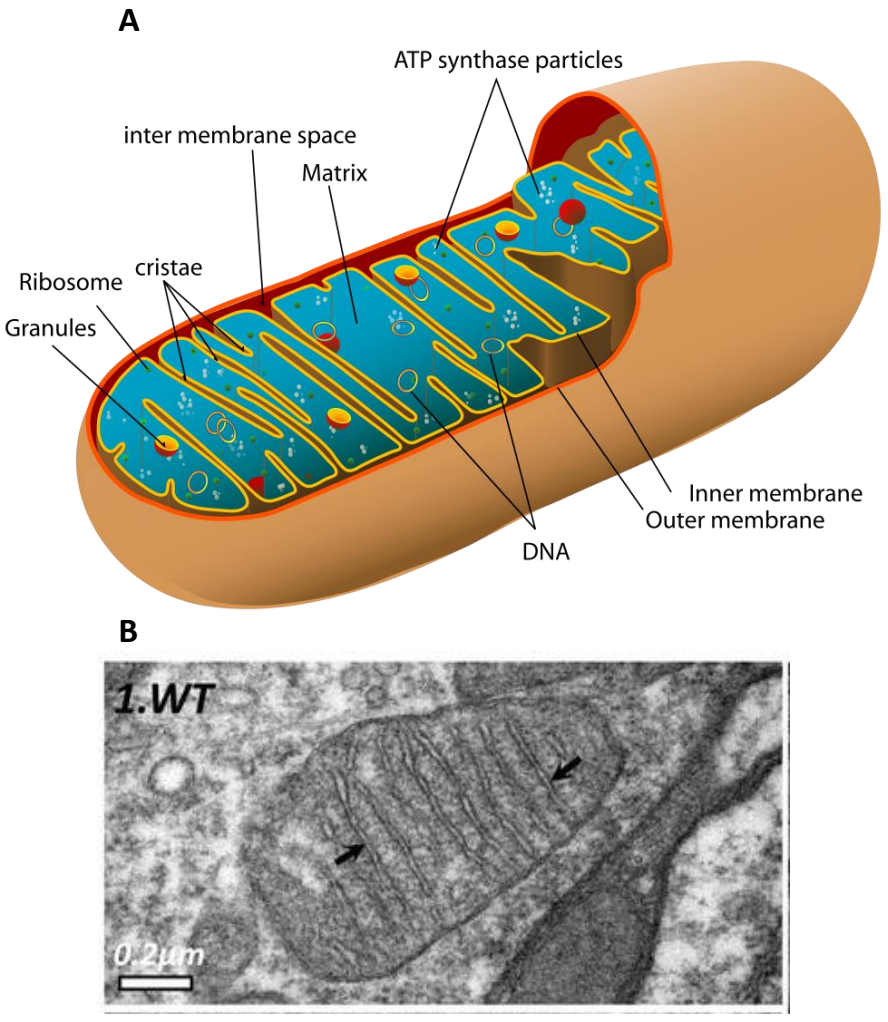

Figure 1.1: Mitochondrial structure. The schematic depicts mitochondrial double membraned architecture. The superfolded inner membrane (yellow) houses ETC. The mitochondrial matrix (blue) consists of DNA, ribosomes and granules (**A**). An electron micrograph shows mitochondria in *Drosphila* brain. Electron dense cristae (black arrows) are organized in parallel array (**B**). Adapted from (Macchi et al., 2013) (**B**)

Mitochondrial reactive oxygen species (ROS) is produced as a by-product of electron leakage from the ETC, primarily from Complex I and III of the ETC (Fig. 1.2) (Bell et al., 2007; Liu et al., 2002). A number of defence systems are utilized in cells to reduce ROS. Superoxides generated are modified by superoxide dismutase (SOD) to diffusible hydrogen peroxide (H_2O_2). Glutathione peroxidase silences ROS by oxidizing glutathione. ROS is scavenged in peroxisomes by the catalase enzymes (Ray et al., 2012). Mitochondrial shape and signalling interacts and modifies ROS. This is discussed later on in this section.

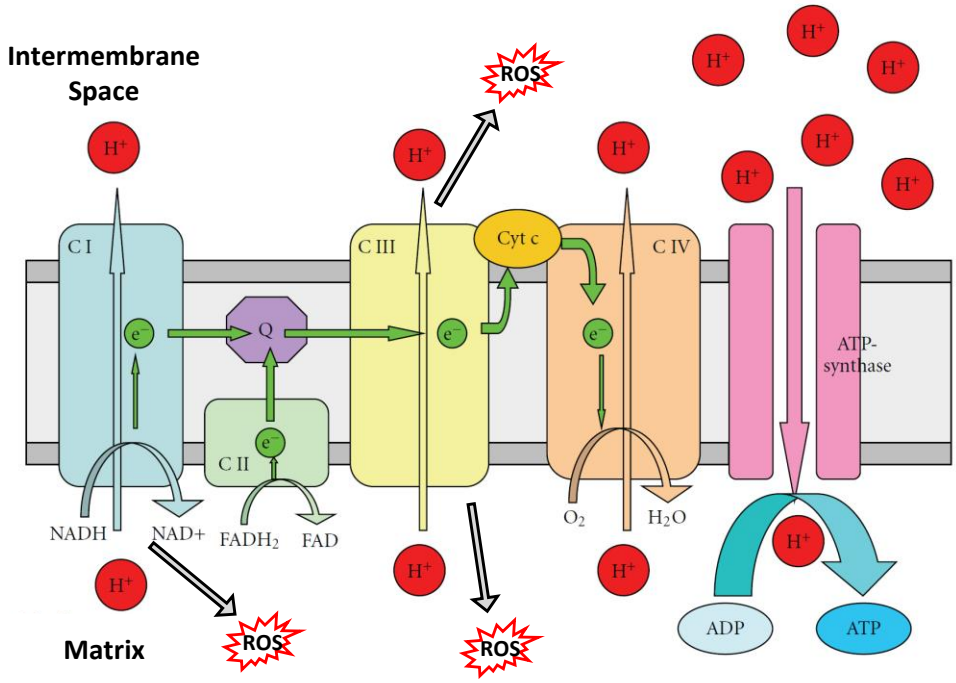

Figure 2.1 ATP is genetated by mitochondrial electron transport chain. The ETC complexes reside in the mitochondrial inner membrane (grey). The electrons (green) are relayed from complex I to complex IV by oxidizing NADH at Complex I (light blue), FADH2 at Complex II (light green), reduction and oxidation of Cytochrome C (yellow) by Complex III (light yellow) and IV (light orange) respectively. Protons (red) are pumped in the intermembrane space by Complex I, III and IV. Complex V (ATP synthase, pink) uses proton flux to generate ATP (blue) in the matrix. ROS is generated by leaky electrons from Complex I and III. Adapted from (Keane et al., 2011)**.**

1.1.2 Mitochondria undergo fission and fusion

1.1.2.1 Mitochondrial morphology is regulated by fission-fusion machinery

Distinct mitochondrial morphologies have been observed in different cell types and according to cell requirements. First observation of mitochondrial morphology changes was done about a hundred years ago (Lewis and Lewis, 1915). Authors used light microscopy and hand drawings to describe their observations. Since then, in the last couple of decades mitochondrial fission and fusion have been very well characterized. Mitochondrial morphology regulators were first found in yeast. A temperature sensitive yeast mutation in the dynamin mgm1 showed defects in the mitochondrial DNA maintenance (Jones and Fangman, 1992). Similar phenotype was observed with mutation in mitochondrial outer membrane GTPase protein Fzo in *Drosophila* sperms (Hales and Fuller, 1997). Mutations in Fzo lead to mitochondrial fragmentation (Hermann et al., 1998) and loss of mtDNA copies from the mitochondrial fragments (Rapaport et al., 1998). Mitochondria were visualized with mitochondrial GFP tag and mitochondrial dye: Mitotracker using an epifluorescence microscope (Rapaport et al., 1998). Mgm1 was later characterized as the mitochondrial inner membrane fusion protein and was shown to co-localize with mitochondria (Wong et al., 2000). The protein homolog was also found to be involved in neuropathies and was named as Optic atrophy 1 or Opa 1 in mammals and *Drosophila* (Delettre et al., 2000) (Fig. 1.3 A). The mammalian orthologs of Fzo, Mitofusins (Mfn1 and Mfn2) (Fig. 1.3 A) (Santel and Fuller, 2000) were shown to have partially redundant functions and both were shown to be essential for mouse embryonic development (Chen et al., 2003). Mitochondria assembly

regulating factor (Marf), another outer membrane fusion protein in *Drosophila,* along with Opa1 has been shown to be essential for cardiomyocyte function (Dorn et al., 2011).

Mitochondrial fission protein, Dnm1p, was discovered in a yeast genetic screen and was found to be associated with fission sites (Mozdy et al., 2000; Otsuga et al., 1998; Shaw and Nunnari, 2002). The protein, most commonly known as Dynamin related protein 1 (Drp1) is conversed in most eukaryotes and resulted in mitochondrial fragmentation (Labrousse et al., 1999; Smirnova et al., 1998a). Using *in vitro* EM studies, it was observed in the yeast that Dnm1 can oligomerize around tubules of the size of mitochondria in vitro (Ingerman et al., 2005), similar to the activity of dynamin at the endocytic vesicles. Drp1 is present largely in cytoplasm and localizes to the mitochondria upon fission cues. Outer membrane scaffolding protein Fis1 (or Fis1p in yeast) is required for binding of Drp1on the mitochondria (Mozdy et al., 2000) which then results in membrane scission. More recently additional adapter proteins were found to play a role in recruit Drp1 on the mitochondrial outer membrane. Mdv1 (Koirala et al., 2010; Zhang and Chan, 2007) and Caf4p (Griffin et al., 2005) are proteins that bind to Fis1 and facilitate Dnm1 binding in yeast. In higher eukaryotes, since there are not mdv1 homologs found, other adapters seem to have taken over this function. Mitochondrial fission factor (Mff) binds to Drp1 independent of Fis1 and is responsible for mitochondrial fission in mammalian cells (Otera et al., 2010) (Fig. 1.3 A). Proteins like Mid49, GDAP1 and Mid51/Mief (Loson et al., 2013) have been shown to recruit Drp1 and cause mitochondrial fragmentation as well, indicating that there may be redundancy in the regulation of mitochondrial fission in higher eukaryotes such as mammals. The final scission of the membrane after oligomerization of Drp1 is done by the bar domain protein Endophilin B1 (Karbowski et al., 2004).

The activity of fission and fusion proteins is regulated by a number of post translational modifications. Fission protein Drp1 is known to be modified with phosphorylation, SUMOylation, Ubiquitination and S-nitrosylation. Mitochondrial fission during mitosis in mammalian cells is promoted by phosphorylation of Drp1 at GTPase effector domain (GED) by cyclic-AMP dependent kinase A (PKA) in calcium dependent manner (Chang and Blackstone, 2007; Cribbs and Strack, 2007; Taguchi et al., 2007). This is mediated by RalA, effector RalB and Aurora kinase A in an Mff dependent manner (Kashatus et al., 2011). Ser 637 is a putative phosphorylation site in Drp1 conserved in metazoans and is regulated by

multiple mechanisms. Phosphorylation and dephosphorylation at this site by PKA and calcineurin respectively regulate localization of Drp1 on the mitochondria (Cereghetti et al., 2008; Taguchi et al., 2007). Drp1 is shown to be SUMOylated by mitochondrially anchored protein ligase (MAPL) and leads to mitochondrial fragmentation (Braschi et al., 2009). The SUMOylation is dependent on BAK/BAX protein kinases and could be essential to initiate apoptosis in cells (Wasiak et al., 2007). SUMO protease activity of SENP5 inhibits Drp1 activity and makes mitochondrial network more fused (Zunino et al., 2007). Regulation of Drp1 activity is also achieved by ubiquitination. Loss of function variant of another mitochondrial E3 ubiquitin ligase, MARCH5 resulted in mitochondrial elongation (Karbowski et al., 2007). MARCH5 was later shown to play a role in clearing misfolded SOD protein from mitochondria and protecting the cells from oxidative damage (Yonashiro et al., 2009).

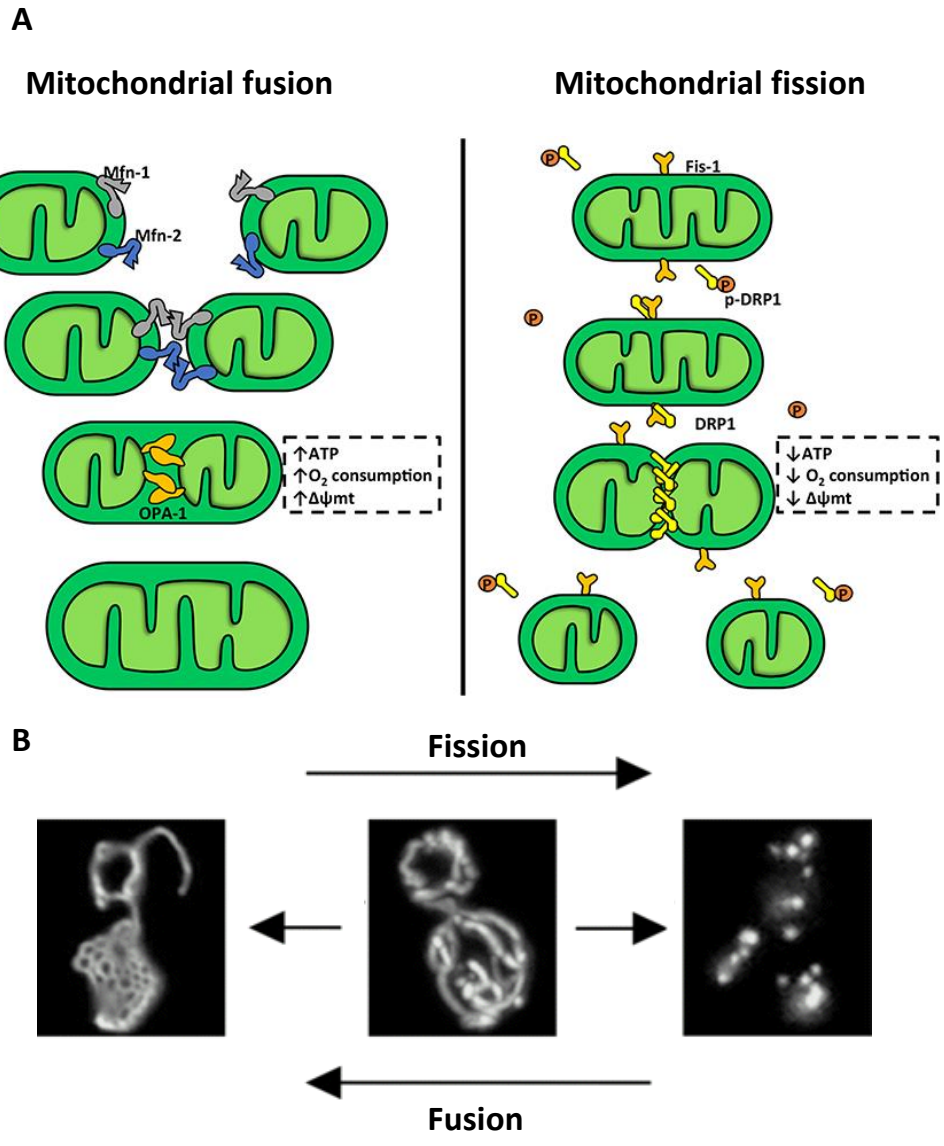

Figure 1.3 Mitochondria undergo fusion and fission. Mitochondrial fusion is regulated by Mfn1 and Mfn2 located on the mitochondrial outer membrane (**A, fusion, blue**). Transmembrane protein Opa1 is required from inner mitochondrial membrane fusion (**A, fusion, orange**). Cytosolic Drp1 (**A, fission, yellow**) binds to mitochondrial membrane localized Fis1 (**A, fission, orange**) upon activation. Active Drp1 oligomerizes around the mitochondrion to drive fission (**A, fission**). Fusion is associated with increased ATP output, oxygen consumption and membrane potential and vice versa with fission (**A**). Schematic is adapted from (Chiong et al., 2014) (**A**) Fluorescence imaging of mitochondria in yeast cells shows conversion of mitochondrial network to a hyperfused state upon fusion and punctate structures upon fragmentation (**B**). Adapted from (Mozdy et al., 2000) (**B**).

Observations through EMs have suggested proximal localization of mitochondrial outer membrane (OMM) and ER (Csordás et al., 2006). Mitochondria associated ER membranes (MAMs) have been shown to be essential for lipid synthesis (Stone and Vance, 2000; Vance, 1990), ATP synthesis, trafficking and calcium regulation and this depends on the distance between the ER and the OMM (Csordás et al., 2006, 2010; Rowland and Voeltz, 2012). Localization of mitochondrial morphology proteins at MAMs regulate mitochondrial shape, and thereby the function in the vicinity of ER. Studies using E.M. and super-resolution microscopy (STORM) demonstrated the presence of ER tubule loops winding around mitochondrial fission sites allowing constriction of the mitochondria prior to Drp1 recruitment (Friedman et al., 2011; Shim et al., 2012). Inverted formin 2 (INF2), a regulator of actin polymerization and depolymerization (Chhabra and Higgs, 2006) localizes at the ER-mitochondria contact sites, where it polymerizes F-actin around mitochondria to cause a constriction initiation such that binding of Drp1 at these sites is enhanced (Korobova et al., 2013). Microtubule motors dynein and dynactin complexes transport Drp1 to the mitochondria (Varadi et al., 2004). A recent study suggests a relationship between microtubule polymerization and mitochondrial size in yeast (Mehta et al., 2017).

Therefore, mitochondria can acquire a variety of shapes and sizes in cells by activity and regulation of fission fusion machinery. Remodelling of mitochondria is essential for

physiological processes in cells. A constant cycling between fusion and fission is said to be present in mammalian cells (Fig. 1.4 A, B). Mitochondrial biogenesis occurs by creating new mitochondria from an existing mitochondrial pool by fission (Goto et al., 2006; Marti et al., 2009) (Fig. 1.4 C). Association of mitochondria is enhanced on fusion and maintains calcium homeostasis in the cells (Grimm, 2012) (Fig. 1.4 A). Apoptotic cues lead to mitochondrial fragmentation and release of Cytochrome C which activates the caspases (Estaquier and Arnoult, 2007; Kluck and Newmeyer, 2013) (Fig 1.4 E). Mitochondrial fission and depolarization of the membrane potential lead to mitophagy (Burman et al., 2017) (Fig. 1.4 D). Additionally, there is a link between mitochondrial architecture and their metabolic capacity and ROS generation (Chan, 2006). Together, mitochondrial architecture coupled with the metabolic function has been studied in the context of cellular signalling pathways as discussed further.

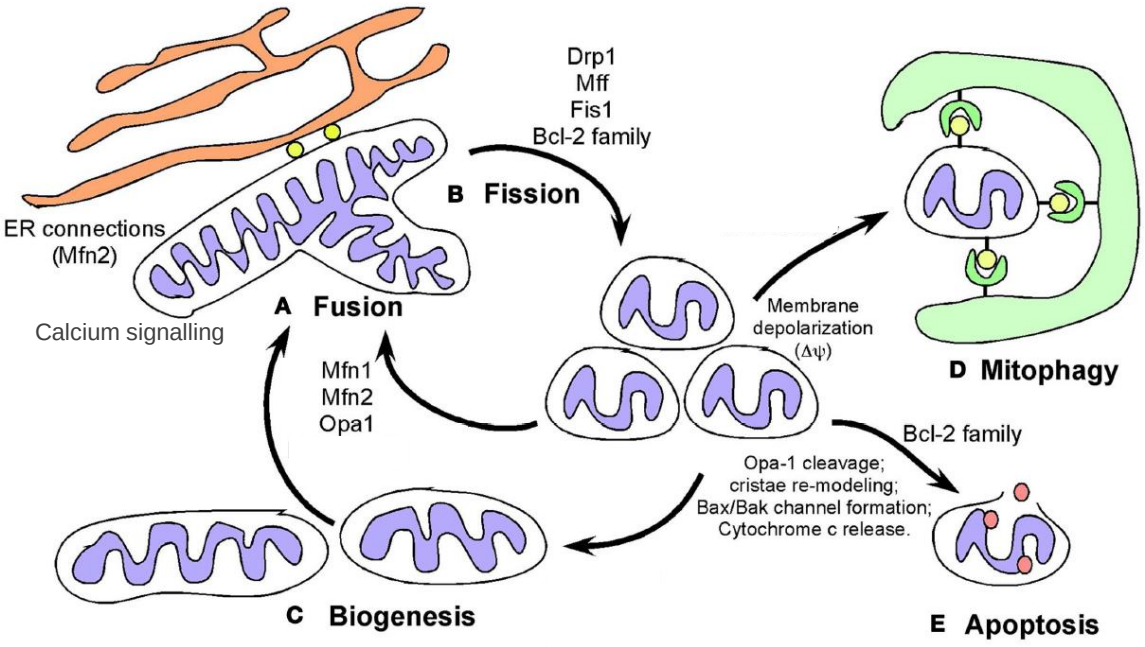

Figure 1.4: Physiological roles of mitochondrial morphology. Mitochondrial fusion is regulated by Opa1, Mfn1 and Mfn2 (**A**). Calcium based signalling occurs at the ER – mitochondria interphase (**A**). Mitochondrial fission is promoted by the Drp1 (**B**). Biogenesis of mitochondria requires fusion and promotes cell growth and metabolism (**C**).Mitochondrial fission depolarizes mitochondria leading to mitophagy by lysosome fusion followed by degradation (**D**). Apoptosis is promoted by Bcl-2 family proteins. Apoptosis requires mitochondrial fission for Cytochrome C release (**E**). Schematic adapted from (Boland et al., 2013).

1.1.2.2 Mitochondrial morphology and metabolism are interrelated.

There is a close connection between mitochondrial shape and their function. Mitochondrial shape is regulated in cells based on energy requirements, cell type and resources (Kuznetsov et al., 2009). Early embryos (Motta et al., 2000; Sathananthan and Trounson, 2000) and stem cells (Chen et al., 2012) contain small, dispersed mitochondria. Differentiated cells, such as muscles (Skulachev, 2001), rat cardiomyocytes (Ong and Hausenloy, 2010) , pancreatic cells (Kuznetsov et al., 2010), *Drosophila* oocyte main body follicle cells (Mitra et al., 2012) contain an intercalated mitochondrial network. These interconnected mitochondrial networks are said to be electrically coupled, have efficient regulation membrane potential to provide for high energy requirements. Mitochondrial structures are regulated based on cellular states. Growth phase yeast cells which depend on aerobic respiration have elaborate mitochondria (Egner et al., 2002; Hoffmann and Avers, 1973). A shift to glycolytic, fermentation state resolves the mitochondrial network (Jakobs et al., 2003). Comparably, mitochondria in G1-S phase of mammalian cells are more reticular compared to M phase, where they fragment to ensure proper distribution between daughter cells (Mitra et al., 2009). Mitochondria hyperfuse and produce more ATP upon presentation of stress stimuli to the cells (Tondera et al., 2009). Mitochondrial hyperfusion may be necessary to protect cells from degeneration (Chen et al., 2007). Mitochondrial fusion by inhibition of fission protein Drp1 during starvation stress via mTOR signalling is also proposed to have similar protective role (Gomez et al., 2011; Rambold et al., 2011).

Mitochondrial inner membrane houses the ETC complexes and maintenance of cristae structure with the help of inner membrane fusion protein Opa1 essential for ETC

supercomplex assembly and function (Cogliati et al., 2013; SchaÈgger and Pfeiffer, 2000). A number of studies associate increased mitochondrial fusion with OXPHOS activity elevation (Chan, 2006), membrane potential (Chen et al., 2003; Tomer et al., 2018) and reduction in ROS. On the other hand, smaller mitochondria are associated with minimal ATP production (Chen and Chan, 2005; Westermann, 2012). Mitochondrial fusion ensures maintenance of mtDNA. Depletion of mitochondrial fusion proteins in yeast, neurons and mouse skeletal muscles led to mutations and loss of mtDNA (Chen et al., 2010, 2007; Jones and Fangman, 1992; Merz and Westermann, 2009). mtDNA is required for synthesis of ETC components . The loss of mtDNA in the fusion mutants leads to further reduction in the mitochondrial metabolic output. Increased fission shortens yeast life span (Scheckhuber et al., 2011). Conversely, mitochondrial fission is aids removal of damaged mitochondria and maintains healthy, productive mitochondria in the system (Twig et al., 2008). Loss of fission increased life span of the yeast (Scheckhuber et al., 2006). Increased fusion also extended the lifespan of *C. elegans* (Chaudhari and Kipreos, 2017).

Mitochondrial morphology is regulated based on cellular resources, ATP levels and ETC activity. Inhibition of ETC by dissipation of the membrane potential leads to mitochondrial fragmentation in yeast and mammalian cells (Ishihara et al., 2003; Legros and Lombès, 2002; Meeusen et al., 2004). Uncouplers cause Opa1 cleavage and calcium mediated activation of Drp1 to cause mitochondrial fission (Cereghetti et al., 2008; Cribbs and Strack, 2007). Decrease in the ATP concentration activate AMP-Kinase (AMPK) pathway that leads to increased mitochondrial fragmentation followed by cell death (Toyama et al., 2016).

1.1.3 Microtubules regulate mitochondrial transport

Mitochondrial transport has been extensively analysed in neuronal cells and is essential acquiring mitochondria from the cell body (Saxton and Hollenbeck, 2012). Mitochondria are transported bi-directionally on microtubules on Dynein and Kinesin motors (Saxton and Hollenbeck, 2005) (Fig. 1.5). Kinesin-1 motors primarily carry mitochondria in the anterograde direction, or to the microtubule plus ends, whereas Dynein carries them in the opposite direction. The transport is facilitated by binding and activation of microtubule motor with adapters such as Dynactin and Milton (Koutsopoulos et al., 2010; Martin et al., 1999; Steffen et al., 1997). Mitochondrial Rho-like GTPases (Miro1 and Miro2) facilitate

mitochondrial binding to microtubule motor adapters and are responsible for carrying mitochondria to either plus or minus ends of microtubule motors (López-Doménech et al., 2018; Saotome et al., 2008). Neurotransmitter mediated Ca^{+2} signalling can initiate mitochondrial transport in axons (Mironov, 2006; Rintoul and Reynolds, 2010; Saotome et al., 2008). Studies from *Drosophila* demonstrate that Miro (Fransson et al., 2006a) and Milton (Glater et al., 2006; Górska-Andrzejak et al., 2003; Stowers et al., 2002) act as Ca^{+2} sensors and form a complex with Kinesin-1 which mediates mitochondrial transport (Glater et al., 2006; Wang and Schwarz, 2009). Milton based mitochondrial transport is essential for mitochondrial inheritance in *Drosophila* (Cox and Spradling, 2006).

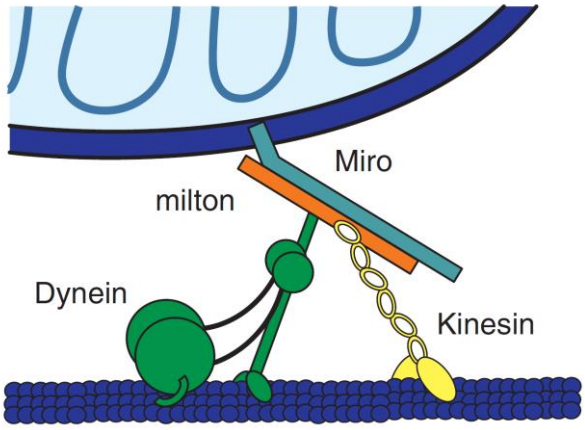

Figure 1.5. Mitochondrial transport of microtubules. Microtubule (**royal blue**) motors Kinesin-1 (**yellow**) and Dynein (**green**) carry mitochondria in anterograde and retrograde direction respectively. They bind to mitochondria by interacting with mitochondrion specific adapters: Milton (**orange**) and Miro (**blue**). Reproduced from (Schwarz, 2013).

Reduction in ATP levels or hypoxia at the axons stimulates mitochondrial transport by AMPK and HIF-1α signalling respectively (Li et al., 2009; Tao et al., 2014). A selective population of mitochondria with higher membrane potential are transported in the anterograde direction (Amiri and Hollenbeck, 2008; Miller and Sheetz, 2004). Mitochondria with lower membrane potential are carried to the neuronal cell bodies (Miller and Sheetz, 2004). Depolymerization of mitochondria using ETC inhibitors halts their transport in either direction (Baqri et al., 2009).

Defects in mitochondrial fission and fusion render them immobile in neurons (Chen et al., 2003; Li et al., 2004; Verstreken et al., 2005). Additionally, Miro and Milton over-expression can induce mitochondria fusion affecting mitochondrial transport (Fransson et al., 2006b; Koutsopoulos et al., 2010; Saotome et al., 2008). Lack of mitochondrial transport results in severe consequent neurodegenerative disorders including Parkinson's, Alzheimer's, ALS, Charcot-Marrie-Tooth type 2A and Schizophrenia (Lovas and Wang, 2013). Thus, it is essential to examine the mitochondrial transport dynamics in a developmental system to track down the mechanism leading to disorders.

1.1.4 Mitochondria are involved in signalling

Mitochondrial regulation of signalling pathways is an emerging field of research. The signalling pathways are more or less conserved across species. Role of mitochondrial shape and metabolism in the regulation of cell death, cell growth and differentiation and cell cycle has been explored in the field.

1.1.4.1 Mitochondria are key components of apoptosis

The earliest discovered signalling cascade to interact with mitochondria was apoptosis machinery (Liu et al., 1996). Apoptosis cues lead to Drp1 dependent mitochondrial fragmentation (Karbowski et al., 2002). Mitochondrial fragmentation is essential for release of cytochrome C to the cytoplasm and activation of the downstream caspase cascade (Estaquier and Arnoult, 2007; Frank et al., 2001). Also, inhibition of Drp1 leads to delayed apoptotic signalling (Frank et al., 2001). Release of Opa1 and breakdown of cristae structure by mitochondrial membrane permeability transition is also required from Cytochrome C release (Zhang et al., 2008a) and downregulation of Opa1, leading to mitochondrial fragmentation leads to spontaneous apoptosis. Bax protein, a regulator of caspase cascade (Youle and Strasser, 2008), localizes onto mitochondria on apoptotic stimuli (Dewson and Kluck, 2009) and triggers cytochrome C release (Kluck and Newmeyer, 2013; Walensky and Gavathiotis, 2011). The apoptotic signals localize more on the ER associated mitochondria (Csordás et al., 2006). This association increases upon Ca^{+2} exchange between the two organelles (Weaver et al., 2004). Pro-apoptotic proteins like Bax and Bak increase the Ca^{+2} dependent mitochondria (Oakes et al., 2005) and ER interaction where as anti-apoptotic Bcl-2 and Bcl-XL release Ca^{+2} (Chen and Dickman, 2004; Pinton et al., 2000; White et al., 2005).

1.1.4.2 Mitochondria regulate cellular growth and differentiation

Activation of epidermal growth factor (EGFR) triggers cellular growth and is correlated with cancer progression (Sharma et al., 2007). EGFR localizes to the mitochondrial outer membrane (Boerner et al., 2004; Che et al., 2015; Demory et al., 2009; Zhang et al., 2005) and regulates mitochondrial dynamics (Che et al., 2015; Mitra et al., 2012). EGFR causes Drp1 dependent mitochondrial fragmentation in *Drosophila* follicle cells and activates Notch pathway (Mitra et al., 2012) through regulation of mitochondrial membrane potential (Tomer et al., 2018). Likewise, dominant negative mutation of ERK, a downstream kinase in EGFR pathway, led to depletion of membrane potential and ATP levels in human alveolar macrophages (Monick et al., 2008) and ATP synthase depletion in astrocytes (Yung et al., 2004). Notch pathway increases mitochondrial fusion by prevention of mitochondrial fragmentation by Akt pathway (Perumalsamy et al., 2010). Mitochondrial fusion increases with Yorkie activation, leading to cell proliferation in *Drosophila* pupal eye discs and mammalian cell (Nagaraj et al., 2012; Ohsawa et al., 2012). On the other hand, mitochondrial fission increases cell proliferation in hepatocellular carcinomas in p53 dependent manner (Zhan et al., 2016).

Mitochondrial morphology is also regulated temporally during cell cycle. Mitochondrial hyperfusion during G1-S phase of cell cycle regulates energy output and is required for maintenance of cyclin E during the S phase (Mitra et al., 2009; Parker et al., 2015). Drp1 mediated mitochondrial fragmentation is essential for mitochondrial segregation in daughter cells (Mitra et al., 2009).

In summary, mitochondria interact with major cellular growth and differentiation pathways and the mechanisms of these interactions are yet to be uncovered.

1.1.4.3 Mitochondrial activity and ROS based signalling

Maintaining energy homeostasis is essential for cellular survival. AMP-activated protein kinase (AMPK) is activated by liver kinase B1 (LKB1) when the AMP:ATP or ADP:ATP ratios increase in the cells and inhibits cellular activities high energy requirements (Hardie et al., 2006). Other modes of mitochondrial dysfunction include signalling by mitochondrial ETC intermediates (Bohovych and Khalimonchuk, 2016). Depletion of mitochondrial activity by

reducing ETC Complex I and IV leads to cell cycle arrest followed by cell death (Owusu-Ansah and Banerjee, 2009). Also, mitochondrial membrane potential is necessary for proliferation (Martínez-Reyes et al., 2016). Reduction in cellular division potential by inhibition of mitochondrial ETC components is applied in usage of various anti-cancer drugs (Han et al., 2008; Wheaton et al., 2014).

Conversely, reduction in ETC components leads to increased lifespan in *Drosophila* and *C. elegans* (Copeland et al., 2009; Feng et al., 2001; Lee et al., 2002; Rea et al., 2007). Decreased mitochondrial activity converts metabolism of ESCs to glycolysis and activates pluripotency genes (Mandal et al., 2011).

Mitochondria ROS is generated as a by-product of activity of mainly Complex I and III of the ETC and serves as an important signalling molecule. Presence of ROS or oxidative stress is sensed by p38 kinase (p38K) that activates Mef transcription factor that upregulates manganese superoxide dismutase (MnSOD or SOD2) (Vrailas-Mortimer et al., 2011) for ROS quenching. During hypoxic (low oxygen concentration) conditions ROS is essential for localization of hypoxia induced factor α (HIF-α) (Chandel et al., 1998) to activate transcription to reduce cellular oxygen usage and energy consumption (Weidemann et al., 2008). Additionally it also induces endocytosis of sodium-potassium ion pumps to stop further energy utilization by activating AMPK signalling (Gusarova et al., 2011). Activation of ROS signals cellular senescence program via Akt pathway (Nogueira et al., 2008) which inhibits ROS scavenging to further increase ROS levels. ROS scavenging is regulated by forkhead box O (FOXO) transcription factors by activating mitochondrial superoxide dismutase (SOD2) and catalase (Kops et al., 2002; Nemoto and Finkel, 2002). Knockdown of FOXO leads to terminal differentiation of hematopoietic stem cells (Tothova et al., 2007). SOD2 is also one of the key interactors in (nuclear factor kappa-light-chain of activated B cells) NF-κB pathway in immunity. Activation of T cell receptor leads to Drp1 dependent mitochondrial fragmentation (Röth et al., 2014), decrease in Opa1 levels (Laforge et al., 2016) and increase in the ROS levels (Chandel et al., 2001). ROS also inactivates pro-apoptotic c-Jun N-terminal kinase (JNK) to promote T-cell proliferation (Kamata et al., 2005).

ROS can also chemically alter protein activity by oxidizing disulphide linkages (Yang et al., 2007). Thus phosphatase enzymes that contain cysteines are a target for ROS induced

modification (Brandes et al., 2009). Protein tyrosine phosphatase 1B, phosphatase and tensin homolog (PTEN) and MAPK family proteins have been demonstrated to be regulated by ROS (Kamata et al., 2005; Kwon et al., 2004; Levinthal and DeFranco, 2005). Modulation of Myosin II based contractility by ROS levels was demonstrated in *Drosophila* embryo dorsal closure (Muliyil and Narasimha, 2014). Therefore, protein modification by ROS also appears relevant in the context of other Myosin II related kinase cascade during embryonic development.

1.2 Mitochondria in metazoan embryogenesis

1.2.1: Mitochondria are maternally inherited

Mitochondria contain their own DNA (mtDNA) which is responsible for synthesis of most of the ETC component proteins (Breton et al., 2014). Mitochondria containing the mtDNA are maternally inherited in most metazoan embryos. Mitochondria along with other organelles such as Golgi Complex and ER aggregate form a cloud like structure or fusome (Warren and Wickner, 1996; Wilsch-Bräuninger et al., 1997) in oocytes of many species such as mouse, human, beetle, *Xenopus*, Zebrafish, chick and *Drosophila* (Dumollard et al., 2006; Hertig, 2018; Pepling and Spradling, 2001; Ukeshima and Fujimoto, 2018; Wilding et al., 2001a; Zhang et al., 2008b). This specialized structure is called Balbiani body and is inherited in the embryo. In *Drosophila* oogenesis mitochondria and other organelles are transported from the nurse cells to the oocyte through ring canals in the form of Balbiani body (Cox and Spradling, 2003; Wilsch-Bräuninger et al., 1997). Microtubule motor Kinesin along with adapter Milton are responsible for this anterior to posterior transport (Cox and Spradling, 2006). Formation of Balbiani body aggregates is aided by microtubule Dynein-Dynactin complex and around centrioles. (Cox and Spradling, 2003).

It appears that only a selective population of mitochondria cluster together to form Balbiani body. Mitochondria activity, in terms of mitochondrial potential, read using potentiometric dyes like JC1 and Mitotracker, is clearly higher in the Balbiani body mitochondria in *Xenopus* (Wilding et al., 2001a), Zebrafish (Zhang et al., 2008b), *Drosophila* (Akiyama and Okada, 1992), Mouse (Van Blerkom et al., 2003) and Human(Van Blerkom, 2011) oocytes. The mitochondria with higher potential are segregated during mouse oocyte division during polar body extrusion (Dalton et al., 2013). Balbiani body consists of maternal RNAs, mostly

essential for germ plasm (Hurd et al., 2016; Kloc and Etkin, 1995; Kloc et al., 1996; Mahowald, 2001). Inheritance of high membrane potential containing mitochondria (Akiyama and Okada, 1992) in *Drosophila* germ cells depends on *oskar* (Hurd et al., 2016).

Additionally there is a significant increase in the mtDNA copy number in Balbiani body mitochondria in various species like *Drosophila* (Hurd et al., 2016), human (Reynier et al., 2001), mouse (Wai et al., 2010) and *Xenopus* (Callen et al., 1980) during oocyte maturation. A threshold number of mtDNA is required from embryonic survival (Cotterill et al., 2013; Reynier et al., 2001; Wai et al., 2010). A strong selection seems also seems to work against mitochondria containing severe mtDNA mutations (Fan et al., 2008; Hill et al., 2014; Stewart et al., 2008). mtDNA replication and mitochondrial biogenesis works in the favour of healthy mitochondria, thereby gradually removing the severe mtDNA in *Drosophila* ovaries (Hill 2014). Mutations in mtDNA are a cause of many known inherited diseases in humans (Stewart and Chinnery, 2015). Accumulation of these mutations correlates with aging and lack of fertility (May-Panloup et al., 2016).

1.2.2: Mitochondrial shape and distribution in embryogenesis

The mitochondrial distribution shown using mitochondrial GFP showed perinuclear localization of mitochondria in mouse embryos (Nagai et al., 2008). Similar mitochondrial pattern was also observed using mitochondrial auto-fluorescence, TMRE staining and JC1 staining (Acton et al., 2004; Dumollard et al., 2004, 2007). Mitochondria also distribute in the perinuclear space in human (Acton et al., 2004; Van Blerkom et al., 2000; Motta et al., 2000; Sathananthan and Trounson, 2000; Wilding et al., 2001b), hamster (Squirrell et al., 1999), primate (Squirrell et al., 2003), porcine (Katayama et al., 2006) blastocyst stage embryos. These mitochondria are small in size and consist of relatively less developed cristae (Akiyama and Okada, 1992; Romek et al., 2011; Sathananthan and Trounson, 2000). Thus, mitochondrial localization scheme in mammalian embryos is almost similar to one another.

Sperm triggered calcium waves at fertilization reorganize cytoplasm and mitochondria of *Xenopus* and ascidian oocytes (Dumollard et al., 2006; Roegiers et al., 1995; Savage and Danilchik, 1993) thereby establishing an animal-vegetal pole asymmetry (Roegiers et al., 1995). Mitochondrial density is higher at the oral axis in sea urchin embryos and therefore

has more redox activity compared to the arboral axis (Coffman et al., 2004) (Coffman 2004) and possibly interacts with nodal signalling pathway (Coffman et al., 2014). Aggregation of mitochondria at the prospective dorsal marginal zone was seen using mtlr-RNA in embryogenesis of *Xenopus* (Yost et al., 1995).

Studies in mouse embryogenesis shows maintenance of mitochondrial morphology and function is essential for embryonic survival. Mice with Drp1, Mfn1, Mfn2 or Opa1 are defective in development, and die during gestation (Chen et al., 2000; Ishihara et al., 2009; Moore et al., 2010; Wakabayashi et al., 2009).

Studies in the mammalian systems so far have limited mitochondrial characterization presented in the early blastoderm stages. Although mitochondrial functions have been characterized slightly better in sea urchin embryos, a systematic analysis of the alterations in mitochondrial distribution has not been studied. Examining interactions of mitochondria with cytoskeleton will possibly shed light at these questions.

1.2.3: Regulation of mitochondrial metabolism in embryogenesis

A number of studies characterize the mitochondrial activity in oocytes and early embryos using a variety of ways that include using membrane potential dyes, analysis of cristae structure and metabolic profiling. Mitochondria are usually nascent and inactive in the oocytes and contain low amounts of ETC complexes. Mature *Drosophila* and *Xenopus* oocytes depend on glycolysis for their energy demands. This is regulated by decreased insulin signalling and activation of glycogen synthase kinase 3 (GSK3) signalling (Sieber et al., 2016) leading to glycogen accumulation. Similarly, mitochondria l activity is low in amphibian, fish, mouse and human oocytes (Van Blerkom, 2011; Dumollard et al., 2007; Pepling et al., 2007; Trimarchi et al., 2000; Wallace and Selman, 2018). Mitochondrial activity is triggered by sperm induced Ca^{+2} waves during fertilization in starfish, ascidian and mouse eggs (Campbell and Swann, 2006; Dumollard et al., 2003; Schomer and Epel, 1998). Kreb's cycle is initiated upon sperm entry into the oocyte (Dumollard et al., 2004; Roegiers et al., 1995). The ionic flux that occurs during fertilization regulates cortical granule exocytosis in mice (Blerkom and Davis, 2007). Successful implantation of human embryos requires a critical amount of ATP present in unfertilized stage. Embryos with dysfunctional ETC do not survive (Van Blerkom et al., 1995). This is consistent with findings suggesting the

cause of fertilization competence decrease in oocytes from older females is due to reduced mitochondrial activity (Wilding et al., 2001b). Mitochondria are inactive in the cultured embryonic stem cells (ESCs) and oxidative phosphorylation is initiated as a result of activation and remodelling of mitochondrial structure (Suhr et al., 2010). This is thought to protect mitochondria from ROS produced during oxidative phosphorylation. Optimum oxygen consumption is essential for embryonic survival (Ottosen et al., 2007). The oxygen consumption rate increases to 2 fold in mouse blastocyst stage embryos. At the same time primitive cristae found in oocytes (Stern et al., 1971) become more elaborate (Van Blerkom, 2004). These embryos have increased pyruvate consumption (Leese and Barton, 1984). Pyruvate based metabolism was later demonstrated using auto-fluorescence based imaging of reduced pyridine nucleotides (NADH and NADPH) and oxidized flavoproteins (FAD^{++}) in mouse embryos (Dumollard et al., 2007). Mitochondrial membrane potential also increases in the blastocyst stages of mouse and human embryos (Acton et al., 2004). Metabolism of *Drosophila* embryos was studied by analysing concentrations of metabolic substrates using mass spectrometry during development. Glycolysis substrates like Glucose-6-phosphate, pyruvate and lactate levels do not significantly change during embryogenesis (Tennessen et al., 2014). 0-4 hrs old, blastoderm staged *Drosophila* embryos largely use amino acids as metabolic substrates. Levels of amino acids Glutamate and Aspartate dramatically declined during this period (Thuy An et al., 2014). Additionally, amino acid Proline was identified as a metabolic substrate in the early *Drosophila* embryos (Tennessen et al., 2014). Amino acids are substrates of metabolism through ETC and thus these studies also indicate that mitochondrial ETC is active in early *Drosophila* embryos.

Mitochondrial activity reported using various potential based dyes is not uniform in the embryos. Highly polarized mitochondria are located in subcortical regions of mouse and human pre-implantation embryos using mitochondrial potential dye JC1 (Van Blerkom et al., 2002, 2003; Nagaraj et al., 2016; Wilding et al., 2001a). Other studies using Mitotracker or TMRE dye do not report such a distinction between mitochondrial activity (Dumollard et al., 2004; Newhall et al., 2006; Nishi et al., 2003). Differences in mitochondrial activity across embryonic axes has been described in sea urchin embryos. Experiments involving exposure of sand dollar embryos to respiratory inhibitor suggested asymmetry in redox activities in the oral-arboral axis. Asymmetric distribution of mitochondria in sea urchin embryos is

responsible for redox and ROS differences (Coffman, 2009; Coffman et al., 2004). It has been shown recently that hypoxia inducing factor α (HIFα) may regulate transcription on the dorsal side of sea urchin embryos and may aid the functioning of axis determination pathways (Chang et al., 2017). A dorso-ventral gradient of mitochondrial membrane potential was observed in *Drosophila* embryo using a fluorescent dye JC1 (Schiffmann, 1997) suggesting a possible development coupled regulation. Proteomic analysis of *Drosophila* embryos indicated reduced amount of Transferrin1 and transferrin 2 light chain homologs are reduced in ventralized embryos compared to lateralized embryos suggesting metabolic differences between ventral and lateral cells (Gong et al., 2004).

Mitochondria can most likely regulate morphogenesis via signalling through molecules like ATP, ROS, TCA cycle intermediates or through calcium buffering. Actomysin assembly and disassembly that lies at the core of shaping the cells requires high amount of energy, derived from mitochondrial ATP. Neurons with inactive mitochondria fail to elongate (Chen and Chan, 2009, Miller and Sheetz, 2004). Mitochondrial biogenesis promotes axonal growth in an AMPK dependent manner (Varrmann et al., 2016). pAMPK signalling can regulate actin dynamics to regulate cellular architecture (Cook et al., 2014). ROS at the same time can activate Myosin II through the RhoGEF2 kinase cascade and lead to cell contraction that causes shape change (Brandes et al., 2009, Muliyil and Narasimha, 2014). It is possible that mitochondrial localization, as discussed in relation with embryonic systems above, can help in local delivery of necessary signalling molecule. Mitochondrial calcium buffering with the ER is necessary for regulation of actin dynamics and polarity to help cell migration (Prudent et al., 2016).

Mitochondrial outer membrane has been predicted to serve as a platform of protein interactions. PKAs (Harada et al., 1999), innate immunity regulators (West et al., 2011, Zhou et al., 2011), cyclin E (Parker et al., 2015) have been shown to latch on to mitochondrial outer membrane. Essential signalling pathways such as EGFR (Mitra et al., 2012), Hippo-Yorkie (Nagaraj et al., 2012), Notch (Perumalsamy et al., 2010) and Fog (Ratnaparkhi, 2013) have been demonstrated to impact mitochondrial shape and activity, leading change mitochondrial metabolic properties and localization, thereby regulating downstream morphogenesis. TCA intermediates can act as transcription factors (Nagaraj et al., 2016).

Although different studies indicate mitochondrial involvement in the regulation of embryonic development, a link between mitochondrial function and signalling during development is not understood. I decided to address some of the pertaining questions in the field using *Drosophila* embryo as model system.

1.3 Model System: *Drosophila* embryo for studying role of mitochondrial morphology and function in embryogenesis

The patterning blueprint to define the embryonic axes is maternally laid in the *Drosophila* embryo. Apart from patterning cues, organelles like mitochondria, ER and Golgi complex are maternally inherited. *Drosophila* embryos are dynamic, develop faster compared to other embryonic systems and are also amiable to fluorescence imaging based on transgenic tags (Mavrakis et al., 2008).

In a fertilized *Drosophila* embryo the first 13 nuclear division cycles (NC) occur synchronously. After fertilization, the initial 9 nuclear division cycles (NC) occur deep inside the embryo, where nuclei are embedded in the cytoplasm. This stage is known as preblastoderm. During the NC 9, nuclei start migrating to the periphery of the embryo and are present at the cortex as NC 10 starts. Following 4 rapid divisions, NC10 - NC13 occur at the cortex. At this stage, the nuclei are covered partially with the plasma membrane at their apical side, which faces the cortex and the cells undergo partial cleavage (Karr and Alberts, 1986a). This stage is known as syncytial blastoderm, since nuclei are not completely enclosed with a membrane. Despite being a syncytial system, organelles like ER and Golgi complexes localize within a refined boundary around each nucleus (Frescas et al., 2006). Plasma membrane proteins thus delivered by the Golgi complexes to the membrane are not shared between the membranes of adjacent nuclei (Mavrakis et al., 2009). The system is therefore “compartmentalized” and each nuclear-cytoplasmic region which we call a “syncytial cell”. The only complete cells present during this stage are germ cells or pole cells present at the posterior side of the embryo (Akiyama and Okada, 1992a). During NC 14 interphase, the plasma membrane starts to ingress deeper towards the basal side and encloses the nuclei, eventually forming first true epithelial cells in the embryo forming cellular blastoderm in process known as cellularization (Lecuit and Wieschaus, 2000; Mazumdar and Mazumdar, 2002). Cellularization consists of 2 distinct phases of membrane

ingression, early slow phase and the late fast phase (Figard et al., 2013; He et al., 2016; Lecuit and Wieschaus, 2000). The membrane invagination during cellularization is assisted by acto-myosin assembly at the growing furrow tips (He et al., 2016; Schejter and Wieschaus, 1993; Warn and Robert-Nicoud, 1990; Young et al., 1991). In the early cellularization, acto-myosin assembly progressively localizes onto hexagonal furrow tips and membrane constrict to a circular shape in myosin dependent manner. The ring thus formed constricts with the help of actin cross linkers and eventually myosin falls off (Barmchi et al., 2005; He et al., 2016; Xue and Sokac, 2016; Young et al., 1991). Gastrulation begins right after the completion of cellularization and forms cephalic and ventral furrows. During ventral furrow formation, a set of cells at the ventral mesoderm acquire apical myosin activity that results in their apical constriction followed by invagination (Martin et al., 2009; Vasquez et al., 2014). Toll signalling mediates nuclear localization of transcription factor Dorsal creating a gradient of signalling at the ventral axis of *Drosophila* embryo (Morisato, 2001). Dorsal further activates *twist*, *snail* and *fog* genes which are required for initiation and stabilization of Myosin II activity at the apical regions of the ventral mesoderm cells (Dawes-Hoang, 2005; Leptin, 1991; Leptin and Grunewald, 1990). NC 14 division later takes place asynchronously in different regions of the embryo.

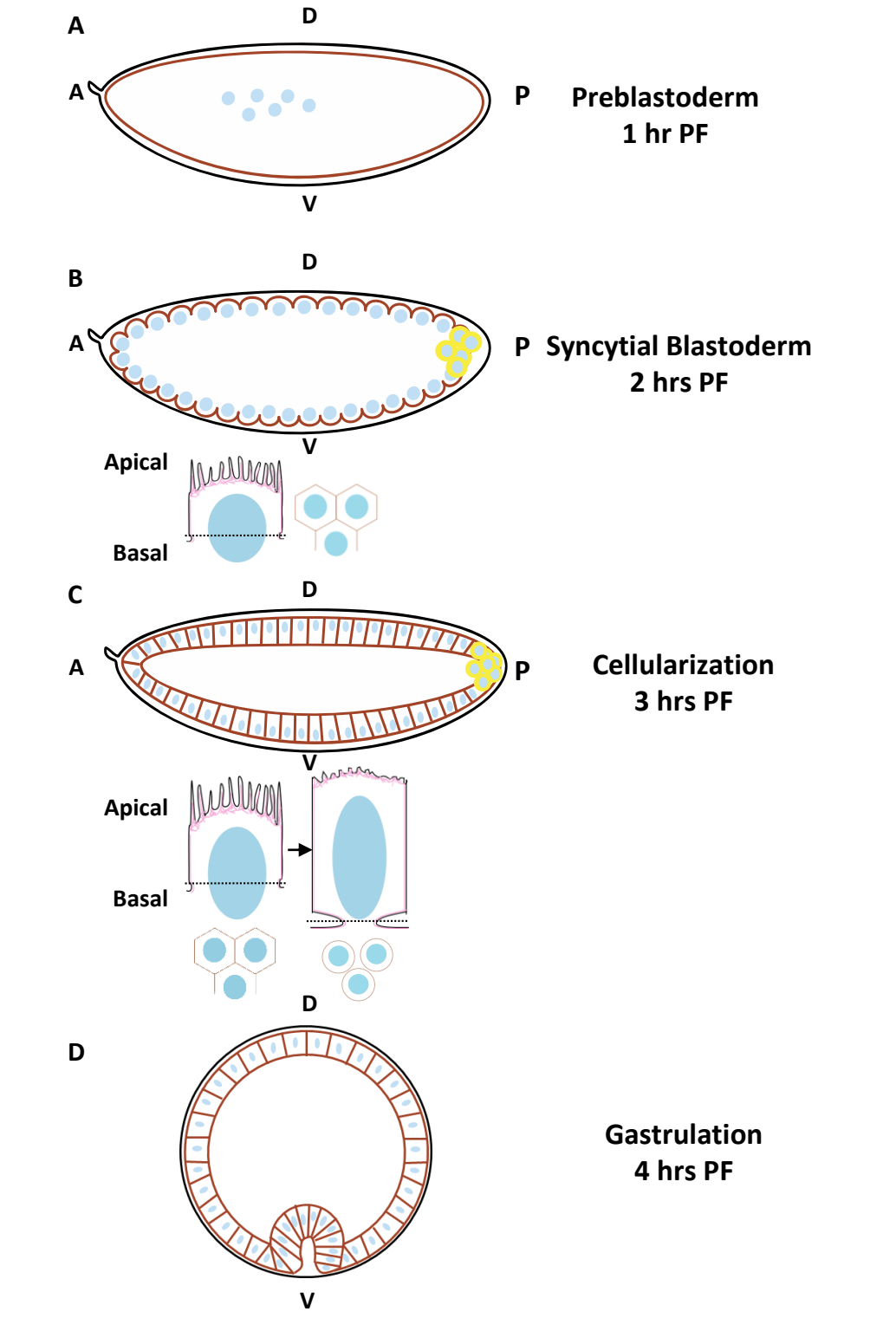
A
D
A
P
V
Preblastoderm
1 hr PF
B
D
A
P
V
Syncytial Blastoderm
2 hrs PF
Apical
Basal
C
D
A
P
V
Cellularization
3 hrs PF
Apical
Basal
D
D
V
Gastrulation
4 hrs PF
Vitelline membrane
Plasma membrane
Nucleus
Germ cell

Figure 1.6: *Drosophila* embryogenesis as a model system to study mitochondria. Post fertilization, nuclei divide deep inside the embryo from NC1 - 9 (**A**). Nuclei migrate cortically at NC10 and undergo synchronous divisions till NC 13 (**B**). Plasma membrane is covers the nuclei apically as seen in zoomed in sagittal schematics. Grazing section through membrane tips (dashed black line) shows hexagonal arrangement of cells (**B**). Pole cells (yellow) are the only complete cells at this stage (**B**). Membranes ingress to enclose the nuclei completely during cellularization at NC 14 (**C**). The morphology at the basal sections (grazing sections from sagittal indicated by black dotted lines) changes from hexagonal to circular as the membrane constricts (**C**). Cells at the ventral region constrict and invaginate during gastrulation (**D**).

1.4 Objectives of the project

The role of mitochondria during embryogenesis has been largely addressed using complex mammalian systems that develop *in ovo.* Hints from literature, as mentioned above suggest regulation of mitochondrial shape, metabolism and localization during embryonic development and patterning. However, a systematic and descriptive analysis of whether mitochondria can regulate signalling in the embryos has not been critically analysed which motivated me to ask the following question:

Is mitochondrial morphology, dynamics and function regulated in a systematic manner during organism development and does it influence patterning?

I used *Drosophila* embryogenesis as the model system to address the above mentioned question. It is divided in following aims for this thesis

1.4.1 Characterization of mitochondrial morphology, localization and function in the early *Drosophila* embryo

1.4.2 Analysis of cytoskeletal regulation of mitochondrial distribution and transport in the embryo.

1.4.3 Investigation of mitochondrial morphology mutations and their impact on the *Drosophila* early development

1.4.4 Studying interactions of mitochondria with embryonic patterning pathways.

Using the *Drosophila* embryo as the model system I first characterized mitochondrial localization and shape using transgenic GFP tag. Based on results obtained, we identified their interaction with microtubules and proposed a regulation of mitochondrial distribution and activity based on the axis specification signalling.

Chapter 2

Methods and Materials

2.1 *Drosophila* stocks and genetics

All fly stocks were raised on standard cornmeal agar at 25°C. All RNAi lines, transgenic mutants and transgenic fluorescently tagged lines were expressed using maternally expressed *nanos*-Gal4 or *mat*-Gal4 (Fig 2.1). Genomic deletion mutants of mitochondrial fission protein Drp1, $drp1^{KG}$ and $drp1^{nrd}$ were used in combination with RNA polymerase II 140 wimp mutant allele (*wimp*) and also with each other to generate heteroallelic combination. Embryos were obtained from F1 flies containing desired genetic combination to acquire maternally derived phenotype in the early embryos. Gal4 driver, RNAi or transgene combinations used are described in respective chapters. Following is a list of the fly stocks used.

Fly stock	**Source (Reference)**
Gal4 lines	
nanos-Gal4	BDRC 4937
mat-Gal4	Girish Ratnaparkhi
RNAi stocks	
khci	BDRC 35770
*dhc*i	BDRC 36583
$miro^{i}$	BDRC 43973
$cova^{i}$	BDRC 27548
$pdsw^{i}$	BDRC 29592

drp1^{i} (Valium 20)	VDRC
drp1^{i}	BDRC 51483
marf^{i} (Valium 1)	BDRC 31157
marf^{i} (Valium 20)	BDRC 55189
marf^{i} (MG)	Ming Guo Lab
opa1^{i} (Valium 20)	BDRC 32358
opa1^{i} (MG)	Ming Guo Lab
rhogef2^{i}	BDRC 34643
mbs^{i}	BDRC 41625
fog^{i}	Anuradha Ratnaparkhi (Ratnaparkhi and Zinn, 2007)
Genomic mutants	
drp1^{KG}	(Mitra et al., 2012; Rikhy et al., 2007)
drp1^{nrd}	(Mitra et al., 2012; Rikhy et al., 2007)
wimp	BDRC 5874
Mutant/ WT overexpression stocks	
UASp-*drp1*^{SG}	Generated in the lab by Darshika Tomer
UASp-*drp1*^{SD}	Generated in the lab by Darshika Tomer
UASp-*drp1*	Generated in the lab by Darshika Tomer
UASp-*hSOD1*^{A4V}	BDRC 33607

UASp-Sqh^{A20A21}	BDRC 64114
dl^{1},UASp-*dl*^{WT}	Girish Ratnaparkhi
Tagged transgenic lines	
UASp-Mito-GFP	Rachel Cox lab (Cox and Spradling, 2003)
UASp-mito-PAGFP	Generated in the lab
UAS-Tub-mCherry	Krishanu Ray lab
UAS-Marf-GFP	
Sqh-mCherry	BDRC 59024
Sqh-GFP	BDRC 57145
Recombinant and double balancer stocks	
nanos-Gal4::UASp-Mito-GFP	Generated by recombining *nanos*-Gal4 and UASp-Mito-GFP
nanos-Gal4::UASp-Mito-GFP::Sqh-mCherry	Generated by recombining *nanos*-Gal4:UASp-Mito-GFP and Sqh-mCherry
UASp-*drp1*^{SG}; *opa1*i	Generated in the lab

Table 2.1 2. List of *Drosophila* stocks used

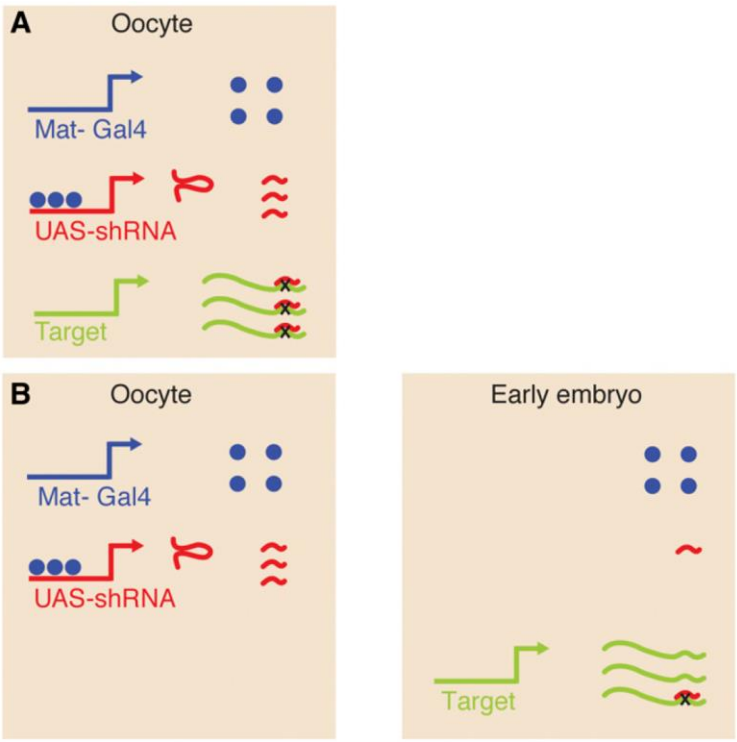

Figure 2.1: Knockdown of genes in the embryos using maternally expressed Gal4. Gal4 is expressed in the oocytes leading to production of UAS-shRNA that binds to and depletes maternally expressing target transcripts in the oocyte itself (**A**). Zygotic transcripts are depleted by maternally expressed UAS-shRNA dumped in the embryos (**B**). Adapted from (Staller et al., 2013)

2.2 Embryonic lethality estimation

3 hr old embryos were collected from cages containing yeast supplemented 3% sucrose agar plates. The embryos were aligned in 10 × 10 array (or a smaller one based on number of embryos obtained) on fresh 3% sucrose agar plates and incubated at the same temperature as the cross they were obtained from. The number of unhatched embryos was counted after 24 and 48 hrs of incubation and represented as a percentage.

2.3 Immunostaining

F1 flies of desired genotype were added to embryo collection cages containing yeast paste supplemented, 3% sucrose-agar plates. 3 hr old or 3.5 - 4hr old embryos were obtained for syncytial or cellularization-gastrulation stages respectively. Embryos were then washed, dechorionated with bleach for 1 min, fixed using 1:1 heptane and 4% paraformaldehyde

(PFA) in phosphate buffered saline (PBS - , 137 mM NaCl, 2.7 mM KCl, 10 mM Na_2HPO_4 and 1.8 mM KH_2PO_4) for 20 mins and devitellinized by shaking in 1:1 Heptate: Methanol or hand devitellinized using insulin needles. Hand-devitellinization was used for staining with F-actin label, phalloidin. 4% PFA was replaced by 8% PFA for Twist and dpErk immunostaining. The embryos were then washed thrice with PBS-T (Triton X-100, 0.3%), blocked using 2% bovine serum albumin (BSA) and incubated with primary antibodies diluted in BSA overnight at 4°C. Fluorescently labelled secondary antibodies diluted in PBST (1:1000) were added after washing excess primary antibody and incubated in dark conditions at room temperature for 45 mins, followed by 3 washes with PBST. Nuclear stain Hoechst 33342 (1:1000) was added in the second wash. The embryos were mounted on slides using Slowfade Gold (Life Technologies). The samples were imaged using Plan Apochromat 63x/1.4 NA, oil immersion objective on confocal laser scanning microscope (Zeiss, LSM 710 or 780 or Leica sp8). Z stacks with an interval of 1 µm were imaged. High resolution images of mitochondria were obtained using Light sheet, Zeiss LSM 800 microscope. The primary antibodies and fluorescently tagged compound used are listed below.

Antibody/Probe	**Source**	**Host Species (Ab)**	**Dilution**	**Catalogue Number**
pAMPK antibody	Cell Signalling	Rabbit	1:200	2535L
AMPK-alpha antibody	Abcam	Mouse	1:200	ab80039
Drp1 Antibody	Leo Pallanck	Rabbit	1:500	NA
Dorsal antibody	DSHB	Mouse	1:500	7A4-C
Twist antibody	Siegfried Roth, Koln University, Germany	Rabbit	1:200	NA
dpErk Antibody	Cell Signalling	Mouse	1:200	9106S
Fluorescently tagged streptavidin	Molecular Probes	NA	1:1000	S32354/ S11226

Fluorescently tagged phalloidin	Molecular Probes	NA	1:500	A12379/ A12380
Hoechst 33342	Molecular Probes	NA	1:1000	H3570

Table 2.2 List of antibodies and fluorescent probes

2.4 Inhibitor treatment and dye staining

Mito-GFP embryos of desired stage (2.5 - 3 hr old) were dechorionated in 100% bleach and incubated with drugs diluted using D-Limonene (Sigma): Heptane (1:1) (LH) at RT (Schulman et al., 2013) for the time mentioned below. Embryos were then fixed and stained as mentioned above (2.3). Drug concentrations and incubation time used were mentioned in the table below (Table 2.3). 10 mM FCCP stock was prepared in ethanol and 5 mM Rotenone, 10 mM Oligomycin and 5 mM 2-DG were made in DMSO. Treatment with an equivalent volume of ethanol or DMSO for the same duration as of the drugs was used as control.

To analyse changes in the membrane potential caused by the mitochondrial drugs, we used mitochondria permeable dye Mitotracker CMXRos Red (CMXRos). Embryos were incubated with 500 nM CMXRos from a stock of 1 mM was added to for 15 mins. CMXRos was incubated along with FCCP and Rotenone during the treatment. Oligomycin treated embryos and their controls were incubated with only CMXRos for additional 10 mins after the 5 mins of drug treatment to maintain the total incubation period. Embryos were then fixed and mounted on slides. Control and treatment samples were imaged at the same time using identical imaging settings.

For estimation of ROS, embryos were stained using dihydroethidium (DHE). Embryos were fixed using Heptane: 4%PFA, washed with PBS and incubated with 30nM DHE for 7 mins in PBS. The embryos were then washed with PBST and mounted on slides.

Reagent	Source	Incubation time	Concentration	Catalogue Number
Drugs				
FCCP	Sigma Aldrich	15 mins	10 µM	C2920-10 mg
Rotenone	Sigma Aldrich	30 mins	5 µM	R8875-5g
Oligomycin	Sigma Aldrich	5 mins	10 µM	75351-5MG
2-DG	Sigma Aldrich	15 mins	100µM	D6134
Fluorescent dyes				
Mitotracker CMXRos Red	Invitrogen	15 mins	500 nM	M7512
DHE	Invitrogen	7 mins	30 nM	D11347

Table 2.3 List of inhibitors and fluorescent dyes

2.5 Live imaging

1.5 hr old *nanos*Gal4-Mito-GFP embryos were collected from embryo collection cages. Embryos were dechorionated using 100% bleach for 1 min and washed. Embryos were mounted in 2 chambered cover glass dishes (LabTek, Germany) in PBS and imaged live at 25degC using 63x/1.4 NA objective on confocal laser scanning microscope (Zeiss LSM 710/780). 40 Z stacks with 1 µm interval were recorded. For visualizing the dorso ventral axis of embryos, they were placed in an end on fashion (Mavrakis et al., 2008; Witzberger et al., 2008). Two chambered cover-glass dishes (LabTek, Germany) were incubated with 200 µl of Sigmacote (Sigma Aldrich) per well for 5 mins (or till it evaporated) and washed with distilled water. The hydrophobicity of the cover-glass can be tested by adding a few drops of water. The embryos were initially mounted in laid down orientation in PBS. Then they were oriented with the posterior end towards the coverslip side using a small pointed brush.

Embryos were then imaged using Zeiss LSM 710/780, 63x 1.4 NA objective with temperature maintained at 25 °C.

2.6 Photobleaching

Photobleaching (Fluorescence recovery after photobleaching: FRAP) on Mito-GFP expressing embryos was performed using 488 nm laser at 100% and 30 iterations at a selected region of interest (ROI) of 4 µm2 using 63x/1.4 NA oil immersion objective on confocal laser scanning microscope (Zeiss LSM 780). For continuous photobleaching (Fluorescence loss in photobleaching: FLIP) the ROI was bleached every 18 sec. The images were acquired using 488 nm laser at 2%. Fluorescent intensities in the ROI and a neighbouring reference region were monitored and measured using Time Series Analyser Plugin in ImageJ. Background fluorescence intensity values were obtained from nuclear region for every photobleaching experiment. Background subtracted mean fluorescence intensity values were normalized using the pre-bleaching background subtracted intensity. The data were plotted using Graphpad Prism 6.0

2.7 Photoactivation

Embryos expressing Mito-PAGFP were photoactivated at selected ROIs using 405 nm laser at 100% power and 30 iterations using 63x/1.4 NA objective on confocal laser scanning microscope (Zeiss LSM 780). Images were obtained using 488 nm excitation wavelength. ROIs were drawn covering either entire cell or half the cell in a grazing section through nucleus in the syncytial embryos. Photoactivation in cellularizing embryos was performed in a rectangular ROI (10 – 15 μm^2) at basal regions (below the nuclei) in sagittal sections. Mean fluorescence intensities in photoactivated ROIs and reference ROIs were measured using ImageJ. They were normalized with mean intensity of the photoactivated ROI at the first time point. The averaged normalized intensity values for multiple embryos were plotted with standard error of mean (SEM) using Graphpad Prism 6.0.

Photoactivation in gastrulation was performed by aligning embryos in end on orientation (2.5). An ROI of 5 µm was drawn in a ring shape at the basal regions at cellularization end using 405 nm laser at 80% power, for 2 repeats using 63x/1.4 NA Plan apochromat objective on Leica sp8 confocal microscope. Fluorescence was measured in apical regions of ventral

cells and lateral cells using ImageJ. A ratio of apical:basal intensity was plotted with time using Graphpad Prism 6.0.

2.8 Western blotting

WT and mutant embryos aged 2.5 hrs were collected, dechorionated and homogenized using 150 µl of lysis buffer (1%Triton-X 100, 50 mM Tris HCl; pH 8.0, 150 mM NaCl, Protease Inhibitor Cocktail; PIC 1:50). The homogenate was sonicated for 50 sec with successive on and off cycles of 5 seconds each and centrifuged at 14000 g at 4 °C for 10 mins. The supernatant obtained was stored at -80 °C. Total protein concentration in the supernatent was estimated using BCA kit (Thermo Fisher Scientific). The supernatant (15 µg protein) with gel loading buffer was loaded in was loaded in 10% SDS gel wells and resolved at 90V. Separated proteins were blotted onto activated PVDF membrane at 4 °C at 90V for 3 hrs followed by 3 washes using TBST (20 mM Tris, 150 mM NaCl, 0.1% Tween 20). The blot was blocked using 5% milk for 1hr at RT and incubated with primary antibodies overnight. After 3 washes with TBST, the blot was incubated with HRP conjugated secondary antibodies at RT and developed using ECL prime blot detection reagent in ImageQuant™ LAS 4000. The protein concentration was estimated based on densitometric analysis in ImageJ.

2.9 ATP estimation assay

ATP estimation was carried out from embryo extracts by using luciferase based ATP determination Kit (Thermofischer scientific). 3 hr old embryos were collected and rinsed in heptane twice for permeabilization and subsequently dried completely. Embryos were manually crushed on ice using 1.5 ml microfuge tube pestle in homogenisation buffer (Tris (100 mM) and EDTA (100 µM)) till a uniform extract was obtained. The extract was lysed by boiling for 5 min and the supernatant was collected by spinning at 21000 g at 4 °C. Supernatant was diluted (1:10) in dilution buffer (25 mM Tris, 100 µM EDTA) and again spun at 21000 g at 4^{O}C. After diluting appropriately, Luciferin and firefly luciferase in buffer provided in the kit were added to the samples in 96 well white plates and ATP concentration dependent luminescence was measured immediately on a Varioskan Spectrometer at 560 nm. In order to ascertain reproducibility, both experimental and control samples were assayed at three different dilutions. Each dilution was loaded in triplicates and readings for the entire plate were taken thrice. All measurements were normalized to total protein

content of the embryos. Protein estimation was done using BCA kit (Thermofischer scientific) against standard BSA concentrations. Each sample was loaded in three different wells and emission for each well was measured thrice. All the experiments were repeated 3 times. The graph represents the percentage reduction corresponding to controls estimated at the same time. Means were compared using one tailed Mann-Whitney test in Graphpad prism 6.0.

2.10 Image analysis and quantification

2.10.1 Mitochondrial intensity in Z stacks

Mean mitochondrial fluorescence intensity was measured in Z stacks in live imaged Mito-GFP containing syncytial and cellularizing embryos using ImageJ. The mean intensity was normalized to the highest intensity value in each set. Average of 3 normalized intensities from 3 embryos was plotted with SEM using Graphpad Prism 6.0

2.10.2 Mitochondrial size and object number

Images obtained from either Mito-GFP containing or streptavidin tagged embryos were intensity thresholded by subtracting 1.5 times the mean intensity value of single image plane and mean intensity of projected images for Z stacks. Particles of size greater than 0.05 μm^2 were marked using particle analyser tool in ImageJ. Mean particle size was obtained for each embryo. To measure mitochondrial density, total area of threshold selected particles was divided by image area. The data were plotted and analysed using Graphpad Prism 6.0.

2.10.3 Mean fluorescence intensity quantifications

Difference between the levels of antibody signals and dye concentration between control and experiment embryos were estimated based on fluorescence intensity. The mean intensities were measured using ImageJ and represented as a fold change with respect to the control embryos. The data were plotted using Graphpad Prism 6.0.

To measure intensity of Sqh, total intensity of basal most section showing sharpest mCherry signal and 2 stacks above and below it (total Z depth - 4 µm) was measured using ImageJ and background corrected. A section below the nuclei containing uniform cytoplasmic mCherry signal in the first cellularization time point (membrane length - 3 µm) was chosen

to measure the background intensity (He et al., 2016). Mean for 3 embryos each with length was plotted using Graphpad Prism 6.0

2.10.4 Membrane length measurements

Lines were drawn in the sagittal section images from apical region to the membrane tips using the line tool in ImageJ. The data were plotted using Graphpad Prism 6.0.

2.10.5 Measurement of actin ring area and circularity

Circularity and area of the contractile rings were measured at the basal most membrane section from 5 contractile rings per embryo for fixed images or per time point for live samples. The ring area was marked manually using polygon tool in ImageJ. The membrane length for live samples were obtained from orthogonal projections of the Z stacks and sagittal section images for fixed samples. Circularity and area were plotted with membrane length using Graphpad Prism 6.0

2.10.6 Mitochondria and Myosin fluorescence in gastrulation.

The mean fluorescence during gastrulation was measured by drawing ROIs covering apical and basal regions in ventral, ventral flanking and lateral region cells at selected timepoints in the live end on movies. Ratios of apical:basal mean intensity was plotted with time using Graphpad Prism 6.0.

The experimental details of the analysis are mentioned in the each chapter wherever necessary.

Chapter 3

Mitochondrial morphology and dynamics in the syncytial *Drosophila* embryo

3.1 Introduction

Mitochondria along with almost every other essential organelles like Golgi and Endoplasmic reticulum (ER) are transferred from the oocyte to the embryo by cytoplasmic inheritance. Mitochondrial transport towards the oocyte in *Drosophila* oogenesis occurs with the help of microtubule motor Kinesin and its adapter Milton (Cox and Spradling, 2003, 2006; Wilsch-Bräuninger et al., 1997). Stem cells have small dispersed mitochondria that form more filamentous structures as the cells specialize (Chen et al., 2012). Mitochondria have nascent small globular structure in mammalian early blastoderm embryos and any imbalance in mitochondrial morphology by knocking down fission or fusion proteins leads to developmental arrest and embryonic lethality as shown by studies in the mammalian systems (Chen et al., 2000; Ishihara et al., 2009; Moore et al., 2010; Wakabayashi et al., 2009).

Reorganization of mitochondria and other cytoplasmic organelles is thought to occur due to calcium waves at the time of sperm entry at the time of fertilization (Roegiers et al., 1995; Savage and Danilchik, 1993). Mitochondria are localized around the nuclei in mammalian embryos and show distinct regions of active and inactive mitochondria. Reorganization of mitochondria and establishment of polarity occurs by calcium spikes during sperm entry in ascidian eggs. Site of relocalization of mitochondria also marks the future gastrulation site (Roegiers et al., 1995). This mitochondrial reorganization is essential for embryonic axis specification (Coffman et al., 2004). In summary mitochondrial shape, localization and function are seemingly essential for embryonic development but has not been explored in great details.

Drosophila embryogenesis begins with the nuclei dividing deep inside the embryo at preblastoderm stage (Fig. 3.1 A). Nuclei arrive at the cortex at nuclear division cycle (NC) 10 also leading to global reorganization of cytoskeletal structures in the embryo. Plasma membrane and actin assemble at NC10 and partially enclose the nuclei from the apical side giving rise to syncytial blastoderm embryo (Fig. 3.1 B). Microtubules orient apicobasally with centrioles present towards the apical side of every nucleus forming an inverted basket like structure with microtubule polymerizing ends towards the basal side. Despite the presence of free cytoplasm at the basal regions of the nuclei, each nucleo-cytoplasmic territory is defined and does not share its organelles and plasma membrane components with the neighbours (Frescas et al., 2006; Mavrakis et al., 2009). We call each such territory a syncytial cell. Nuclei divide 4 times in the syncytial stage. The cytoskeletal organization remains more or less similar during this stage. Mitochondria have been observed in *Drosophila* embryos using EMs earlier (Akiyama and Okada, 1992). We developed and standardized live imaging techniques to observe and analyse mitochondrial distribution and shape dynamics in the *Drosophila* embryo and found that they are small and dispersed around the syncytial nuclei and their distribution is regulated by microtubules. Data from this chapter are published as a part of (Chowdhary et al., 2017).

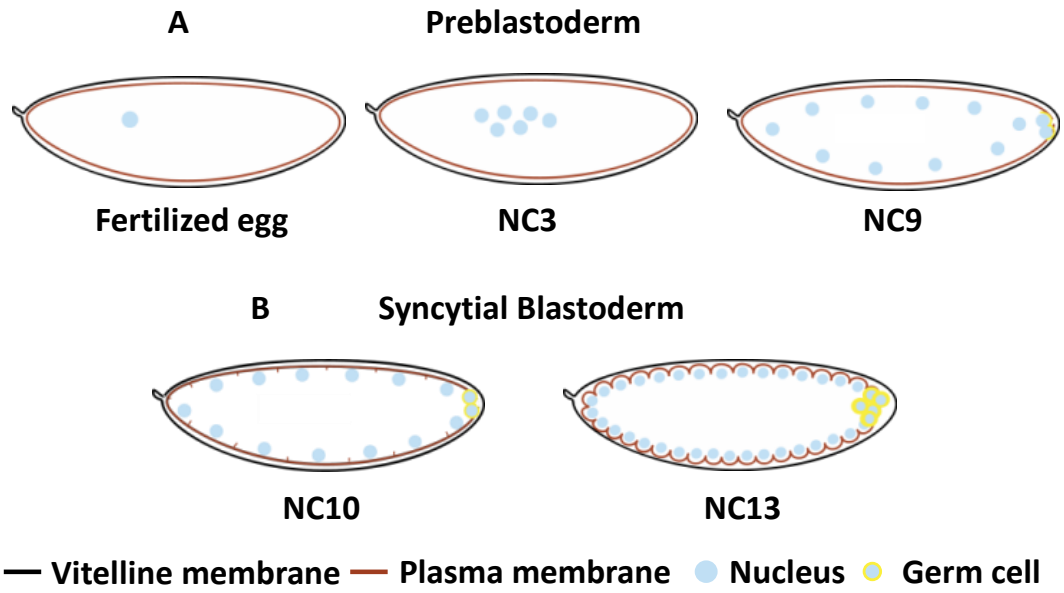

Figure 3.1: Schematic representing NCs during syncytial stage of *Drosophila* embryogenesis. After fertilization (**A, first image**), nuclear divisions (NC) 1-9 take place deep inside the embryo during preblastoderm stage (**A**). Nuclei migrate to the cortex at NC 10 (**B,**

First image) and divide 4 times till NC 13 (**B, Second image**) during the syncytial blastoderm stage (**B**). Adapted from (Chowdhary et al., 2017).

3.2 Materials and methods

3.2.1 Fly Stocks

All *Drosophila* stocks and crosses were maintained at 25 °C on standard cornmeal agar medium. UASp-MitoGFP and UASp-MitoPAGFP were expressed using *nanos*-Gal4. *nanos*-Gal4, Mito-GFP recombinant line was made using standard genetic crosses. *khc* and *dhc64C* RNAi lines were obtained from Bloomington and expressed using *nanos*-Gal4. UASp-Tub-mCherry was from Krishanu Ray (TIFR, Mumbai). Nanos is present embryonic posterior side and is a key body axis patterning determinant. It is expressed in the nurse cells, and thus amount RNAi is dumped maternally, or the amount of protein inherited by the embryo is reduced. The F2 embryos from F1 flies containing both *nanos*-Gal4 and the RNAi were collected as mentioned below (2.2.3, 2.2.4). UASp-MitoGFP stock was obtained from Rachel Cox(Cox and Spradling, 2003). UASp-MitoPAGFP stock was made by Devashree Sambre as described below.

Name	Source (Reference)
nanos-Gal4	BDRC 4937
UASp-Mito-GFP	Rachel Cox lab (Cox and Spradling, 2003)
UASp-mito-PAGFP	Generated in the lab
UAS-Tub-mCherry	Krishanu Ray lab
khc^{i}	BDRC 35770

dhc^{i}	BDRC 36583

Table 3.1: List of fly Strains used.

3.2.2 Cloning

pUASp-Mito-PAGFP

The Mito-YFP construct in the pUASP vector was obtained from Rachel Cox. This construct contains the mitochondrial targeting sequence from human cytochrome oxidase VIII fused to YFP. The PAGFP-N1 vector was restriction digested with BamH1 and Xba1 and the PAGFP fragment obtained was subcloned into the pUASP-Mito-YFP vector to replace YFP with PAGFP. The pUASP-Mito-PAGFP vector injection into *Drosophila* embryos and selection of transgenic animals was done by the NCBS injection facility, Bangalore, India.

3.2.3 Immunostaining

F1 flies containing *nanos*-Gal4 and fluorescently tagged transgenes were selected and transferred to embryo collection cages. 3 hrs old embryos were collected on 3% sucrose agar plates, supplemented with yeast paste. Embryos were dechorionated with 100% bleach for 1 min, washed and then fixed using heptane: 4% paraformaldehyde (1:1) followed by hand devitellinization as mentioned in Chapter 2 (2.). Embryos were stained using fluorescently tagged streptavidin (1:1000, Molecular Probes, Bangalore, India) and phalloidin (1:500, Molecular Probes, Bangalore, India) diluted in PBS-T (0.3% Triton-X 100). Hoechst 33342 (1:1000, Molecular Probes, Bangalore, India) was added during washes. Embryos were mounted in Slowfade Gold (Life Technologies). Slides were stored at 4 °C.

Antibody/Probe	Source	Host species	Dilution
Fluorescently tagged streptavidin	Molecular Probes	NA	1:1000
Fluorescently tagged	Molecular Probes	NA	1:500

phalloidin			
Hoechst 33342	Molecular Probes	NA	1:1000

Table 3.2 List of reagents

3.2.4 Live Imaging

1.5 hr old *nanos*-Gal4::Mito-GFP (Mito-GFP) and *nanos*-Gal4/UASp-Mito-PAGFP (Mito-PAGFP) embryos were collected from embryo collection cages. Embryos were dechorionated using 100% bleach for 1 min and washed. Embryos were mounted in 2 chambered coverglass dishes in PBS and imaged live at 25 °C using Zeiss LSM 710/780, 63x 1.4 NA objective. Z stacks of 1 µm were recorded for duration of 2 hrs.

3.2.5 Photobleaching

Photobleaching (Fluorescence recovery after photobleaching: FRAP) on Mito-GFP expressing embryos was performed using parameters mentioned in chapter 2 (2.6) at selected region of interest (ROI) of 4 µm2 using Zeiss LSM 780, 63x, 1.4 NA objective. For continuous photobleaching (Fluorescence loss in photobleaching: FLIP) the ROI was bleached every 18 sec. The images were acquired using 488 nm laser at 2%. Fluorescent intensities in the ROI and a neighbouring reference region were monitored and measured using Time Series Analyser Plugin in ImageJ.

3.2.6 Photoactivation

Embryos expressing Mito-PA-GFP were photoactivated at selected ROIs using 405 nm laser at 100% power and 30 iterations using Zeiss LSM 780, 63x, 1.4 NA objective. Fluorescence intensities in photoactivated ROI and reference ROI were measured using ImageJ.

3.2.7 Analysis

3.2.7.1 Mitochondrial fluorescence across syncytial cycle

Mean mitochondrial fluorescence intensities were measured in optical sections from NC10 to 13 interphase, corrected using minimum intensity value and normalized to maximum

intensity for individual NCs. Average of 3 embryos was plotted against depth with standard error. Position of nuclei is shown with dotted lines.

3.2.7.2 Mitochondrial object number and density measurement

Bright mitochondrial punctae in apical sections of Mito-GFP live embryos were intensity thresholded and total numbers of optically separable objects in a fixed apical optical plane were measured using particle analyser tool with a threshold cut-off of 0.05 µm2 in ImageJ for every cell cycle stage of NC12. Particle size cut off was decided visually. The number of caps was counted based on the number of H2A-RFP tagged nuclei in any given field. Mitochondrial punctae per syncytial cell in NC12 were compared using one-way Kruskal Wallis test. Total number of punctae in NC12 and NC13 interphase were compared using two-tailed Mann-Whitney test using Graphpad prism 6.0.

Mitochondrial density was measured by obtaining total mitochondrial area post thresholding and normalization with total imaging field area in nocodazole treated embryos and *khc*^{i} embryos and compared with corresponding controls using two tailed Mann-Whitney test using Graphpad prism 6.0 software.

3.2.7.3 Photobleaching and Photoactivation

Mean fluorescence intensities of ROIs in the time series were measured using Time Series Analyser plugin in ImageJ. The minimum intensity value from the entire imaging field was subtracted from each image. The background subtracted mean intensity values were normalized using pre-bleach intensity and post activation intensity values for FRAP, FLIP and photoactivation (PA) respectively in each embryo. Mean of 3 embryos was plotted with standard error using Graphpad Prism 6.0.

To calculate relative intensities in daughter cells after PA, ROIs were drawn around photoactivated cells and their daughter cells and mean fluorescence intensities of ROIs were measured using ImageJ and corrected using average background intensity for each in interphase of NC11, 12 and 13 respectively. Average fluorescent intensities of all NC12 and 13 daughter cells of photoactivated NC11 mother cell in each embryo were calculated and normalized to mean fluorescence intensity of NC11 mother cells in individual embryos.

Histogram represents average of normalized intensities across 5 embryos. Means were compared using Student's t-test using Graphpad prism 6.0 software.

3.3 Results:

3.3.1: Mitochondria are fragmented and enriched basally in the syncytial *Drosophila* embryo

We visualized mitochondria using mitochondrial localized GFP (Mito-GFP) driven maternally using *nanos*-Gal4. Mito-GFP contains mitochondrial localization sequence from cytochrome C oxidase subunit VIII (COX 8A), targeting GFP to the mitochondrial matrix (Cox and Spradling, 2003). Biotinylated proteins are enriched in mitochondrial matrix of certain tissues(Hollinshead et al., 1997). We stained mitochondria in the syncytial embryo using fluorescently tagged streptavidin which colocalized with Mito-GFP (Fig. 3.2).

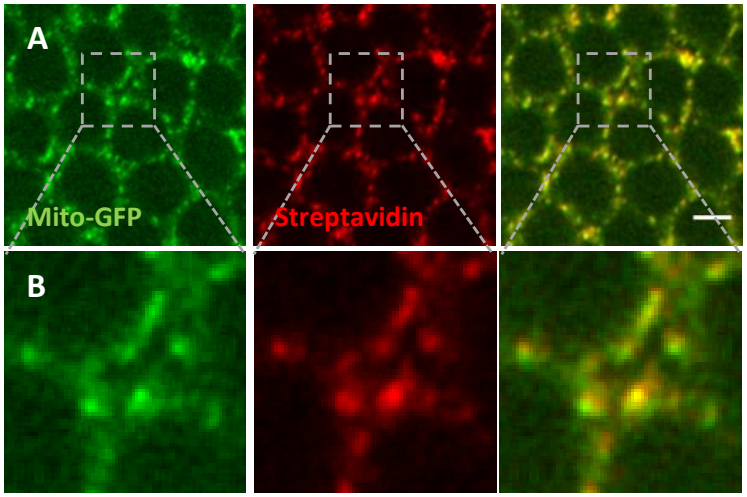

Figure 3.2 Mito-GFP colocalizes with streptavidin. Mito-GFP (green) embryos stained with fluorescently labelled streptavidin (red) (**A**) and zoom in (**B**). Scale Bar 5 µm. Adapted from (Chowdhary et al., 2017).

Mitochondria Major population of mitochondria was present at the cortex, around 5 - 10 um deep from the plasma membrane (Fig 3.3 A, B; 3.4 A, B). We observed that mitochondria were small and dispersed around the nuclei in preblastoderm and syncytial blastoderm

embryos. Despite absence of any cytoskeletal boundaries we found that mitochondria surround preblastoderm nuclei located deep within the embryo at NC9 (Fig. 3.3).

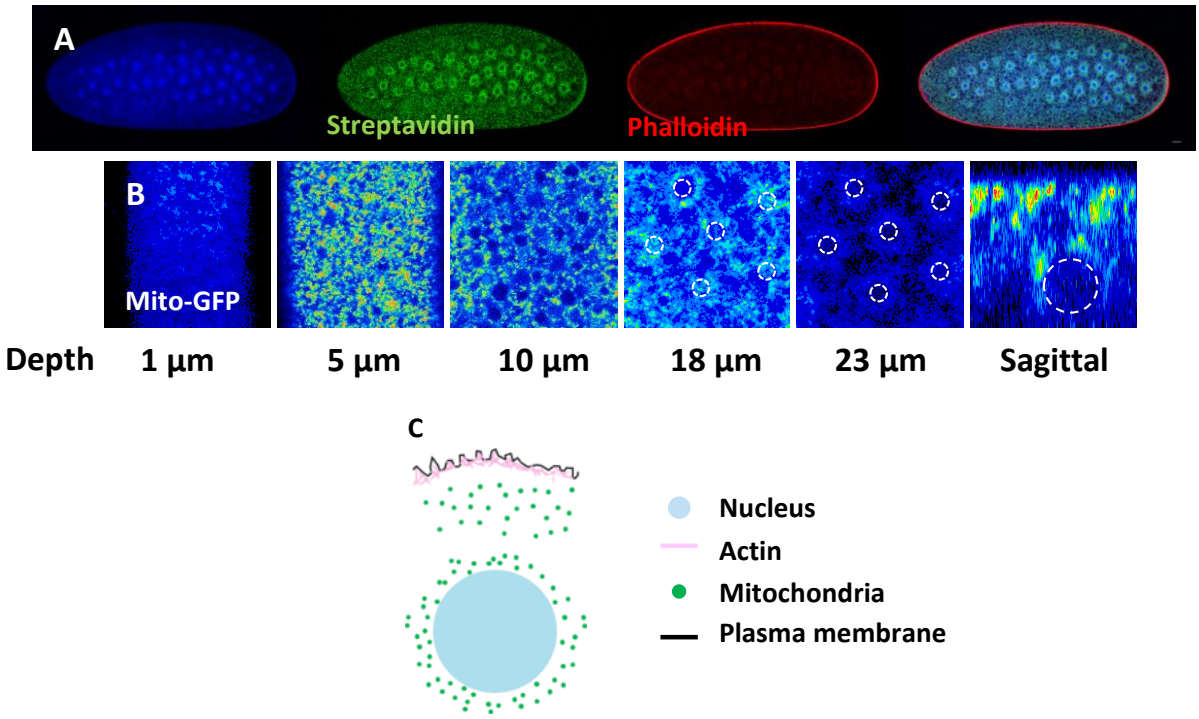

Figure 3.3 Mitochondrial distribution in preblastoderm embryos. Mitochondria (streptavidin, green) are seen around nuclei (Hoechst, blue) deep inside the embryo with f-actin staining (phalloidin, red) (**A**). Mitochondria visualized with Mito-GFP (rainbow scale) are present cortically and around nuclei (white dashed lines) at 23 µm depth from the cortex at NC9 and as seen in the sagittal section (**B**). Schematic depicting mitochondrial localization (green) around the preblastoderm nuclei (blue). Scale bar A: 100 µm, B: 10 µm. Adapted from (Chowdhary et al., 2017).

We then went on to characterize mitochondria in the syncytial blastoderm stage. Mitochondria majorly localized near the nuclei close to the cortex (Fig. 3.4 A). Using live imaging of Mito-GFP embryos, we quantified mean intensity of GFP signal from across depth apical to basal side in Z sections in the interphase of NC 10 to 13 and found that the intensity increased towards the basal side (Fig. 3.4 B-D). The basal localization of mitochondria became more pronounced with each NC (Fig. 3.4 D). The highest mean mitochondrial intensity was at 7 µm, 11 µm, 13 µm and 14 µm depths for NC10, 11, 12 and

13 respectively (Fig. 3.4 D). The mitochondria looked round punctate structures and the mean mitochondrial size was 0.2 μm^2 in the syncytial blastoderm embryo. The mean mitochondrial area per embryo was calculated around nuclei remained constant across NCs (Fig. 3.4 F) and during one syncytial NC (Fig. 3.4 G). We could also see using high resolution imaging that mitochondria were indeed small around the nuclei (Fig 3.4 H, 5 µm) and also in the crowded basal regions (Fig. 3.4 H 15 µm). The characteristic spatial distribution of mitochondria during the syncytial NCs hinted that regulation of their distribution in a polarized manner could be via microtubule based transport machinery or binding to another organelle such as the ER. We further characterized the mitochondrial dynamics using photo manipulation techniques.

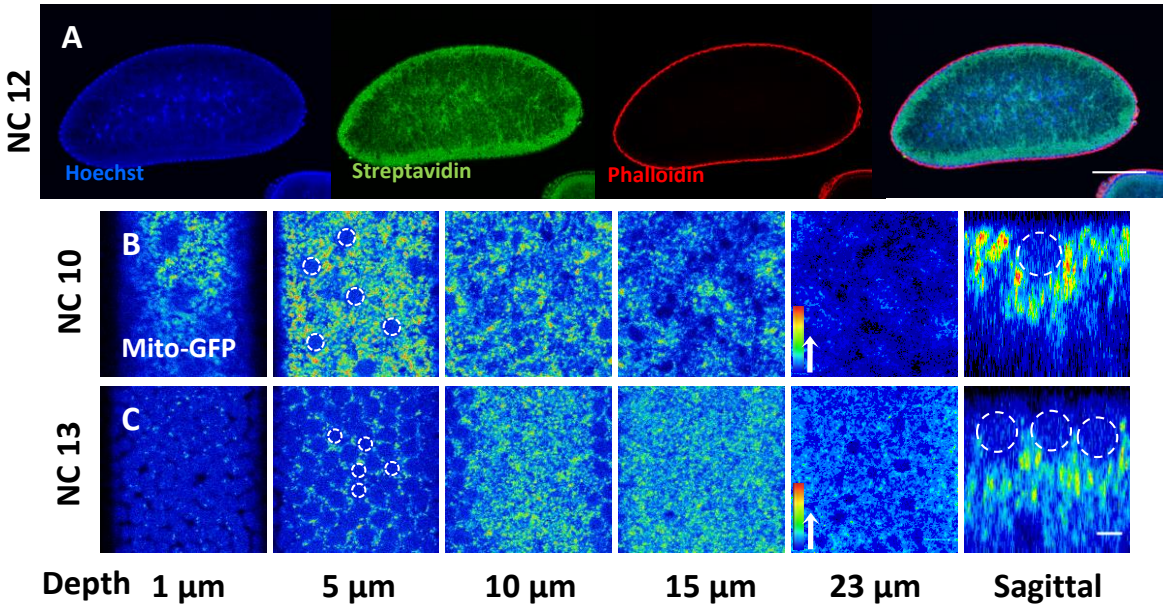
A
NC 12
Hoechst
Streptavidin
Phalloidin
B
NC 10
Mito-GFP
C
NC 13
Depth
1 µm
5 µm
10 µm
15 µm
23 µm
Sagittal

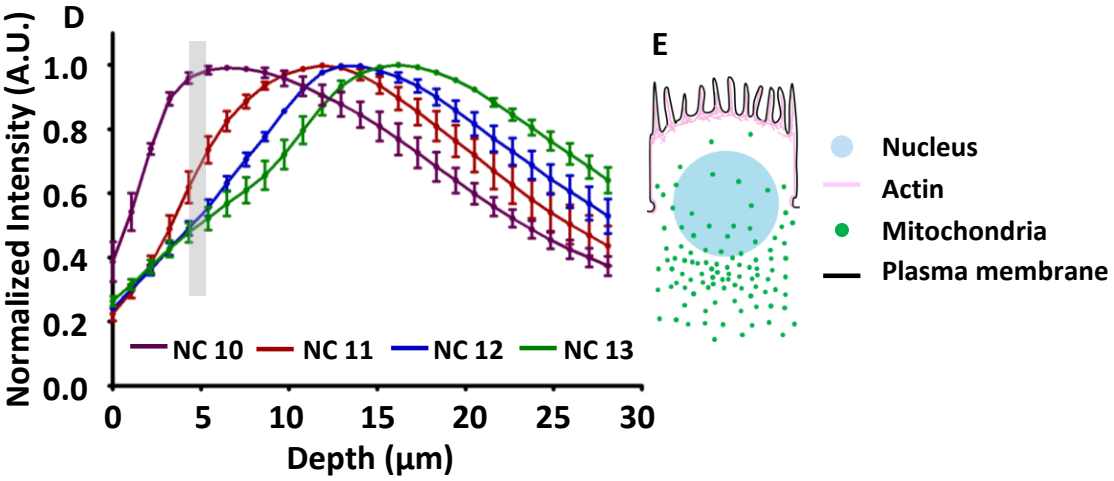
D
Normalized Intensity (A.U.)
1.0
0.8
0.6
0.4
0.2
0.0
NC 10
NC 11
NC 12
NC 13
0
5
10
15
20
25
30
Depth (µm)
E
Nucleus
Actin
Mitochondria
Plasma membrane

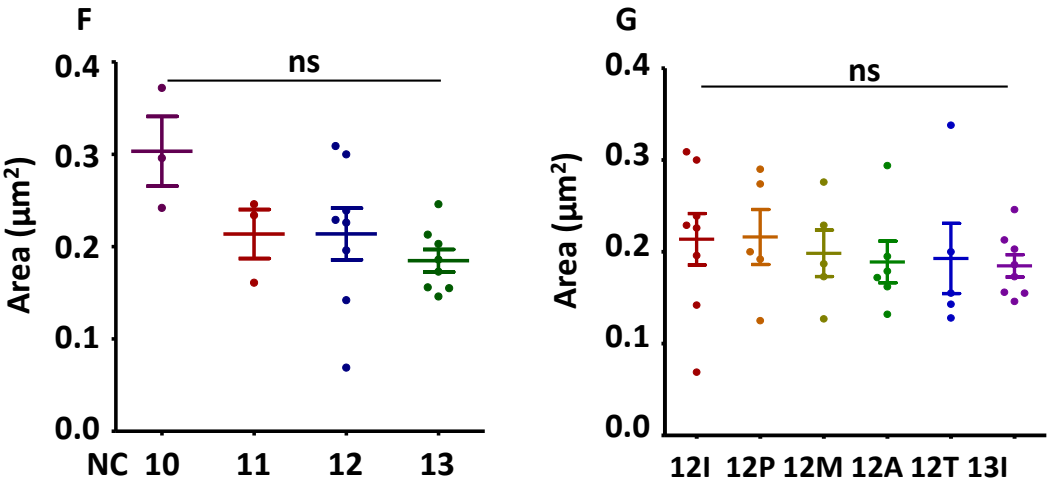
F
Area (µm²)
0.4
0.3
0.2
0.1
0.0
ns
NC 10
11
12
13
G
Area (µm²)
0.4
0.3
0.2
0.1
0.0
ns
12I
12P
12M
12A
12T
13I

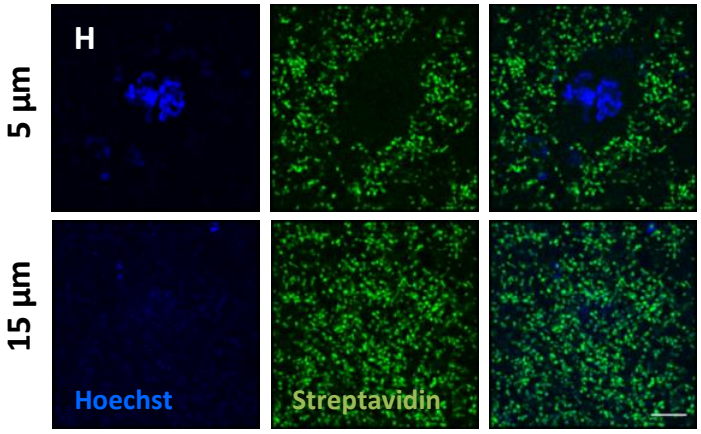

Figure 3.4: A-E: Mitochondrial distribution in syncytial blastoderm embryo. NC12 *Drosophila* embryos show cortical localization of mitochondria (streptavidin, green) (**A**). Mitochondria (Rainbow scale, Mito-GFP) distribute around nuclei as they arrive at the cortex (5 µm) in NC10 (**B**) and localize below the nuclei (**B**, sagittal). Mitochondrial intensity in NC 13 as well is higher below the nuclei at 10–15 µm depth (**C**) and also seen in sagittal section (**C**). Rainbow scale represents pseudocoloured intensity values (**B, C**). Quantification of mean Mito-GFP intensity is plotted with SEM for n = 3 embryos/NC and 15, 30, 60 and 120 syncytial cells for NC10 (Purple), 11 (Red), 12 (Blue) and 13 (Green) respectively shows peak values deeper than nuclear location (Grey box) (**D**). Schematic of mitochondrial localization during syncytial blastoderm stage (**E**). **F-H:** Mitochondria are small and dispersed in syncytial blastoderm. Quantification of mean mitochondrial area quantified from Mito-GFP embryos in NC10I (Purple), 11I (Red), 12I (Blue) and 13I (Green) shows no difference in mitochondrial morphology (**F**). Mitochondrial morphology does not change during NCs as shown by quantification of mean mitochondrial area per embryo in NC12I, 12P, 12M, 12A, 12T and 13I (12I: interphase NC12, 12 P: prophase, 12 M: metaphase 12 A: anaphase 12 T: telophase 13I: interphase NC13) (**G**). Numbers represent the number of embryos quantified (**F, G**). (ns, P>0.05, one way Kruskal – Wallis test). High resolution imaging of dispersed mitochondria in NC11, Streptavidin (green); Nucleus (blue) at section through nucleus (5 µm) and basal section (15 µm) (**H**). Scale bar A: 100 µm, B-C: 10 µm, H: 2 µm. Adapted from (Chowdhary et al., 2017).

3.3.2: Mitochondria show restricted lateral movements in syncytial blastoderm embryo

Single layer of *Drosophila* blastoderm nuclei is organized at embryonic cortex with partial enclosure of plasma membrane at the apical side. Despite the presence of "free" cytoplasm at the basal region of the nuclei, organelles like the endoplasmic reticulum (ER) and Golgi Complexes are compartmentalized to one nucleo-cytoplasmic region. Protein cargo delivery from ER, Golgi to the plasma membrane is seemingly regulated locally (Frescas et al., 2006). Plasma membrane bound protein also display very slow diffusion across neighbouring syncytial cells (Mavrakis et al., 2009). Compared to these organelles and the plasma membrane, mitochondria are more distinct and smaller units, spread throughout the syncytial cells. Therefore we decided to test whether like Golgi complexes and ER, mitochondria also displayed compartmentalization. This was done using photobleaching and photoactivation techniques as described in section 3.2.5 and 3.2.6.

We tracked mitochondrial dynamics using photobleaching. We bleached a region of interest (ROI, red) close to the nucleus in the syncytial cells using high intensity 488 nm laser as mentioned in materials and methods (3.2.5) (Fig 3.5 A) and looked for recovery in the fluorescence after photobleaching (FRAP) (Fig 3.5 B). Drop in the intensity post photobleaching did not recover significantly within 2 mins (Fig. 3.5 C). This indicates that mitochondria either do not move or move very slowly.

To analyse the extent of the mitochondrial movements and also if they can be transported to the neighbouring cell due to the presence of shared basal cytoplasmic pool we performed fluorescence loss after photobleaching (FLIP) experiment. We used FLIP of Mito-GFP, and monitored fluorescence loss in neighbouring syncytial cells to assess if mitochondria were moving between them in interphase of the syncytial cycle (Fig. 3.5 D). We continuously photobleached an ROI in one cell (red), analysed and observed no reduction in Mito-GFP fluorescence on monitoring an ROI in neighbouring syncytial cells (green) (Fig. 3.5 D, E) showing that mitochondrial movement is restricted to individual syncytial cells in the embryo over the time scale of 100 s within interphase of the same syncytial cycle when the plasma membrane length is known to be the shortest. No depletion of signal from the neighbouring syncytial cell was observed in photobleaching experiments in previous studies

over a similar time scale for the Golgi Complex, ER and plasma membrane (Frescas et al., 2006).

We used photoactivation to highlight a specific mitochondrial population more precisely in syncytial cells and monitored their distribution within and across adjacent syncytial cells over time. This allowed us to monitor mitochondrial movements for a longer duration in the syncytial cells. We used *nanos*-Gal4 to drive the expression of UAS-Mito-PAGFP in the embryos. The Mito-PAGFP localization specificity was tested using fluorescent streptavidin. Both fluorescence signals completely colocalized showing that it targets appropriately to mitochondria (Fig. 3.5 F). We photoactivated Mito-PAGFP fluorescence (3.2.6) in an entire syncytial cell in interphase and monitored neighbouring cells for appearance of fluorescent mitochondria (Fig. 3.5 G, H). The fluorescence of photoactivated mitochondria did not change significantly in the photoactivated cell and did not increase in the neighbouring syncytial cells confirming that there was no exchange of mitochondria between them over the time scale of more than 270 s within the same syncytial cycle (Fig. 3.5 I).

Moreover, we activated a syncytial cell partially, with the ROI covering approximately half the area around nucleus, and followed the remaining non- activated area of the same cell (Fig. 3.5 J). Interestingly no fluorescence gain was observed in the control area (Fig, 3.5 K). This strongly suggests that mitochondria are considerably stationary in the given imaging plane of analysis i.e. the lateral region. This is different in comparison with ER and Golgi complexes that exchange fluorescence within one syncytial cells as shown by using FLIP previously (Frescas et al., 2006). This hints towards binding of mitochondria to a structurally rigid moiety such as microtubules.

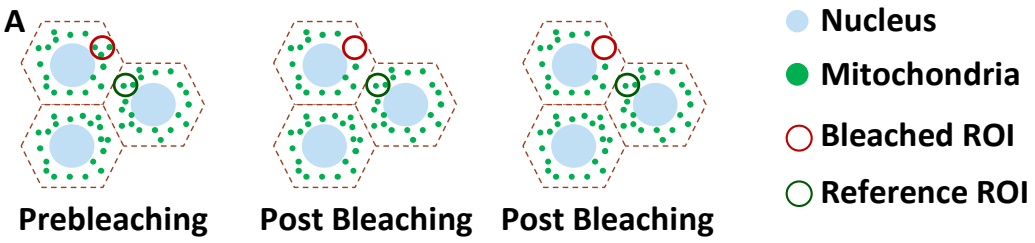
A
Nucleus
Mitochondria
Bleached ROI
Reference ROI
Prebleaching
Post Bleaching
Post Bleaching

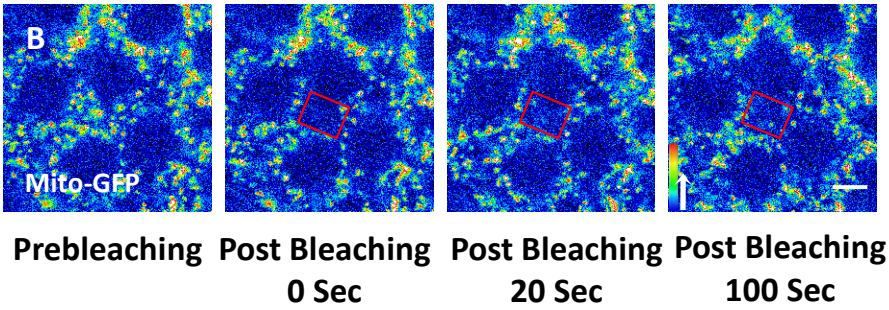
B
Mito-GFP
Prebleaching
Post Bleaching
0 Sec
Post Bleaching
20 Sec
Post Bleaching
100 Sec

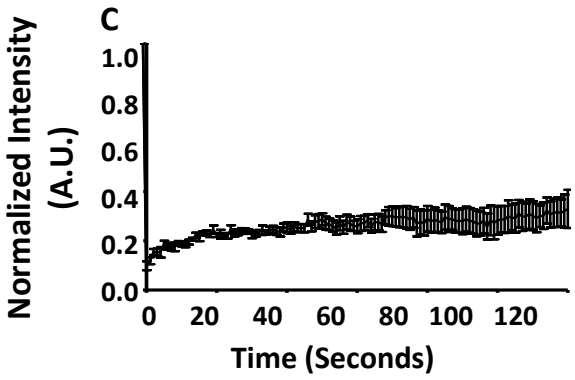
C
Normalized Intensity
(A.U.)
1.0
0.8
0.6
0.4
0.2
0.0
0
20
40
60
80
100
120
Time (Seconds)

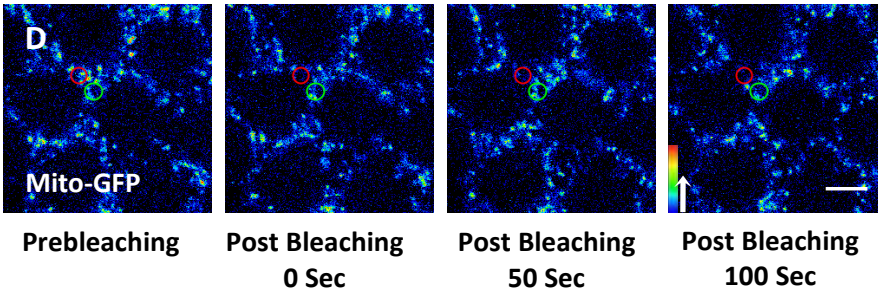
D
Mito-GFP
Prebleaching
Post Bleaching
0 Sec
Post Bleaching
50 Sec
Post Bleaching
100 Sec

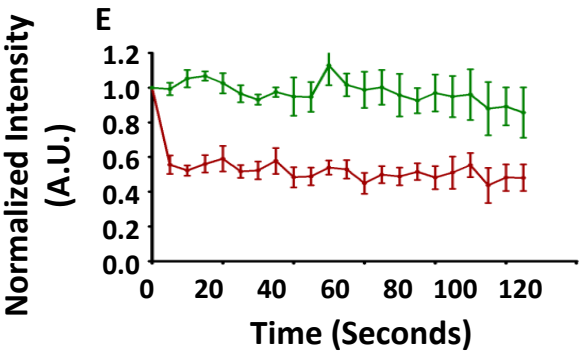
E
Normalized Intensity
(A.U.)
1.2
1.0
0.8
0.6
0.4
0.2
0.0
0
20
40
60
80
100
120
Time (Seconds)

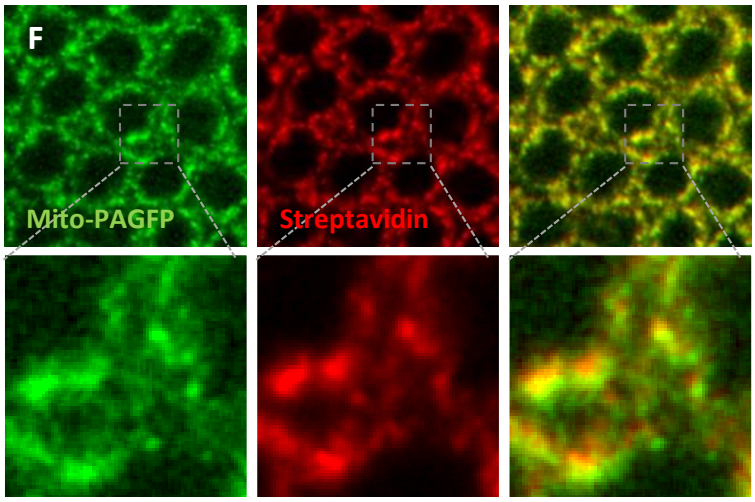
F
Mito-PAGFP
Streptavidin

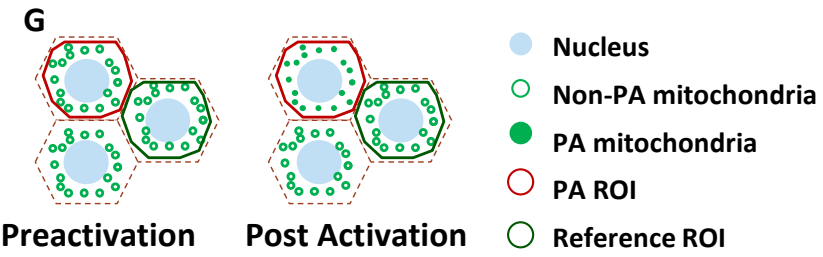
G
Nucleus
Non-PA mitochondria
PA mitochondria
PA ROI
Reference ROI
Preactivation
Post Activation

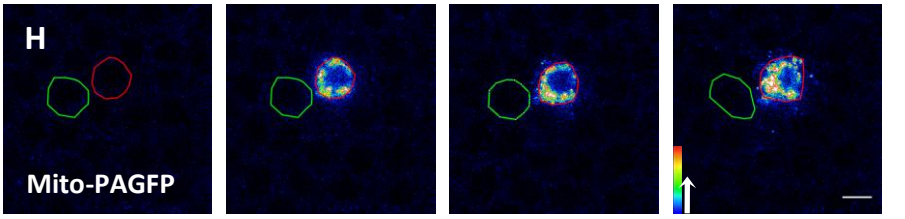
H
Mito-PAGFP
Preactivation
Post Activation 0 Sec
Post Activation 52.4 Sec
Post Activation 183.4 Sec

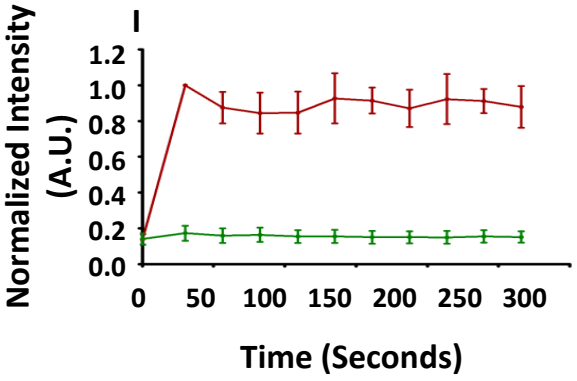
I
Normalized Intensity (A.U.)
1.2
1.0
0.8
0.6
0.4
0.2
0.0
0
50
100
150
200
250
300
Time (Seconds)

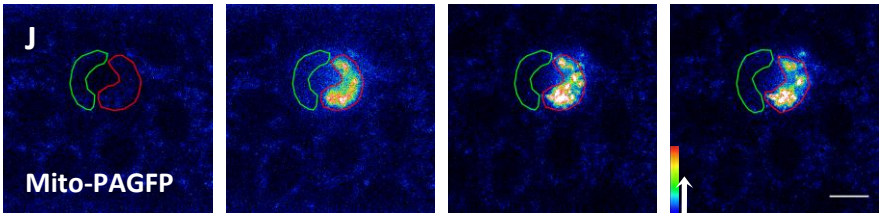
J
Mito-PAGFP
Preactivation
Post Activation 0 Sec
Post Activation 50 Sec
Post Activation 100 Sec

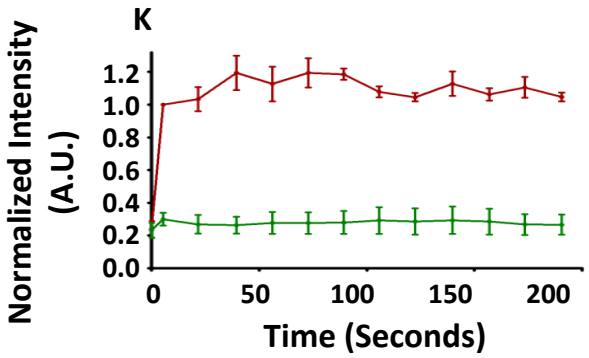

Figure 3.5 Mitochondria show restricted movements in the lateral plane of syncytial cell. (**A-E**) Photobleaching of Mito-GFP embryos as shown in schematic with photobleached ROI (red) and reference ROI (green) (**A**). FRAP in the ROI of 5 μm^2 (red) done with Mito-GFP NC 12 interphase embryos does not show significant recovery (**B**). Normalized mean intensity is plotted (**C**). FLIP experiment in Mito-GFP is done in an ROI of 4 μm^2 (red) in interphase of the NC13 (**D**). Fluorescence in the neighbouring syncytial cell ROI (green) does not deplete. Normalized mean intensity of bleached (red) and non-bleached (green) ROI with SEM is plotted with respect to time (**E**). (**F-K**): Restricted localization of mitochondria is observed in photoactivation, Mito-PAGFP colocalizes with streptavidin (**F,** zoomed in images, bottom panel). Schematic representation of photoactivation experiment with photoactivated (red) and non-photoactivated (green) cells. Photoactivated and non-photoactivated mitochondria are shown as filled and open green circles respectively (**G**). Mito-PAGFP is activated in one syncytial cell (red) and fluorescence is monitored in neighbouring cell (green) that does not gain fluorescence in the given time (**H**) in NC12 interphase. Normalized mean fluorescence intensity of activated (red) and neighbouring (green) cell is plotted (**I**). Mito-PAGFP is activated in half the syncytial cell (red) and remaining region (green) from the same cell is monitored (**J**). Non-activated part of the cell (green) does not have an increase in fluorescence with time. Normalized mean fluorescence intensity of activated (red) and non-activated (green) region is plotted against time (**K**). n = 5 for C and 3 for E, I and K each. Rainbow scale represents pseudo-coloured intensities. Scale Bar = 5 µm. Adapted from (Chowdhary et al., 2017).

3.3.3 Mitochondria are symmetrically distributed in daughter cells

We could follow the photoactivated mitochondria across cell division cycles in the *Drosophila* syncytial embryo. We photoactivated mitochondrial signal in the whole syncytial cell and followed it across NCs and measured the mitochondrial fluorescence in the daughter cells in each division with respect to the photoactivated mother cell (Fig 3.6 A,B). We found that the mitochondrial pool was halved with successive NCs (Fig. 3.6 C). When we activated a cell partially, only on one side of the spindle, the mitochondrial fluorescence was seen only in the daughter cell formed on that side (Fig. 3.6 D). This shows that mitochondria are symmetrically distributed in the daughter cells, reiterating that they are immobile in the lateral plane. Also, the static localization of mitochondria may in fact be necessary for symmetric distribution and specialized function in the given set of cells.

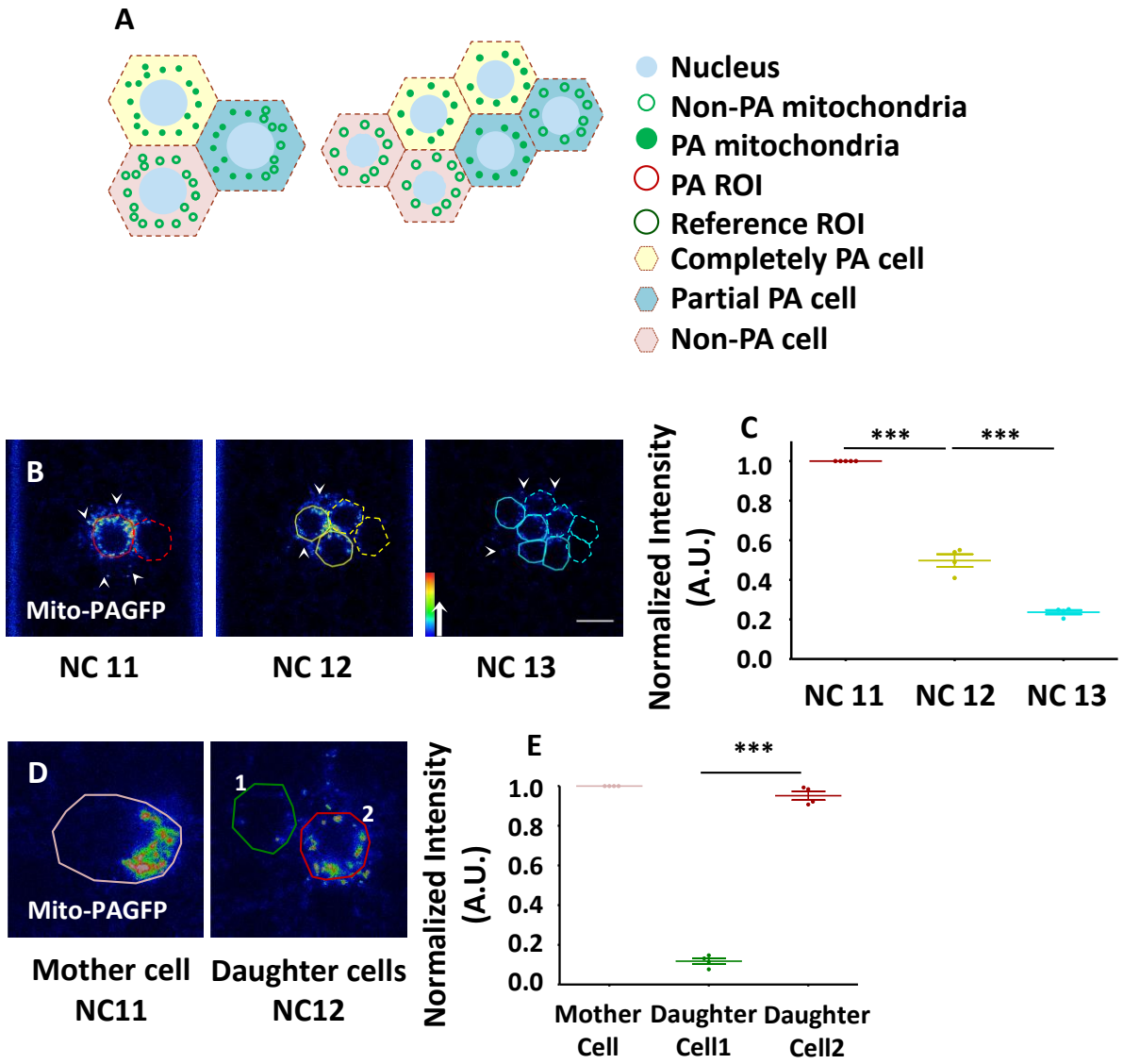

Figure 3.6 Mitochondria are symmetrically distributed to syncytial daughter cells. Schematic of photoactivation experiment that shows mitochondrial distribution from mother to daughter syncytial cells (**A**). Mother cell and respective daughter cells in the next NC are represented by the same colour. Mitochondrial fluorescence is activated in a complete cell (yellow) and partial cell (green). Non-photoactivated cell is shown (orange). Photoactivated and non photoactivated mitochondria are shown by filled and open circles (green) (**A**). Mito-PAGFP is activated in the ROI comprising an entire syncytial cell in 11I (red) and partially in the neighbours (white arrows) and daughter syncytial cells in 12I (yellow, solid line) and 13I (cyan, solid line) are followed. (**B**): Mean intensity in measured NC11–13 is normalized to corresponding NC11 intensities and plotted with SEM (**C**). Photoactivated mitochondria on one side of mother syncytial cell (light red) are distributed to the daughter cell formed on the same side (red, 2) and not to the other cell (green, 1) (**D**). Normalized fluorescence intensity is shown in the two daughter cells (**E**). (***P ≤ 0.001, Student's t-test, n = 4 embryos for C and E) The intensity is shown as a pseudocolored rainbow scaled image. Adapted from (Chowdhary et al., 2017).

3.3.4 Mitochondria move apico-basally during cell divisions

The mitochondria are distributed asymmetrically in the apico-basal axis of the syncytial cells, with a high density towards the basal regions. The apical regions are sparse and discrete mitochondria can be seen just below the apical plasma membrane and actin meshwork at the caps. On inspecting carefully, we observed that the mitochondrial number at these sections changed in a stage specific manner. We counted the number of mitochondria present at these apical regions using an intensity based threshold across different stages of NCs (Fig. 3.7 A). Firstly we counted the number of mitochondria in each apical cap in interphase (12I), prophase (12 P), metaphase (12 M), anaphase (12 A) and telophase (12 T) of NC12 and interphase of NC13 (13I), and noticed an increase in during 12 M and 12 A and 12 T. The number of mitochondria per cap in the interphase of different NCs were similar (Fig 3.7 B). We then calculated the total number of mitochondria in a fixed area in the interphase of the division cycles and found that the mitochondrial number almost doubled in the successive NCs (Fig 3.7 C). The increase in the mitochondria accounts for the

maintenance of the distribution in each NC where the number of nuclei double with every NC. Also since mitochondria are compartmentalized to one nucleo-cytoplasmic region and do not travel between neighbouring syncytial cells, the increase in mitochondrial number is most likely due to transport of mitochondria from the basal side to the apical side.

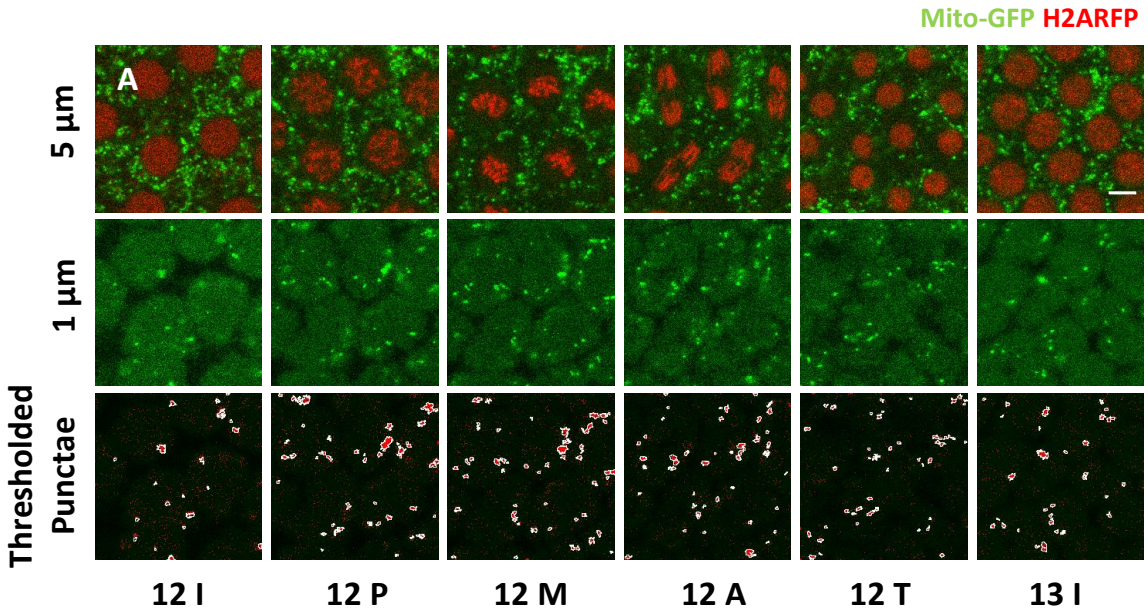

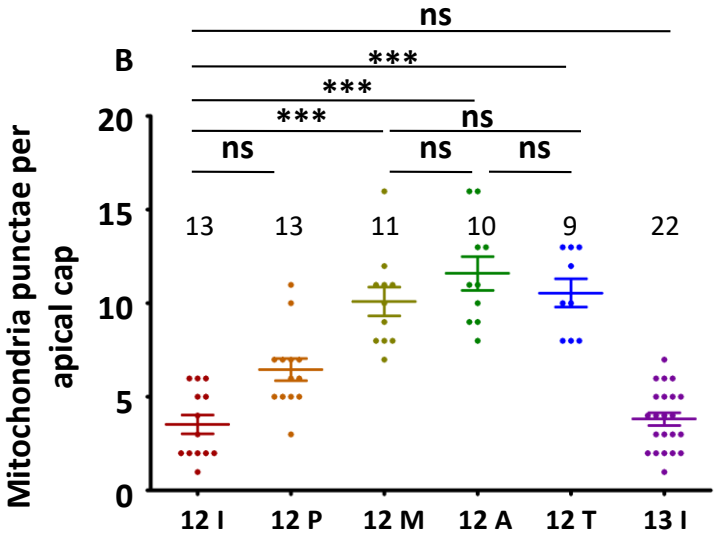

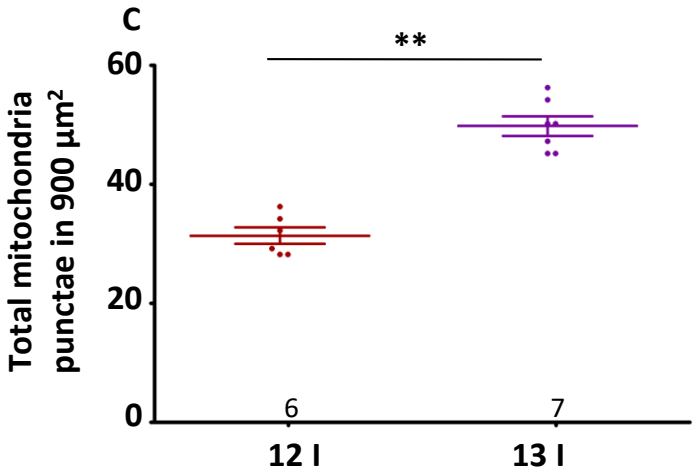

Figure 3.7 (**A**) **Apical mitochondrial number increases during metaphase of the syncytial cycle**. Mito-GFP (green) and Histone2A-RFP (red) embryo is shown across the NC12 at 5 µm (1st panel) and 1 µm (2nd panel) depths from the apical side. Distinct mitochondrial punctae seen at 1 µm depth (2nd panel) are marked after thresholding (3rd panel) (**A**). (**B**, **C**) Quantification of mitochondria across syncytial cycles. Number of mitochondrial puncta per syncytial cell significantly increases in metaphase (12M) and the number is conserved between 12I and 13I (**B**) (n = 4 embryos, 13, 13, 11, 10, 9, 22 syncytial cells for 12I, 12 P, 12 M, 12 A, 12 T and 13I respectively. ns–not significant; ***P ≤ 0.001, one way Kruskal Wallis test). Total number of mitochondria in 900 µm^2 area are compared between 12I and 13I (**C**) (n = 6 and 7 embryos; each point is an average from 20 and 50 syncytial cells for 12I and 13 I respectively, **P ≤ 0.01, two tailed Mann-Whitney test). Scale bar A: 5 µm. Adapted from (Chowdhary et al., 2017).

3.3.5 Mitochondrial distribution is regulated by microtubules

Syncytial cells are apico basally polarized with microtubules present in an inverted basket manner around the nuclei with centrioles present apically and the polymerizing positive ends towards the basal side. Such organization of microtubules has been reported and studied in polarized epithelial cells (Müsch, 2004) and is essential for polarized sorting of proteins and vesicles (Mostov et al., 2000; Nelson and Yeaman, 2001) with the help of Golgi Complexes (Kreitzer et al., 2000; Toomre et al., 1999). In the *Drosophila* embryo lipid droplets redistribute based on microtubules at different stages in development (Edgar et al.,

1987; Welte et al., 1998). The compartmentalization of ER in the syncytial embryos is dependent on intact microtubules (Frescas et al., 2006). Mitochondria have been shown to travel long distances in cells with the help of microtubule motors and adapter proteins (Fransson et al., 2006a; Glater et al., 2006; Morris and Hollenbeck, 1995; Saotome et al., 2008; Schwarz, 2013; Varadi et al., 2004).

Since we had observed that mitochondria are asymmetrically distributed correlating with the microtubular arrangement, we decide to test if mitochondria too, like other organelles in the syncytium and also as observed in other cell systems localize onto microtubules.

3.3.5.1 Mitochondria are juxtaposed with microtubules

Actin is closely present next to the apical plasma membrane in the syncytial embryos. We used phalloidin to label actin and streptavidin to label the mitochondria. We did not see an appreciable colocalization between the two (Fig 3.8 A).

To study how mitochondria distribute with respect to microtubules, we imaged embryos for mitochondria and microtubules together using Mito-GFP and Tub-mCherry tags respectively. We found that mitochondria were present proximal to perinuclear microtubules during interphase and prophase and the spindle and astral microtubules during metaphase (Fig 3.8 B, D). Line profiles of mitochondria and microtubules were plotted using ImageJ and these showed a significant overlap (Fig. 3.8 C, E). This led us to test microtubule perturbations and their effect on mitochondrial distribution in the embryo.

3.3.5.2 Intact microtubules are needed to maintain mitochondrial distribution

To test whether intact microtubules regulate mitochondrial distribution, we depolymerized microtubules using nocodazole. Compared to DMSO control embryos, nocodazole treatment disrupts microtubules partially (34%) or completely (64%) (Fig. 3.8 F). We visualized mitochondria using streptavidin staining and found a significant reduction in the density of sub apical mitochondria (materials and methods) (Fig. 3.8 G, H). This shows that mitochondria are likely bound to the microtubules. We then knocked down microtubule motors kinesin and dynein motors to look at how the mitochondrial distribution is regulated.

3.3.5.3 Basal localization of mitochondria is Kinesin dependent

Kinesin heavy chain (Khc) is highly expressed in the early embryo from 0 - 2 hrs (modENCODE). It is the functional subunit of the microtubule motor Kinesin 1 and is responsible for mitochondrial trafficking in neurons (Glater et al., 2006; Martin et al., 1999). It is also responsible for acquisition of mitochondria during oogenesis with the help of adapter Milton (Cox and Spradling, 2006). We performed RNAi mediated knockdown of *khc* using *nanos*-Gal4 (*khc*i) and measured mitochondrial density in the sub apical regions of the syncytial cells. The mitochondrial density was significantly increased around the nuclei in the *khc*^{i} embryos compared to the control Mito-GFP embryos (Fig. 3.8 I, J).

Mitochondria are transported on dynein motors with the help of adapters (Haghnia et al., 2007; Martin et al., 1999). Microtubule minus ends are towards the apical side in the syncytial cells and dynein therefore is likely to be important for apical transport. We checked whether knocking down dynein makes mitochondrial orientation more basal as compared to the WT embryos and in a way opposite to the *khc*^{i} phenotype. We used dynein heavy chain RNAi (*dhc*^{i}) to deplete dynein activity and assessed mitochondrial distribution in syncytial cells. Although we observed slightly larger mitochondria in *dhc*^{i} (Fig. 3.8 I, white arrows), we did not find any difference between mitochondrial densities at subapical regions in *dhc*^{i} compared to control Mito-GFP (Fig. 3.8 I, J).

Mitochondria possibly move only in the apico basal direction and *khc*^{i} but not *dhc*^{i} showed an imbalance in their distribution. These data together indicate that mitochondrial distribution along microtubules is regulated by their transport towards the basal regions on Kinesin motors during syncytial blastoderm stage.

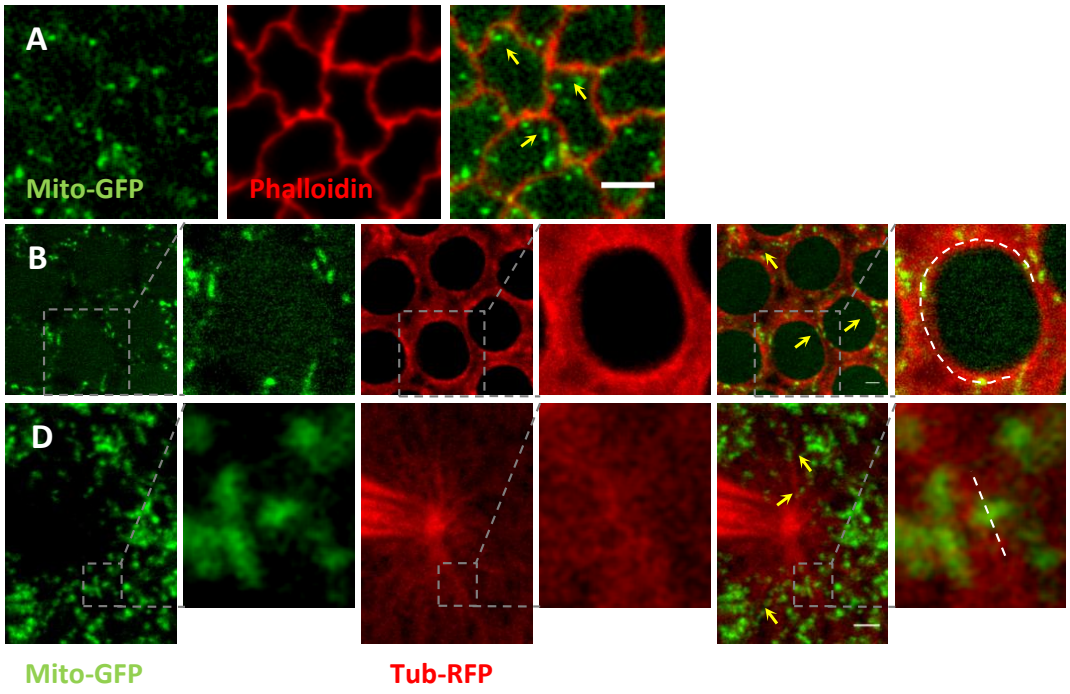
A
Mito-GFP
Phalloidin
B
D
Mito-GFP
Tub-RFP

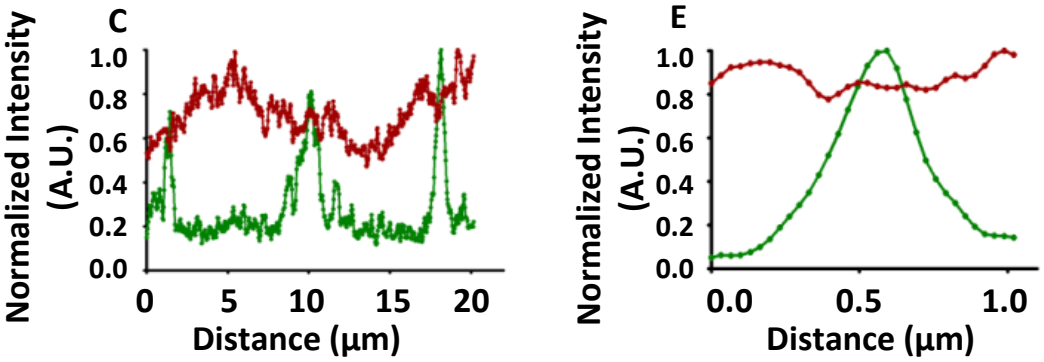
C
Normalized Intensity (A.U.)
1.0
0.8
0.6
0.4
0.2
0.0
0
5
10
15
20
Distance (μm)
E
Normalized Intensity (A.U.)
1.0
0.8
0.6
0.4
0.2
0.0
0.0
0.5
1.0
Distance (μm)

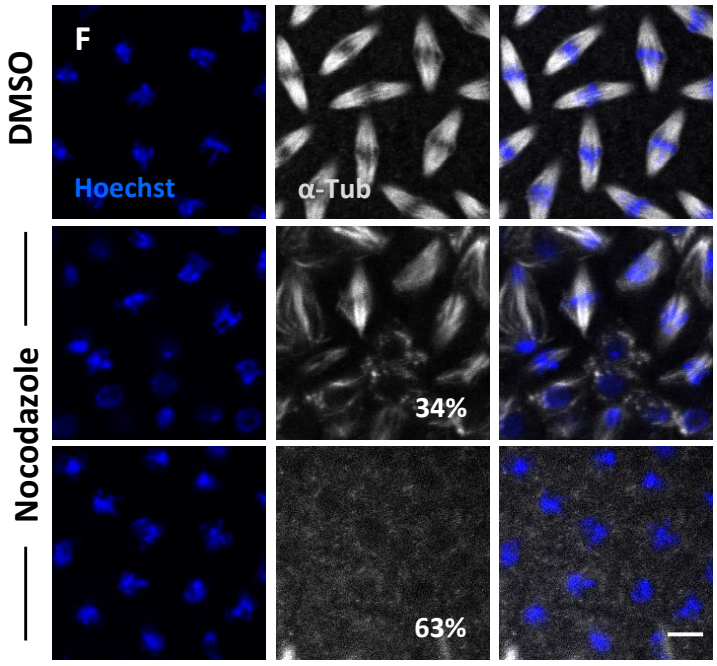
F
DMSO
Nocodazole
Hoechst
α-Tub
34%
63%

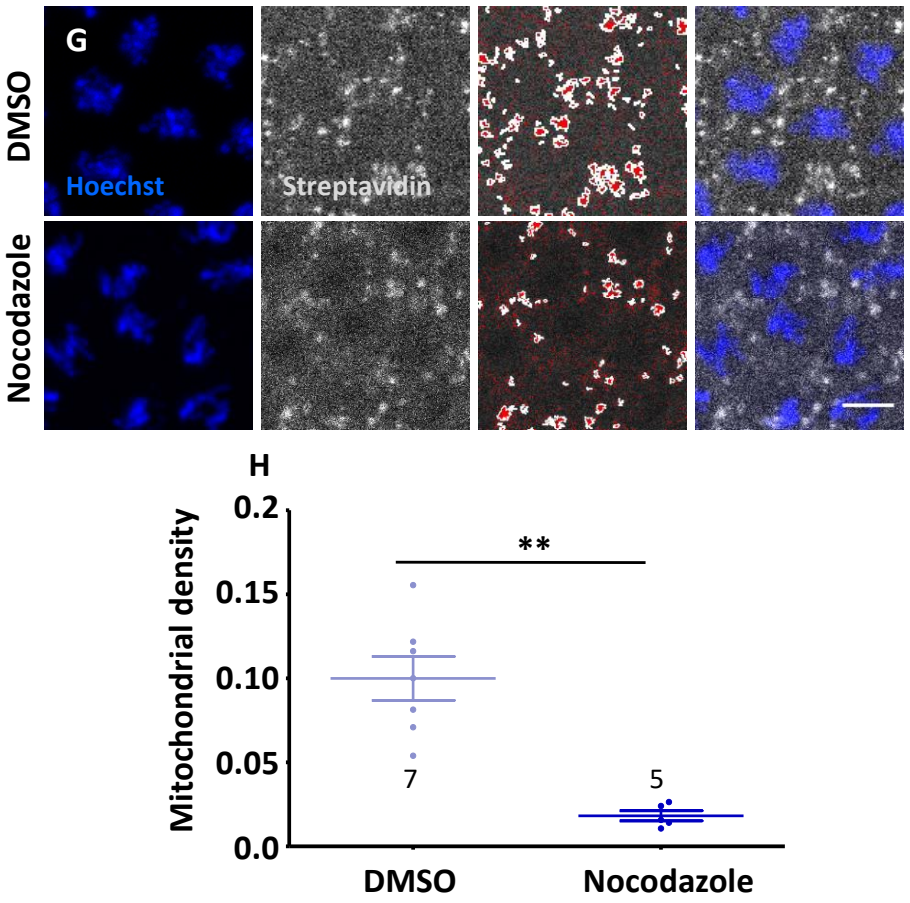
G
DMSO
Nocodazole
Hoechst
Streptavidin
H
Mitochondrial density
0.2
0.15
0.10
0.05
0.0
**
7
5
DMSO
Nocodazole

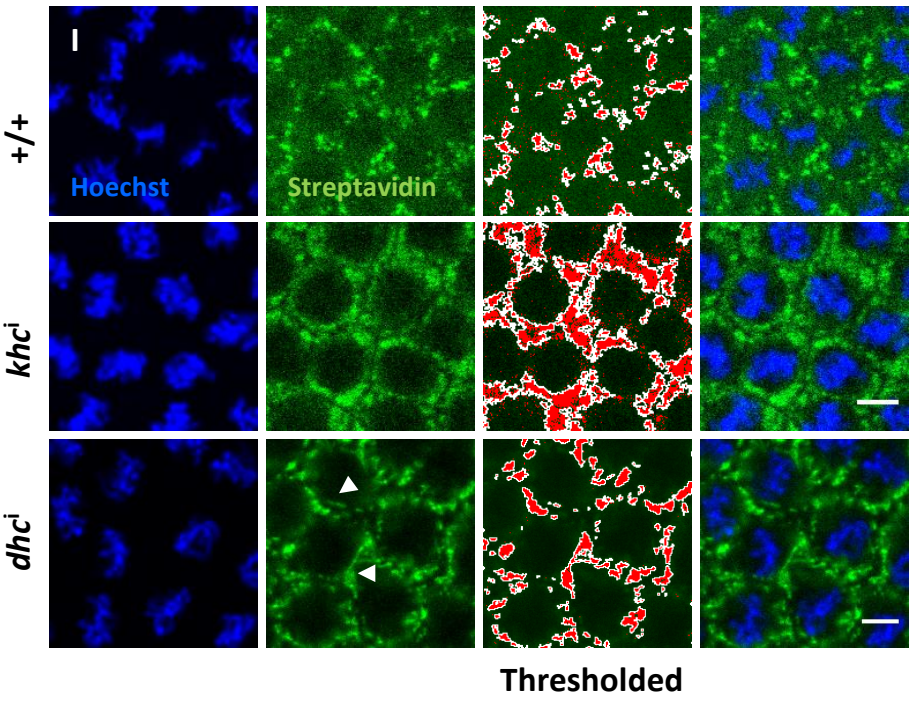
I
+/+
khc^i
dhc^i
Hoechst
Streptavidin
Thresholded

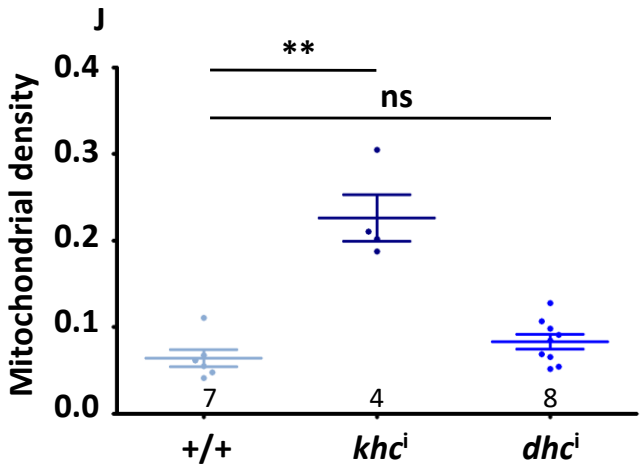

Figure 3.8: **Microtubules regulate mitochondrial distribution in syncytial embryos**. (**A**) Mitochondria (Mito-GFP, green) do not colocalize with cortical actin (phalloidin, red). (**B-E**): Mitochondria are juxtaposed with microtubules. Mitochondria (Mito-GFP, green) are present along perinuclear microtubules (Tub-mCherry, red) during prophase (**B,** zoomed in selections to the right) and as seen in the intensity profile (**C**). Mitochondria (Mito-GFP, green) are aligned at astral microtubules (Tub-mCherry, red) during metaphase (**D,** zoomed in selections to the right) and intensity profile (**E**). **(F-H)**: Mitochondrial distribution is altered on depolarization of microtubules. Nocodazole treatment leads to partial (34%) or complete loss (63%) of spindle microtubules (grey) compared to DMSO control (**F**). Mitochondria (streptavidin, grey) in 13M are marked thresholded and quantified compared to DMSO control. DNA is marked with Hoechst (blue) (**G**) Mitochondrial density in subapical regions is reduced on nocodazole treatment in syncytial embryos (**H**). **(I-J)**: Mitochondrial distribution in *khc*^{i} and *dhc*^{i}. Subapical mitochondrial density (green and thresholded) increases in *khc*^{i} and does not change in *dhc*^{i} (**I**) and is quantified (**J**). Long mitochondria in are marked with white arrows (**I**). Adapted from (Chowdhary et al., 2017).

3.3.6 Mitochondria distribute asymmetrically in pole cells

Pole cells or the germ cells present at the posterior of the embryo are the very first complete cells formed during the embryogenesis at NC9. Germ plasm is segregated from rest of the embryo during oogenesis itself to the posterior under the influence of *nanos, pgc* and *germ cell less* and is abundant in mitochondria, P granules, ribosomes and RNAs (Illmensee et al., 1976; Mahowald, 2001; Thomson and Lasko, 2005; Thomson et al., 2008).

P granules are evidently associated with ER exit sites, suggesting post translational regulation of germplasm components (Thomson et al., 2008). Mitochondrial inheritance in the pole cells is regulated by the long variant of Oskar and Tudor in an actin dependent manner (Hurd et al., 2016; Thomson and Lasko, 2005). Mitochondrial DNA (mtDNA) is inherited maternally and mutations can lead to a large variety of diseases and therefore it is probably essential to segregate the mitochondria in the germ plasm during the oocyte development itself.

Accumulation of mitochondria at the posterior side of preblastoderm embryo was observed using ATP synthase antibody (Hurd et al., 2016). We imaged mitochondria in the PGCs using Mito-GFP. When PGC nuclei arrive to the embryonic cortex, the posterior mitochondria associate with them and are localized in the PGCs as show using photoactivation experiments previously (Hurd et al., 2016). PGCs divide almost synchronously with syncytial somatic cells. Mitochondria were arranged in a crescent like manner on one side of the PGCs, mostly close to the somatic cells during interphase. During the cell division of PGCs, they accumulate at the cytokinetic furrow. Daughter cells rearrange the mitochondria back to the asymmetric localization as the next interphase begins (Fig. 3.9). Mitochondria have been shown to localize to cytokinetic furrow in the mammalian cells with the help of Kinesin1 and Miro at astral microtubules (Lawrence and Mandato, 2013; Lawrence et al., 2016). Distribution of mitochondria during *Drosophila* PGC division is more clustered compared to mammalian cells and this may indicate change of mitochondrial morphology and/or functional status during the cell division. This distribution is also different from somatic syncytial cells where although mitochondria populated towards the basal regions, no change in morphology or clustering was observed during the syncytial NCs (Fig. 3.4 G).

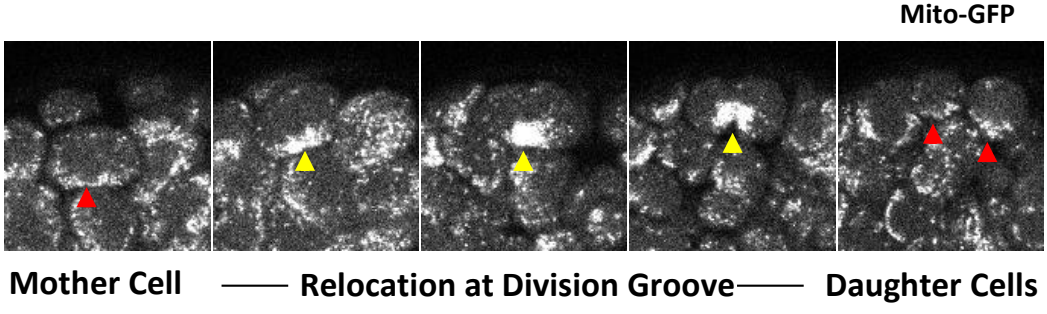

Figure 3.9: Mitochondrial localization in pole cells. Mitochondria (Mito-GFP, grey, red arrow) are asymmetrically localized in interphase pole cells and at cytokinetic furrow during cell division (yellow arrows).

3.4 Discussion

A large pool of mitochondria is inherited by the oocyte from its sister nurse cells. Special transport machinery inclusive of Kinesin1 and adapter protein Milton is important for this transport. These maternally inherited mitochondria are small spherical structures spread symmetrically throughout the oocyte (Cox and Spradling, 2003). Similar mitochondrial morphology is present in the early embryogenesis. We found that small round mitochondria are mostly present cortically, but also around deep located preblastoderm nuclei, despite the absence of any cellular boundaries. This has not been noted for other organelles like ER and the Golgi complexes previously (Frescas et al., 2006). Microtubules that regulate the preblastoderm NC may be responsible for mitochondrial entrapment. They are likely to be important for giving energy for rapid nuclear divisions.

Cortical mitochondria get entrapped around the nuclei as the move to the embryonic cortex at NC10. They have basal localization in all the 4 syncytial NCs. Microtubules are present in an apico-basally polarized manner around the interphase syncytial nuclei with centrioles apical to the nuclei and long polymerizing plus ends to the basal side. Compartmentalization and distribution of the ER and the Golgi complexes has been shown to be microtubule dependent (Frescas et al., 2006). Mitochondria are distributed asymmetrically, populating densely towards the basal side. The show negligible lateral movements and very little apically directed movements during syncytial NCs. The mitochondria were juxtaposed with microtubules, and depolymerization of microtubules depleted mitochondria from the subapical regions. This indicates that the preferred direction of mitochondrial transport is likely to be towards the apical side. We used metaphase staged embryos for our quantification. During the metaphase, mitochondrial numbers increase at the apical caps. It is possible that we saw the reduced numbers in the nocodazole treated embryos by stopping the apical transport by depolymerization of microtubules. We showed that mitochondrial distribution is regulated by microtubules and that plus ended motor Kinesin-1

is responsible for their basal trafficking. Kinesin may be inhibiting the apical transport of mitochondria and that is possibly why we see the mitochondrial intensity increase in the *khc*^{i} embryos. Subapical mitochondria density is unaffected in *dhc*^{i} embryos, since kinesin is probably functional is these mutants and manages to maintain mitochondrial distribution. But *dhc*^{i} embryos do contain clustered mitochondria. We have not analysed whether this could be due to changes in the microtubular architecture (Mehta et al., 2017). Dynein is also known to carry the fission protein Drp1 which could be mislocalized in *dhc*^{i} embryos resulting in mitochondrial clustering (Varadi et al., 2004).

During mammalian cell divisions, mitochondria attain a fused structure during G1-S phase and dispersed smaller structure during M phase. Fragmentation of mitochondria during cell division ensures proper distribution of mitochondria to the daughter cells (Kanfer and Kornmann, 2016; Mitra et al., 2009). Mitochondrial hyperfusion and metabolic flux has been show to regulate the cyclin E activity during mammalian call divisions (Mandal et al., 2005, 2010; Parker et al., 2015). We did not observe significant changes in mitochondrial structure during syncytial NCs of the *Drosophila* embryo. This is possibly to keep up with the rapid duration of the NCs.

The compartmentalization of mitochondria observed using photoactivation and photobleaching is likely due to their binding to microtubules. Confinement of organelles is important for specific localized functions between different cells and within a cell. Restricted localization of mitochondria may be essential for maintaining protein compartments in the cells. Cyclin E, responsible for maintenance of cell cycles has been shown to localize on the mitochondria (Parker et al., 2015). Additionally, as a consequence of being spatially restricted, photoactivated mitochondria in a single syncytial cell were divided equally between the progeny of that particular cells. Symmetric inheritance of mitochondria to the daughter cells in fission yeast is required for cell cycle progression (Yaffe et al., 1996, 2003). Mammalian cell culture studies have also represented symmetric mitochondrial distribution (López-Doménech et al., 2018; Rohn et al., 2014). This suggests lineage specific inheritance of mitochondria in the somatic cells of embryonic blastoderm. This may also be essential for inheritance of mitochondrially localized proteins differently in different cell populations.

Inheritance of germplasm associated mitochondria occurs with other organelles, clustered together in the form of Balbiani body (Cox and Spradling, 2003; Wilsch-Bräuninger et al., 1997) and are segregated towards the posterior of the oocyte and the embryo and later enclosed in the pole cells. Pole plasm is rich in P granules, ribosomes and mitochondria that are associated with one another (Illmensee et al., 1976) and is sufficient for germ cell induction (Okada et al., 1974). Pole cells later migrate in the dorsal midgut and their contents, including the mtDNA, are later inherited by the next generation. Therefore it may be essential to segregate pole cells earlier than the blastoderm stage to maintain the integrity of mtDNA. Mitochondrially encoded large ribosomal RNA (mtlrRNA), is an essential component of the pole plasm in *Drosophila* (Iida and Kobayashi, 1998), *Xenopus* (Kobayashi et al., 1998) and is necessary for pole cell formation and their localization is mediated by Tudor (Amikura et al., 2001a). mtlrRNAs are proposed to translate proteins required for pole cell formation (Amikura et al., 2001b).

To summarize, mitochondria localize asymmetrically in the syncytial cells due to microtubule binding and transport. They are compartmentalized and get equally shared between daughter syncytial cells. We further looked at functional relevance of these strictly localized mitochondria in the syncytial cells, as described in the next chapter.

Chapter 4

Mitochondria dependent ATP generation is important for syncytial furrow formation

4.1 Introduction

Mitochondria are abundantly deposited in the embryo by the mother in metazoan embryos. Oocytes with dysfunctional mitochondria have a lack of fertilization competence and can cause embryonic developmental arrest.

Although mitochondria in mammalian oocytes do not have well defined cristae (Stern et al., 1971), they are metabolically active (Dumollard et al., 2004). Mitochondrial ETC is activity increases post fertilization in response to calcium waves (Van Blerkom, 2004; Dumollard et al., 2003) and cristae gradually become elaborate (Van Blerkom, 2004) along with increased pyruvate uptake (Leese and Barton, 1984) and oxygen consumption (Trimarchi et al., 2000). Mitochondrial activity can be assessed using potential based dyes or by direct ATP measurements. Mitochondria with higher membrane potential display subcortical localization in mouse and human embryos and persists during division of blastomeres such that mitochondrial activity is differentially distributed in the daughter cells (Acton et al., 2004; Van Blerkom et al., 2000, 2003; Wilding et al., 2001b).

Mitochondrial activity can be ascertained by the characterization of metabolites in the electron transport chain. Early embryos utilize maternally deposited energy reserves such as glycogen, lipids and triglycerides (TAG) which indicates a possible activity glycolysis and aerobic respiration mode of ATP generation (Tennessen et al., 2014). In *Drosophila* embryos, using of dye Rhodamine 123, that only labels the active mitochondria, it was observed that mitochondrial activity is uniform across the syncytial cells from anterior to posterior during early and late blastoderm stages. Posterior pole plasm, especially after germ cell formation, had stronger accumulation of Rhodamine 123 indicating higher activity of mitochondria (Akiyama and Okada, 1992). A detailed analysis of metabolite levels during embryogenesis done using mass spectrometry showed that glycolysis pathway intermediates, glucose-6-phosphate, pyruvate and lactate remained more or less constant throughout embryogenesis. Whereas, TCA cycle intermediates gradually increase with time (Tennessen

et al., 2014). 0-4 hr embryos largely seem to utilize amino acids for their metabolic needs. Glutamate and Aspartate depleted largely during this period (Thuy An et al., 2014). Tennessen et al observed an increase in glutamate levels till 10 hours after egg laying, followed by depletion. In addition to Aspartate, Proline metabolism was also represented (Tennessen et al., 2014) which are substrates for activity through ETC.

Early *Drosophila* embryo contains small and dispersed mitochondria around the nuclei during the syncytial NCs. In literature smaller mitochondria are correlated with poorly formed cristae structure and low ATP production (Chen and Chan, 2005; Westermann, 2012). We decided to analyse the mode of ATP production in the syncytial embryos that consist of small mitochondria by acute and prolonged perturbation of ETC components using small permeable drug molecules and genetic knockdown approach. We also tested the glycolysis activity by using glucose analog 2-deoxy-D-glucose (2DG). We found that mitochondrial ETC in indeed active in syncytial *Drosophila* embryos and its functioning is necessary for rapidly ingressing membrane furrows during metaphase of the syncytial NCs. The data from this chapter are a part of (Chowdhary et al., 2017).

4.2 Methods and Materials

4.2.1 Fly Stocks

Embryos obtained from Mito-GFP (3.2.1) expressing flies were used to conduct all drug treatment experiments. Nanos-Gal4 was used induce expression of RNAi against *cova* and *pdsw*. *cova*^{i} and *pdsw*^{i} stocks were obtained from Bloomington fly stock centre. All fly stocks and crosses were maintained at 25 ^{o}C in standard cornmeal agar.

Fly Stock	Source
cova^{i}	BDRC 27548
pdsw^{i}	BDRC 29592

Table 4.1: List of fly stocks

4.2.2 Treatment with mitochondrial potential dye and inhibitors

Mito-GFP embryos of desired stage (2.5 - 3 hr old) were dechorionated in 100% bleach and incubated with drugs diluted using D-Limonene (Sigma): Heptane (1:1) (LH) at RT (Schulman et al., 2013) for the time mentioned below. Embryos were then fixed and stained as mentioned below (3.2.3). Drug concentrations and incubation times used were, FCCP: 10 µM (Sigma Aldrich, Bangalore, India); 15 mins, Rotenone: 5 µM; 30 mins (Sigma Aldrich, Bangalore, India), Oligomycin: 10 µM; 5 mins (Sigma Aldrich, Bangalore, India), 2-Deoxy-D-glucose (2-DG): 100µM; 15mins (Sigma Aldrich, Bangalore, India). 10 mM FCCP stock was prepared in ethanol and 5 mM Rotenone, 10 mM Oligomycin and 5 mM 2-DG were made in DMSO. Treatment with an equivalent volume of ethanol or DMSO for the same duration as of the drugs was used as control.

To analyse changes in the membrane potential caused by the mitochondrial drugs, we used mitochondria permeable dye mitotracker CMXRos Red (CMXRos). 500 nM CMXRos from a stock of 1 mM was added in the *pdsw*^{i},*cova*^{i}, drug treatment samples and respective controls and incubated for 15 mins. CMXRos was incubated along with FCCP and Rotenone during the treatment. Oligomycin treated embryos and their controls were incubated with only CMXRos for additional 10 mins after the 5 mins of drug treatment to maintain the total incubation period. Embryos were then fixed and imaged at the same time using identical imaging settings.

4.2.3 Immunostaining

Embryos were collected and fixed using 4% PFA as mentioned in Chapter 2 (2.3). Embryos were either methanol or hand devitellinized for primary antibody and Phalloidin staining respectively. Primary antibodies were diluted in BSA at following concentrations: pAMPK 1:200 (Cell Signaling, MA, USA), AMPK-α 1:200 (Abcam, MA, USA). Fluorescently coupled secondary antibodies (Alexa Fluor, Molecular Probes Bangalore India) were diluted in PBST at 1:1000. Fluorescently tagged streptavidin (1:1000) and Phalloidin (1:500) (Molecular Probes, Bangalore, India) were added with secondary. Embryos were then washed thrice with PBST for 5 mins each. DNA stain Hoechst 33342 (1:1000, Molecular Probes, Bangalore, India) was added in the second wash. All steps from secondary antibody onwards were done in dark condition by covering the tubes with aluminium foil. Embryos were mounted on

slides using Slowfade Gold (Life Technologies) and stored at 4 ˚C. Embryos were imaged using Plan apochromat 40X/63X/1.4 objectives on the Zeiss LSM 710/ 780.

Reagent	Source	Host Species (Ab)	Dilution/ Concentration
FCCP	Sigma aldrich	NA	10 µM
Rotenone	Sigma aldrich	NA	5 µM
Oligomycin	Sigma aldrich	NA	10 µM
2-DG	Sigma aldrich	NA	100µM
Mitotracker CMXRos Red	Invitrogen	NA	500 nM
pAMPK antibody	Cell Signaling	Rabbit	1:200
AMPK-alpha antibody	Abcam	Mouse	1:200

Table 4.2: list of reagents

4.2.4 Western blotting

Western blotting was done in collaboration with Dnyanesh Dubal. WT and mutant embryos aged 2.5 hrs were collected from cages, dechorionated and processed for protein extraction as mentioned in Chapter 2 (2.8). The proteins were separated using 10% SDS gels, and blotted onto PVDF membranes. The blots were blocked using 5% milk for 1hr at RT and incubated with pAMPK antibody (Rabbit, 1:1000, Cell Signaling), AMPK antibody (Mouse, 1:1000, Abcam) and mouse anti beta-tubulin (Mouse, 1:10,000, Sigma Aldrich) overnight at 4 ˚C. Blot was incubated with respective HRP conjugated secondary antibodies for 1hr at room temperature and developed using ECL prime blot detection reagent in ImageQuant™ LAS 4000. Tubulin was used as protein concentration control. Concentration of pAMPK and AMPK was estimated by intensity based densitometric analysis in each protein band using ImageJ. pAMPK intensity was normalized using AMPK intensity in each sample and represented as fold change between every control and treatment or RNAi set. Mean fold

change from 3 experiments was plotted with SEM and compared using Student's t-test using Graphpad Prism 6.0

4.2.5 ATP assay

ATP estimation was carried out from embryo extracts by using luciferase based ATP determination Kit (Thermofischer scientific) as mentioned in Chapter 2 (2.9) in collaboration with Darshika Tomer. Briefly, 3 hr old embryos dried using heptane were crushed on ice in homogenisation buffer (Tris (100 mM) and EDTA (100 µM)) and a uniform extract was obtained and samples were prepared as mentioned in Chapter 2 (2.9). Luciferin and firefly luciferase in buffer provided in the ATP estimation kit (Thermofischer scientific) were added and luminescence was measured on a Varioskan Spectrometer at 560 nm to estimate ATP concentration in the samples. All measurements were normalized to total protein content of the embryos. All the experiments were repeated 3 times. The graph represents the percentage reduction corresponding to controls estimated at the same time. Means were compared using one tailed Mann-Whitney test in Graphpad prism 6.0.

4.2.6 Analysis

4.2.6.1 Mitochondrial object number and density measurement

This was done as mentioned in section 3.2.7.2.

4.2.6.2 CMXRos and pAMPK intensity

All treatments and their respective controls were incubated with the same aliquot of reagents divided into different tubes. The imaging was performed using the same laser power and gain settings at the microscope, adjusted using the brightest stained sample. Mean fluorescence intensities of Mitotracker CMXRos red and pAMPK were measured and corrected with the background. The values are normalized using mean fluorescence intensities of the control embryos in each control and treatment set to obtain fold change. The analysis was performed using imageJ. The values are compared using two tailed Mann-Whitney test on Graphpad Prism 6.0.

4.2.6.3 Metaphase furrow length measurement

The furrow length was measured from sagittal images of the embryos using length measurement tool in ImageJ. The mean and variation was compared using two tailed Mann-Whitney test on Graphpad Prism 6.0

4.3 Results

4.3.1 Mitochondria are metabolically active in the syncytial *Drosophila* embryo

To find out if mitochondrial ETC is active, we performed acute as well as prolonged inhibition of ETC. In the acute treatment, we treated the embryos with inhibitors of ETC: FCCP, Rotenone and Oligomycin. FCCP (Carbonyl cyanide-*4*-(trifluoromethoxy) phenylhydrazone) is an ionophore decouples the ETC and depletes the proton gradient across the inner mitochondrial membrane (Park et al., 2002). Rotenone inhibits complex I activity by blocking electron transfer to the next complex, coenzyme Q (Gielisch and Meierhofer, 2015). Oligomycin inhibits the Fo subunit ATPase complex; and therefore does not allow the membrane potential to be used for phosphorylation of ADP (Penefsky, 1985). We used heptane-limonene combination (Schulman et al 2013) for drug treatments as mentioned in methods and materials section (4.2.2). We also used nanos-Gal4 to maternally deplete PDSW subunit of NADH dehydrogenase (Complex I, Pdsw) and Cytochrome oxidase subunit Va (Complex IV, Cova) using RNAi mediated knockdown.

Inhibition of ETC using FCCP and Rotenone causes depolarization of the mitochondrial inner membrane by reducing proton generation. On the other hand, inhibition of ATPase complex by oligomycin retains hyperpolarized inner membrane. In *pdsw*^{i} and *cova*^{i} the membrane potential is expected to drop due to the knockdown of the ETC components themselves directly. We checked the mitochondrial activity using a cell permeable dye Mitotracker CMXRos Red which accumulates in the mitochondria in a potential dependent manner and can be retained post fixation (Fig 4.1). Although we could not get perfect mitochondrial localization of the dye due to problems with permeability of the embryo, we did observe the intensity of the same change in the expected manner. FCCP and Rotenone block the activity of ETC complexes and thus inhibit the proton flux, reducing the membrane potential. The normalized mean fluorescence intensity of CMXRos in the embryos treated with FCCP and

Rotenone reduced to 0.64 and 0.48 respectively compared to their controls with normalized mean intensity at 1 (Fig 4.1 A, C). Oligomycin inhibits the ATP synthase complex and thus the membrane potential is retained. Oligomycin treated embryos showed an increase of 1.5 fold (Fig 4.1 A, C). Similar to FCCP and Rotenone treated embryos, *pdsw*^{i} and *cova*^{i} embryos had

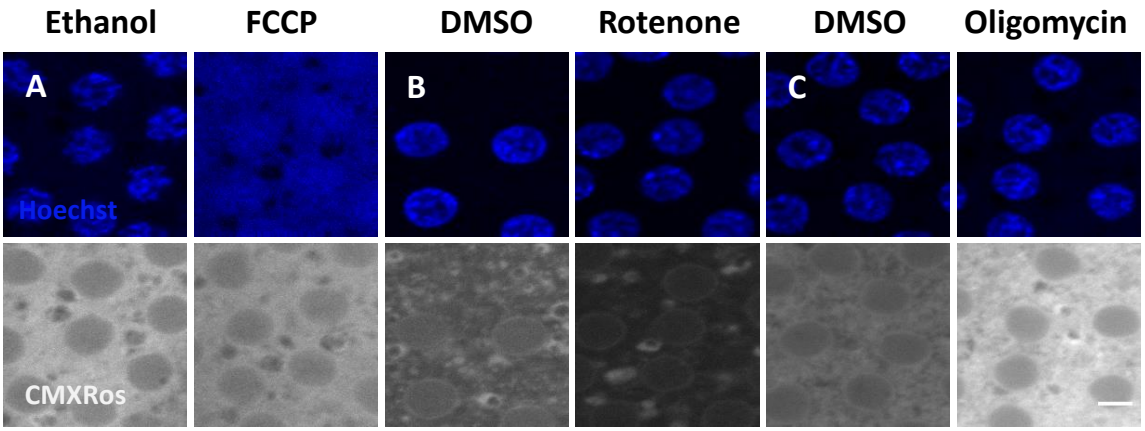

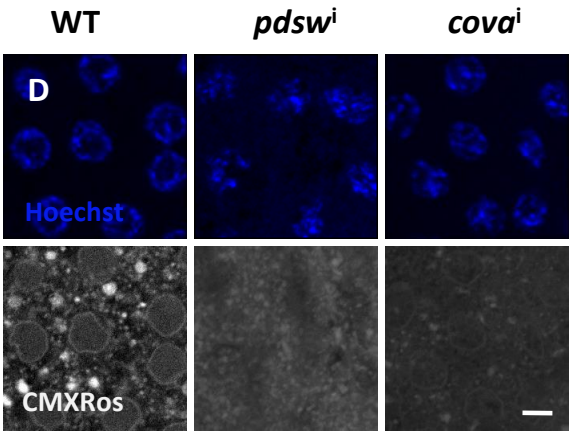

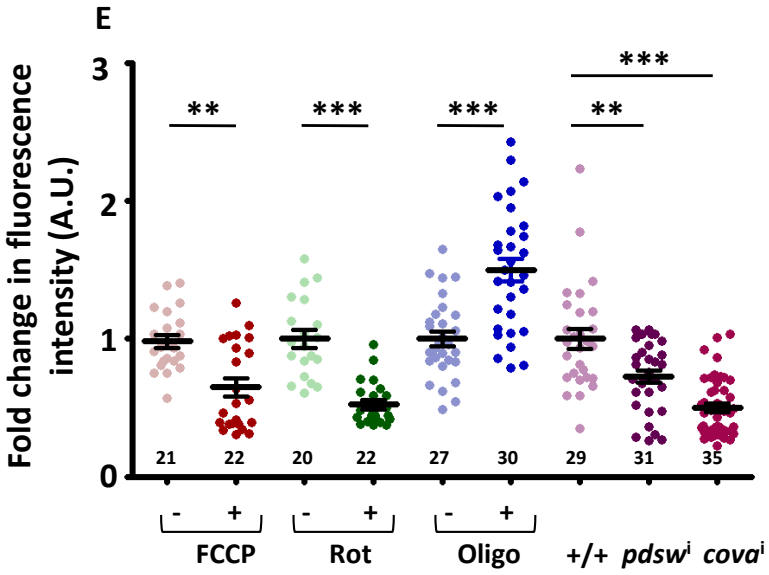

Figure 4.1 CMXRos staining after ETC inhibition in *Drosophila* embryos. Mitochondrial membrane potential visualized by Mitotracker CMXRos red (grey) reduces with FCCP (A, E, red) and Rotenone (B, E, green) treatment and increases with Oligomycin (C, E, blue) treatment compared to their controls represented in lighter shades of the respective colour (E). CMXRos intensity is also reduced in *pdsw*^{i} (D, E purple) and *cova*^{i} (D, E magenta) embryos compared to the WT control (D, E, pink). Numbers and data points represent embryos analysed. Mean fluorescent intensities for every treatment are normalized with the respective control (E). (**, P ≤ 0.01, ***, P ≤ 0.001, two tailed Mann - Whitney test) N = 3, n = 21, 22 embryos for control and FCCP; 20, 22 embryos for control and Rotenone; 27, 30 embryos for control and Oligomycin; 29, 31 and 35 embryos for control, *pdsw*^{i} and *cova*^{i} respectively (**E**). Scale bar: 5 µm

lowered signal (0.72 and 0.5 respectively) compared to control Mito-GFP embryos (Fig 4.1B, C). Because mitotracker did not localize to the mitochondria, we decided to check the effectiveness of our treatments by directly measuring ATP using a luciferase based assay.

To measure ATP content in the treated embryos, we used ATP estimation assay. This was standardised and done by Darshika Tomer. We found that ATP content in FCCP (colours in the plot), Rotenone and Oligomycin embryos was significantly reduced compared to their respective controls. A significant reduction in ATP levels was also seen in *pdsw*^{i} and *cova*^{i} (Fig 4.2).

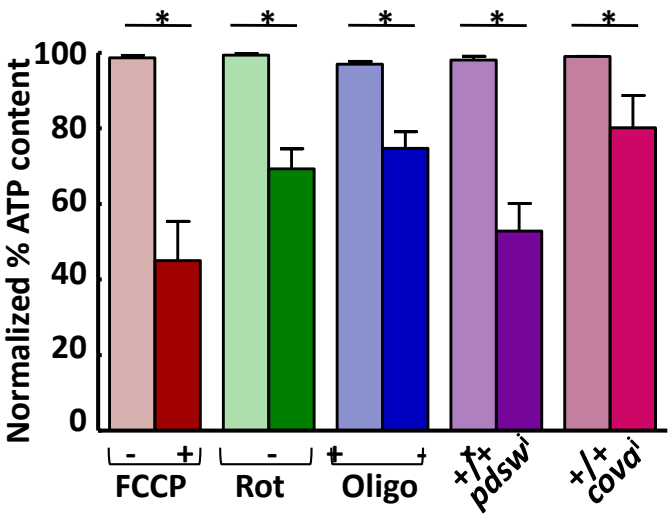

Figure 4.2: Inhibition of ETC depletes ATP in the syncytial *Drosophila* embryo.
Luciferase based assay shows significantly reduced levels of ATP in FCCP (red), Rotenone (green) and Oligomycin (blue) treatments and *pdsw*^{i} (purple) and *cova*^{i} (pink) embryos compared to their respective control represented in lighter shades. Normalized values are represented as percentage. (*, P ≤ 0.05, n = 9, N = 3, one tailed Mann - Whitney test). Adapted from (Chowdhary et al., 2017).

Another way to analyse ATP stress between different embryos is comparing the levels of phosphorylated AMP kinase (pAMPK). AMPK is a very well-known metabolic biosensor for cellular energy levels and has been previously used. AMPK is phosphorylated by an upstream kinase Lkb1 when more ATP is consumed or AMP is accumulated (Lee et al., 2007; Sakamoto et al., 2004). Immunostaining pAMPK antibody showed cytoplasmic as well as nuclear signal. Interphase syncytial cells largely had uniform cytoplasmic localization (Fig 4.3A). The intensity of pAMPK was higher at kinetochore, especially in prophase (Fig 4.3B) and metaphase stages (Fig 4.3C).

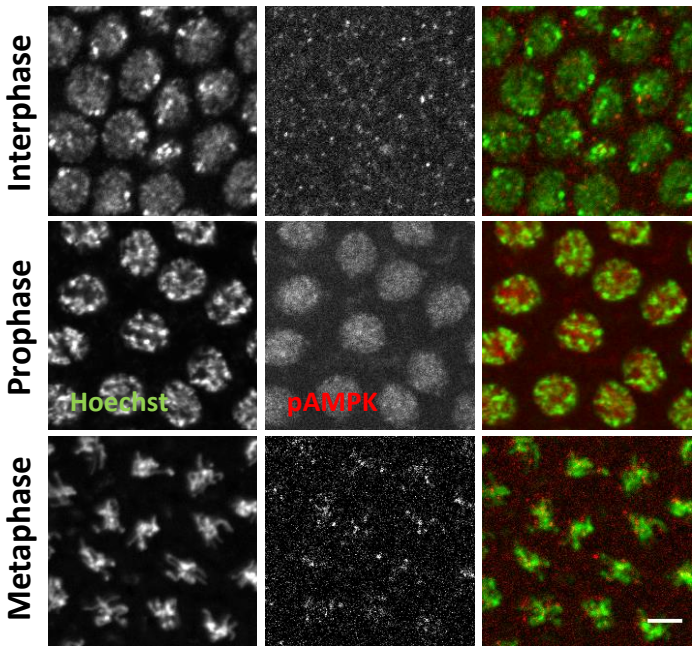

Figure 4.3: pAMPK localization in syncytial NCs. (**A-C**): pAMPK (red) is localized to cytoplasm and nuclei (green) of WT syncytial embryos. pAMPK is cytoplasmic in interphase (**A**). Enhanced nuclear signal of pAMPK is seen in prophase (**B**) and is on kinetochore in metaphase embryos (**C**). Scale bar: 5 µm Adapted from (Chowdhary et al., 2017).

Since AMPK phosphorylation occurs due to ATP depletion, we immunostained embryos treated with ETC and glycolysis inhibitors. FCCP, Rotenone and Oligomycin treated embryos showed a mean increase of 1.3, 1.4 and 1.8 fold in pAMPK staining compared to their respective controls (Fig: 4.4 A-C, E). A similar increase of pAMPK staining was present in *pdsw*^{i} and *cova*^{i} embryos. They showed a mean fold change of 1.9 and 1.8 respectively compared to the control Mito-GFP embryos (Fig. 4.4 D, E). An increase of 3.2 fold and 2.5 in the pAMPK normalized with total AMPK was also seen in the western blotting experiments in *pdsw*^{i} and *cova*^{i} embryos respectively (Fig 4.6). Total AMPK levels remained constant as seen in the western blotting as well as immunostaining experiments in WT, *pdsw*^{i} and *cova*^{i} (Fig 4.6A, Fig 4.5). We also tested if inhibition of glycolysis affects ATP production by using 2-deoxy glucose (2-DG) and we did not observe any changes in the levels of pAMPK (Fig 4.9 A, B). These experiments suggest that embryo is highly dependent on ATP produced via ETC and does not rely on glucose for its energy needs. It has been previously shown that glucose metabolising enzymes are active only in the pre-larval stages of embryonic development and in the larvae (Tennessen et al., 2011, 2014). The data is also consistent with utilization of amino acids as the primary metabolites in the early *Drosophila* embryogenesis (Tennessen et al., 2014; Thuy An et al., 2014).

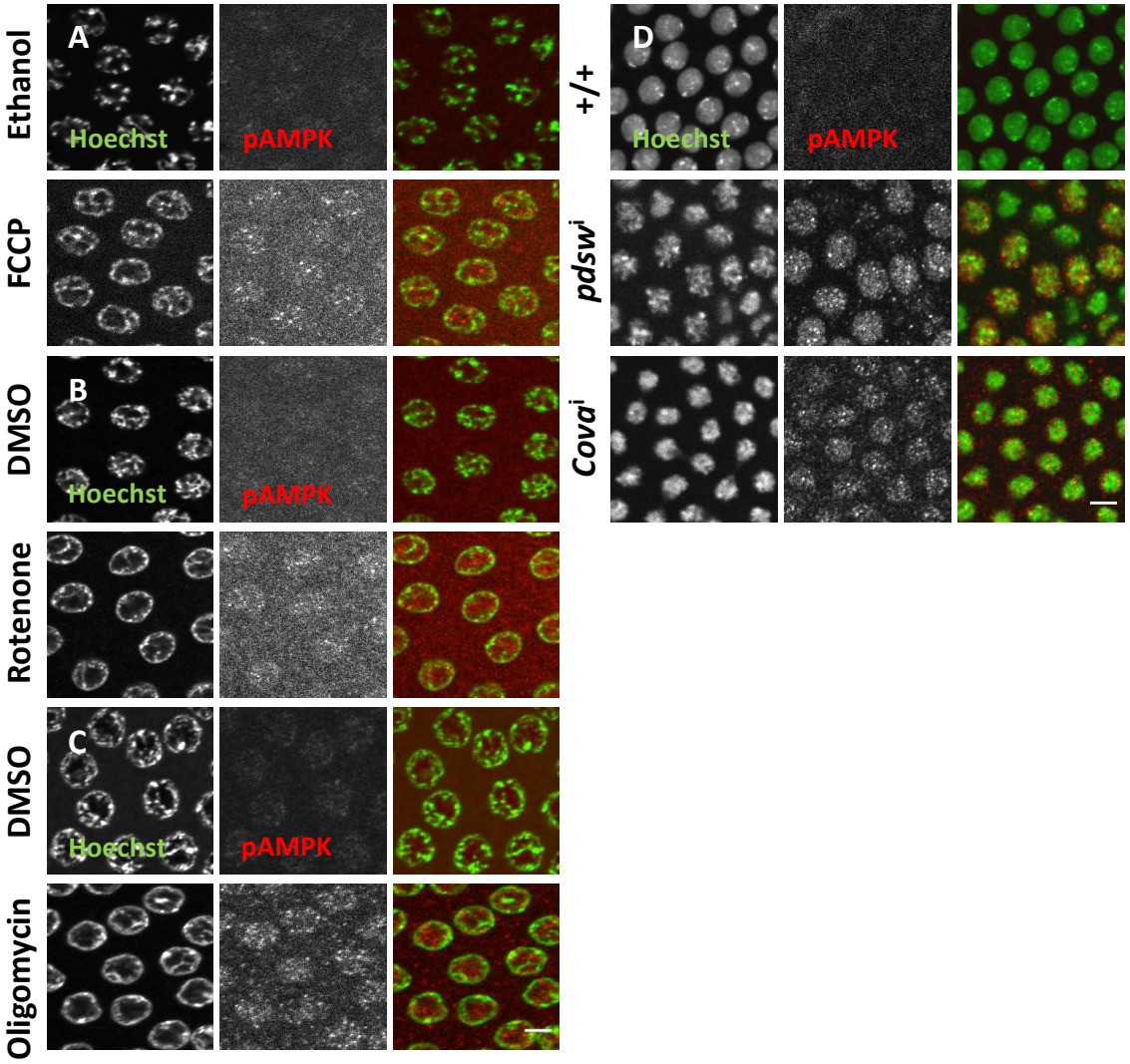
A
B
C
D
Ethanol
FCCP
DMSO
Rotenone
DMSO
Oligomycin
+/+
pdsw^i
Cova^i
Hoechst
pAMPK

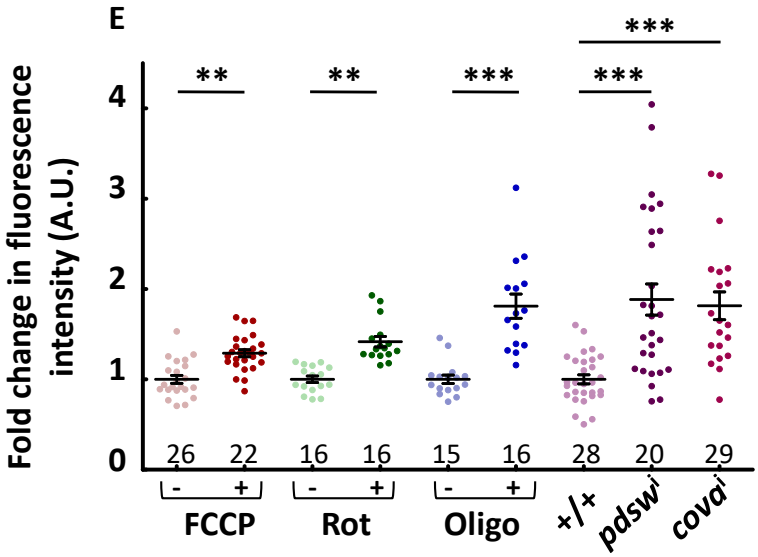
E
Fold change in fluorescence intensity (A.U.)
0
1
2
3
4
**
**
***
***
***
26
22
16
16
15
16
28
20
29
-
+
-
+
-
+
FCCP
Rot
Oligo
+/+
pdsw^i
cova^i

Figure 4.4 ETC inhibition elevates pAMPK signal in syncytial embryos. pAMPK (red) signal is increased in FCCP (**A**), Rotenone (**B**) and Oligomycin (**C**) treatments compared to their respective controls. *pdsw*^{i} and *cova*^{i} (**D**) show increased pAMPK signal compared to control embryos. Normalized fluorescence intensity of pAMPK in embryos treated with FCCP (red), Rotenone (green) and Oligomycin (blue) and *pdsw*^{i} (purple) and *cova*^{i} (pink) compared to their respective controls represented by lighter shades (**E**). Numbers and data points represent embryos analysed (**; $P \leq 0.01$, ***; $P \leq 0.001$, two tailed Mann-Whitney test.). n = 22, 26 embryos for control and FCCP; 16, 16 embryos for control and Rotenone; 16, 15 embryos for control and Oligomycin; 29, 28 and 20 embryos for control, *pdsw*^{i} and *cova*^{i} respectively (**E**). On an average 21 syncytial cells per embryo were measured. N: FCCP-3, Rotenone and Oligomycin - 4, *pdsw*^{i} and *cova*^{i} - 3. Scale bar: 5 µm. Adapted from (Chowdhary et al., 2017).

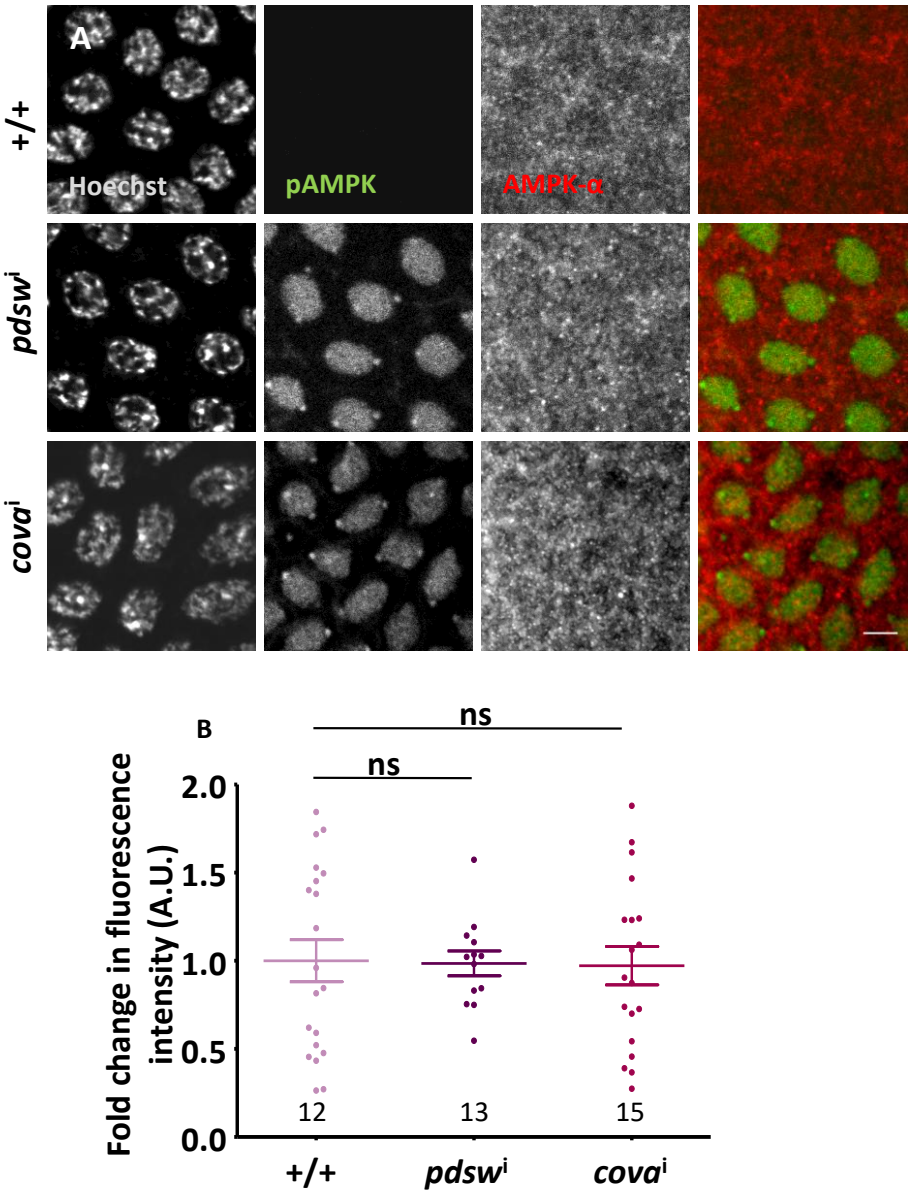

Figure 4.5: Total AMPK levels do not change on genetic depletion of ETC. (**A-B)**: Total AMPK-α (red) is seen more uniformly distributed in the cytoplasm of syncytial embryos, pAMPK (green) is increased significantly in *pdsw*^{i} and *cova*^{i} expressing embryos and seen in the nucleus and at the centromere, however total AMPK-α (red) intensity is not changed. Normalized intensity of AMPK-α is plotted with SEM (**B**). Data points and numbers represent embryos analysed. (ns; $P \geq 0.05$, two tailed Mann-Whitney test.). N =3. Scale bar: 5 µm. Adapted from (Chowdhary et al., 2017).

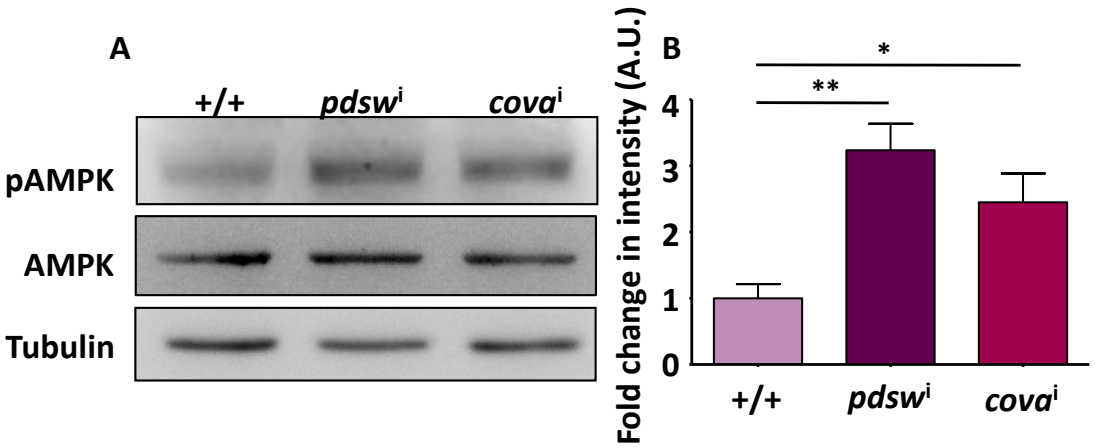

Figure 4.6: Western blotting of pAMPK and total AMPK in WT, *pdsw*^{i} and *cova*^{i} embryos. Band intensity of pAMPK is normalized with total AMPK (**A**) for each genotype and represented as fold change with respect to WT (**B**). Error bars represent SEM, N = 3, (**; P ≤ 0.01, *; P ≤ 0.05, Student's t test). Adapted from (Chowdhary et al., 2017).

4.3.2 Inhibition of ATP generation does not affect mitochondrial morphology

Mitochondrial morphology is known to be altered in eukaryotic cells when mitochondrial ETC is inhibited. We measured mitochondrial density in the apical sections of *pdsw*^{i} and *cova*^{i} embryos compared to the wild type; we did not find any significant difference (Fig 4.7). This suggests that after blocking ETC the fission machinery of mitochondria is intact and they are already at their threshold smallest size.

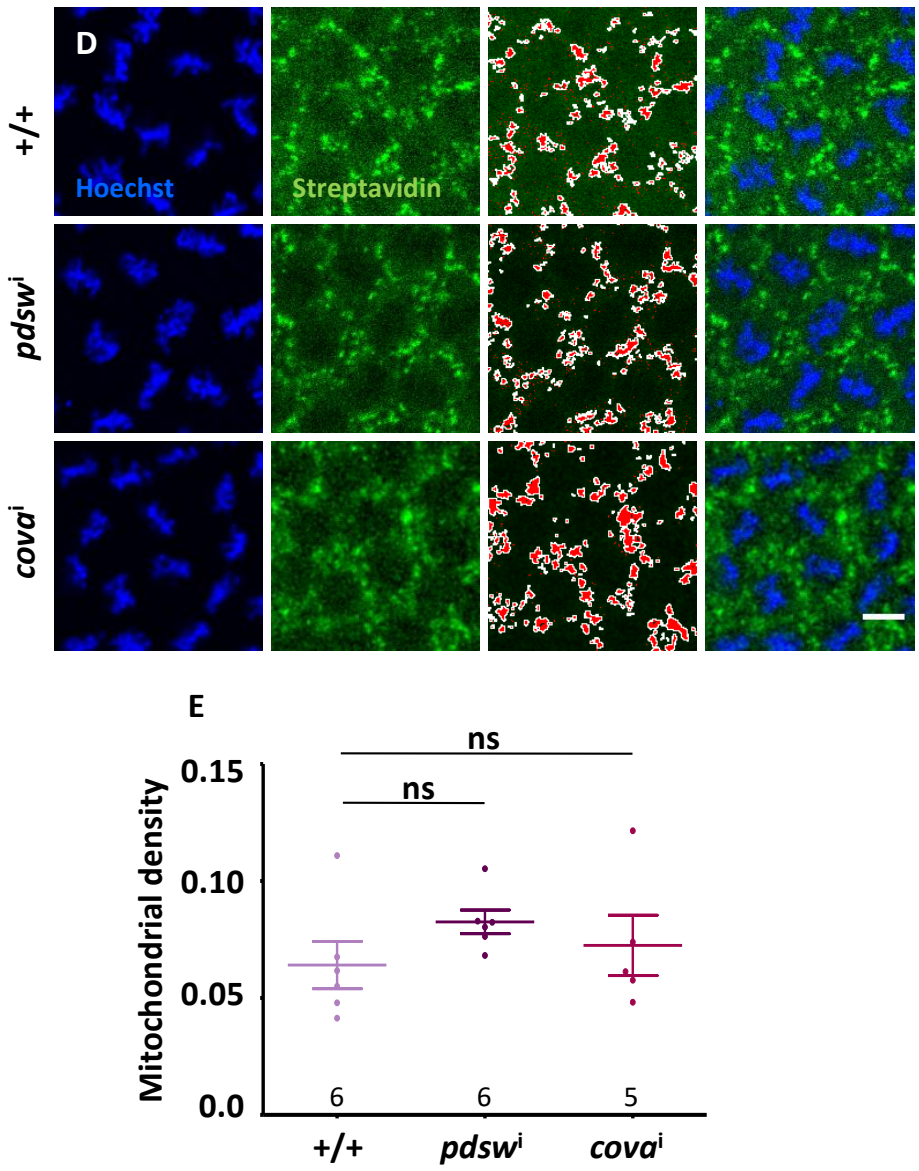

Figure 4.7 Mitochondrial distribution in genetic inhibition of ETC. (A-B):Mitochondrial density at apico-lateral regions in not affected in NC13 metaphase *pdsw*^{i} and *cova*^{i} embryos compared to control and quantified in the graph (ns; P ≥ 0.05, two tailed Mann-Whitney test.), n = control - 6, *pdsw*^{i} - 6, *cova*^{i} - 5, N=3. Scale: 5 µm. Adapted from (Chowdhary et al., 2017).

4.3.3 Inhibition of ATP generation decreases metaphase furrow ingression

Syncytial nuclei undergo rapid cycles of cell division. These cell divisions involve dynamic membrane ingression to the basal side till metaphase and regression by the next interphase. The highest membrane length is achieved at metaphase and keeps getting longer with successive division cycles from NC 10-13. The ingression and regression is coupled with rapid actin assembly and disassembly that might need abundant energy supply locally. To understand if mitochondrial ETC is important for this process we decided to measure the highest length achieved at the metaphase in the embryos where ETC was inhibited. We used phalloidin to visualise f-actin associated with the membrane and imaged the embryos in XY as well as sagittal sections. Compared to the respective controls, the membrane was floppy and loose or absent at some places in FCCP (Fig 4.8 A), Rotenone (Fig 4.8 C) and Oligomycin (Fig 4.8 E) treated embryos (marked by arrows). We found, as expected, the metaphase membrane length was significantly reduced to an average of 3.86, 3.57 and 3.68 µm compared to the controls that had 7.23, 4.97 and 5.56 µm lengths respectively in NC 12. Similarly in NC 13 the average membrane lengths in FCCP, Rotenone and Oligomycin were 4.77, 4.55 and 3.75 µm compared to the controls with 7.27, 6.48 and 6.42 µm respectively (Fig 4.8 B, D and F). The membrane loosening phenotype also was observed in *pdsw*^{i} and *cova*^{i} embryos (Fig 4.8 G). In some percentage of *pdsw*^{i} (26 %) and *cova*^{i} (33 %) membrane ingression was absent (Fig 4.8 G). Similar to the drug treatments, the metaphase furrow lengths in the embryos with membrane ingressions were significantly reduced in NC12 and NC13 embryos. The mean length was found to be 5.22 µm and 5.38 µm in NC12 and 6.29 µm and 6.8 µm in NC 13 in *pdsw*^{i} and *cova*^{i} embryos respectively compared to Mito-GFP embryos that reached an average length of 8.08 µm in NC 12 and 9.12 µm in NC 13 (Fig 4.8 H). These data suggest that ingression of metaphase furrow requires energy from ETC. We did not find any difference in the metaphase lengths of embryos treated with 2-DG, compared to the controls (Fig, 4.9 C, D), suggesting that inhibiting glycolysis does not affect the metaphase furrows.

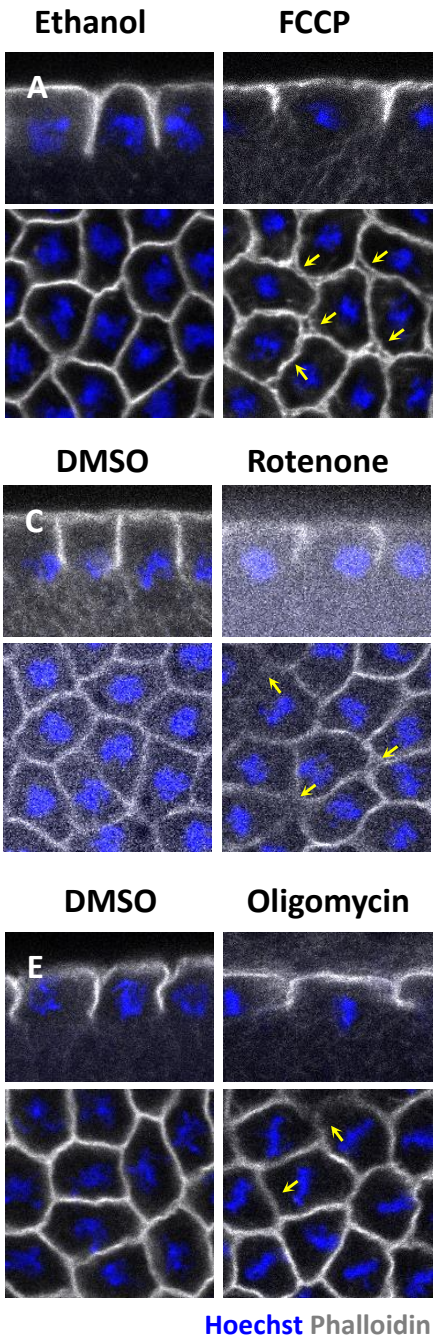
Ethanol
FCCP
A
DMSO
Rotenone
C
DMSO
Oligomycin
E
Hoechst Phalloidin

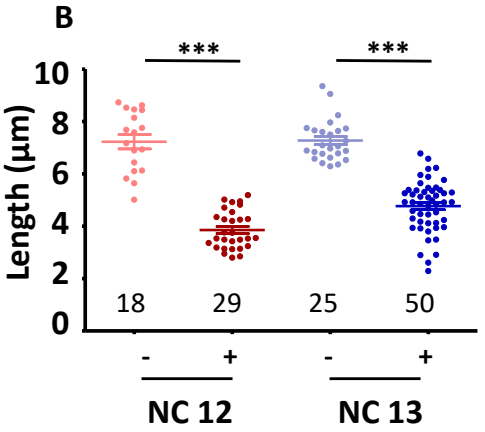
B
***
***
Length (µm)
10
8
6
4
2
0
18
29
25
50
-
+
-
+
NC 12
NC 13

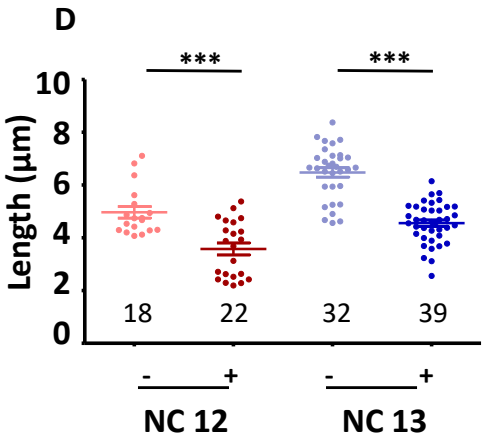
D
***
***
Length (µm)
10
8
6
4
2
0
18
22
32
39
-
+
-
+
NC 12
NC 13

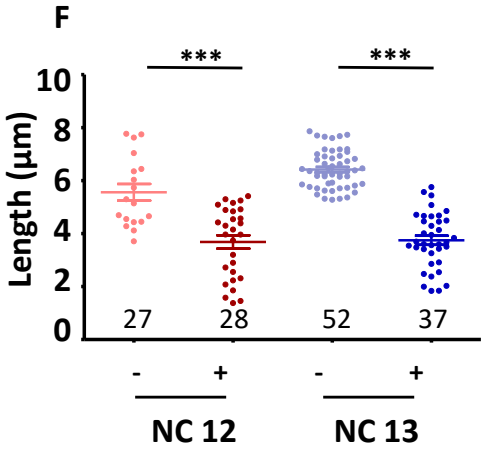
F
***
***
Length (µm)
10
8
6
4
2
0
27
28
52
37
-
+
-
+
NC 12
NC 13

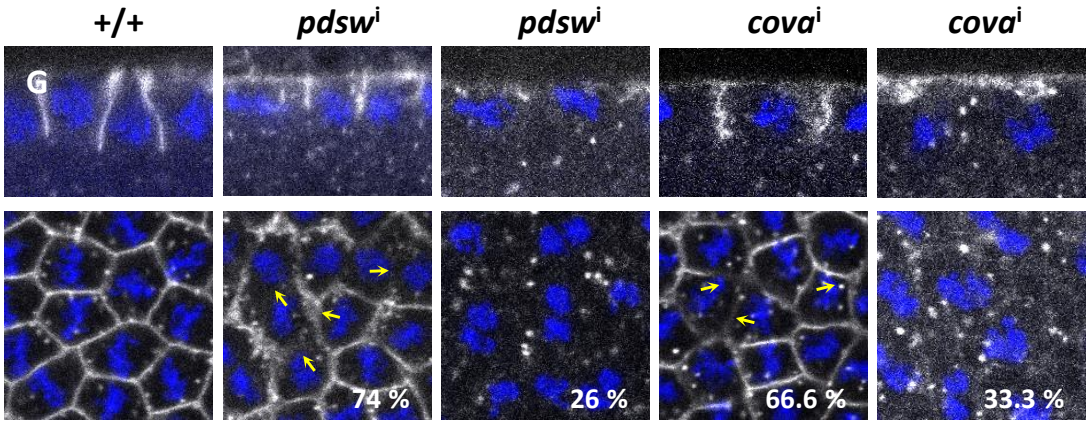
+/+
pdsw^i
pdsw^i
cova^i
cova^i
G
74 %
26 %
66.6 %
33.3 %

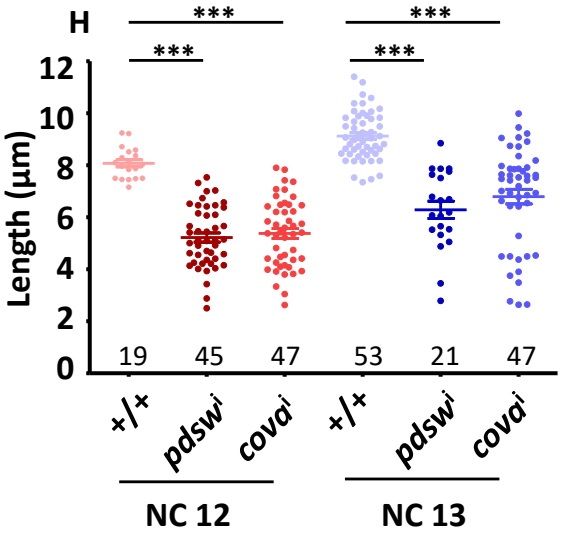
H
***
***
***
***
Length (µm)
12
10
8
6
4
2
0
19
45
47
53
21
47
+/+
pdsw^i
cova^i
+/+
pdsw^i
cova^i
NC 12
NC 13

Figure 4.8: Inhibition of ETC decreases metaphase furrow extension in syncytial *Drosophila* embryos.

A-F: Pharmacological inhibition of ETC decreases metaphase furrow length in NC12 and 13. Shorter metaphase furrows (Phalloidin; grey) are observed in FCCP treated embryos compared to control in sagittal views through metaphase furrows and surface views show loose actin organisation (**A**). Furrow length similarly decreased in Rotenone (**C**) and Oligomycin (**E**) compared to respective controls. Quantification shows a significant decrease in metaphase furrow length (**B, D, F**) in NC12 and 13. Each data point represents individual metaphase furrows, NC12 Control n = 18 (4 embryos), FCCP: 29 furrows (6); NC13 control n=25 (6) and FCCP: 50 (11), (**B**); NC12 control n=18 (5), Rotenone n=22 (4) ; NC13 control n= 32 (5), Rotenone n= 39 (6) and (**D**); NC12 control n= 18 (4) and Oligomycin n= 28 (7) and NC13 control 52 (10) and Oligomycin 37 (7) (**F**) (***; P ≤0.001, two tailed Mann Whitney test). Yellow arrows (**A, C, E**) mark loose membrane/actin on drug treatment. N: FCCP, Rotenone and Oligomycin-3.

G-H: Genetic inhibition of ETC decreases metaphase furrow length in NC12 and 13. Metaphase furrows are shortened (74%) or completely absent (26%) in *pdsw*^{i} compared to control WT embryos (**G**). Metaphase furrows in *cova*^{i} embryos are also short (66.6%) or absent (33.3%). Yellow arrows mark loosening or loss of the membrane/actin (**G**). Quantification of metaphase furrow lengths in *pdsw*^{i} and *cova*^{i} mutant as compared to control embryos (**H**) in NC12 and 13. NC12 control 19 (4 embryos) *pdsw*^{i} n = 45 metaphase furrows (8) and *cova*^{i} 47 (8), and; NC13 control 53 (8), *pdsw*^{i} 21 (4) and *cova*^{i} 47 (7) and (**H**) (***; P≤0.001, two tailed Mann Whitney test). N: *pdsw*^{i} - 4, *cova*^{i} - 3. Scale bar: 5 µm.

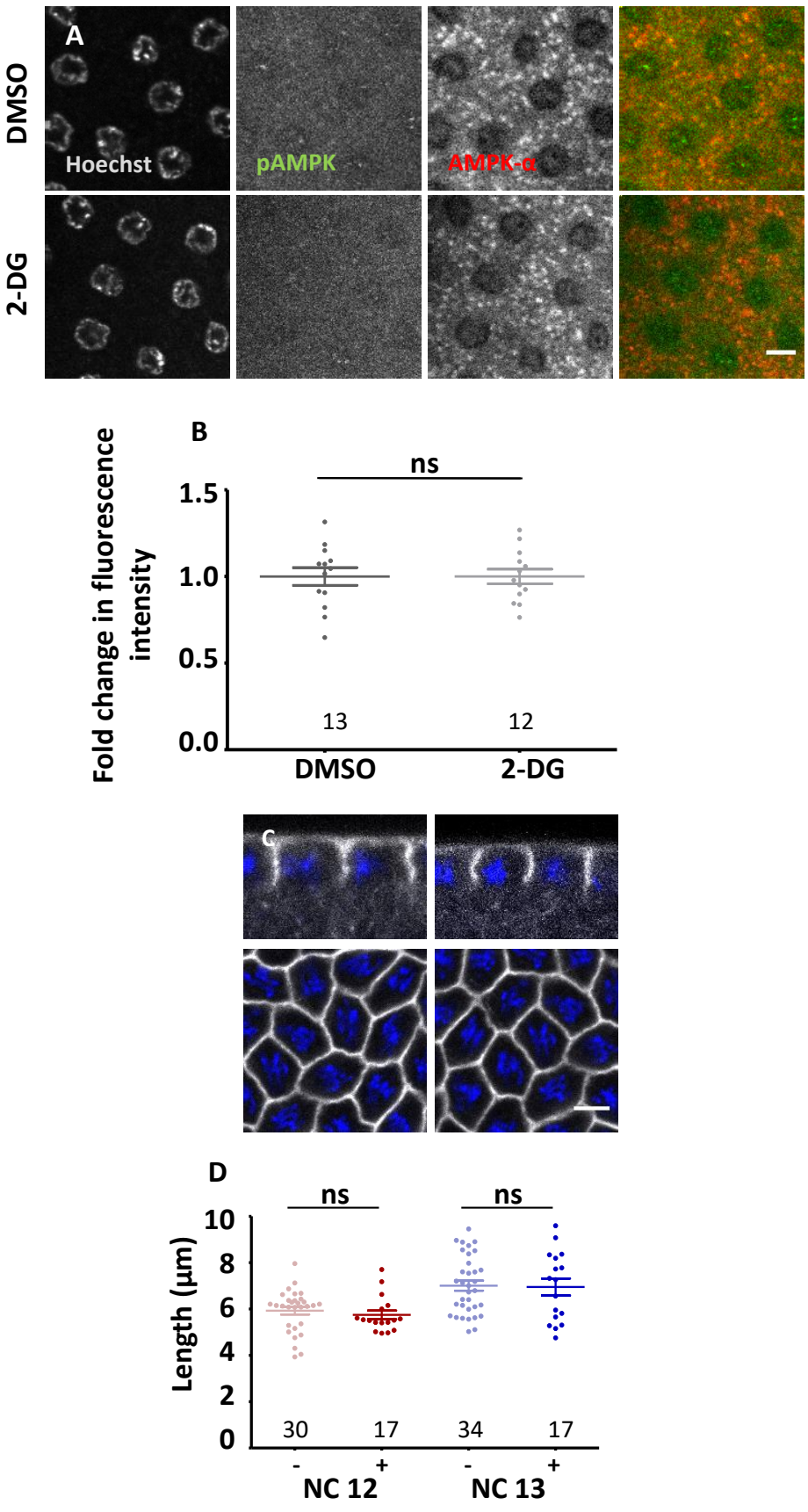
A
DMSO
2-DG
Hoechst
pAMPK
AMPK-α
B
Fold change in fluorescence intensity
ns
1.5
1.0
0.5
0.0
13
12
DMSO
2-DG
C
D
Length (µm)
ns
ns
10
8
6
4
2
0
30
17
34
17
-
+
-
+
NC 12
NC 13

Figure 4.9: Inhibition of glycolysis does not affect pAMPK levels and metaphase furrow length.

A-B: Treatment of syncytial *Drosophila* embryos with 2-DG does not show increase in the levels of pAMPK (green). n = 13, 13 embryos and 310 and 300 cells, N = 2; for treated and control embryos respectively. (ns, P>0.05, two tailed Mann Whitney test).

C-D: Metaphase furrow length is not reduced in 2-DG treated embryos compared to control embryos. NC 12 control metaphase furrows n = 30 furrows (8 embryos), 2DG n = 17 (5); NC13 control n = 32 (7), 2-DG n = 17 (5), N = 3. (ns, P>0.05, two tailed Mann Whitney test). Scale bar: 5 µm. Adapted from (Chowdhary et al., 2017).

4.4 Discussion

In the literature, smaller and dispersed mitochondria are thought to be poor ATP producers (Chen and Chan, 2005; Westermann, 2012). Our data show that despite the smaller structure, mitochondria produce ATP with the help of the ETC and syncytial cells do not rely on glycolysis for their energy requirements. Early embryos mainly utilize amino acids, especially aspartate and glutamate for energy production (Sieber et al., 2016; Tennessen et al., 2011; Thuy An et al., 2014) that enter the ETC via beta-oxidation pathways. Depletion of ATP via genetic and acute manipulation of the ETC components; and not inhibition of glycolysis; showed increased pAMPK staining in the embryos, clearly indicating that the metabolites of glycolysis pathway are not involved in the ETC production. This in accordance with previously known literature with ascidian and mammalian embryos where ETC is activated post fertilization under the influence of calcium signalling (Van Blerkom et al., 2002; Dumollard et al., 2007).

Mitochondrial hyperfusion during G1-S phase of cell division is necessary for cyclin E activity (Mitra et al., 2009). This also corresponds with mitochondrial activity cycling with depolarization of mitochondria occurring at M phase (Hirusaki et al., 2017). These studies were performed in mammalian cells using TMRE to monitor mitochondrial activity. AMPK phosphorylation is considered as a biomarker for analysing ATP levels in the cells. AMPK is phosphorylated by kinase Lkb1 (Hardie et al., 2006; Koh et al., 2008; Sakamoto, 2006; Sakamoto et al., 2004) under stressed conditions which leads to its localization in the nucleus, where it regulates transcription with the help of downstream transcription factors

such as FOXO-1 to maintain ATP levels (Greer et al., 2007). Even though mitochondrial architecture does not significantly change during syncytial NCs in the *Drosophila* embryo (Chapter 3), pAMPK localized in the nuclei or on the kinetochore, particularly during prophase and metaphase. These data may suggest changes in the energy profile of the syncytial cells during NCs, in accordance with the observations in the mammalian cells. pAMPK present in WT syncytial nuclei may be regulating transcriptional activity (Leff, 2003) in the cell division phase specific manner. pAMPK levels in the nuclei are further elevated in acute as well as genetic abrogation of ETC activity. Inhibition of ETC activity can lead to mitochondrial fission (Leonard et al., 2015). In our experiments, no change in the mitochondrial morphology or distribution was observed.

We show that ATP production from ETC is essential for rapid ingression of the membrane during the syncytial NCs. Inhibition of ETC, and not glycolysis, led to shortening of metaphase membrane furrows. pAMPK can modulate cells shape by phosphorylating Myosin regulatory light chain (MRLC) and affecting cell polarity (Lee et al., 2007). However, myosin 2 is not required for metaphase furrow invagination in syncytial cells (Royou et al., 2004). AMPK mutants have increased filamentous actin ratio in adult *Drosophila* brains (Cook et al., 2014). Increase pAMPK in the syncytial embryos after ETC inhibition can possibly lead to decrease in the f-actin and increase in the g-actin levels ratio which may result in shorter metaphase furrows. Actin regulator RhoGEF2 (Barmchi et al., 2005) and Dynamin (Rikhy et al., 2015) are also involved in metaphase furrow formation and elongation in syncytial *Drosophila* embryos. Both these proteins are GTPases and therefore require energy in the form of ATP. Inhibition of ETC and lowering of ATP could influence activity of these proteins, resulting in shorter metaphase furrows. Oxygen is essential for metabolism of ETC substrate. Hypoxia, that may lead to depletion of ATP in cells, impairs microtubule motor assembly on mitotic spindles (Pandey et al., 2007) and results in cell cycle arrest (DiGregorio et al., 2001; Fischer et al., 2004) in *Drosophila* embryogenesis. Mutations in the ε subunit of ATP synthase result in disorientation of syncytial blastoderm nuclei (Kidd et al., 2005). We have not analysed whether shorter metaphase furrows observed due to ETC inhibition are an outcome of impairment of spindle assembly during the syncytial NCs. Keeping mitochondria localized closely to the furrows in a compartmentalized manner (chapter3) probably helps in local delivery of energy in

abundance to the very dynamic actin remodelling. Future experiments involving significant reorganization of mitochondrial distribution and local assessment of ATP levels in the apico-basal axis may provide a link between mitochondrial distribution and local requirement of energy.

Chapter 5

Mitochondrial morphology and dynamics in cellularization and gastrulation

5.1 Introduction

After rapid 13 syncytial divisions, the embryo enters the stage of cellularization to form complete somatic epithelial cells for the first time. Cellularization is a prolonged interphase of NC14 wherein the small cell membranes of height around 3-5 µm extend deep towards the basal regions of almost 6000 nuclei, eventually enclosing them and forming a sheet of 40-45 µm tall cuboid shaped epithelial cells in about 45-50 mins (Lecuit and Wieschaus, 2000; Mazumdar and Mazumdar, 2002; Schejter and Wieschaus, 1993) (Fig. 5.1 A).

The membrane extension is driven by assembly of acto-myosin contractile structures (He et al., 2016; Schejter and Wieschaus, 1993; Warn and Robert-Nicoud, 1990; Young et al., 1991), membrane remodelling proteins such as septins (Grosshans, 2005; Mavrakis et al., 2014) and Anillin (Field, 2005) as well as cytoskeleton remodelling proteins such as Rho1 GTPase (Grosshans, 2005) and Diaphanous (Afshar et al., 2000) at the extension front which helps the membrane constriction as it progresses towards the basal side. The membrane extension during cellularization takes place in distinct initial slow phase followed by a rapid ingression phase. The slow phase is further distinguished into 2 phases as flow phase and recruitment phase based on the myosin dynamics (Figard et al., 2013; He et al., 2016; Lecuit and Wieschaus, 2000; Xue and Sokac, 2016). The addition of lipids to the basal regions is facilitated by endocytosis of membrane reservoirs from the apical villi which flatten completely by the cellularization end (Figard et al., 2016; Frescas et al., 2006; Pelissier et al., 2003; Sokac and Wieschaus, 2008).

Microtubules are oriented as an inverted basket structure around the nuclei with centrioles at the apical side and growing microtubule ends extending towards the basal sides during cellularization (Foe and Alberts, 1983; Foe et al., 2000; Karr and Alberts, 1986b). This entails an inherent polarity for transport of various molecules and organelles towards the apical or

the basal sides of the cells. Additionally disruption of microtubules in early cellularization halts membrane furrow extension (Foe and Alberts, 1983).

Golgi Complex function is associated with the membrane dynamics and small punctate Golgi complexes are trafficked on the microtubules. During late cellularization stages Golgi Complexes reorganize and are transported to the apical regions (Papoulas et al., 2005; Sisson et al., 2000). We wondered whether mitochondria could also be regulated in a similar manner during cellularization.

Gastrulation initiates immediately after cellularization. It consists of drastic morphogenetic movements which shape the embryo in the three germ layers. Fate of the cells in the embryo is already decided by axis determination cues during oogenesis and are therefore laid down maternally. Gastrulation begins by apical constriction of cells at the ventral side of the embryo, leading to invagination of the mesoderm under the influence of toll-dorsal pathway (Leptin, 1995, 1999; Solnica-Krezel and Sepich, 2012) (Fig. 5,1 B). The mechanism that regulates mesoderm invagination, or ventral furrow formation are clearly described. Under the influence of downstream transcription factors snail and twist (Hemavathy et al., 1997, 2004; Ip et al., 1994; Martin et al., 2010), Myosin II activity is initiated and maintained respectively at the ventral cells that constrict apically and eventually invaginate (Fuse et al., 2013; Lecuit and Lenne, 2007; Martin et al., 2010). Shape and junctional molecules such as RhoGEF2 (Grosshans, 2005; Kölsch et al., 2007), RhoA GTPase (Mason et al., 2016), Myosin II (Martin et al., 2009), E-Cadherin (Schafer et al., 2014) and Armadillo (β-catenin) (Weng and Wieschaus, 2016) have been shown to relocalize to apical regions of constricting cells at the ventral mesoderm.

Hints form literature suggest possible regulation of localization and activity of mitochondria at the prospective morphogenetic regions of embryos. Characterization of mitochondrially derived long ribosomal RNA (mtlr-RNA) showed an upregulation of signal at dorsal lip pore of the *Xenopus* embryos, which marks the future gastrulation site (Yost et al., 1995). It not clear whether mitochondrial localization or transcriptional activity is different in the dorsal regions compared to rest of the embryo. A study in *Drosophila* early embryos showed presence of dorso-ventral gradient of mitochondrial membrane potential. Interestingly

ventral side that has higher membrane potential is the future gastrulation site of the *Drosophila* embryo (Schiffmann, 1997).

We have demonstrated regulation of mitochondrial distribution and dynamics by microtubules during syncytial *Drosophila* embryogenesis. We then attempted to characterize mitochondria in cellularization and ventral furrow formation using Mito-GFP. The resultant observations are described in this chapter. We found that mitochondria, which are basally present in the syncytial cells, are actively transported on microtubule motors to the apical side during cellularization and in the ventral furrow during gastrulation.

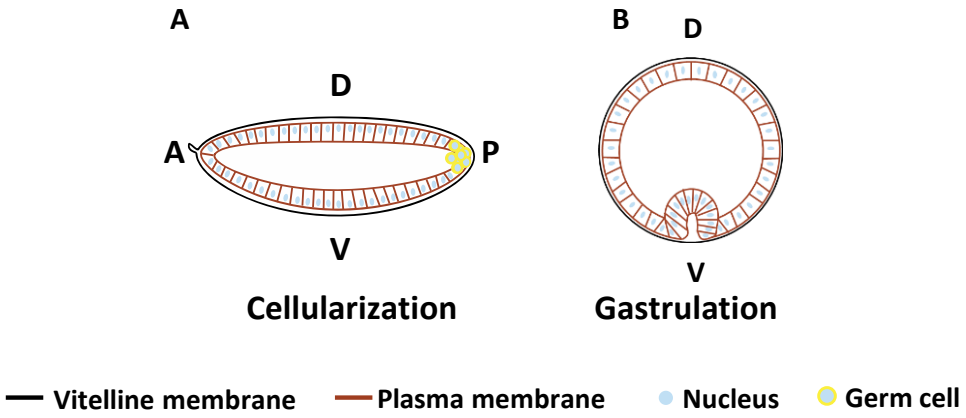

Figure 5.1: **Schematic representing cellularization and gastrulation stage of *Drosophila* embryogenesis.** Tall epithelial cells arranged in a single layer are formed during cellularization (**A**). Cells at the ventral mesoderm region apically constrict and invaginate during gastrulation (**B**).

5.2 Materials and methods

5.2.1 Fly stocks

All stocks were maintained at 25 °C in standard cornmeal agar. Mito-GFP and Mito-PAGFP and Tub-mCherry stocks described in 3.2.1 were used for live imaging and photoactivation respectively. Microtubule motor knockdown was done using *khc*i and *dhc*i as described in 3.2.1 *miro*^{i} was expressed using *nanos*-Gal4 and crosses were maintained at 28 °C. *rhogef2*^{i} and *mbs*^{i} were crossed to *mat*-Gal4.

Stock	Source (ref)
rhogef2^{i}	BDRC 34643
mbs^{i}	BDRC 41625

Table 5.1 List of fly stocks

5.2.2 Live Imaging

2 hr old embryos were collected from cages at 28 °C and processed for imaging as mentioned in materials and methods section of chapter 2 (2.5). For imaging dorso ventral axis, embryos were placed in an end on fashion (Mavrakis et al., 2008; Witzberger et al., 2008) as mentioned in Chapter 2 (2.5). Embryos were then imaged using Zeiss LSM 710/780, 63x 1.4 NA objective with temperature maintained at 25 °C.

5.2.3 Photoactivation

Imaging parameters used for photoactivation are mentioned in Chapter 2 (2.7). For photoactivation during cellularization, a rectangular ROI of 10-15 μm^2 was drawn at basal regions, chosen based on nuclear position as seen in white field imaging (Fig. 5.2 E). Images were taken every 2 mins. Fluorescence intensity at apical and basal regions was measured using ImageJ. Mean fluorescence intensity in the photoactivated ROI and an apical ROI in the same cells was measured, background corrected using mean cytoplasmic intensity and normalized to the first post activation value of the photoactivated ROI. The normalized intensities of these two regions for 3 embryos were plotted with SEM using Graphpad Prism 6.0

Photoactivation during gastrulation was performed in embryos oriented end on (4.2.5.2). A ring like ROI of 5 µm thickness, as shown in the schematic (Fig 5.3 G), was drawn at the basal region of all cells in the whole embryo. Photoactivation was performed using parameters mentioned in Chapter 2 (2.7). Post activation images were taken every 2 mins. Fluorescence was followed in apical and basal regions of the ventral furrow central cells and lateral cells. Ratios of mean apical to basal intensities for these three regions were measured and plotted across time in gastrulation.

5.2.4 Immunostaining

Embryos were stained for mitochondria and cell boundary using streptavidin and actin label phalloidin respectively as mentioned in 2.3 and 3.2.3. Fixation with heptane: 4% PFA (1:1) followed by hand de-vitellinization method was used.

5.2.5 Analysis

5.2.5.1: Mitochondrial fluorescence distribution during cellularization

Mean fluorescence in the apical most section of 3 embryos at 1 min time intervals during cellularization was measured using ImageJ, normalized using the highest intensity value and plotted against time with SEM using Graphpad prism 6.0.

To quantify mitochondrial intensity in the apico basal axis, mean Mito-GFP fluorescence intensity was measured across z stacks at 3 different time points: early (0 mins), mid (20 mins) and end (45 mins). The intensity was corrected using minimum intensity of the field and normalized to the highest intensity value at each time point for each embryo. Normalized intensity of 3 embryos was plotted with standard error. The quantification was done using ImageJ and plotted using Graphpad prism 6.0.

5.2.5.2: Mitochondrial fluorescence distribution during gastrulation

Mean mitochondrial fluorescence was measured at the apical regions (above nuclei) and basal region (below nuclei) in 3 regions: Ventral region (red), on the sides next to the ventral region (green) and lateral region (blue) (Fig. 5.3 D) and 7 different timepoints beginning from cellularization end and followed by successive time points in mesoderm invagination. The background intensity was measured from an area which did not contain visible fluorescent signal in the middle of the embryo. Time points across 3 movies were chosen based on the extent of furrow invagination and shape. Ratios of background subtracted apical to basal intensities across the timepoints were normalized with the ratio at cellularization end and plotted with SEM. The image analysis was done using ImageJ and plotted using Prism Graphpad 6.0.

5.2.5.3: Mitochondrial density across apico-basal axis

Mitochondrial density was measured as mentioned in 3.2.7.2. Briefly, mitochondrial punctae were intensity thresholded and total area of particles with sizes greater than 0.05 μm^2 was divided by area of the imaging field to get the mitochondrial density.

5.3 Results

5.3.1 Mitochondria are fragmented and migrate apically during cellularization

We imaged apical-basal sections of cellularizing Mito-GFP embryos and observed a gradual increase in apical mitochondrial density during cellularization (Fig 5.2A). We measured fluorescence intensity at this optical section and observed two phases of intensity change. Initially, mitochondrial intensity showed a non-linear increase till 30 mins and increased linearly till the end of cellularization (50 mins) (Fig 5.2 B). Membrane ingression and furrow canal ring closure during cellularization consist of similar slow and rapid phase (Lecuit and Wieschaus, 2000; Xue and Sokac, 2016) and the timing of switch between mitochondrial non-linear and linear transport phase is similar to the switching time point of membrane ingression from slow to fast (Fig. 5.2 B).

To analyse mitochondrial distribution in the entire cell along the apico basal axis in cellularization, we imaged 30 sections of 1 µm each from apical to basal side and quantified mitochondrial mean fluorescence intensity from apical to basal sections at 3 different time points during cellularization: early (0 min), mid (22 min) and end (45 min) (Fig. 5.2 C). We observed that mitochondria are enriched basally in the early cellularization, similar to their distribution in syncytial embryos (Fig 5.2 C, D). In the mid cellularization mitochondria accumulated at both apical and sides (Fig 5.2 C, D). By the end of cellularization, most mitochondria appeared apical (Fig 5.2 C, D). This change in the distribution of fluorescence intensity can possibly be due to either production of more mitochondria at the apical sections by mitochondrial biogenesis (Shiota et al., 2015) or by transport of mitochondria to the apical side. It is difficult to assay total mitochondrial density, or increase in the mitochondrial numbers using confocal microscopy due to depth and resolution limits. Also, a huge number of mitochondria is already added maternally in the embryo. One can possibly estimate mitochondrial biogenesis by estimating mitochondrial genome quantity or

a mitochondrial DNA associated protein. We were able to test the possibility of mitochondrial transport. Cells in the *Drosophila* blastoderm embryo are compartmentalized and therefore this suggests the existing possibility of gaining fluorescence at the apical regions is by the mitochondrial transport from the basal sides.

To demonstrate basal to apical mitochondrial transport during cellularization, we used photoactivation. We activated mitochondrial signal basally in an ROI (red) at 12-15 µm from the apical surface in sagittal sections and followed the fluorescence signal across successive time points during the entire cellularization process using Mito-PA-GFP embryos (Fig. 5.2 E,F). Fluorescence signal rapidly moved from basal region (red) to apical (green) immediately after photoactivation within one min which kept increasing with successive time points (Fig. 5.2 F). By the end of cellularization, fluorescence was almost entirely lost from the basal regions and was seen apically (Fig 5.2 F). We measured the apical and basal intensities as the cellularization progressed. The basal intensity reduced by 5 fold and apical intensity increased to about 7 fold of the initial intensity value in 40 mins (Fig 5.2 G). We therefore concluded that mitochondria are trafficked apically during cellularization from the basal pool. Temporal colour projection of photoactivated cells showed mitochondria migrating apically in linear tracks, suggesting a role of microtubule-based transport.

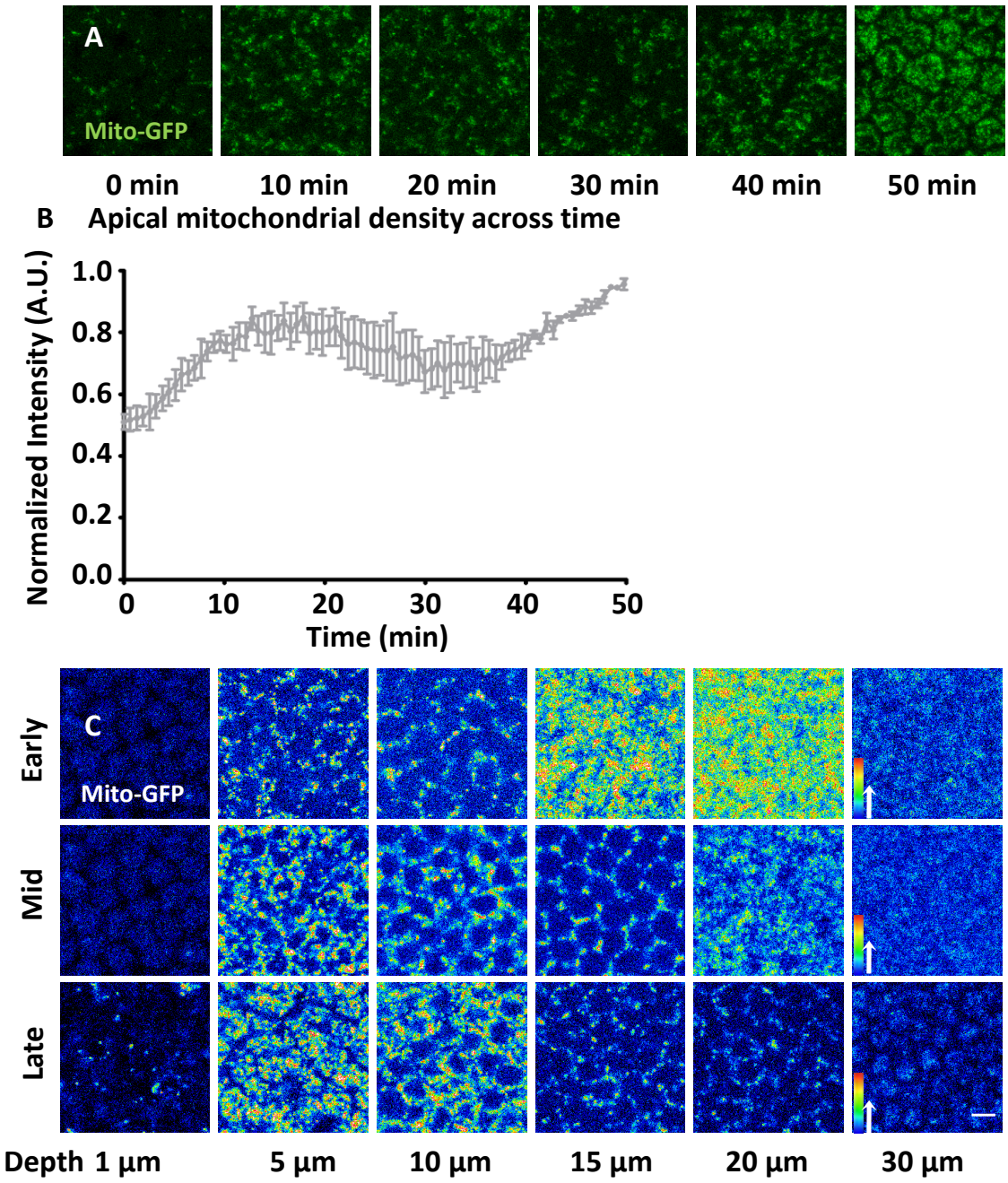
A
Mito-GFP
0 min
10 min
20 min
30 min
40 min
50 min
B Apical mitochondrial density across time
Normalized Intensity (A.U.)
1.0
0.8
0.6
0.4
0.2
0.0
0
10
20
30
40
50
Time (min)
C
Mito-GFP
Early
Mid
Late
Depth 1 µm
5 µm
10 µm
15 µm
20 µm
30 µm
D Mitochondrial density across cell depth
Normalized Intensity (A.U.)
1.0
0.8
0.6
0.4
0.2
0.0
Early
Mid
Late
0
5
10
15
20
25
30
Depth (µm)

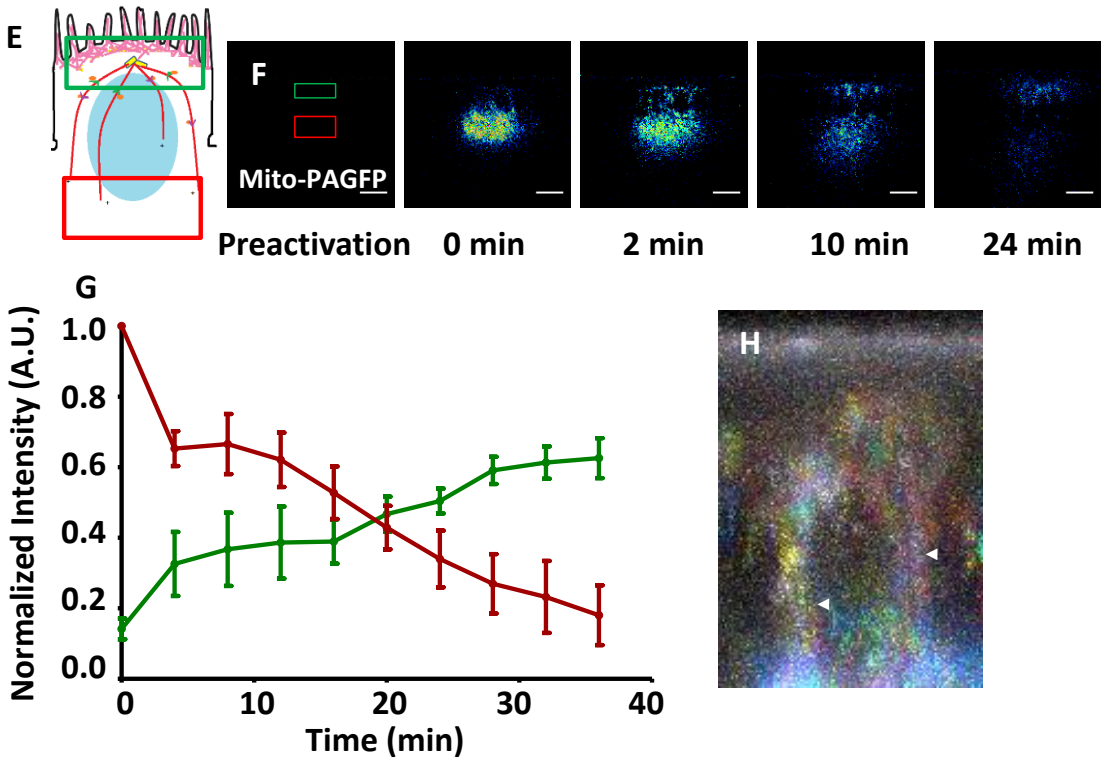

Figure 5.2: Mitochondria migrate apically during cellularization. Gradual accumulation of mitochondrial punctae is seen at the apical-most (1-2 µm) regions in cellularizing embryos (**A**). Mean fluorescence intensity at apical region is quantified across time and plotted with SEM for n = 3 embryos and total 200 cells (**B**). Apico basal distribution of mitochondria changes during cellularization (**C-D**). Mitochondria are present around the nuclei and have higher density at cellularization beginning (**C, Top panel**). Some mitochondria are present apically by mid cellularization (**C, Middle panel**) and are completely apical by cellularization end (**C, Bottom panel**). Mean mitochondrial intensity across depth is plotted with SEM for n = 3 embryos and total 200 cells for early, mid and late cellularization stages. The fluorescence is highest at basal regions in early (red), shifts towards apical regions in mid (green) and is completely apical in late (blue) cellularization. (**D**)**.** (**E-H**): Apical migration of mitochondria is observed using photoactivation. Schematic of photoactivation experiment showing basal photoactivated ROI (red) and non-photoactivated apical ROI (green) (**E**). Mito-PAGFP, activated at basal region of early cellularization (red) shows gradual decrease and apical region (green) gains fluorescence signal with time during cellularization (**F**). Normalized mean fluorescence intensity is plotted with SEM for basal (red) and apical regions (green) for n = 4 embryos (**G**). Temporal colour coded image shows mitochondrial tracks (white arrow, **H**).

5.3.2 Mitochondria migrate apically at the ventral furrow

We stained embryos with fluorescently labelled mitochondrial marker streptavidin and phalloidin to mark the cellular boundaries. We noticed an enrichment of mitochondria in the epithelial cells of the ventral furrow, compared to the rest of the epithelial cells. Such an enrichment was not observed in the cephalic furrow (Fig 5.3A, white arrowheads). The mitochondrial enrichment was observed at apical regions of the ventral furrow cells (Fig 5.3 B). To analyze this distribution more carefully live imaging was performed. Mito-GFP embryos were placed in an end on orientation using sigmacote on labtek chambers (5.2.2) (Fig 5.3 C). This enables to visualize the cross-sectional surface and therefore the dorso-ventral axis of the embryo. Cellularized embryo has uniform mitochondrial distribution in the whole embryo irrespective of the embryonic axes (Fig.5.3 C, 0 min). We observed an increase in the intensity of mitochondria specifically at the ventral furrow with time upto 6 mins where the mesoderm invagination initiates (Fig 5.3 C). Apical and basal mean mitochondrial intensity in different timepoints at ventral mesoderm region (red), mesoderm neighbouring region (green) and lateral region (blue) as shown in the schematic (Fig. 5.3 D) were measured and the normalized ratio of apical: basal was plotted at successive time points in gastrulation (Fig 5.3 E). Analysed time points from different embryos were matched according to shape of the ventral furrow or extent of the invagination. The normalized mitochondrial intensity ratio almost doubled at the 2nd time point, became five times at the 3rd time point and stabilized then onwards in specifically the mesoderm region (red). The neighbouring region (green) showed slight increase (1.2 fold) but was insignificant compared to the central region. The mitochondrial apical: basal ratio was unchanged at the lateral regions during gastrulation (Fig 5.3 E). This raises two possible explanations, as discussed in (5.3.1). Firstly, there could be increased mitochondrial biogenesis, we have not tested this possibility. Second, mitochondria are transported to the apical side, we have only been able to test the second possibility.

We then used photoactivation to monitor how mitochondria are moving at these stages. We activated mitochondrial signal at the basal regions of an entire embryo placed in the end on orientation as mentioned in materials and methods (4.2.5.3) (Fig 5.3 F). The photoactivation was performed at the end of cellularization at the basal regions of cells in the entire embryo (Fig 5.3 G, red ROI). Fluorescence activated mitochondria were observed rapidly moving to

the apical side at the ventral furrow within one minute after photoactivation and the intensity kept increasing with time (Fig 5.3 F). Such a shift in the distribution was not seen in the lateral cells (Fig. 5.3 F).We quantified fluorescence intensity at apical and basal regions of ventral (green) and lateral (blue) cells with time. Mitochondrial signal at the ventral region (green) increased to about 3.5 fold. The lateral region (blue) did not have a significant intensity change (Fig. 5.3 H). This showed that post cellularization, mitochondrial apical migration is enhanced at the ventral furrow cells as compared to the neighbours and lateral cells. The increase in the mitochondrial intensity correlates with the time of apical constriction of the ventral mesoderm cells and saturates during mesoderm invagination. The temporal colour coded images of ventral and lateral region cells reiterate these results (Fig 5.3 I). Lateral cells have the temporal signal completely colocalized, indicating lack of migration (Fig 5.3 I). The linear tracks of migration can be seen in the temporal colour coded image for the ventral cells (Fig 5.3 I, white arrowheads) suggesting to specific regulation of mitochondrial transport towards the microtubular minus ends.

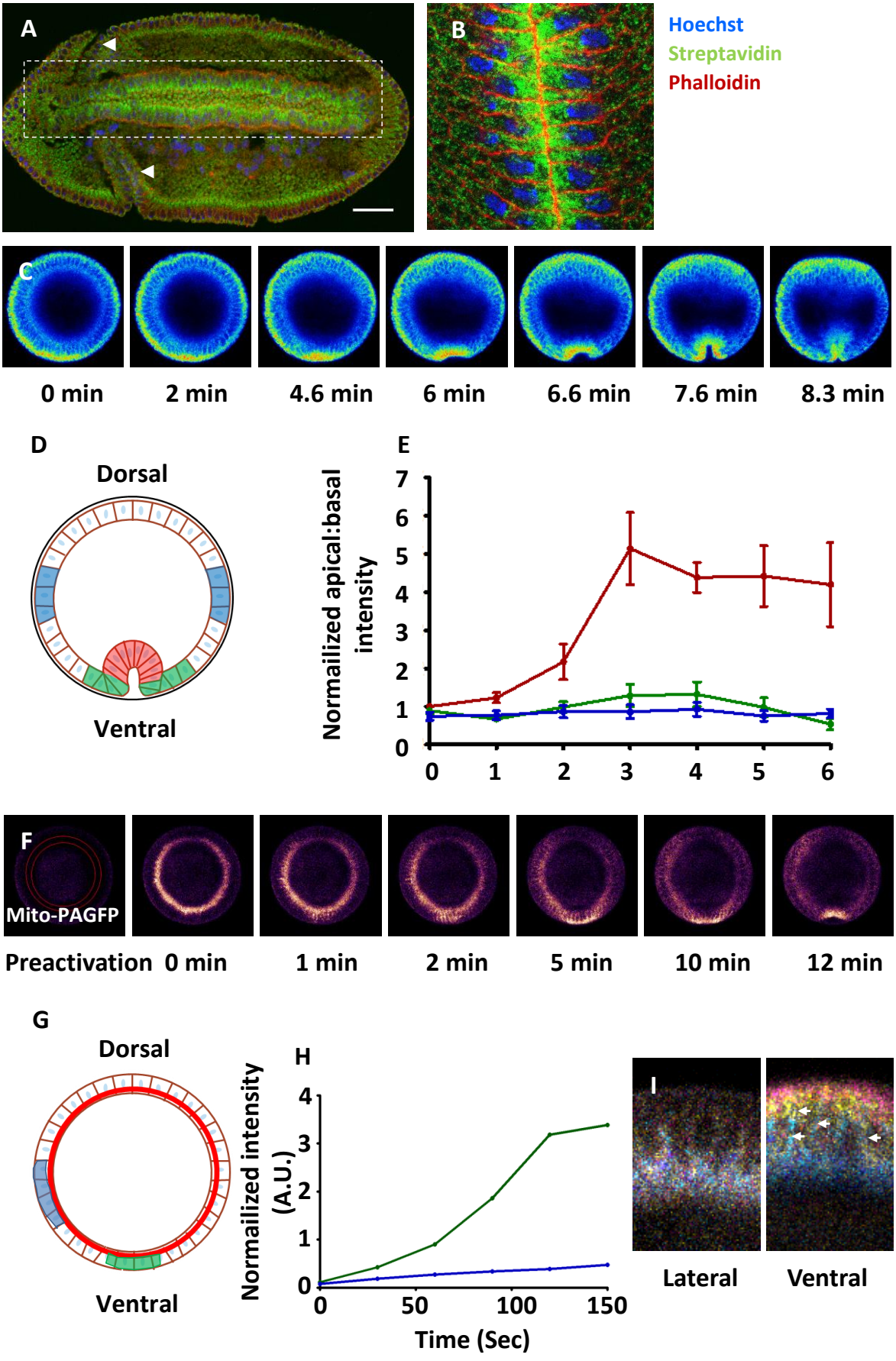
A
B
Hoechst
Streptavidin
Phalloidin
C
0 min
2 min
4.6 min
6 min
6.6 min
7.6 min
8.3 min
D
Dorsal
Ventral
E
Normailized apical:basal intensity
0
1
2
3
4
5
6
7
F
Mito-PAGFP
Preactivation
0 min
1 min
2 min
5 min
10 min
12 min
G
Dorsal
Ventral
H
Normailized intensity (A.U.)
0
1
2
3
4
0
50
100
150
Time (Sec)
I
Lateral
Ventral

Figure 5.3: Mitochondrial distribution during gastrulation. Wild type embryo stained with streptavidin (green) and phalloidin (red) show mitochondrial localization at the ventral furrow (**A**). Zoomed in image shows mitochondria (streptavidin, green) apical to the nuclei (Hoechst, blue) in ventral furrow cells (**B**). End on live imaging of Mito-GFP shows increase in the fluorescence apically at ventral furrow and not at the lateral sides (**C**). Apical: Basal intensity is quantified at ventral mesoderm region (red), neighbouring region (green) and lateral region (blue) (**D, E**). Normalize apical: basal intensity for n = 3 embryos is plotted with SEM (**E**). Photoactivation reveals specific relocalization of mitochondrial at the ventral furrow (**F-I**). Mitochondrial fluorescence is activated in the whole embryo at basal region at the cellularization end in Mito-PAGFP embryos (**F, G**). Normalized fluorescence intensity post PA is plotted for ventral (green) and lateral (blue) region (**H**). Temporal colour coded images at lateral and ventral cells show mitochondrial migration in ventral cells and not in the lateral cells (**I**)

5.3.3 Mitochondrial migration during cellularization is regulated by microtubules

Microtubules are oriented in apico-basal axis and for long filaments during cellularization. Apical transport of Golgi Complexes (Papoulas et al., 2005; Sisson et al., 2000) and basal transport of lipid droplets along microtubules has been reported before during late cellularization (Arora et al., 2016). Mitochondria are transported bi-directionally on axons on the microtubules (Morris and Hollenbeck, 1993).

Similar to experiments done in the syncytium, we used Mito-GFP and Tub-mCherry to image mitochondria and microtubules together. We found that mitochondria are juxtaposed to microtubule filaments (Fig 5.4 A, 6 µm), and could follow them moving to the apical regions along (Fig 5.4 A, sagittal, white arrow heads). Intensity profile of mitochondria (green) and tubulin (red) plotted for depicted region (white dashed line, 6 µm).

To study the role of microtubule motors, we used RNAi based approach to knockdown *khc* and *dhc* using *nanos*-Gal4. Since mitochondria are basally present during early cellularization, apical regions have few distinct and sparse mitochondria (Fig 5.4 C, D top panel). Similar to observations in syncytial blastoderm embryo, mitochondria were clustered sub-apically in the early cellularization stages in the *khc*^{i} embryos (Fig 5.4 D bottom panel).

Apical transport during cellularization is towards the microtubule minus end via dynein. Since mitochondria are localized at apical regions in the late cellularization, the basal sections have fewer distinct mitochondria (Fig 5.4 E, F top panel). We observed clumping of mitochondria in late cellularization stages in *dhc*^{i} embryos (Fig 5.4 F middle panel), which is likely to be due to lack of transport. The mitochondrial morphology in *dhc*^{i} embryos also appeared clustered, similar to what was observed in syncytial stages. But syncytium did not have obvious distribution changes compared to cellularization (Fig 3.8 I, J).

Mitochondrial Rho GTPases (Miro) are involved in mitochondrial transport on microtubules (Fransson et al., 2006a; Guo et al., 2005). They can interact with microtubule motors Kinesin (Fransson et al., 2006a) and Dynein (Morlino et al., 2014), as well as adapter protein Milton (Melkov et al., 2016) and facilitate bidirectional transport of mitochondria (Russo et al., 2009) in the axons. Miro can also interact with Myosin 19 and couple mitochondria to actin cytoskeleton (López-Doménech et al., 2018). We knocked down Miro in the embryos using RNAi (*miro*^{i}). This experiment was done N = 4 times. Most early embryos showed mild Kinesin knockdown like phenotype with mitochondrial accumulation at the basal region in 2 out of 4 experimental trials. This is likely because the RNAi against *miro* is weak and is unable to knockout the mRNA efficiently. In the other 2 trials, similar to *dhc*^{i}, mitochondria were clustered more at the basal regions during early as well as late cellularization in *miro*^{i} embryos. But unlike *dhc*^{i}, mitochondrial morphology was not altered in these embryos (Fig 5.4 F bottom panel).

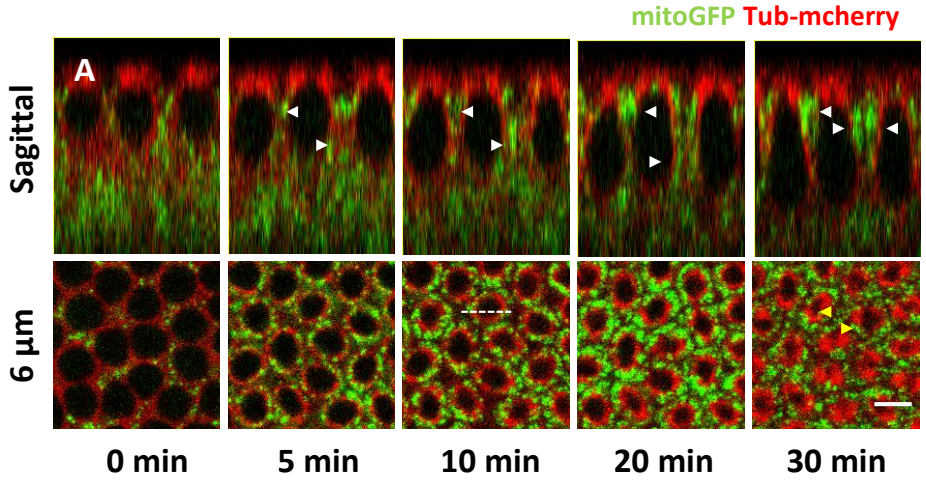
mitoGFP Tub-mcherry
A
Sagittal
6 µm
0 min
5 min
10 min
20 min
30 min

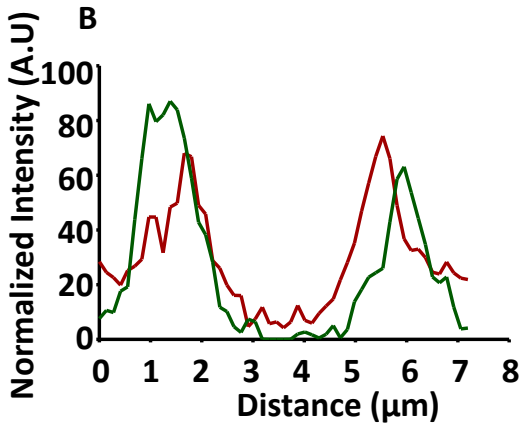
B
Normalized Intensity (A.U)
100
80
60
40
20
0
0 1 2 3 4 5 6 7 8
Distance (µm)

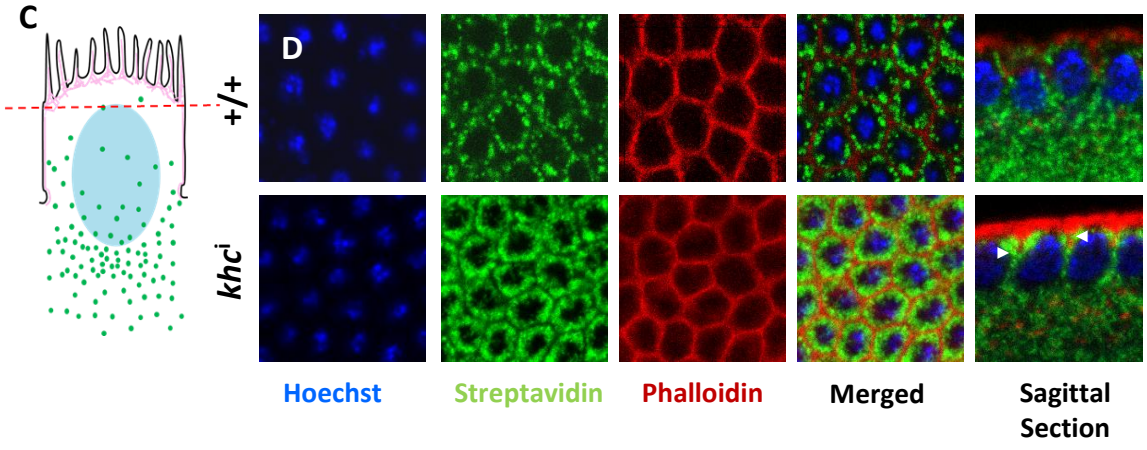
C
+/+
khc^i
D
Hoechst
Streptavidin
Phalloidin
Merged
Sagittal Section

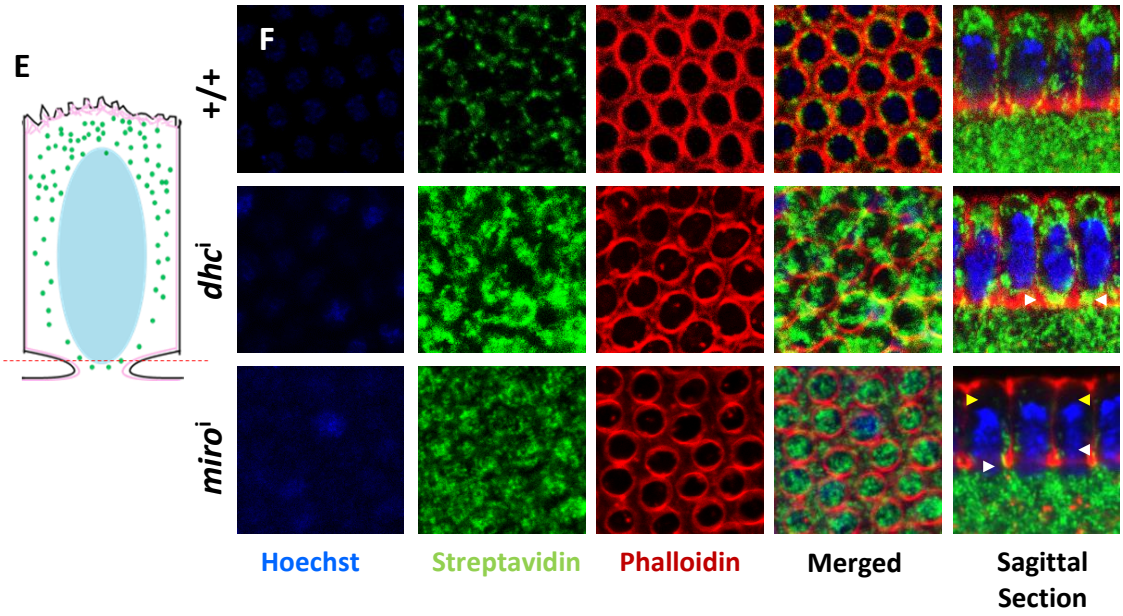

Figure 5.4: Apical migration of mitochondria is regulated by microtubules. (**A-B**): Mitochondria localize next to microtubules. Live imaging using Mito-GFP and Tub-mCherry shows mitochondria (green) along microtubule tracks (red) during cellularization progression (white arrowheads) (**A, sagittal**). Mitochondria localize on the microtubules and gradually accumulate around the centrioles (yellow arrowheads) (**A, 6 µm**). Intensity profile of Mito-GFP (green) and Tub-mCherry (red) is plotted as shown by white dashed line (**A, 6 µm, 10 mins**) (**B**). (**C-F**): Mitochondrial localization depends on microtubule motors. Mitochondria (streptavidin, green) localize at subapical regions around nuclei (hoechst, blue) in *khc*^{i} in early cellularization (**C-D**) and marked by white arrows in sagittal (**D**). The chosen region during early cellularization is depicted in the schematic (**C**). Mitochondria (streptavidin, green) are observed at basal sections of late celluarization in *dhc*^{i} and *miro*^{i} as shown in the schematic (**E**). Mitochondria (streptavidin, green) are more clustered near contractile rings (phallodin, red) in *dhc*^{i} and *miro*^{i} embryos as compared with WT (**F**). Mitochondrial clusters in *dhc*^{i} and *miro*^{i} are marked by white arrows in the sagittal sections (**F**). Absence of apical mitochondria is denoted by yellow arrows in *miro*^{i} embryos (**F**).

Next we checked whether affecting acto-myosin dynamics can affect the mitochondrial localization. We used RNAi against *rhogef2* (*rhogef2*^{i}) and *mbs* (*mbs*^{i}). RhoGEF2 activity is essential for actin dynamics during cellularization (Wenzl et al., 2010). Myosin phosphatase (MBS) inhibits Myosin II activity, thus knocking it down hyper-constricts the contractile rings in cellularization (Munjal and Lecuit, 2014). Although there were expected defects in the

membrane constriction in *rhogef2*^{i} and *mbs*^{i}, the mitochondria were present apically in late cellularization staged embryos (Fig. 5.5).

We hence conclude that mitochondrial trafficking from basal to apical regions during cellularization does not depend on actin dynamics and is based on the Dynein motors on the microtubules, possibly via Miro.

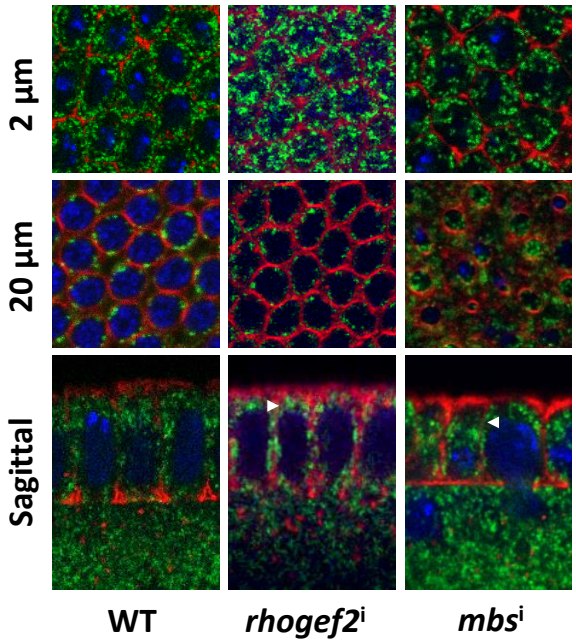

Figure 5.5: Acto-myosin dynamics is not essential for mitochondrial apical migration. Mitochondria (streptavidin, green) at the apical (2 µm) and basal sections (20 µm) of *rhogef2*^{i} and *mbs*^{i} are shown. Mitochondria properly localize at the apical sections above the nuclei (Hoechst, blue) in *rhogef2*^{i} and *mbs*^{i} at late cellularization stage, also marked with white arrows in sagittal sections. Few mitochondria are seen at basal sections around the contractile ring (phalloidin, red)

5.4 Discussion

We observed that mitochondria were small spherical structures throughout cellularization and gastrulation. Mitochondria gradually populated at the apical regions during cellularization in 2 phases. Cellularization dynamics is redundantly classified into 2 distinct phases: slow early phase and rapid late phase. The gradual apical localization of mitochondria during cellularization seemingly follows this trend. Mitochondrial density

switched from being highly basally localized to apically localized. Although Golgi complexes display apical migration during cellularization, similar to mitochondria, their dynamics of migration is not very well followed (Papoulas et al., 2005; Sisson et al., 2000). We could clearly show mitochondrial relocalization from the basal to the apical regions by photoactivating fluorescence in the basal mitochondrial populations at early cellularization in the sagittal planes of the embryos.

Microtubules are apico-basally polarized with minus ends at the apical side and growing plus ends towards the basal side (Foe and Alberts, 1983). Golgi complexes move apically during the late stages of cellularization (Sisson et al., 2000). Golgi complexes associate with microtubule motor Dhc and dynactin via Golgi specific adapter, Lava lamp (Papoulas et al., 2005). Inhibition of Golgi activity leads to disruption of membrane extension during cellularization (Sisson et al., 2000). On the other hand, lipid droplets are transported to the basal regions (Arora et al., 2016). We looked at the role of microtubule motors in transporting mitochondria during cellularization by using RNAi against Khc and Dhc. Consistent with data from syncytial stage embryos (Chowdhary et al., 2017) (3.3.5.3) knocking down Kinesin showed accumulation of more mitochondria in the subapical planes during early cellularization. Mitochondrial distribution in the WT embryos is similar to syncytial stages just when the cellularization begins. It is possible that either the defect in mitochondrial localization during syncytial stages in *khc*^{i} is retained when the cellularization begins or mitochondria prematurely accumulate apically. Eventually by the end of cellularization, the mitochondrial density became equivalent to the WT in *khc*^{i} embryos. Apical transport of mitochondria towards the microtubule ends during cellularization is dependent on dynein, similar to Golgi Complexes. Mitochondria can bind to both Dynein and Kinesin adapters with the help of Miro. Based on our data, there is a possible involvement of Miro in the apical mitochondrial transport.

Toll-Dorsal pathway, activates downstream cascade of transcription factors and kinases that lead to apical activation of myosin II at the ventral furrow that leads to apical constriction and invagination of ventral mesoderm cells (Hemavathy et al., 2004; Ip et al., 1992; Jiang et al., 1991; Leptin, 1995; Martin et al., 2010). We observed a very peculiar relocalization of mitochondria after the cellularization completion at the ventral side of the embryo during this stage. Using live imaging and photoactivation we found that mitochondrial apical

migration during cellularization occurs globally but additional apical migration post cellularization is present very specifically in the ventral furrow cells. Apical transport during gastrulation is likely to be via dynein motors. We propose an interaction between Toll-Dorsal pathway and mitochondrial relocalization, either directly or by regulation of microtubule based apical transport. We have attempted to modify toll-dorsal activity either by up-regulation or down-regulation of components such as Dorsal, Twist and Fog, and also Myosin regulators to analyse whether mitochondria interact with this pathway and will be described in chapter 7.

There is an apparent switch of regulation of mitochondrial transport starting in cellularization and is continued during gastrulation at the ventral furrow. We wonder if this is due to modifications in activity of microtubule motors. *khc* transcripts reduce in 3-4 hr old embryo (ModEncode), suggesting overall reduction in the number of Kinesin motors could discontinue basal mitochondrial trafficking. Cytoplasmic dynein can activate and bind to microtubules based on cargo or adapter binding (McKenney et al., 2014; Schroeder and Vale, 2016). The adapter Miro can regulate bi-directional transport by binding mitochondria to both, Kinesin and Dynein motors (Russo et al., 2009). An interesting possibility is regulation of Miro and mitochondrial transport during cellularization by calcium (Cai and Sheng, 2009; Fransson et al., 2003; Saotome et al., 2008) and ROS (Debattisti et al., 2017) as suggested by data from mammalian cell lines and hippocampal neurons. Increased calcium levels reduce bind of Miro to Kinesin motors (Wang and Schwarz, 2009). Whether there are changes in calcium or ROS activity during cellularization and gastrulation is yet to be tested.

Finally, what could be functional relevance of the mitochondrial redistribution in this stage specific manner? Mitochondria produce cellular energy, ROS and regulate calcium. Mitochondrial energy could be responsible for apical constriction and furrow invagination. Inhibition of ATP synthesis in zebrafish embryos arrested gastrulation (Pinho et al., 2013). A gradient of mitochondrial activity in the dorso-ventral axis has been reported in the *Drosophila* embryos (Schiffmann, 1997). Mitochondrial ROS regulates mitochondrial morphology and Myosin II based contractions in dorsal closure stage of *Drosophila* embryogenesis (Muliyil and Narasimha, 2014). A similar local regulation of Myosin II may exist during gastrulation as well. This is being tested using ROS reporters and mitochondrial mutations.

Chapter 6

Mitochondrial morphology regulates cell elongation and contractile ring formation in cellularization

6.1 Introduction

Mitochondrial size and shape is regulated by fission and fusion machinery and can modulate various cellular functions and signalling. Different cell types have different mitochondrial architecture and it is modulated based on the cellular requirements (Kuznetsov et al., 2009). Mitochondrial fission and fusion is carried out by well characterized GTPases. Fission protein Drp1 (Dynamin related protein 1) binds to the outer mitochondrial membrane receptor Fis1 (Fission, mitochondrial1). Opa1 (Optic atrophy 1) and Mfn1 and Mfn2 (Mitofusins) (Mitochondrial assembly regulating factor, *marf* in *Drosophila*) assist the fusion of inner and outer membrane respectively (van der Bliek et al., 2013). One of the major mitochondrial functions is to generate ATP by oxidative phosphorylation. Additionally, reactive oxygen species (ROS) is generated, primarily by Complex I and III of the electron transport chain (ETC) (Bell et al., 2007; Liu et al., 2002). Mitochondrial shape and cristae architecture is usually correlated with their metabolic output, ROS and calcium buffering (Cogliati et al., 2013; Hom et al., 2010; Mishra and Chan, 2016; Toyama et al., 2016; Williams et al., 2016; Yu et al., 2006). Studies demonstrate a link between metabolism, and cellular pluripotency and differentiation. Stem cells largely contain nascent mitochondria with underdeveloped cristae and mainly generate ATP using glycolysis (Khacho et al., 2016; Mandal et al., 2011; Suhr et al., 2010; Williams et al., 2016; Zhang et al., 2011). Mitochondrial DNA production, copy number and activity increases upon induction of differentiation in neurons (Birket et al., 2011), cardiomyocytes (Hom et al., 2011; St. John et al., 2005), mesenchymal stem cells (Li et al., 2017), germ cells (Hayashi et al., 2017; Teixeira et al., 2015), follicles cells (Tomer et al., 2018), embryonic stem cells (Kelly et al., 2012; Mandal et al., 2011) and iPSCs (Xu et al., 2013).

Recent advances demonstrate the involvement of mitochondrial morphology regulation is differentiation related signalling pathways. Differentiation regulated by EGFR pathway regulates mitochondrial morphology and membrane potential in the *Drosophila* follicle stem

cells (Mitra et al., 2012; Tomer et al., 2018). The growth inducing Hippo/Yorkie pathway regulates mitochondrial fusion and ROS (Nagaraj et al., 2012). Additionally mitochondrial morphology is cyclically regulated during cell division. Mitochondrial fusion during G1-S phase allows accumulation of resources and fragmentation during M phase ensures proper distribution to the daughter cells (Mandal et al., 2010; Mitra et al., 2009; Owusu-Ansah et al., 2008a; Parker et al., 2015). Also, mitochondrial fragmentation and release of cytochrome C in a pro-apoptotic signal which activates the caspase cascade downstream (Abdelwahid et al., 2007; Frank et al., 2001; Lee et al., 2004; Wasiak et al., 2007; Zhang et al., 2008a).

Mitochondrial morphology in the early blastoderm vertebrate and invertebrate embryos is punctate and dispersed (Bavister and Squirrell, 2000; Van Blerkom et al., 2002; Chowdhary et al., 2017; Dumollard et al., 2007; Sathananthan and Trounson, 2000). Maintaining mitochondrial morphology is essential for embryonic survival. Mutant knockout Drp1, Mfn and Opa1 mouse embryos die early in development and their growth is retarded compared to control embryos of same age (Chen et al., 2000; Ishihara et al., 2009; Moore et al., 2010; Wakabayashi et al., 2009). But, how is mitochondrial morphology regulated during embryogenesis, the consequent phenotypes of morphology alterations or the steps and signalling during embryogenesis affected due to morphology alterations is unknown.

We attempted to alter mitochondrial fission and fusion proteins in the *Drosophila* embryo. Mitochondrial fission protein, Drp1 mutant embryos showed lack of mitochondrial transport and formed smaller cells with larger contractile rings. A rescue was observed by knocking down fusion protein Opa1 in the background of Drp1 mutation.

6.2 Materials and Methods

6.2.1 Fly Stocks

All stocks were maintained at 25 °C in standard corn meal agar. All RNAi stocks were crossed with *nanos*-Gal4 and maintained at 28 °C. *opa1*^{i} (Valium 20) crossed to *nanos*-Gal4 was also tested at 25 °C. UAS-Marf-GFP was crossed to *mat*-Gal4 at 28 °C. Drp1 mutants, UASp-*drp1*^{SG} and UASp-*drp1*^{SD} were crossed to either *nanos*-Gal4 or Mito-GFP, and maintained at 28 °C. UASp-*drp1*^{SG}; *opa1*i flies were crossed to *nanos*-Gal4. UASp-*hSOD1*^{A4V} and UASp-

Sqh^{A20A21} were crossed to Mito-GFP flies at 28 °C. Genomic deletion mutants, *drp1*^{KG} and *drp1*^{nrd} were used in combination with RNA polymerase II 140 wimp mutant allele (*wimp*) and also with each other to generate heteroallelic combination. These crosses were maintained at 25 °C. The stocks are listed in the table 6.1. Embryos obtained from F1 generation flies (F2 embryos) were imaged and analysed.

Stock	Source (ref)
drp1^{KG}	(Mitra et al., 2012; Rikhy et al., 2007)
drp1^{nrd}	(Mitra et al., 2012; Rikhy et al., 2007)
drp1^{i}	VDRC
drp1^{i} (Valium 20)	BDRC 51483
UASp-*drp1*^{SG}	Generated in the lab by Darshika Tomer
UASp-*drp1*^{SD}	Generated in the lab by Darshika Tomer
UASp-*drp1*	Generated in the lab by Darshika Tomer
marf^{i} (Valium 1)	BDRC 31157
marf^{i} (Valium 20)	BDRC 55189
marf^{i} (MG)	Ming Guo Lab
UAS-Marf-GFP	
opa1^{i} (Valium 20)	BDRC 32358
opa1^{i} (MG)	Ming Guo Lab
UASp-*drp1*^{SG}; *opa1*i	Generated in the lab
wimp	BDRC 5874
Sqh-mCherry	BDRC 59024

Sqh-GFP	BDRC 57145
Mito-GFP:Sqh-mCherry	Generated by recombining *nanos*-Gal4:UAS-Mito-GFP and Sqh-mCherry
UASp-*hSOD1*^{A4V}	BDRC 33607
UASp-Sqh^{A20A21}	BDRC 64114
nanos-Gal4	BDRC
mat-Gal4	Girish Ratnaparkhi

Table 6.1 List of fly stocks

6.2.2 Live Imaging

Live Imaging of Mito-GFP, *drp1*^{i}; Mito-GFP, Mito-GFP:Sqh-mCherry and *drp1*^{SG}; Mito-GFP:Sqh-mCherry was performed as mentioned in Chapter 2 (2.5) on Zeiss LSM 780 confocal microscope using 63x 1.4 NA objective. 40 Z stacks with 1 µm interval between stacks were obtained during cellularization.

To visualize the ingressing furrows, sagittal sections were chosen from Sqh-mCherry containing embryos such that the cells were visible in the apico-basal axis and present linearly. Single plane images were taken at 2 mins time interval using either Zeiss LSM 780 or Leica sp8 confocal microscopes.

6.2.3 Immunostaining

Embryos were fixed with Heptane: 4% PFA, hand- devitallinized and stained with streptavidin to mark mitochondria and phalloidin to mark F-actin as mentioned in 3.2.3. Anti-Drp1 antibody (Leo Pallanck) was used in 1:500 dilution.

6.2.4 DHE staining

Embryos were permeabilized and fixed using Heptane: 4% PFA for 20 mins (2.4). Embryos were then washed once with PBS and incubated with 30nM DHE for 7 mins. This was

followed by 3x, 5 mins washes with PBS-T. Hoechst was added in the second wash. Embryos were mounted using Slowfade Gold (Life Technologies).

Reagent	Source	Host Species (Ab)	Dilution/ Concentration
Drp1 Antibody	Leo Pallanck	Rabbit	1:500
DHE	Invitrogen	-	30 nM

Table 6.2 List of reagents

6.2.5 Embryonic lethality estimation

3 hr old embryos were obtained from flies grown in embryo cages with yeast supplemented, 3% sucrose - agar plates. The embryos were washed and laid onto fresh 3% sucrose - agar plates in a 10 × 10 array (or smaller when number of eggs obtained was less). Lethality was estimated as percentage of unhatched embryos after 24 and 48 hrs of incubation.

6.2.6 Analysis

6.2.6.1: Mitochondrial size

Mitochondrial size per embryo was measured as mentioned in 2.10.2 and 3.2.7.2. Briefly, background subtracted images were intensity thresholded and particles above 0.05 µm2 were chosen using ImageJ. To measure mitochondrial size at apical and basal regions, sections at 2 µm depth and around the contractile ring respectively were chosen. The mitochondrial sizes per embryo with SEM were plotted using Graphpad prism 6.0 and compared using Mann-Whitney test.

6.2.6.2: Mitochondrial density across apico basal axis

Mean mitochondrial fluorescence across the apico-basal axis was measured and mentioned in 2.10.1 and 5.2.5.1.

6.2.6.3: Measurement of cell length and contractile ring area

Membrane length was measured every 2 mins by drawing a line from apical most region to the membrane ingression front, identified by highest intensity of Sqh-mCherry signal, localized basally in the sagittally live imaged Mito-GFP:Sqh-mCherry and *drp1*^{SG}; Mito-GFP::Sqh-mCherry embryos using ImageJ. Mean lengths measurements from 5 furrows per embryo were plotted for 3 embryos using Graphpad Prism 6.0. Lengths at the last cellularization time point for 5 embryos were plotted with SEM and compared with Mann – Whitney test using Graphpad prism 6.0

Circularity and area of the contractile rings were measured at the basal most membrane section. 5 contractile rings per embryo for fixed images or per time point for live samples were drawn manually using polygon tool in imageJ. The membrane length for fixed samples was obtained from sagittal images as mentioned in 4.2.6.3. The membrane length for live samples were obtained from orthogonal projections of the Z stacks. Circularity and area were plotted with membrane length using Graphpad Prism 6.0

6.2.6.4: Myosin Intensity

Total intensity of basal most section showing sharpest mCherry signal and 2 stacks above and below it (total Z depth - 4 µm) was measured using ImageJ and background corrected. A section below the nuclei containing uniform cytoplasmic mCherry signal in the first time point (membrane length - 3 µm) was chosen to measure the background intensity. Measurements from WT and *drp1*^{SG} were normalized with mean background subtracted intensity value of the first cellularization time point in WT (He et al., 2016). Mean for 3 embryos each with length was plotted using Graphpad Prism 6.0

6.2.6.5: pAMPK and DHE Intensity

Mean fluorescence intensity of DHE was measured at sections through nuclei using ImageJ (4.2.6.2). The intensity values obtained for WT, *drp1*^{SG}and *hSOD1*^{A4V} embryos were normalized using mean WT intensity for every experiment. Experiment was repeated thrice of pAMPK and twice for DHE. Number of WT and *drp1*^{SG} embryos analysed for pAMPK and DHE were 31, 24 and 25, 21 respectively. 5 embryos were analysed for *hSOD1*^{A4V}. Graphs were plotted and analysed using Mann-Whitney test in Graphpad Prism 6.0.

6.3 Results

6.3.1 Fission and fusion proteins localize on the mitochondria in *Drosophila* embryo

Mitochondrial morphology proteins are localized to the cytoplasm and bind to the mitochondria on fission and fusion cues. The mitochondria in the *Drosophila* embryo are small and punctate and fission fusion events are not often seen. We therefore assessed the localization of fission protein Drp1 and fusion protein Marf in the embryos. We immunostained WT embryos with Drp1 antibody and streptavidin to visualize mitochondria. We observed that mitochondria and Drp1 colocalized (Fig. 6.1 A). We then used embryos containing GFP tagged Marf and stained them using streptavidin. Marf-GFP also localized with mitochondria (Fig 6.1 B).

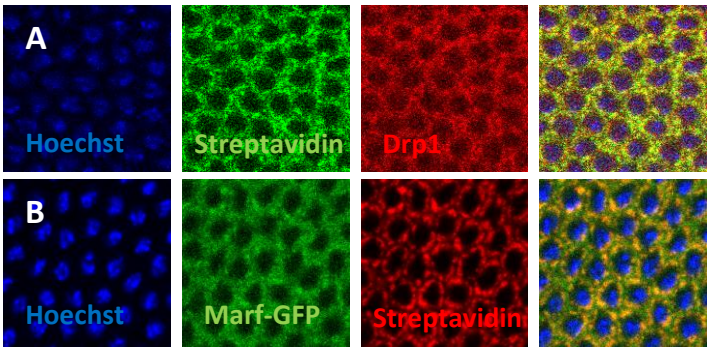

Figure 6.1: Marf and Drp1 localize on the mitochondria. WT embryos stained for mitochondria (streptavidin, green) and Drp1 (red) show colocalization (merged) (**A**). Marf-GFP (green) colocalizes with mitochondria (streptavidin, red) (**B**).

6.3.2 Drp1 deficient embryos contain clustered mitochondria

We tested different strategies to knock fission protein Drp1 in the embryos in order to standardise the efficient combination of mutations based on embryonic lethality and mitochondrial morphology. These genetic combinations are described in Table 6.3.

We used RNA polymerase II 140wimp mutant allele (*wimp*) in the background of heterozygous *drp1*^{KG} and *drp1*^{nrd} to reduce the transcription further in a heterozygous mutant to create hypomorphic scenario. This strategy has been previously used to achieve reduced transcription of proteins in *Drosophila* oogenesis and embryogenesis (Abreu-Blanco

et al., 2014; Jackson and Blochlinger, 1997; Magie and Parkhurst, 2005; Parkhurst and Ish-Horowicz, 1991). Heteroallelic *drp1*^{KG}/*drp1*^{nrd} flies are sensitive to temperature and they are motion sensitive paralytic (Rikhy et al., 2007). These flies laid few eggs and they were lethal eggs only when they were grown in cages with corn meal medium instead of standard sucrose agar. We also crossed *drp1*^{i}, *drp1*^{SD} and *drp1*^{SG} flies with Mito-GFP and obtained embryos from F1 progeny. *drp1*^{SD}; Mito-GFP flies did not lay sufficient eggs. We found a distinct morphology with clustered mitochondria in *drp1*^{KG}; *wimp*, *drp1*^{nrd}; *wimp*, *drp1*^{i}, *drp1*^{SD} and *drp1*^{SG} compared to the control *wimp*/+ and Mito-GFP embryos (Fig 6.2 A, B). We quantified mean mitochondrial area based on thresholded fluorescence particle sizes per embryo in cellularization stages as mentioned in materials and methods as an approximate measure of mitochondrial size (6.2.4.1). Mito-GFP (WT) embryos have a mean mitochondrial fluorescence based area (fluorescence spread) per embryo of 0.25 μm^2. Mitochondrial fluorescence was spread over a larger area per thresholded particle in *drp1*^{i} and *drp1*^{SG} with mean size of 2.2 μm^2 and 0.7 μm^2 respectively indicating clustering or elongation or fusion of mitochondria in the Drp1 mutant embryos. Mitochondria in *wimp*/+ are similar in size to the WT embryos. Mitochondrial size in *drp1*^{KG}; *wimp* and *drp1*^{nrd}; *wimp* are increased significantly with sizes at 0.63 μm^2 and 0.55 μm^2 compared to *wimp*/+ embryos with mean size 0.21 μm^2 (Fig. 6.2 C). The embryos obtained from *drp1*^{KG}; *wimp* and *drp1*^{nrd}; *wimp* flies showed a weak phenotype compared to Mito-GFP and *drp1*^{i}, *drp1*^{SG} set in terms of shape alteration as well as lethality (Table 6.3). Hence we chose to proceed with *drp1*^{i}; Mito-GFP and *drp1*^{SG}; Mito-GFP for further analysis based on the embryo availability, lethality and phenotype. The optimal expression of *drp1*^{i} and *drp1*^{SG} using *nanos*-Gal4 at 28 °C resulted into very early developmental arrest of the embryos in stages even prior to preblastoderm leading to a completely lethal phenotype (Table 6.3). Expression of Mito-GFP with the same Gal4 in the background possibly diluted the phenotype and we could obtain some embryos that reach cellularization. *drp1*^{SG} embryos were also noted to be smaller than the wild type and had shorter appendages. This could be related to EGFR dysfunction during oogenesis (Goff et al., 2001; Mitra et al., 2012; Tomer et al., 2018). Over-expression of Drp1 did not affect the lethality and did not change mitochondrial morphology. This could be because Drp1 is already highly expressed in the embryos, and additional protein does not affect the fission fusion dynamics further. Also mitochondria are small in embryos and this is consistent with them being highly fragmented possibly rendering them in a confirmation

which is the smallest possible. To understand whether embryonic lethality is due to defects in the oogenesis or due to lack of fertilization, we replaced *drp1*^{i};*nanos*-Gal4 males with WT males. This did not rescue the embryonic lethality. When we crossed *nanos*-Gal4 female to males containing *drp1*^{SG} on X chromosome, all F1 females were heterozygous for *drp1*^{SG} and males did not have any copy of the transgene in this cross. Therefore males in this cross were similar to WT. This clearly indicates that the defects in embryos lacking *drp1* are purely from the maternal contribution. `

F1 genotype (Temperature)	Lethality (sd), (n)	Mitochondrial Clustering
drp1^{KG}; *wimp* (25 °C)	43%(±9), (n = 300)	+
drp1^{nrd}; *wimp* (25 °C)	51.3%(±10), (n = 300)	+
drp1^{KG}/ *drp1*^{nrd} (25 °C)	100%, (n = 300)	+++
drp1^{i} (vdrc); *nanos*-Gal4 (28 °C)	7% (±1.7), (n = 300)	-
drp1^{i} (Val20); *nanos*-Gal4 (28 °C)	100%, (n = 300)	+++
drp1^{i} (Val20); Mito-GFP (28 °C)	73% (±14.7), (n = 300)	+++
drp1^{SG}; *nanos*-Gal4 (28 °C)	99% (±1.7), (n = 300)	+++
drp1^{SG}; Mito-GFP (28 °C)	84% (±7.8), (n = 300)	+++
drp1^{SD}; Mito-GFP (28 °C)	81.5% (±2.1), (n = 100)	+++
UASp*drp1*; Mito-GFP (28 °C)	16% (±5.6), (n = 100)	-

Table 6.3: Phenotype standardization of various drp1 knockdown strategies.

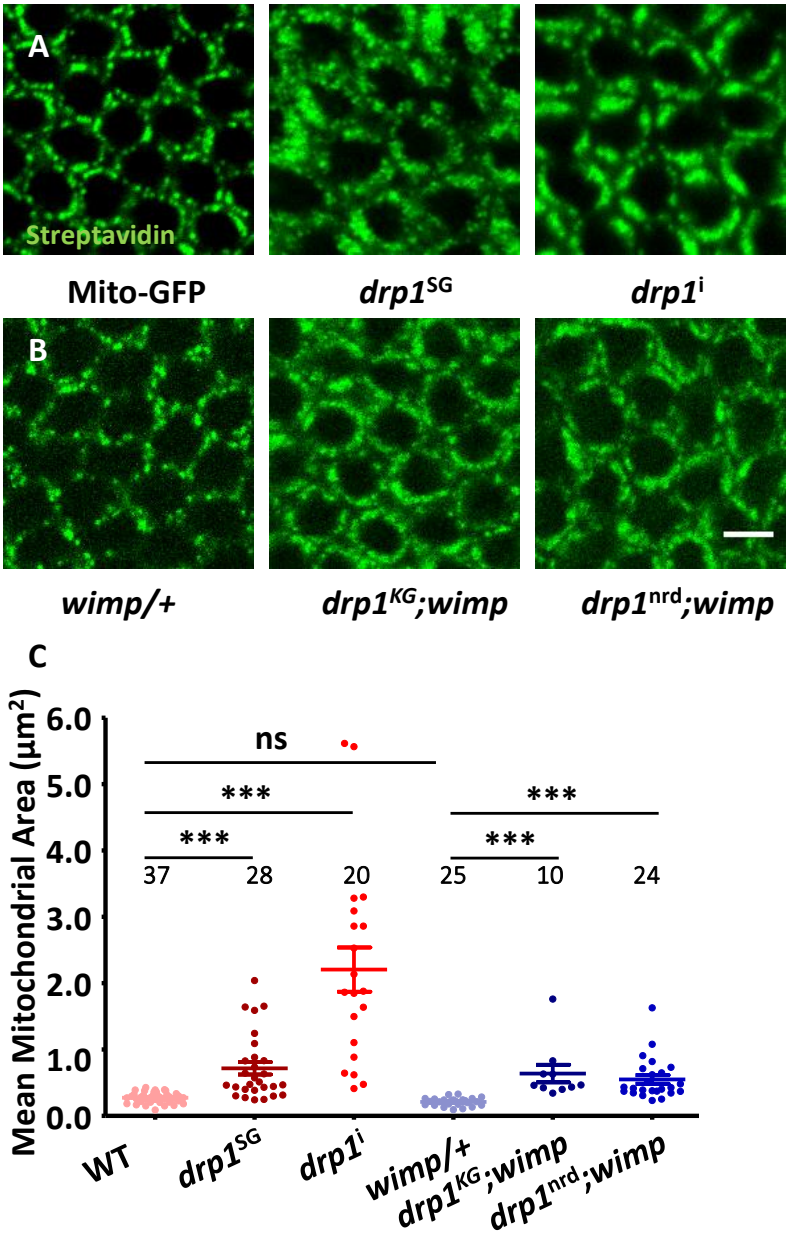
A
Streptavidin
Mito-GFP
drp1SG
drp1i
B
wimp/+
drp1KG;wimp
drp1nrd;wimp
C
Mean Mitochondrial Area (µm2)
6.0
5.0
4.0
3.0
2.0
1.0
0.0
ns
***
***
***
***
37
28
20
25
10
24
WT
drp1SG
drp1i
wimp/+
drp1KG;wimp
drp1nrd;wimp

Figure 6.2: Drp1 mutant embryos have clustered mitochondria. Mitochondria (green) labelled using fluorescent streptavidin are clustered in *drp1*^{SG} and *drp1*^{i} expressing embryos compared to control Mito-GFP embryos (**A**). Mitochondrial clumps are also observed in *drp1*^{KG}*; wimp* and *drp1*^{nrd}*; wimp* compared to control *wimp*/+ embryos (**B**). Mean mitochondrial area per embryo is quantified (**C**). Mitochondrial sizes are significantly larger in *drp1*^{SG} (maroon) and *drp1*^{i} (red) expressing embryos compared to Mito-GFP (light red) embryos. Similar increase in size is seen in *drp1*^{KG}*; wimp* (navy blue) and *drp1* ^{nrd}*; wimp* (blue) embryos compared to *wimp*/+ (light blue) (**C**). Each data point and numbers on the plot represent number of embryos analysed. Approximately 40 cells and 15000 mitochondria were counted per embryo. (ns; P ≥ 0.05, ***; P ≤ 0.001, Kruskal – Wallis test) (**C**). Scale bar: 5 µm (**A, B**)

6.3.3 Mitochondrial morphology is unaffected in fusion protein knockdown embryos

Opa1 and Marf, inner and outer membrane fusion proteins respectively are abundant in the embryo. We saw that Marf-GFP colocalizes with mitochondria. We used RNAi based approach to knock Opa1 and Marf down. The RNAi lines used are listed in materials and methods section.

F1 genotype	Lethality (sd), (n)	Mitochondrial fragmentation
marf^{i} (MG)/Mito-GFP (25 °C)	23.5% (2.1) (300)	-
marf^{i} (Valium1); Mito-GFP (25 °C)	17% (1.4) (300)	-
marf^{i} (Valium20); nanos-Gal4 (28 °C)	100% (300)	-
marf^{i} (Valium20); MitoGFP (28 °C)	65% (4.5) (300)	-
opa1^{i} (Valium20)/*nanos*-Gal4 (28 °C)	No embryos laid	NA
opa1^{i} (Valium20)/ Mito-GFP(28 °C)	No embryos laid	NA

opa1^{i} (Valium20)/ Mito-GFP (25 °C)	60% (9) (50)	-
opa1^{i} (MG)/ Mito-GFP (28 °C)	18.3% (0.6) (300)	-
UAS-Marf-GFP/*mat*-Gal4 (28 °C)	4% (2) (200)	-

Table 6.4: Phenotype standardization of various fusion knockdown strategies.

Based on the lethality, *marf*^{i} (MG)/Mito-GFP, *marf*^{i} (Valium1); Mito-GFP and *opa1*^{i} (MG)/ Mito-GFP (28 °C) likely did not have strong knock down of the proteins (Table 6.4). Optimal knockdown of Marf using *marf*^{i} (Valium20); *nanos*-Gal4 (referred as *marf*^{i} hereafter) was completely lethal for the embryo. When we crossed *marf*^{i} (Valium20) with Mito-GFP, 35% embryos survived likely due to the Gal4 dilution effect (Table 6.4). We imaged mitochondria in these embryos using streptavidin staining and quantified mitochondrial morphology. The mitochondrial size was not changed compared to the WT Mito-GFP embryos (Fig 6.3 A, C). Opa knockdown using the *opa1*^{i} (Valium20) RNAi line driven by either nanos-Gal4 or Mito-GFP (referred as *opa1*^{i} hereafter) failed to lay eggs at 28 °C. This is most probably due to defects in the oogenesis itself. *opa1*^{i} /Mito-GFP flies could lay very few eggs at 25 °C. The mitochondrial morphology was similar to the WT in this case as well (Fig 6.3 B, C).

Taken together, although both fission and fusion machineries reside on the mitochondria, only fission protein knockdown transformed mitochondrial morphology in the embryos. This suggests that fission, not fusion, is more prevalent in the early embryos.

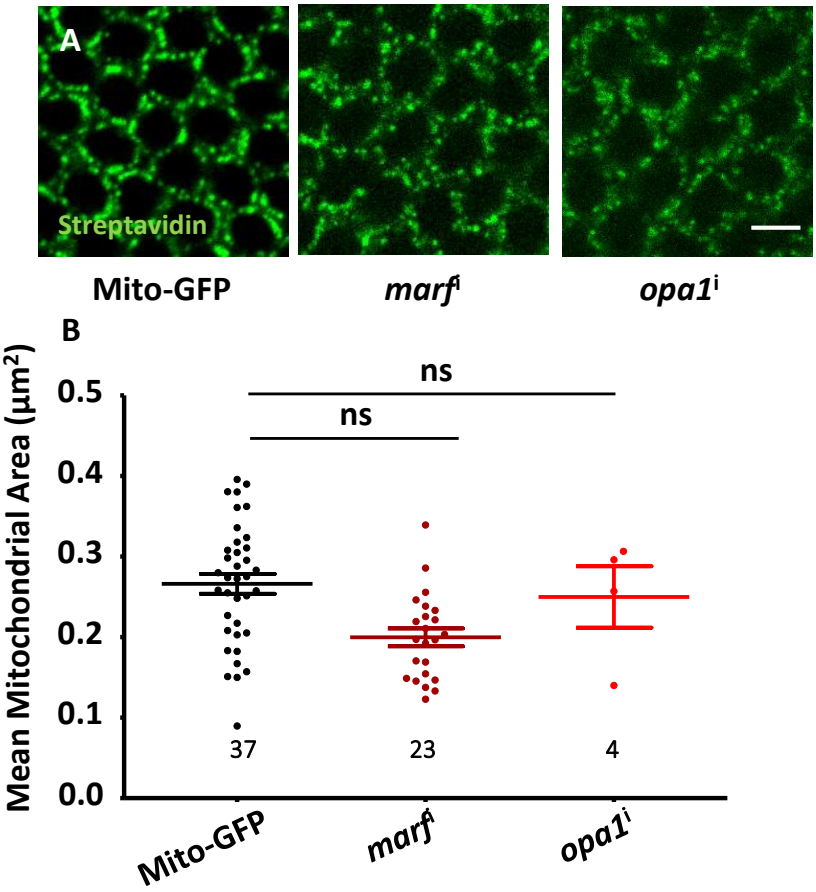

Figure 6.3: Mitochondrial morphology does not change in fusion protein knockdown. Mitochondria (streptavidin, green) in *marf*^{i} and *opa1*^{i} expressing embryos are similar in shape compared to control Mito-GFP embryos (**A**). Mean mitochondrial area per embryo quantified in *marf*^{i} and *opa1*^{i} embryos is not significantly different than Mito-GFP embryos (**B**). Each data point and numbers on the plot represent number of embryos analysed. Approximately 40 cells and 15000 mitochondria were counted per embryo. (ns; $P \geq 0.05$, Kruskal – Wallis test) (**B**). Scale bar: 5 µm (**A**)

6.3.4 Apical migration of mitochondria is abolished in *drp1* deficient embryos

We had observed that during cellularization and gastrulation, mitochondrial migrate apically with dynein motors. Changing mitochondrial morphology has been shown to impact their transport in cells (Misko et al., 2012; Saxton and Hollenbeck, 2005; Shirendeb et al., 2012; Smirnova et al., 1998b; Verburg and Hollenbeck, 2009). We had also observed that small clumps of mitochondria in *dhc*^{i} did not migrate to the apical side (5.3.3). The mitochondrial clustering and sizes that we observed in *drp1* mutants and knockdown were much larger

compared to the dynein knockdown. We decided to systematically assess the mitochondrial transport when mitochondrial morphology was changed to clustered form during cellularization using *drp1*i flies in combination with Mito-GFP and obtained live movies (Fig 6.4 A). We measured mitochondrial mean intensity at 3 time points: early, mid and late, during cellularization in 30 apical to basal Z stacks spaced 1 um apart and compared it to WT Mito-GFP embryos (5.3.1). Similar to the WT embryos, the intensity was basally pronounced in the early cellularization but with more clustered mitochondria (Fig 6.4A Top panel, B). The apical regions did not gain intensity during the following time points at mid (Fig 6.4A Middle panel) and late cellularization (Fig 6.4A Bottom panel) and the intensity remained completely basal at the end of cellularization (Fig. 6.4 B, WT – Fig 5.2 C, D).

Mitochondrial morphology was altered in *drp1*^{KG}, *drp1*^{nrd} and *drp1*^{SG} embryos as well. We stained these with streptavidin and phalloidin to visualize mitochondria and f-actin respectively (Fig 6.4 C). We could identify embryos with longer furrow lengths with the actin staining. We observed mitochondrial clusters stuck at basal regions in these embryos. Apical regions, especially in *drp1*^{SG} were devoid of mitochondrial punctae, indicating a transport defect in these combinations too (Fig 6.4 C).

We confirmed the lack of transport in *drp1*^{SG} embryos by photoactivation using Mito-PAGFP. We activated fluorescence in early cellularization *drp1*^{SG} embryos in an ROI below the nuclei (Fig 6.4D, red) and followed the fluorescence in apical region (Fig 6.4D, green) as depicted. The photoactivated mitochondrial fluorescence at basal regions of *drp1*^{SG} embryos did not migrate to the apical region (Fig 6.4 E). We quantified mean fluorescence intensity in photoactivated basal (red) and apical (green) ROIs. There was no significant depletion in the fluorescence intensity signal of basal ROI and apical ROI did not gain any fluorescence, demonstrating the lack of transport of mitochondria (Fig 6.4 F). The immobile mitochondria at the basal regions can be seen in temporal colour coded image (Fig. 6.4 G, WT – Fig. 5.2 H).

These data indicate that regulation of mitochondrial morphology is necessary for their transport to the apical side during cellularization.

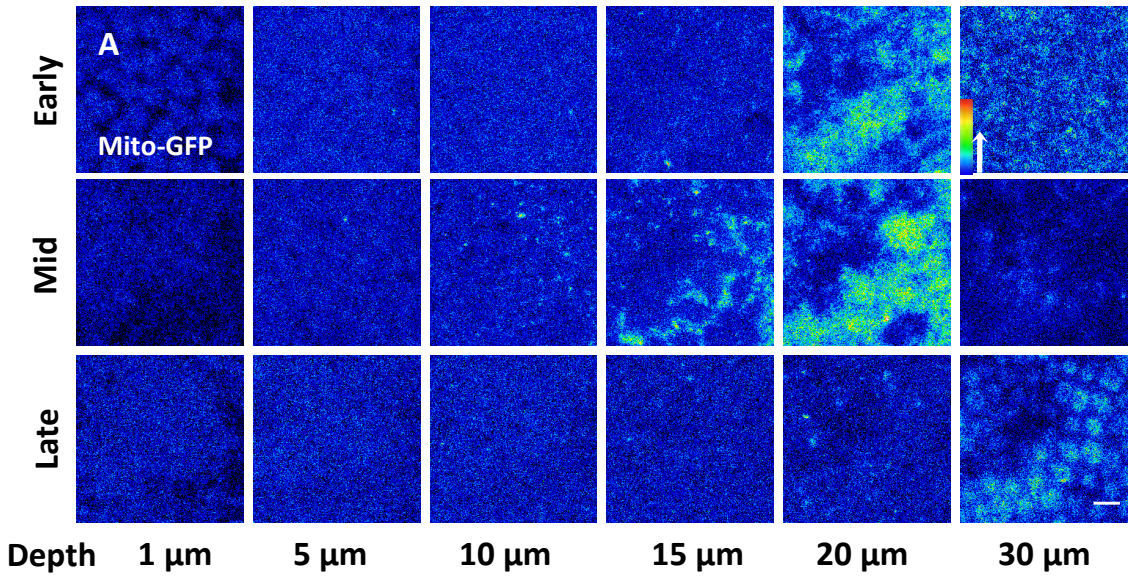
A
Early
Mid
Late
Mito-GFP
Depth
1 µm
5 µm
10 µm
15 µm
20 µm
30 µm

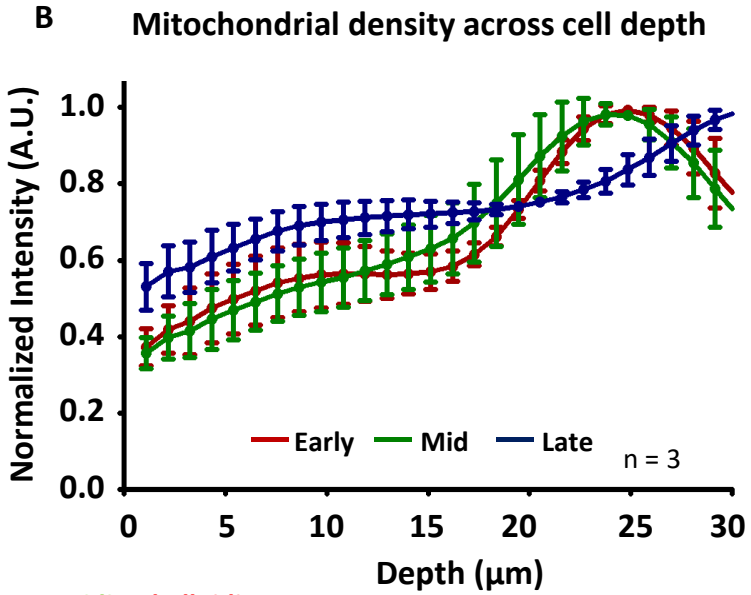
B
Mitochondrial density across cell depth
Normalized Intensity (A.U.)
1.0
0.8
0.6
0.4
0.2
0.0
0
5
10
15
20
25
30
Depth (µm)
Early
Mid
Late
n = 3

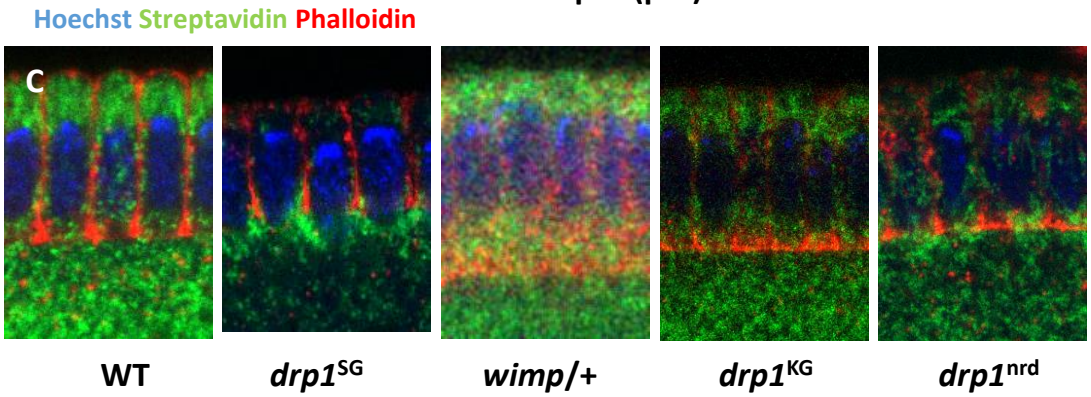
Hoechst Streptavidin Phalloidin
C
WT
drp1SG
wimp/+
drp1KG
drp1nrd

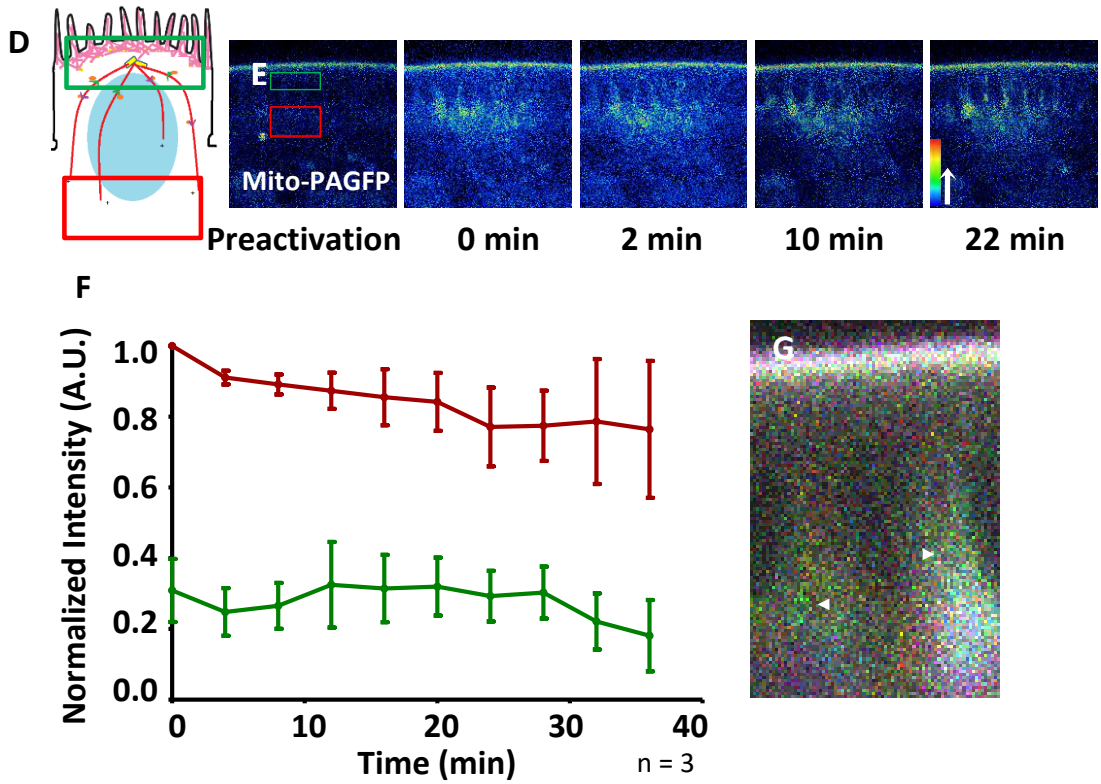

Figure 6.4 Apical migration of mitochondria during cellularization is abolished in Drp1 KD embryos. Mitochondrial clusters are observed in the basal regions of the cells in early (**A, Top panel**), mid (**A, Middle panel**) and late cellularization (**A, Bottom panel**), stages in *drp1*^{i} embryos. Mitochondrial punctae are missing at the apical regions (**A**). Mean Mito-GFP fluorescence across depth is plotted with SEM for n = 3 embryos and total 200 cells for early, mid and late cellularization stages (**B**) Mito-GFP fluorescence peaks at basal regions at early (red), mid (green) and late (blue) cellularization stages. Sagittal sections of *drp1*^{SG} embryos show mitochondria (streptavidin, green) clustered near the furrow tips (marked by actin, phalloidin, red) in cellularization, compared to apical mitochondria in Mito-GFP embryos (**C**). Basal mitochondrial clusters (streptavidin, green) are also observed in *drp1*^{KG}; *wimp* and *drp1*^{nrd}; *wimp* embryos. The clusters are absent in the control *wimp*/+ embryos (**C**).

(**D-G**): Absence of apical migration of mitochondria in *drp1*^{SG} embryos is observed using photoactivation. Schematic of photoactivation experiment showing basal photoactivated ROI (red) and non-photoactivated apical ROI (green) (**D**). No change is seen in the location of activated Mito-PAGFP signal at basal regions of (red) and apical region (green) does not gain significant fluorescence signal with time during cellularization (**E**). Normalized mean

fluorescence intensity is plotted with SEM for basal (red) and apical regions (green) for n = 3 embryos (**F**). Temporal colour coded image shows immobile mitochondria with all time frames appearing colocalized (white arrows, **G**).

6.3.5 *drp1* mutant embryos have shorter cells and wider furrows

During cellularization, cell membranes extend basally synchronous with actomyosin ring assembly and contraction at the leading front of the ingressing membranes. We imaged embryos containing Mito-GFP::Sqh-mCherry in sagittal planes such that the membrane ingression with time. Sqh-mCherry signal localized to the furrow tips (Fig 6.5 A). We measured membrane length using ImageJ, every 2 mins in Mito-GFP::Sqh-mCherry/+ (black) and *drp1*^{SG}; MitoGFP::Sqh-mCherry embryos (red) (Fig 6.5 B). Both the genotypes exhibited similar ingression kinetics with an initial slow phase upto 20 mins, followed by fast phase till the cellularization completion (Fig 6.5 B). Membrane ingression process prematurely stopped and apical constriction initiated at around 40 mins in *drp1*^{SG} embryos (Fig 6.5 B), resulting in significantly shorter, 30 µm tall cells (Fig 6.5 D, red) compared to 40 µm tall WT cells (Fig 6.5 D, black) at cellularization end (Fig 6.5 C, D).

The contractile ring constriction occurs in slow and fast phase, synchronously with the membrane ingression. To analyse ring contraction we used Sqh-mCherry to image WT and *drp1*^{SG} embryos. The shape in the grazing sections of the ingression front or furrow tip is initially hexagonal and then circularizes at slow to fast phase transition and slowly constricting at the same time (Fig. 6.6 A, B). In the fast phase, rings rapidly constrict (Fig. 6.6 A, B). Therefore circularity of the WT rings increases from 0.8 to about 1.0 with time during transition from hexagonal to circular shape and is maintained around 1.0 in the fast phase. The circularity of the contractile rings in *drp1*^{SG} was similar to the WT, indicating that the ring architecture was normal and the membranes were able to circularize (Fig. 6.6 B). The expected constriction trend was observed when we measured area of contractile rings with incremental lengths in the WT (Fig. 6.6 C, black). *drp1*^{SG} embryos had similar area when the cellularization started, but eventually the ring area remained larger compared to the WT embryos (Fig. 6.6 C, red).

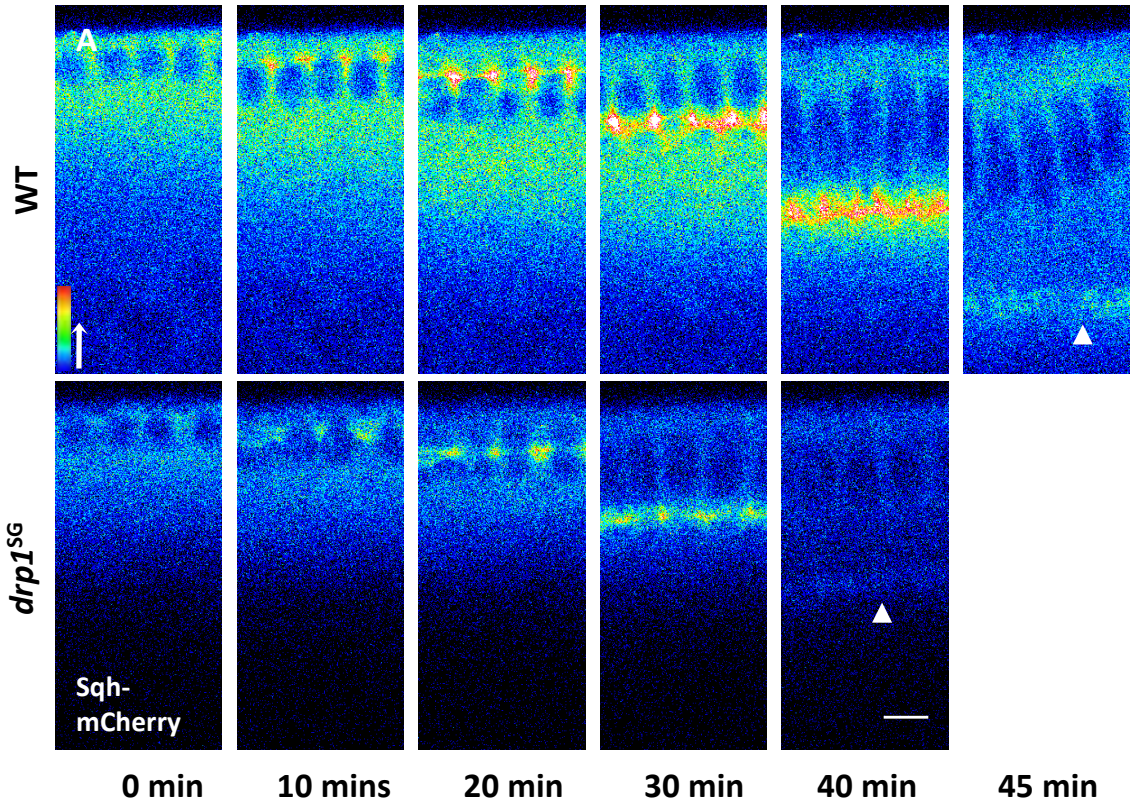

B Cellularization furrow progression

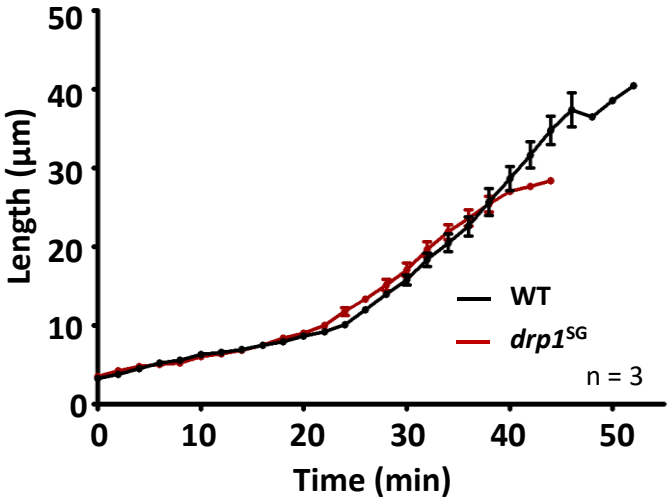

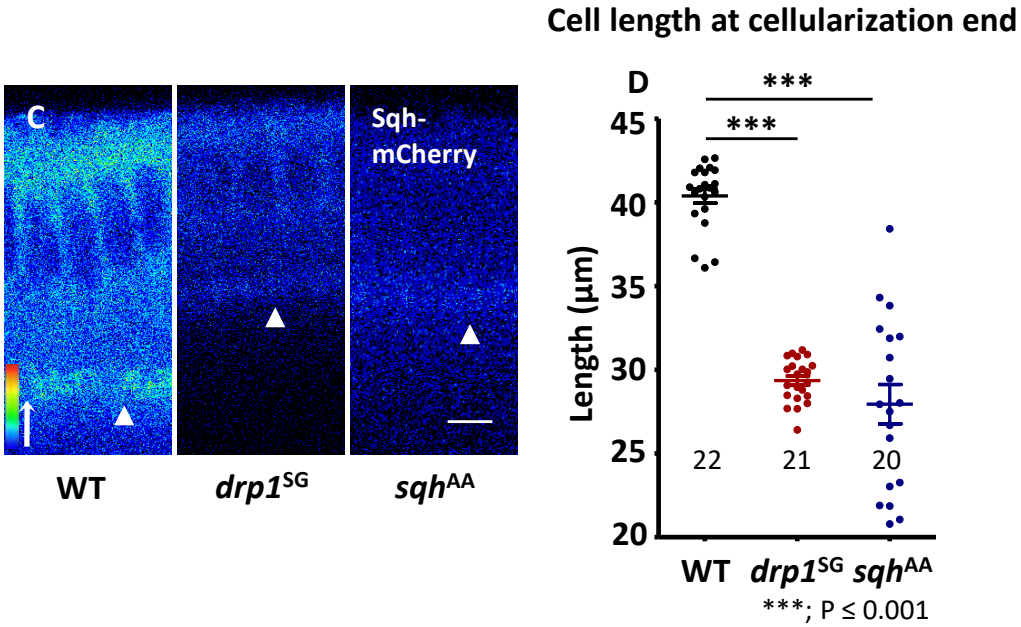

Figure 6.5: Shorter cells are formed in *drp1*^{SG} embryos. WT and *drp1*^{SG} embryos containing endogenous tagged MRLC (Sqh-mCherry) are imaged in sagittal plane. Sqh-mCherry localized to the membrane tips shows membrane ingression during cellularization (**A**). Final achieved length is pointed with white arrowheads in WT and *drp1*^{SG} (**A**) Pseudocolour heat map represents fluorescent intensity. Membrane length quantified across time during cellularization shows similar trend of increase in WT (black) and *drp1*^{SG} (red) (**B**). Final length achieved post cellularization (white arrowheads) in *drp1*^{SG} embryos (red) is significantly reduced compared to WT (black) (**C, D**). Membrane length (white arrowheads) is also reduced in sqh^{AA} embryos (**C, D**). n = 3 embryos for B; 5, 5 and 6 embryos for WT, *drp1*^{SG} and sqh^{AA} respectively (**D**). Numbers on the plot represent total furrows analyzed for each data set. (***; P ≤ 0.001, Mann Whitney test) (**D**). Scale bar: 5 µm (**A, C**)

Membrane extension and ring constriction during cellularization depends on myosin localization and activity (He et al., 2016; Wenzl et al., 2010; Young et al., 1991). We therefore measured Sqh intensity in WT and *drp1*^{SG} embryos (6.2.4.4). WT embryos showed initial increase in the intensity of Sqh till about 15 mins after which then gradually depleted (Fig. 6.6 D, black). *drp1*^{SG} embryos had significantly lower amounts of Sqh, throughout cellularization (Fig. 6.6 D, red).

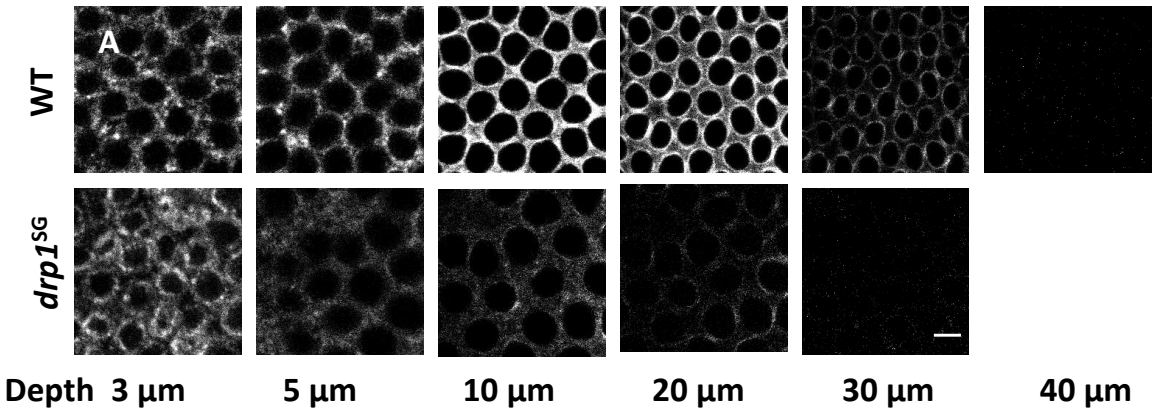
A
WT
drp1SG
Depth 3 µm
5 µm
10 µm
20 µm
30 µm
40 µm

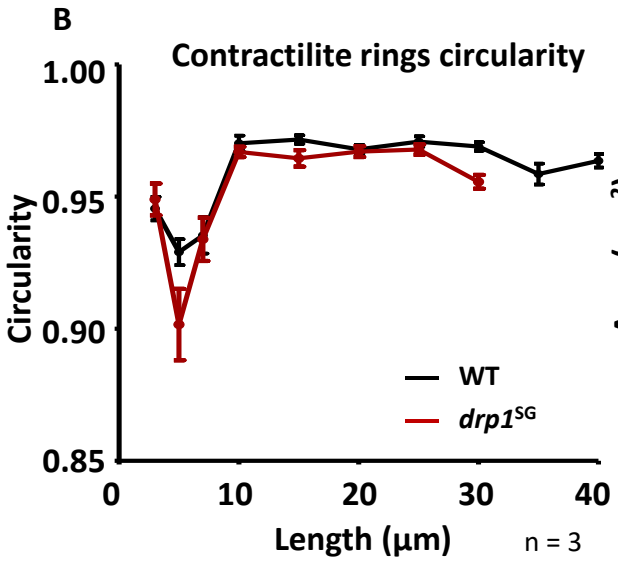
B
Contractilite rings circularity
Circularity
1.00
0.95
0.90
0.85
0
10
20
30
40
Length (µm)
n = 3
WT
drp1SG

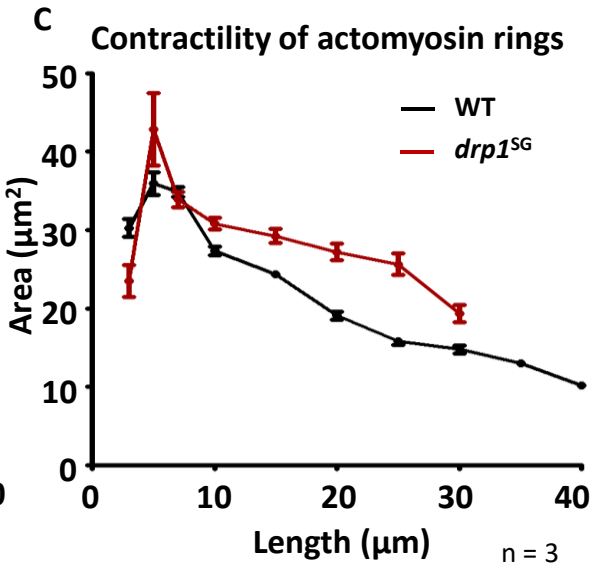
C
Contractility of actomyosin rings
Area (µm2)
50
40
30
20
10
0
0
10
20
30
40
Length (µm)
n = 3
WT
drp1SG

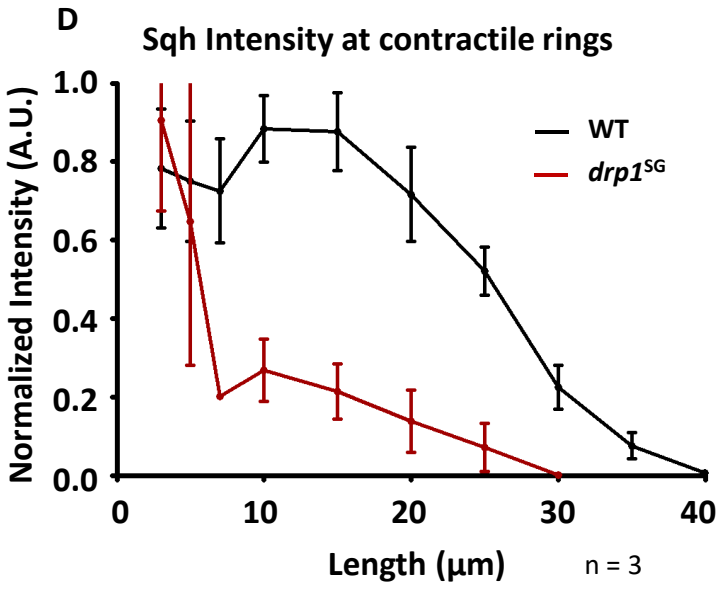
D
Sqh Intensity at contractile rings
Normalized Intensity (A.U.)
1.0
0.8
0.6
0.4
0.2
0.0
0
10
20
30
40
Length (µm)
n = 3
WT
drp1SG

Figure 6.6: Contractility of actomyosin rings is reduced in *drp1*^{SG} cellularizing embryos
Sections through the cellulazation furrow tips in WT and *drp1*^{SG} imaged live using Sqh-mCherry show actomyosin rings decreasing in size with membrane depth (**A**). Circularity of basal membrane quantified in *drp1*^{SG} embryos (red) is similar to WT (black) (**B**). Area of contractile rings quantified with depth in *drp1*^{SG} is greater than the WT embryos (black) (**C**). Normalized mean intensity of Sqh-mCherry at the contractile rings is significantly reduced in in *drp1*^{SG} (red) compared to WT (black) (**D**). n = 3 embryos, 5 contractile rings per embryo are quantified at 5 µm length increments (**B, C**). n = 3 embryos, 40 cells each. Scale bar: 5 µm (**A**).

Myosin regulatory light chain mutant (UASp-*sqh*^{A20A21}, refereed as *sqh*^{AA} hereafter) (Vasquez et al., 2014) has been characterized to observe defects in actomyosin ring assembly and contraction (Xue and Sokac, 2016). Although, *sqh*^{AA} affects ring contractility in slow phase and not in the fast phase of cellularization, the overall ring perimeter at the end of cellularization remains larger than the WT embryos (Xue and Sokac, 2016). This is consistent with our data. We tested if cells are rendered shorter in embryos containing *sqh*^{AA} expressed using nanos-Gal4 with Mito-GFP and Sqh-mCherry and imaged them in sagittal planes (Fig. 6.5 C). We measured cell lengths achieved at the cellularization end. Similar to *drp1*^{SG} the cells were shorter in *sqh*^{AA} embryos (Fig 6.5 D, blue).

The phenotype of shorter cells with wider contractile rings is therefore likely due to lowered myosin levels in the *drp1*^{SG} embryos.

6.3.6 ATP levels are unaffected and ROS levels are reduced in *drp1*^{SG} embryos.

Altering mitochondrial shape can lead to depletion of their metabolic activity. We had earlier observed (Fig. 4.8 that mutations in ETC components lead to elevation of pAMPK levels and a reduction in metaphase furrow lengths in the syncytial *Drosophila* embryo (Chowdhary et al., 2017). Since *drp1*^{SG} embryos had shorter cellularization membrane furrows, we decided to check whether this was due to depletion of ATP. We immunostained WT and *drp1*^{SG} embryos with pAMPK antibody as described earlier in chapter 4. Similar to syncytial embryo interphase, pAMPK is mostly present in the cytoplasm and near the centrioles during cellularization in both WT and *drp1*^{SG} (Fig. 6.7 A). The quantification of

mean pAMPK intensity in these did not show a significant difference indicating that ATP levels were not changed (Fig. 6.7 B).

Next we checked for ROS using dihydroethidium (DHE) staining in the WT and *drp1*^{SG} embryos (Fig. 6.7 C). ROS is produced in cells not only by mitochondria but by other cytoplasmic sources like cell membranes, peroxisomes, ER and cytoplasm (Muller, 2000; Nauseef, 2008) and has been implicated in the regulation of differentiation and morphogenetic movements in embryos (Ji et al., 2010; Muliyil and Narasimha, 2014). DHE fluorescence increases upon oxidation by superoxides (Owusu-Ansah et al., 2008b). We measured mean intensity of DHE in Mito-GFP and *drp1*^{SG} embryos and plotted (Fig. 6.7 D). We observed a lot of variation in the intensity values in the WT itself, likely due to the method we used for dye DHE staining (6.2.4), nevertheless *drp1*^{SG} embryos showed significantly lowered DHE staining compared to WT (Fig. 6.7 D). These data are in agreement with other studies that show reduction of ROS in fission mutants or vice versa (Kim et al., 2018; Röth et al., 2014; Son et al., 2015; Yu et al., 2006). We overexpressed mutated human super-oxide dismutase 1 (hSOD1) as a positive control. There was 3 fold increase in the levels of DHE (Fig. 6.7 C, D).

Thus, forced fusion of mitochondria by using *drp1* mutant in cellularizing *Drosophila* embryos did not affect their ATP levels but reduced ROS levels.

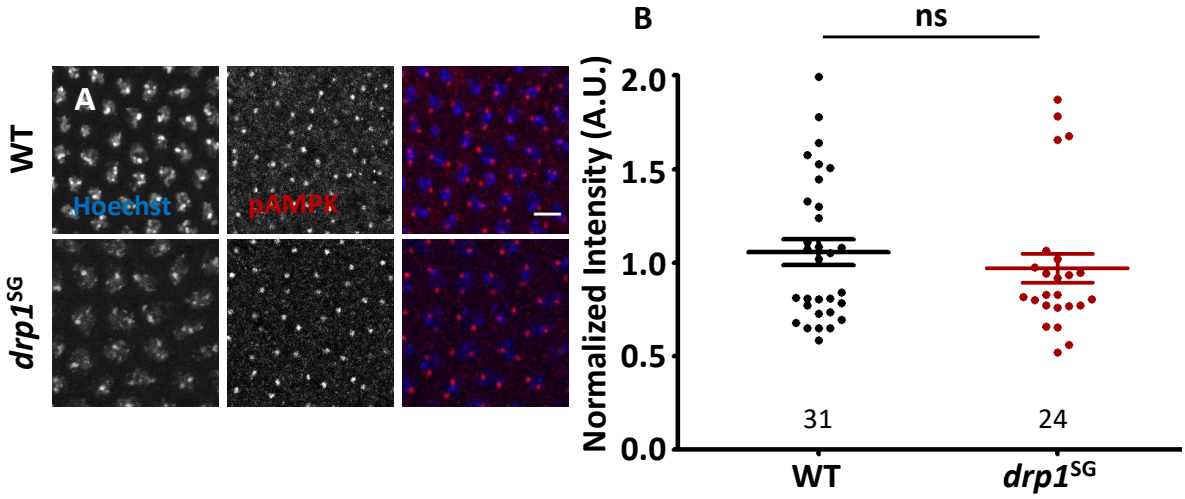

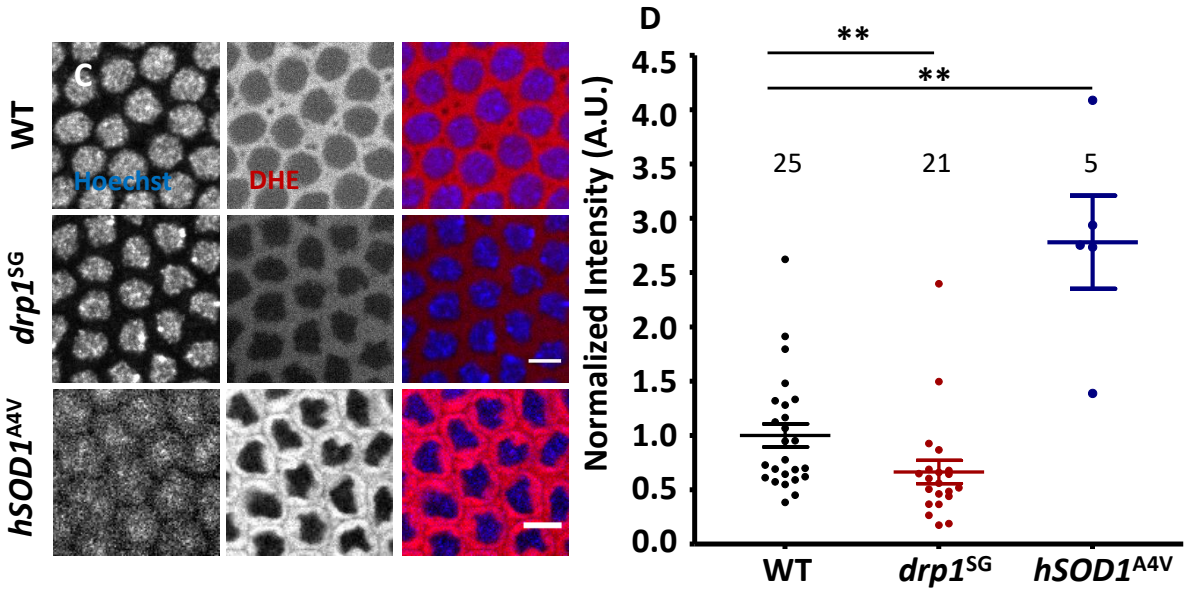

Figure 6.7: ATP and ROS measurements in *drp1*^{SG}. pAMPK (red) localizes to the cytoplasm around nuclei (Hoechst, blue) and on centrosomes in WT and *drp1*^{SG} embryos (**A**). The levels of normalized pAMPK fluorescence intensity are similar in in WT (black) and *drp1*^{SG} (red) embryos (**B**). ROS assessed using DHE staining (red) is cytoplasmic in WT, *drp1*^{SG} and *hSOD1*^{A4V} embryos (**C**). Mean intensity of DHE is significantly reduced in *drp1*^{SG} (red) and increased in positive control *hSOD1*^{A4V} (blue) compared to WT (black) embryos (**D**). N = 3 and 2 for B and D respectively, numbers on the graph represents number of embryos analysed for each data set. (ns; $P \geq 0.05$, **; $P \leq 0.01$, Mann Whitney test). Scale bar: 5 µm (**A, C**).

6.3.7 Apical transport of mitochondria depends on their shape

It is very well known that modifications in mitochondrial shape affects their transport and this was also demonstrated by our observations in cellularizing *drp1* mutant embryos. This suggests that possibly dynein motors are incapable of carrying a larger load on them. Also these data raise a possibility that Drp1 could be an adapter for binding to microtubule motors for apical mitochondrial transport during cellularization. As an attempt to test these possibilities, we expressed *opa1*^{i} in the background of *drp1*^{SG} using *nanos*-Gal4. Although the embryonic lethality due to *drp1*^{SG} was not rescued in this combination, embryos showed a reversal of fused mitochondrial morphology phenotype seen in *drp1* mutants (Fig 6.8 A). Since smaller mitochondria in *drp1*^{SG} are still able to apically migrate, we measured

mitochondrial fluorescence area per embryo at apical (3 µm) and basal sections near the contractile rings. We observed the sizes of apical mitochondrial fluorescence were similar in all the combinations (Fig. 6.8 B, apical). There is not difference between apical and basal mitochondrial sizes in the WT (Fig. 6.8 B, apical). The non-migrating mitochondria at the basal region in *drp1*^{SG} are much larger, average 1 µm^2 compared to the WT mitochondria that are around 0.3 µm^2 in size (Fig. 6.8 B, red, black respectively). The mitochondrial size is completely rescued when *opa1*^{i} is expressed with *drp1*^{SG} (Fig. 6.8 B, blue). In later stages of cellularization as depicted in sagittal images, mitochondria are able to migrate to the apical regions (Fig. 6.8 A).

This showed that mitochondrial transport is independent of functionality of Drp1 or Opa1, but depends on their shape.

6.3.8 *drp1*^{SG} phenotypes are partially rescued in *drp1*^{SG}; *opa1*^{i} embryos

Since mitochondrial morphology and apical transport is rescued in *drp1*^{SG}; *opa1*^{i} combination asked whether the contractile ring phenotype observed in *drp1*^{SG} embryos could also be also reverted. We stained WT and *drp1*^{SG}; *opa1*^{i} embryos with phalloidin to visualize the contractile acto-myosin rings during cellularization (Fig. 6.8 C). We observed that similar to WT, contractile rings formed and constricted in *drp1*^{SG}; *opa1*^{i} embryos (Fig. 6.8 C, basal). We measured circularity and area of contractile rings in the WT and *drp1*^{SG}; *opa1*^{i} embryos with different membrane lengths (Fig. 6.8 D, E). The membrane lengths were estimated using sagittal images (Fig. 6.8 C, sagittal). The circularity and area plotted against length, showed similar trends for both WT and *drp1*^{SG}; *opa1*^{i} embryos (Fig. 6.8 D, E).

Next, we imaged *drp1*^{SG}; *opa1*^{i} embryos using Sqh-GFP to analyse cell length and Myosin II at the contractile rings. Embryos were imaged sagittally and membrane length, based on Sqh-GFP localized at the furrow tips (Fig. 6.8 F). Furrow ingression rates in *drp1*^{SG}; *opa1*^{i} (blue) embryos remained similar to WT (black) (Fig. 6.8 G). The membranes reached more than 35 µm in 86% *drp1*^{SG}; *opa1*^{i} embryos (Fig. 6.8 H, blue, n = 7), which is significantly more compared to *drp1*^{SG} embryos (Fig 6.5 D, red). We then measured Sqh-GFP intensity at the contractile rings in WT (Sqh-GFP/+) and *drp1*^{SG}; *opa1*^{i} embryos and plotted it across cell lengths (Fig 6.8 I, J). Although, the GFP intensity in *drp1*^{SG}; *opa1*^{i} embryos (Fig. 6.8 J, blue) was less compared to the WT (Fig. 6.8 J, black) throughout cellularization and the Myosin II

fell off the rings around 35 µm compared to 40 µm of the WT, it was more compared to *drp1*^{SG} embryos (Fig. 6.6 D) indicating a partial rescue.

Therefore this suggests that, acto-myosin ring contractility depends on mitochondrial shape and is likely to be independent of the morphology proteins themselves. It would be worth analysing whether reversion of mitochondrial ROS levels in *drp1*^{SG}; *opa1*^{i} embryos is responsible for the rescue. Also, other mitochondrial functional aspects such as calcium and membrane potential need to be checked.

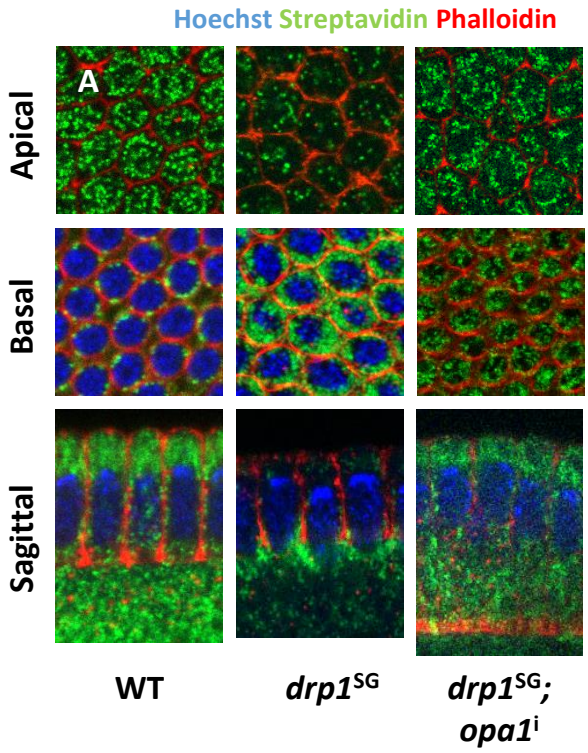

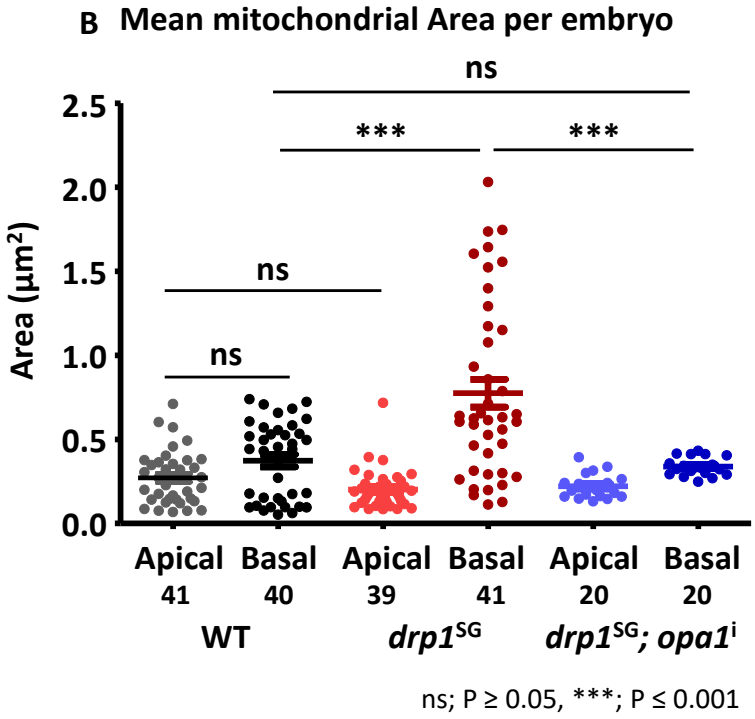

ns; P ≥ 0.05, ***; P ≤ 0.001

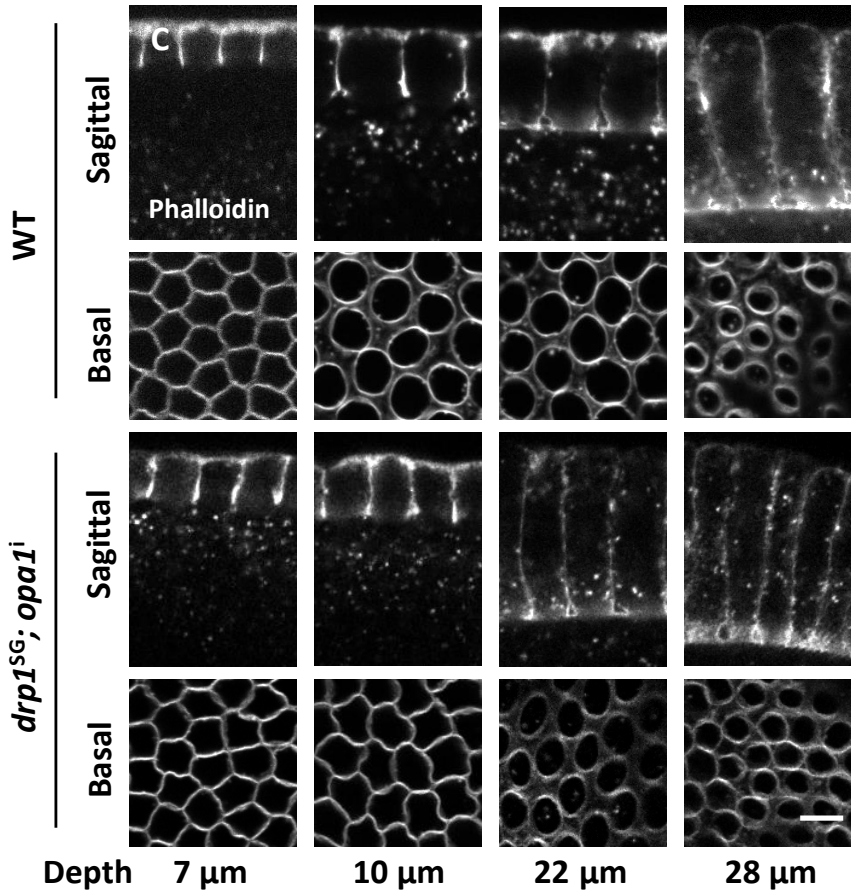

D Contractilite rings circularity

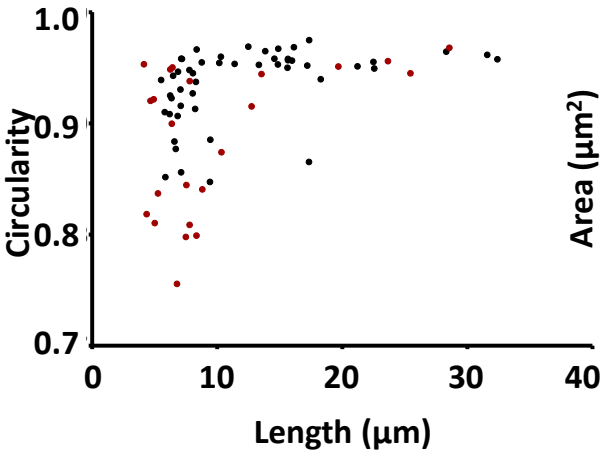

E Contractility of actomyosin rings

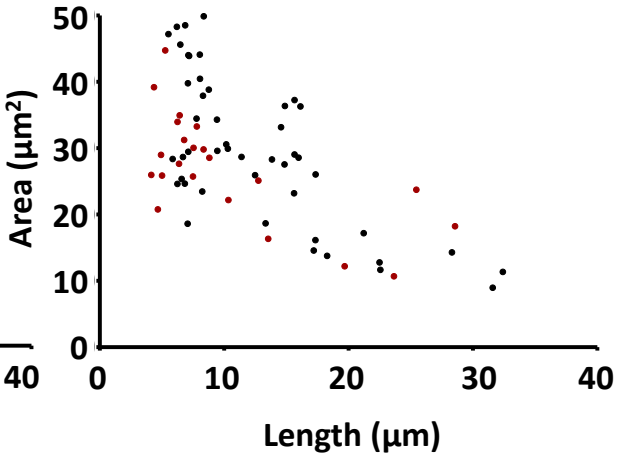

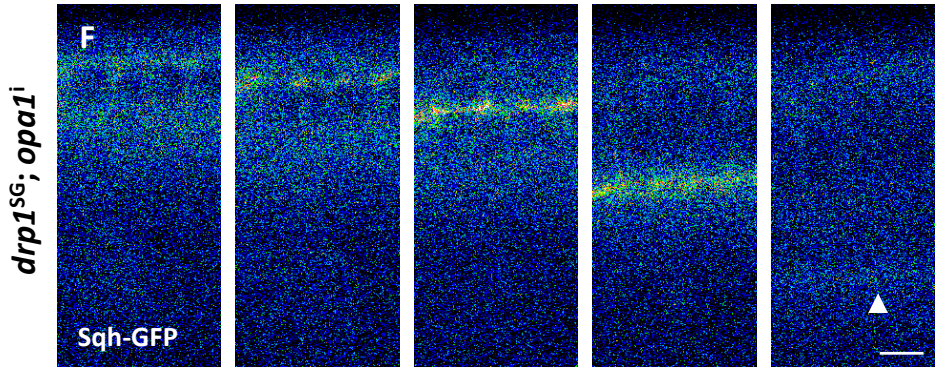
F
drp1SG; opa1i
Sqh-GFP

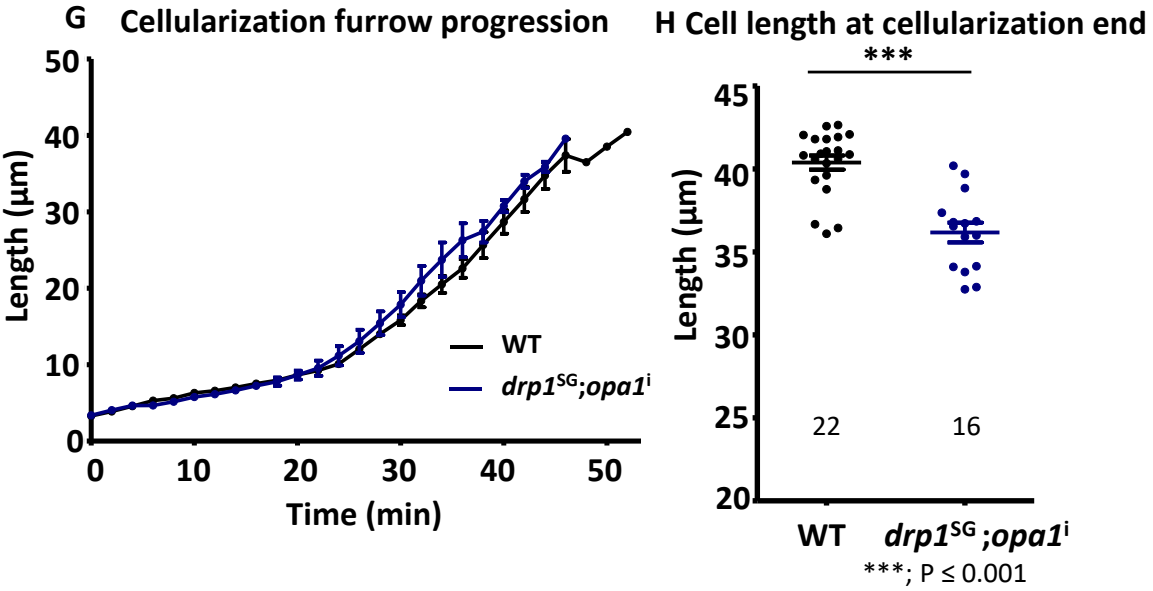
G Cellularization furrow progression
Length (µm)
Time (min)
WT
drp1SG;opa1i
H Cell length at cellularization end
***
Length (µm)
22
16
WT
drp1SG ;opa1i
***; P ≤ 0.001

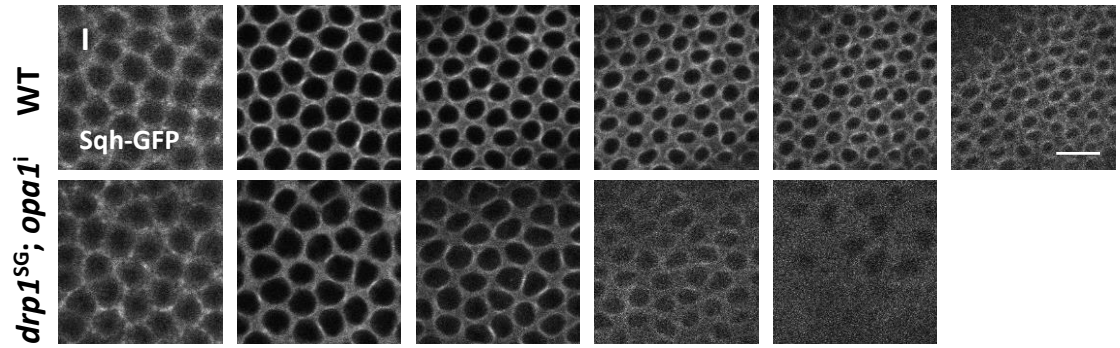
I
WT
drp1SG; opa1i
Sqh-GFP

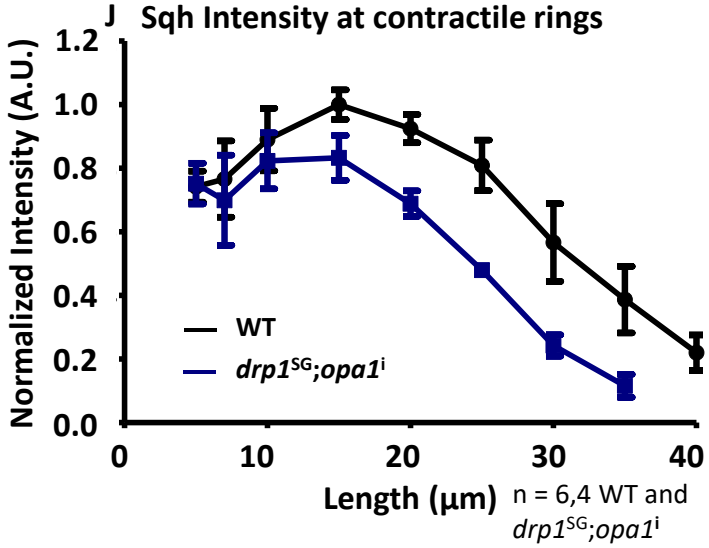
J Sqh Intensity at contractile rings
Normalized Intensity (A.U.)
Length (µm)
WT
drp1SG;opa1i
n = 6,4 WT and
drp1SG;opa1i

Figure 6.8: Mitochondrial migration and contractile ring area are rescued in *drp1*^{SG}*; opa1*^{i} embryos.

(A-B) Mitochondrial morphology in *drp1*^{SG}*; opa1*^{i}. Mitochondrial (streptavidin, green) clusters seen in *drp1*^{SG} are resolved in *drp1*^{SG}*; opa1*^{i} and appear similar to WT embryos at the basal regions marked by contractile rings (phalloidin, F-actin, red), also seen in sagittal sections (**A**). Mitochondria are absent in apical sections in *drp1*^{SG} embryos. Apical mitochondria in *drp1*^{SG}*; opa1*^{i} embryos appear similar to the WT embryos in the late cellularization stage. Presence or absence of apical mitochondria in WT, *drp1*^{SG} and *drp1*^{SG}*; opa1*^{i} embryos (**A**). Mean mitochondrial sizes are quantified in apical and basal section of WT, *drp1*^{SG} and *drp1*^{SG}*; opa1*^{i} embryos (**B**). Sizes of apical mitochondria are similar in all the three sets. Mitochondria in the basal section are significantly larger in *drp1*^{SG} (red) and similar to WT (black) in *drp1*^{SG}*; opa1*^{i} (blue) embryos (**B**). N = 3, each data point and numbers indicate number of embryos analysed in each data set. (ns; $P \geq 0.05$, ***; $P \leq 0.001$, Mann Whitney test) (**B**).

(C-E) Rescue of contractile rings in *drp1*^{SG}*; opa1*^{i}. Sagittal and basal sections of WT and *drp1*^{SG}*; opa1*^{i} embryos stained with phalloidin (grey) are shown. Actin ring seen in the basal sections circularize and constrict in both WT and *drp1*^{SG}*; opa1*^{i} embryos (**C**). Circularity (**D**) and area (**E**) of the contractile rings, quantified with increasing membrane length, have similar trend in both WT (black) and *drp1*^{SG}*; opa1*^{i} (red) embryos. n = 49 and 23 embryos are quantified for WT and *drp1*^{SG}*; opa1*^{i} respectively. Each data point represents an average of 5 rings per embryo (**D, E**). Scale bar: 5 µm (**A, C**).

(F-H) Cell length post cellularization is partially rescued in *drp1*^{SG}*;opa1*^{i} embryos. *drp1*^{SG}*;opa1*^{i} embryos are imaged sagittally using Sqh-GFP (**F**). Final achieved length is pointed with white arrowheads (**F**) Pseudocolour heat map represents fluorescent intensity. Membrane length quantified across time during cellularization shows similar trend of increase in WT (black) and *drp1*^{SG}*;opa1*^{i} (blue) (**G**). Final length achieved post cellularization (white arrowheads) in *drp1*^{SG}*;opa1*^{i} embryos (blue) is plotted (**H**). (***; $P \leq 0.001$, Mann Whitney test) (**D**). Scale bar: 5 µm (**F**)

(I-J) Myosin Intensity at contractile rings is partially rescued in *drp1*^{SG}*; opa1*^{i} embyos. Sections through the cellulazation furrow tips in WT and *drp1*^{SG} *;opa1*^{i} imaged live using Sqh-GFP show actomyosin rings decreasing in size with membrane depth (**I**). Normalized

mean intensity of Sqh-GFP at the contractile rings is quantified in WT and *drp1*^{SG} *;opa1*^{i} (blue) (**J**). n = 6, 4; WT and *drp1*^{SG}*;opa1*^{i} embryos, 40 cells each (**J**). Scale bar: 5 µm (**I**).

6.3.9 Mitochondrial ETC does not affect mitochondrial transport

We had observed that reducing levels of *pdsw* and *cova* led to increased pAMPK and shortening of metaphase furrow length in syncytial embryos (Chapter 4). It is known from neuronal cells that only energetically favoured mitochondria are transported in the axons (Chen and Chan, 2009). We stained cellularizing *pdsw*^{i} embryos with tagged streptavidin, and observed that mitochondria were present apically in late cellularization embryos (Fig. 6.9). This indicates that ETC components are not necessary for their apical migration. We have not tested whether knockdown of *pdsw* or *cova* can affect membrane length or contractile rings.

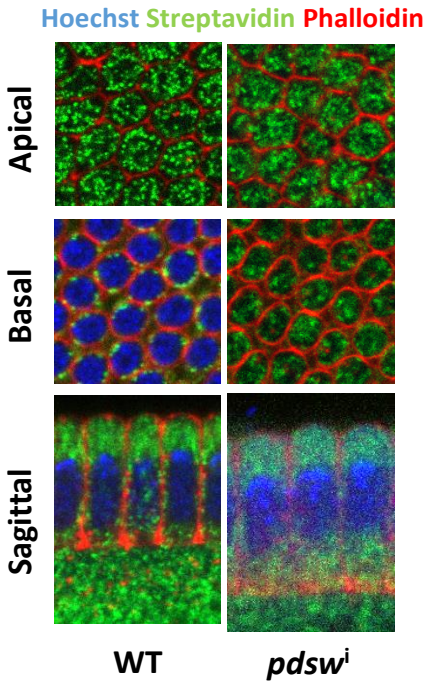

Figure 6.9: Mitochondrial migrate apically in *pdsw*^{i}. Mitochondria stained using streptavidin (green) display apical signal *pdsw*^{i} (apical, sagittal) and appear similar to the WT at the basal regions. Cell lengths are marked by actin staining (phalloidin, red).

6.4 Discussion

In this chapter, we attempted to characterize the role of mitochondrial shape maintenance in *Drosophila* embryo cellularization. Fission and fusion proteins shuttle between a large cytoplasmic pool and mitochondria and bind on fission or fusion cues (van der Bliek et al.,

2013; Scott and Youle, 2010). Mitochondrial morphology proteins are abundant in the embryo and both Drp1 and Marf localize on the mitochondria. (Fig. 6.1). Mitochondria are said to be under constant cycling of fission and fission in eukaryotic cells (Chan, 2006). In the *Drosophila* embryo mitochondria are distinctively small and punctate, at least till gastrulation as described in earlier (Chapter 3, 5). Although, both fission and fusion machinery localizes on the mitochondria, we hardly ever observed any fission-fusion dynamic events. Mitochondrial fragmentation was not observed on reducing the levels of fusion proteins (6.3.3). This possibly meant that either fusion proteins are inactive or mitochondria already at their smallest threshold sizes in the embryo. Mitochondrial shape changed to more clustered form upon Drp1 knockdown (6.3.2). Also, reducing Opa1 levels in the background of Drp1 mutation rescued mitochondrial size (6.3.7). This suggests that both fission and fusion proteins are functional and active in the embryo. What keeps Drp1 active to enforce mitochondrial fragmentation in the early embryo is not clear in this scenario.

The importance of mitochondrial shape in regulating the transport is very well documented in the neuronal cells and has been implicated in axonal degeneration, neuro-degenerative disorders (Costa et al., 2010; Rawson et al., 2014; Wang et al., 2011) and T cell immunity response (Baixauli et al., 2011).Mitochondrial transport is abrogated in fission or fusion deficient cells (Chen et al., 2003; Li et al., 2004; Verstreken et al., 2005). We observed a similar lack of transport in *drp1* mutant embryos which is most likely due to inefficiency of microtubule motors to transport highly clustered structured. Very few small mitochondria were able to localize apically in *drp1* mutant embryos. Mitochondrial shape reverted by to normal when we reduced the amounts of Opa1 in the background of Drp1. These small mitochondria were able to migrate apically. This shows that just by reverting mitochondrial shape we could rescue mitochondrial transport and that drp1 is not essential for the transport but maintenance of mitochondrial shape is.

Regulation of mitochondrial shape is also essential for maintenance of cellular bioenergetics. Preventing mitochondrial fission impairs their ATP production and leading to cellular stress, physiological defects and neuronal synaptic function (Cho et al., 2010; Hu et al., 2017; Kim et al., 2015; Parone et al., 2008; Qian et al., 2012; Shields et al., 2015). We attempted to test ATP levels in *drp1* mutant embryos using pAMPK, a well-known ATP biosensor (Chowdhary et al., 2017; Lee et al., 2007; Sakamoto et al., 2004). We did not

observe any change in the pAMPK levels, indicating that ATP levels in the Drp1 mutant embryos were not altered. There are reports that suggest either increase (Parone et al., 2008; Tomer et al., 2018; Zaja et al., 2014) or depletion (Kim et al., 2018; Muller, 2000; Nauseef, 2008; Röth et al., 2014; Sheffer et al., 2016) in ROS levels upon mitochondrial clustering via Drp1 knockdown. We found using DHE staining that ROS in the *drp1* mutant embryos is reduced. DHE marks the cytoplasmic ROS. We need to test the effect on mitochondrial ROS using a more specific dye. MitoSOX is targeted to mitochondria and fluoresces based on its interaction with superoxides. Staining with this dye did not our with our permeabilization protocols (5.2.4, 4.2.2).

We found that shorter cells formed during cellularization with less contractile actomyosin rings which is likely caused by the reduction of membrane localized Myosin (Sqh). Evidence from in *vitro* studies suggests oxidization of kinases in the presence of ROS (Fedorova et al., 2009; Steinberg, 2013). Hypoxia induced ROS induction in bovine brain endothelial cells leads to increased phosphorylation of Myosin light chain (Kuhlmann et al., 2007). Regulation of Myosin II by redox was also demonstrated during integrin engagement (Fiaschi et al., 2012). Tuning of Myosin II activity by regulation of ROCK by ROS levels has been studied in *Drosophila* embryo dorsal closure (Muliyil and Narasimha, 2014). We would like to further study whether similar regulation exists during *Drosophila* cellularization as well by using SOD mutation in the background of Drp1 mutation, in order to increase ROS. Muliyil and Narasimha showed mitochondrial fragmentation upon ROS level increase (Muliyil and Narasimha, 2014). We did not observe change in mitochondrial shape in *hSOD1*^{A4V} mutant embryos (data not shown). We also observed a rescue of contractile ring area, cell length and Myosin II levels in *drp1*^{SG}; *opa1*^{i}. We are investigating whether ROS levels are rescued in this combination.

Chapter 7

Mitochondrial regulation during gastrulation in *Drosophila* embryos

7.1 Introduction

After the formation of about 6000 tall epithelial cells during cellularization, gastrulation initiates with apical constriction and invagination of mesoderm cells which is regulated by Toll-Dorsal pathway gradient (Leptin, 1995, 1999; Solnica-Krezel and Sepich, 2012). Dorsal activates a cascade of transcription factors including Snail and Twist (Ip et al., 1992; Leptin, 1991). Snail initiates Myosin II pulses at the apical regions of mesoderm cells and Twist is required to maintain this activity (Ip et al., 1994; Leptin, 1991; Leptin and Grunewald, 1990; Martin et al., 2009). Further, another transcription factor, Folded gastrulation (*fog*), leads to apical activation of RhoGEF-2, a kinase that acts upstream of Myosin II (Barrett et al., 1997; Dawes-Hoang, 2005; Fuse et al., 2013; Nikolaidou and Barrett, 2004). At the same time removal of Myosin from the basal furrow tips in the mesoderm cells is essential for furrow formation (Krueger et al., 2018; Royou et al., 2004; Young et al., 1991). Gastrulation furrow does not form in RhoGEF-2 mutant embryos where Myosin II activity is abrogated (Barmchi et al., 2005; Barrett et al., 1997; Kolsch et al., 2007). Also, mutated or reduced amounts of *snail*, *twist* and *fog* affect Myosin II activity leading to deformed gastrulation furrow (Dawes-Hoang, 2005; Ip et al., 1992; Lim et al., 2017; Young et al., 1991). Moreover, increased amounts of these proteins leads to ectopic Myosin II activity in the entire embryo, also inhibiting ventral furrow formation (Dawes-Hoang, 2005).

About 2 decades ago, mitochondrial localization at the prospective gastrulation region has also been suggested in *Xenopus* embryos using mitochondrially derived long ribosomal RNA (mtlr-RNA) (Yost et al., 1995). Functional relevance of such particular relocalization of mitochondria has not been studied so far. We reported enhanced apical migration of mitochondria occurs specifically in the ventral furrow cells during apical constriction (Fig. 5.3). This coincides with the period when Myosin II is also activated apically (Martin et al., 2009; Mason et al., 2016). Additionally adherens junction proteins (Barmchi et al., 2005; Weng and Wieschaus, 2016) and Fog (Dawes-Hoang, 2005) are released apically at the same time. In this regard, we asked if mitochondrial relocalization to the apical regions in the

ventral furrow is also dependent on Toll-Dorsal pathway. Interaction of Fog signaling with Drp1 leads to mitochondrial fragmentation in *Drosophila* muscle cells (Ratnaparkhi, 2013). It is not clear whether it may be necessary for mitochondrial transport in addition to mitochondrial fragmentation. Also, presence of mitochondria at the apical regions of mesoderm cells during gastrulation may be necessary to provide local metabolic inputs to the constricting cells. Mitochondrial transport and Myosin II levels were significantly reduced during cellularization in *drp1*^{SG} embryos (6.3.5). Since maintenance of Myosin II levels is required for furrow progression, we asked whether the process of gastrulation can be affected in *drp1*^{SG} embryos. We also attempted to investigate whether mitochondrial localization is dependent on the Toll-Dorsal pathway by over-expression and downregulation of Toll-Dorsal pathway components.

7.2 Materials and methods

7.2.1 Fly stocks

All crosses were maintained on standard cornmeal agar medium at 28 °C. *rhogef2*^{i} and *mbs*^{i} were crossed with *mat*-Gal4. *fog*^{i} and *dl*^{1},UAS-*dl*^{WT} were crossed with Mito-GFP flies containing *nanos*-Gal4. *fog*^{i} was also crossed with *nanos*-Gal4.

Stock	Source (ref)
rhogef2^{i}	BDRC 34643
mbs^{i}	BDRC 41625
fog^{i}	Anuradha Ratnaparkhi (Ratnaparkhi and Zinn, 2007)
dl^{1},UAS-*dl*^{WT}	Girish Ratnaparkhi

Table 7.1 List of fly stocks

7.2.2 Live imaging

Mito-GFP::Sqh-mCherry, *drp1*^{SG}; Mito-GFP::Sqh-mCherry, *fog*^{i};MitoGFP, *dl*^{1},UAS-*dl*^{WT}; MitoGFP embryos were imaged end on as mentioned in Chapter 2 (2.5) using 63x, 1.4 NA objective on Leica sp8 confocal microscope.

7.2.3 Immunostaining

Mito-GFP, *drp1*^{SG}, *drp1*^{i}, *mbs*^{i}, *rhogef2*^{i} and *fog*^{i} embryos were stained using streptavidin and phalloidin as mentioned in Chapter 2 (2.3). Dorsal and Twist staining was performed in embryos fixed using 8%PFA and heptane (1:1), devitellinized using heptane and methanol (1:1). Embryos were incubated with Anti-dorsal (DSHB, 1:500) and anti-Twist (Siegfried Roth, Koln University, 1:200) overnight at 4 °C. *drp1*^{SG} and WT embryos stained with Dorsal and Twist antibody were imaged using light sheet microscope (Zeiss LSM 800) such that cross sections through dorso-ventral axis were visible.

Reagent	Source	Host Species (Ab)	Dilution/ Concentration
Dorsal antibody	DSHB	Mouse	1:500
Twist antibody	Siegfried Roth, Koln University, Germany	Rabbit	1:200

Table 7.2: List of reagents

7.2.4 Analysis

7.2.4.1 Sqh-mCherry and mitochondrial fluorescence during gastrulation

Mean fluorescence Intensity at the ventral furrow for Sqh-mCherry and Mito-GFP embryos was measured as mentioned in (5.2.5.2). Ratio of background subtracted mean fluorescence intensity value at apical and basal regions of the mesoderm cells was plotted at different timepoints (5.2.5.2). A mean of 3 embryos was plotted for all the combinations using Graphpad Prism 6.0.

Mean apical mitochondrial fluorescence was measured by drawing a segmented line ROI in the apical region of the whole embryos in WT and *dl*^{1},UAS-*dl*^{WT} embryos. The perimeter of the embryo was measured. The perimeter was normalized to arbitrary units in percentage such that the ventral midpoint was ascertained as 0, left half from 0 to -50 and right half from 0 to 50. Mean of the normalized intensity at every 1.0 A.U was plotted for n=3, 6 embryos for WT and *dl*^{1},UAS-*dl*^{WT} embryos respectively using Graphpad Prism 6.0.

7.2.4.2 Dorsal and Twist relative spread

ROIs were drawn passing through the nuclei in the entire WT and *drp1*^{SG} embryos in the dorso-ventral axis using segmented line tool in ImageJ. Mean intensities profiles of Dorsal and Twist were fitted to a Gaussian distribution and full width half max (FHMH) value of the plot was obtained using Matlab as follows.

Equation: $y = a + (b - a)\, e^{(-(x-c)^2/2d^2)}$

Where,

a = y_0, b – a = center of the Gaussian peak, c = height of the peak, d = standard deviation.

FHMH = 2.35482*d

Relative spread was obtained as a ratio of FHMH to the embryo perimeter, plotted and analyzed using Mann-Whitney test in Graphpad Prism 6.0.

7.2.4.3 Dorsal and Twist Intensity

Nuclei on the ventral and dorsal side of Dorsal and Twist stained WT and UAS*dl* embryos were marked using Hoechst staining. Fluorescence intensities of Dorsal and Twist in the marked nuclei were measured. Ratio of average Ventral to Dorsal fluorescence intensities were plotted and analyzed using Mann-Whitney test in Graphpad Prism 6.0

7.3 Results:

7.3.1 *drp1* knockdown affects ventral furrow formation

During gastrulation the ventral cells apically constrict and invaginate in a very coordinated fashion. We looked at mitochondria at ventral furrow in WT and *drp1* mutant embryos using streptavidin and phalloidin to mark the cell boundaries. Mitochondria migrate apically in the ventral furrow cells post gastrulation. These cells align parallelly in the WT embryos and have apical mitochondria present between the layers of invaginating cells. Mitochondria have apical migration defects in *drp1* knockdown embryos and they also formed short cells with wider basal contractile rings in cellularization (6.3.5). Basally accumulated mitochondria were also seen in the gastrulation in $drp1^{SG}$ and $drp1^{i}$ embryos (Fig. 7.1 A). The cells at the ventral did not symmetrically invaginate and they were misaligned as seen by phalloidin staining (Fig. 7.1 A). This is in accordance with a previous report (Ratnaparkhi, 2013).

We had established from the data in cellularization that Myosin II (Sqh) levels are reduced in $drp1^{SG}$ embryos (Fig. 6.6). During gastrulation, Myosin localizes apically in the ventral mesoderm cells and is responsible for apical constriction followed by invagination (Martin et al., 2009; Young et al., 1991). Localization of myosin is also essential for ventral furrow morphology (Dawes-Hoang, 2005; Fuse et al., 2013). Therefore, we next quantified Sqh levels in the ventral furrow using Sqh-mCherry tag in $drp1^{SG}$ embryos. We observed that ventral furrow in $drp1^{SG}$ embryos is flatter compared to the WT. The furrow remained broader compared to the WT as it invaginated and was not completely sealed like the WT embryos (Fig 7.1 B). We then measured Cherry fluorescence intensity apical: basal ratio at the ventral furrow in control and $drp1^{SG}$ embryos (Fig 7.1 C). There was initial gradual increase in Sqh-Cherry signal ratio with time during apical constriction of the mesoderm cells. The apical: basal ratio reached upto 16 by 4^{th} time point and eventually decreased during mesoderm invagination to about 7. In $drp1^{SG}$ embryos (Fig. 7.1 C, red), Sqh-mCherry intensity was half of the WT (Fig 7.1 C, black) to begin with and continued being lower than the WT throughout gastrulation. The intensity ratio values in $drp1^{SG}$ embryos only reached a maximum of 7 which then reduced to 5 at the end of mesoderm invagination.

This suggests that the furrow morphology observed using phalloidin staining and Sqh-mCherry both is likely due to lowered Myosin II levels. Either mitochondrial mislocalization or reduced ROS (Fig. 6.7 C, D) in *drp1*^{SG} may be responsible for Myosin II reduction.

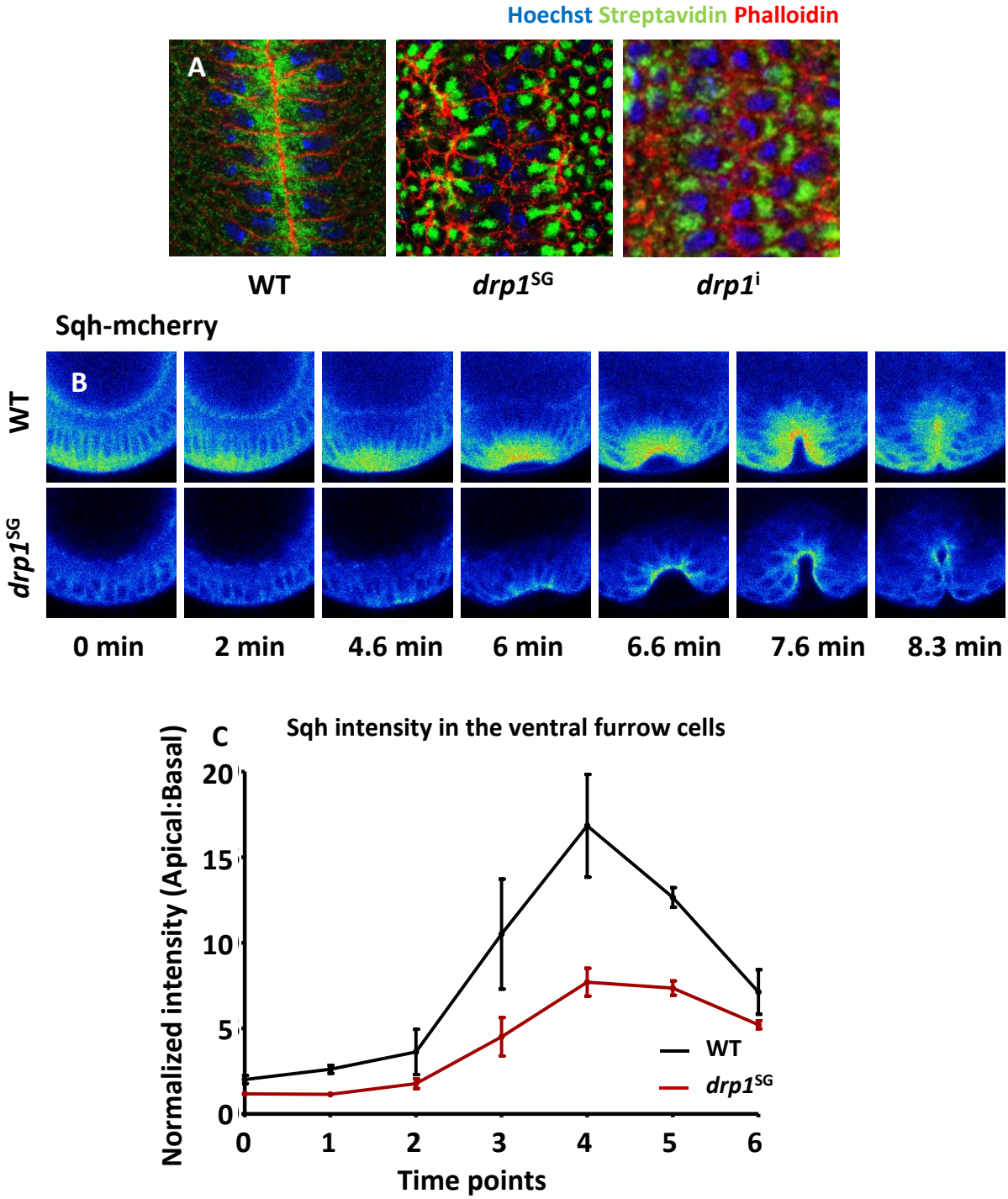

Figure 7.1: *drp1* mutant embryos have misaligned ventral furrow cells with lowered Myosin (Sqh). WT ventral furrow has mitochondria (streptavidin, green) present abundantly at the apical regions above nuclei (Hoechst, blue). Ventral furrow cell boundaries marked by F-actin (Phalloidin, red) are symmetric (**A**). Mitochondrial clumps (streptavidin, green) are seen below the nuclei (Hoechst, blue) in *drp1*^{SG} and *drp1*^{i} embryos. Ventral furrow cells are misaligned (F-actin, phalloidin, red) (**A**). Sqh-mCherry imaged during ventral furrow formation in *drp1*^{SG} embryos show flattened ventral furrow, which does not close completely (White arrowhead) as the WT (**B**). Apical: Basal intensity of Sqh-mCherry fluorescence is significantly reduced in *drp1*^{SG} (red) compared to WT (black) (**C**) n = 3 (**C**)

7.3.2 Distribution of Dorsal and Twist is unchanged in *drp1*^{SG} embryos

Mesoderm fate is determined by Toll-Dorsal pathway, which activates a downstream cascade of transcription factors including Snail, Twist and Fog ultimately leading to apical activation of Myosin II and apical constriction and invagination of mesoderm cells (Jiang et al., 1991; Lim et al., 2017). The phenotype observed in *drp1*^{SG} embryos related to the furrow morphology and Myosin localization is similar to downregulated Toll-Dorsal pathway components (Barmchi et al., 2005; Dawes-Hoang, 2005; Nikolaidou and Barrett, 2004). Mitochondria specifically migrate to the apical regions of the mesoderm cells during gastrulation, therefore we asked if mitochondrial mislocalization in *drp1*^{SG} embryos perturbs Dorsal and Twist by using antibodies against these proteins. These images were taken on Zeiss, light sheet microscope. Due to less resolution obtained, we chose to quantify the spread of nuclear signal of Dorsal and Twist relative to the whole embryo, instead of the intensity (7.2.4.2) (Fig 7.2). No significant difference was observed between WT and *drp1*^{SG} Dorsal and Twist relative spread (Fig 7.2B).

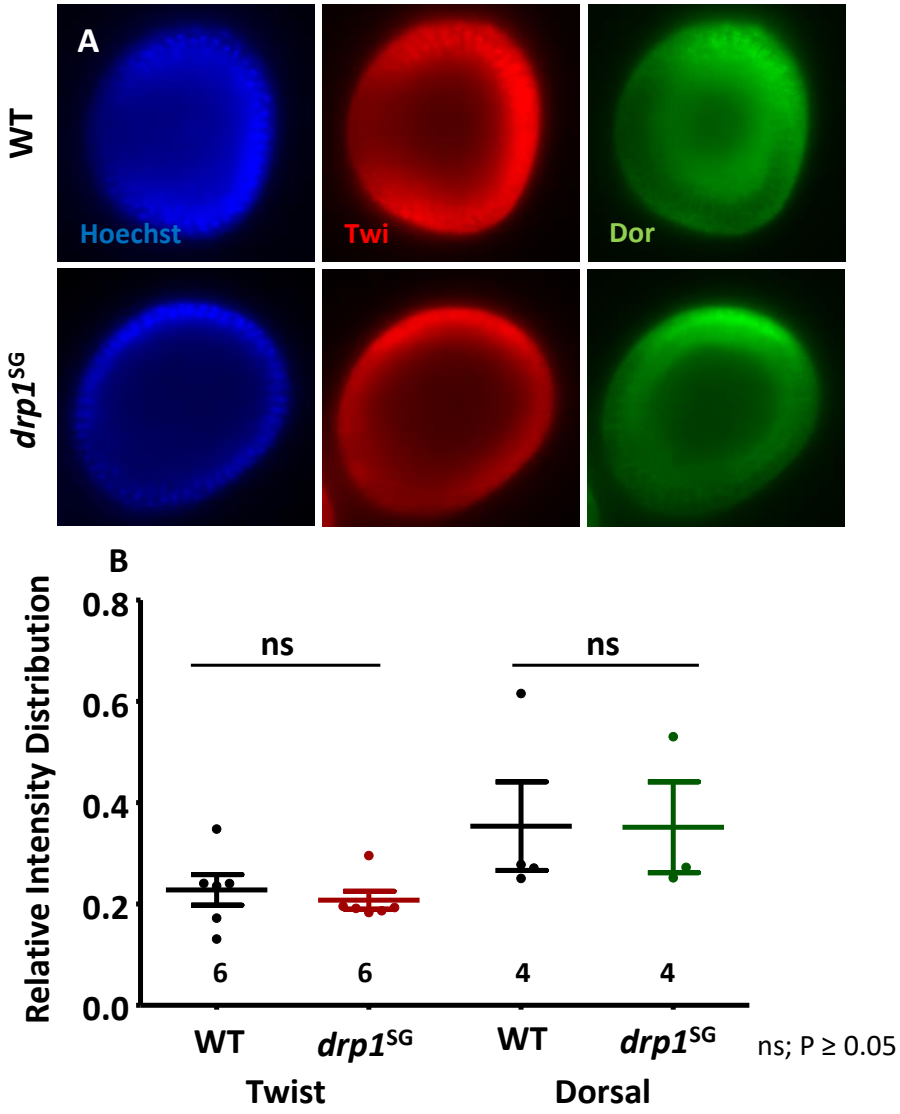

Figure. 7.2: Distribution of Dorsal and Twist in unaffected in *drp1*^{SG} embryos. WT and *drp1*^{SG} embryos have Dorsal (green) and Twist (red), present inside the ventral nuclei (Hoechst, blue) (**A**) Relative distribution of Twist (red) and Dorsal (green) intensity in *drp1*^{SG} is similar to WT (black) (**B**). N = 2, number on the graph represent the number of embryos analysed for each data set. (ns; P ≥ 0.05, Mann Whitney test)

7.3.3 Increased Dorsal elevates apical mitochondria during gastrulation

We had documented an enhancement of mitochondrial transport in the mesoderm cells during gastrulation (5.3.2). We then questioned whether mitochondrial apical migration could work downstream of Toll-Dorsal pathway. We over-expressed WT dorsal in the

background of dorsal null allele (*dl*^{1},UASP-*dl*^{WT}, referred as UASP-*dl* hereafter) using *nanos*-Gal4 along with Mito-GFP. To verify whether the over-expression fly line is effective in increasing Toll-Dorsal activity, we immunostained UASP-*dl* embryos with Dorsal and Twist antibody. Dorsal and Twist staining was only present in the mesoderm nuclei in the WT embryos (Fig 7.3 A, Top panel). 88% of UASP-*dl* embryos showed enhancement in the immunostaining and it was spread throughout the embryo on the ventral as well as dorsal side (Fig 7.3 A, Bottom panel). We then measured a ratio of Twist and Dorsal fluorescence intensity in ventral: dorsal nuclei. Twist and Dorsal staining was about 1.5 and 3 fold respectively in ventral nuclei than the dorsal nuclei (Fig 7.3 B). The ventral: dorsal fluorescence ratio significantly reduced and was closer to 1 in UASP-*dl* embryos for both Twist (Fig 7.3 B, red) and Dorsal (Fig 7.3 B, green) staining. Thus the Toll-Dorsal pathway is elevated in UASP-*dl* expressing embryos.

We then imaged UASP-*dl* embryos using Mito-GFP in endon orientation. Only 16% (1/6) embryos contained invaginating cells, but the furrow formed was not normal. Remaining 84% (5/6) embryos did not form the ventral furrow. Thus, we were only able to test the difference in Mito-GFP in the early gastrulation timepoints. For the quantification, we chose a time point where apical constrictions begin and also where increase in the apical mitochondrial fluorescence is clearly visible. The region of enhanced mitochondrial fluorescence was restricted to a narrow region of around 8 cells in the WT (Fig. 7.3 C). 1/6 of UASP-*dl* embryos showed restricted localization apically increased Mito-GFP. In 3/6 of the embryos the mitochondrial apical fluorescence was enhanced in almost half of the embryo. 2/6 embryos show an enhancement of the signal in all cells (Fig. 7.3 C). We quantified apical mitochondrial fluorescence in WT and UASP-*dl* embryos and plotted it with relative distance (%) from the ventral midpoint (Fig 7.3 D, 0). Mitochondrial fluorescence in the WT embryos was present in the ventral most 20% region (Fig. 7.3 D, black). Intensity profile of the fluorescence in UAS-*dl* was significantly spread compared to the WT (Fig 7.3 D, red).

These data demonstrate that Toll-Dorsal pathway activates mitochondrial apical transport. We need more experiments to point out the component of the pathway necessary in regulating mitochondria.

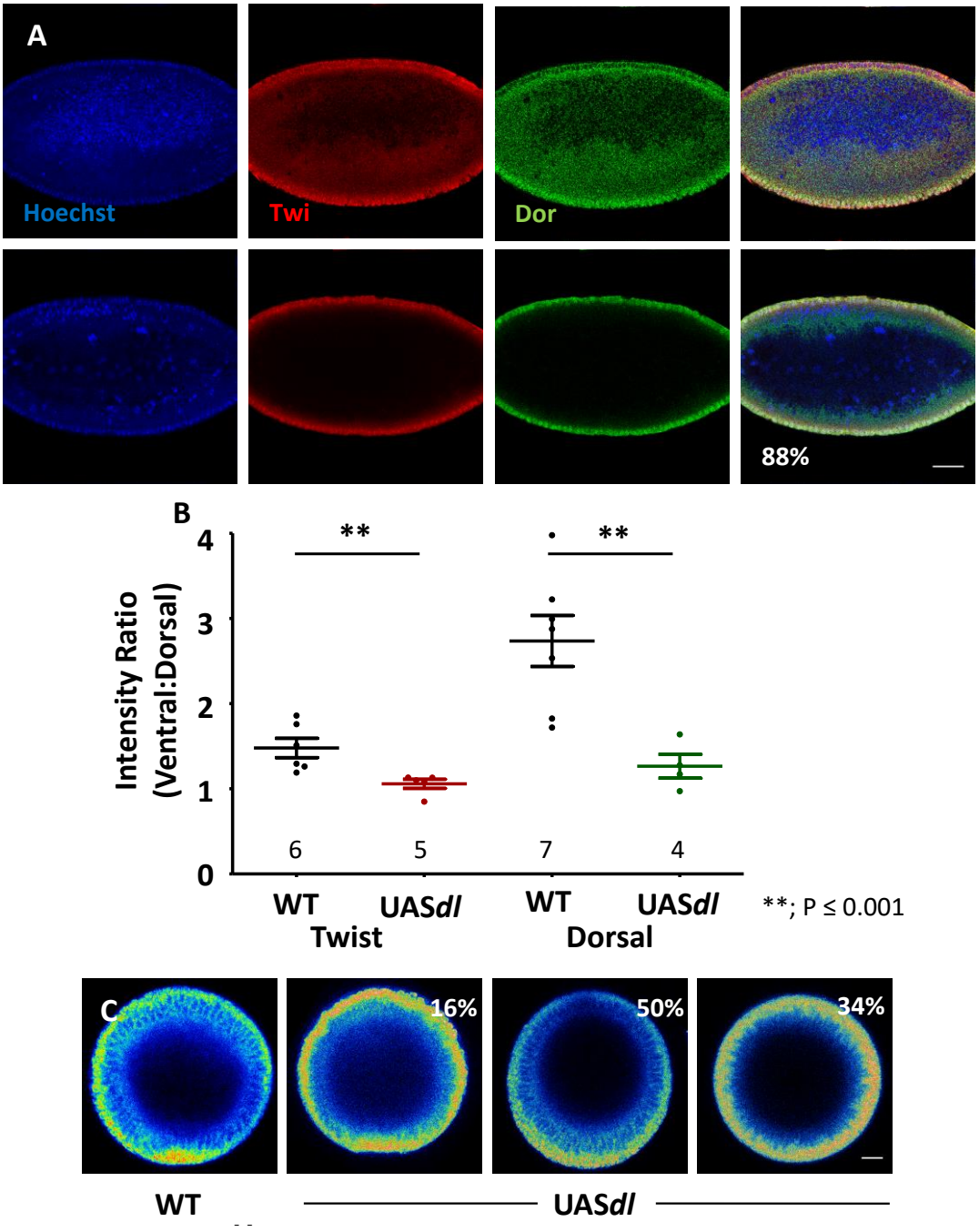

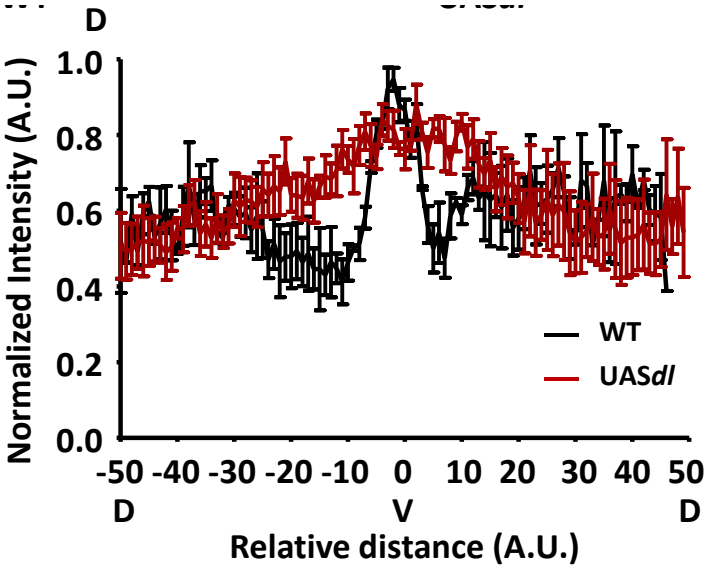

Figure 7.3: Mitochondrial apical migration is enhanced in *dorsal* over-expression. Dorsal (green) and Twist (red) are localized inside the ventral nuclei (Hoechst, blue) in WT cellularizing embryos (**A**). Dorsal (green) and Twist (red) staining is present in almost all of the nuclei in UAS*dl* cellularizing embryos (**A**). Ventral: Dorsal side fluorescence intensity ratio measured in nuclei for Twist (red) and Dorsal (green) is significantly lowered in UAS*dl* compared to WT (**B**). Numbers on the graph represent the number of embryos analysed. Intensity was measured from 5 nuclei on each side per embryo. (**; P ≤ 0.01, Mann Whitney test) (**B**). Mitochondrial signal is enhanced at the apical side of ventral mesoderm cells during apical constriction in WT embryos imaged end on using Mito-GFP (**C**). 16%, 50% and 34% of UAS*dl* embryos have localization of mitochondria in a few ventral cells, almost half of the cells and all cells in the embryo respectively (**C**). Mean normalized apical Mito-GFP fluorescence is spread more in UAS*dl* (red) compared to WT embryos (black) (**D**) n = 3, 6; WT and UAS*dl* respectively. Scale bar: 50 µm (**A**), 20 µm (**C**).

7.3.4 Mitochondria accumulate at the ventral furrow in *rhogef*^{i} and *mbs*^{i}

We then asked whether down-stream components of the Toll-Dorsal pathway affect mitochondrial localization at the ventral furrow. Firstly, we tried to modulate activity of Myosin II by using RNAi against RhoGEF2 (*rhogef2*^{i}) and MBS (*mbs*^{i}) driven using *mat*-Gal4 and observed mitochondria using fluorescently tagged streptavidin. RhoGEF2 is an upstream kinase that activates Myosin II apically in the ventral furrow cells (Barmchi et al., 2005). MBS

inhibits myosin regulatory light chain (MRLC, *sqh*). Thus knocking it down hyperphosphorylates Sqh, thereby increasing Myosin II activity (Mizuno et al., 2002; Xue and Sokac, 2016). Ventral furrow did not form in 100% of *mbs*^{i} and in 67% of *rhogef2*^{i} embryos, indicating that these RNAi lines were effective (Fig 7.4 A). Mitochondria were present apically in the ventral cells, suggesting that mitochondrial localization is not controlled by Myosin II activity (Fig 7.4 A).

7.3.5 *fog* knockdown reduces mitochondrial apical transport in the ventral furrow

Next, we tested mitochondrial localization in *fog*^{i}. *fog* is transcriptionally activated downstream of *twist* in the ventral mesoderm cells. We expressed *fog*^{i} (Ratnaparkhi and Zinn, 2007), using *nanos*-Gal4. 67% of embryos formed ventral furrows with misaligned boundaries, but no mitochondrial phenotype was observed. 33% of embryos showed absence of furrows and random clustering of mitochondria (Fig. 7.4 A). We expected mitochondrial clustering since *fog* and *drp1* are known to complement each other genetically as shown by study using *Drosophila* muscles (Ratnaparkhi, 2013).

In order to systematically analyze mitochondrial localization in *fog*^{i} we used Mito-GFP and imaged the embryos endon (5.2.2) (Fig. 7.4 B). We then measured apical to basal intensity ratios at different time points during gastrulation (5.2.5.2). The normalized apical:basal fluorescence was similar to WT at the beginning of apical constriction indicating a lack of significant effect on cellularization, but the apical:basal fluorescence did not increase significantly with time in gastrulation. Fluorescence ratio increases to about 5 fold by 3rd time point. Intensity ratio in *fog*^{i} embryos was significantly less at 3rd and 4th time point (Fig 7.4 B, C).

These data show that Fog likely regulated mitochondrial apical transport during gastrulation. We are further testing whether stronger depletion of *fog* would lead to a severe mitochondrial transport defect with other available RNAi fly stocks.

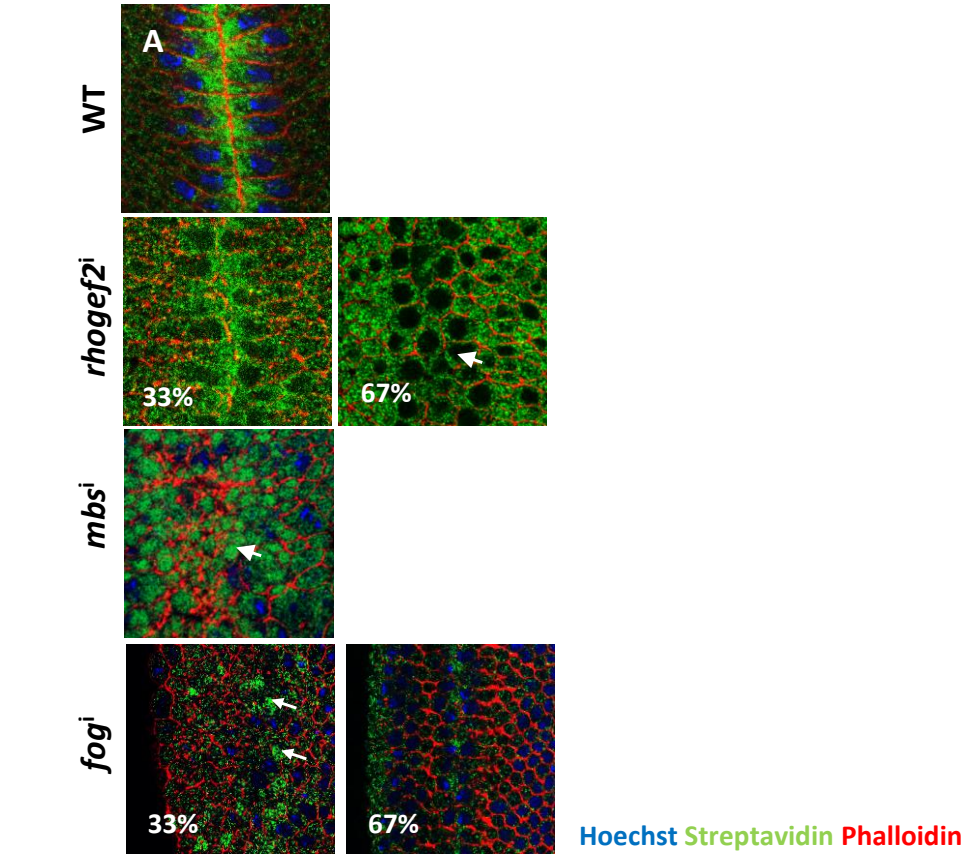
A
WT
rhogef2i
33%
67%
mbsi
fogi
33%
67%
Hoechst Streptavidin Phalloidin

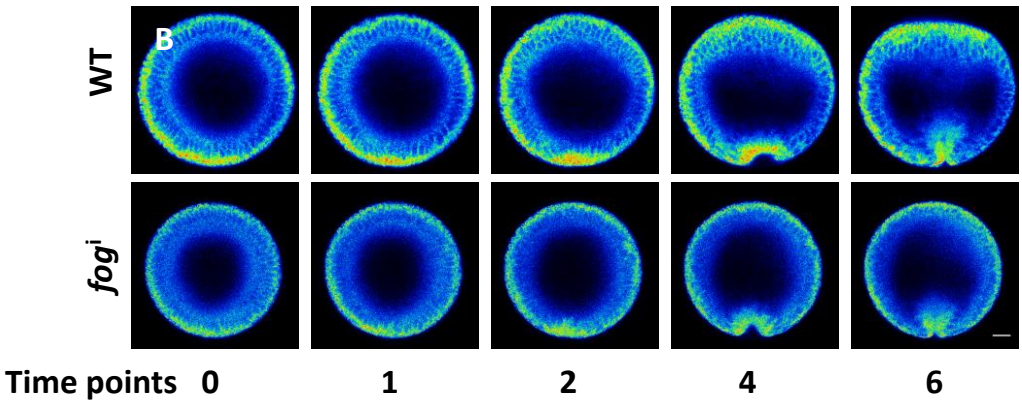
B
WT
fogi
Time points 0 1 2 4 6

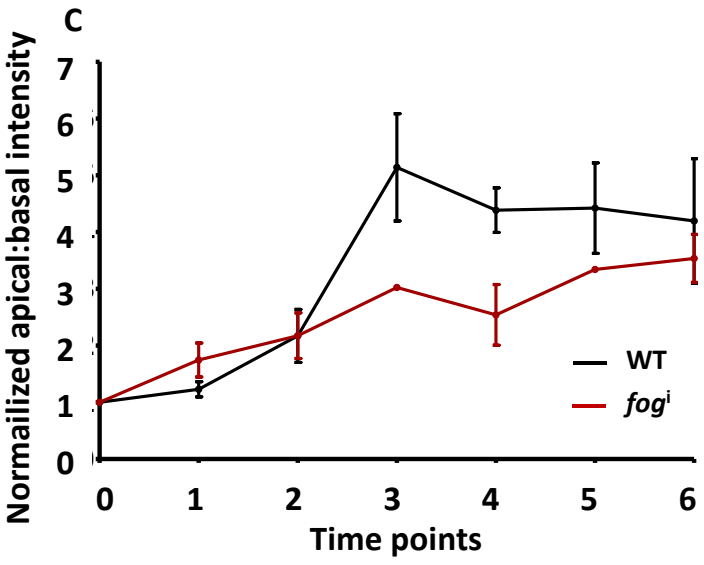
C
Normailized apical:basal intensity
0 1 2 3 4 5 6 7
0 1 2 3 4 5 6
Time points
WT
fogi

Figure 7.4: Downregulation of Toll-Dorsal pathway components. Ventral furrows are misaligned (33%) or missing (67%) (F-actin, phalloidin, red) in *rhogef2*^{i} embryos but mitochondria (streptavidin, green, white arrowheads) localize to the apical regions (**A**). Mitochondria (streptavidin, green, white arrowheads) are present apically in *mbs*^{i} embryos, where ventral furrows do not form (**A**). Ventral furrows are misaligned (67%) or missing (33%) (F-actin, phalloidin, red) in *fog*^{i} embryos. Mitochondrial clusters (streptavidin, green, white arrowheads) are observed in 33% embryos (**A**). Mitochondria are visualized in *fog*^{i} embryos using Mito-GFP. Ventral furrow morphology in *fog*^{i} embryos is not strikingly different than the WT embryos (**B**). Mean normalized Apical: Basal intensity of Mito-GFP signal at ventral cells is lowered in *fog*^{i} (red) compared to WT embryos (black) (**C**). n = 3, Scale Bar: 20 µm (**C**).

7.4 Discussion

Mitochondrial apical migration is disrupted in *drp1*^{SG} embryos in cellularization and gastrulation. Myosin II amounts are reduced at the apical regions of ventral mesoderm cells, resulting in furrow flattening. The furrow is not completely zippered in the end. Myosin II downregulation inhibits apical constrictions and furrow formation (Dawes-Hoang, 2005; Weng and Wieschaus, 2016; Xie and Martin, 2015). Similar to *drp1*^{SG}, *fog* (Dawes-Hoang, 2005) and *rhogef2* (Barmchi et al., 2005; Nikolaidou and Barrett, 2004) mutant embryos also have significantly lowered amounts of Myosin at the ventral furrow. Attenuation of fog signaling by downregulation of *drp1* has been showed in *Drosophila* muscles (Ratnaparkhi, 2013). Additionally, over-expression of fog could fragment mitochondria in Drp1 dependent manner. A small fraction of *drp1* knockdown embryos have been shown to have a misaligned ventral furrow (Ratnaparkhi, 2013). Myosin constricts apical regions of the ventral furrow cells in a ratcheted pulsatile way (Vasquez et al., 2014) and these pulses are dependent on Twist (Xie and Martin, 2015). Ventral furrow was flattened in embryos lacking cumberland-GAP (C-GAP) (Mason et al., 2016). C-GAP inhibits RhoA and thereby reducing Myosin II activity. Although, the amount of active Myosin II is increased in C-GAP knockdown embryos, the pulsatility is reduced leading to lowered apical constriction

(Mason et al., 2016). Measuring the intensity, time and frequency of the Myosin II pulses in *drp1*^{SG} embryos will elucidate the effect on Myosin activity more descriptively.

Flattening of ventral furrow and a lack of apical constriction has been also observed in embryos with reduced actin turnover, obtained by knockdown of Slingshot (*SSh*) (Jodoin et al., 2015). *SSh* inactivates actin severing protein Cofilin by dephosphorylation (Niwa et al., 2002).

Knockdown of ventral fate inhibitor Spn27A, increases the width of ventral domain broadens area of active Myosin, and there by flattening the ventral furrow overall (Chanet et al., 2017; Ligoxygakis et al., 2003). We have not tested the extent to which Myosin II is active in *drp1*^{SG} embryos and whether it may serve as a compensation for its loss. But we have measured the spread of Dorsal and Twist staining in *drp1*^{SG} embryos and it shows no change compared to the WT indicating that the ventral fate determination proteins are at least located in a restricted manner.

Myosin II is required for apical translocation of adherens junction proteins such as Armadillo (Arm, β-catenin) and E-cadherin (Weng and Wieschaus, 2016). The localization and activity of Arm and E-Cadh is essential for proper progression of ventral furrow (Cox et al., 1996; Haruta et al., 2010; Wang et al., 2004). The gastrulation phenotype observed in *drp1* mutant embryos may additionally be due to loss of these adherens proteins.

We tested whether enhanced mitochondrial apical transport in the ventral mesoderm cells is regulated by the Toll-Dorsal pathway. The data with Dorsal over-expression pointed out an interesting possibility of regulation of apical transport. We observed increased apical localization of mitochondria in the Dorsal overexpression embryos compared to WT, most likely in the all the cells that gain Dorsal signaling. When downregulated various components of the Toll-Dorsal pathway, a reduction in the mitochondrial accumulation at the ventral furrow was observed in *fog*^{i} embryos suggesting that this pathway may indeed be regulating mitochondrial transport. We need to test this possibility better by over-expression or stronger knockdown of *fog*. Since *fog* is a zygotically expressed gene, using maternal promoter containing Gal4 constructs is not achieving optimal *fog* knockdown in the embryos. Fog is secreted apically and activates maternally expressed Concertina (Cta) that initiates the Myosin regulatory cascade with the help of G-protein coupled receptors

(Barrett et al., 1997; Fuse et al., 2013). It could probably be more effective to knock Cta down using *nanos*-Gal4 or *mat*-Gal4. Additionally, these data support the known interaction between *fog* and *drp1* (Ratnaparkhi, 2013). We can also test whether gastrulation phenotypes obtained in *drp1* mutant embryos are due to decreased *fog* activity. Mitochondrial apical transport needs mitochondrial fragmentation (Fig 6.8 A, B), it would be worth analyzing whether Fog alters mitochondrial morphology in the ventral furrow cells.

Mitochondrial localization at the apical region may be necessary for either providing energy or ROS or they may be participating in signaling. We showed in cellularizing $drp1^{SG}$ embryos, the ATP levels are likely unchanged, but they have reduced ROS levels (6.3.6). Myosin activity is attenuated by signaling through ROS during dorsal closure in *Drosophila* embryos (Muliyil and Narasimha, 2014). ROS may regulate activity of kinases upstream of Myosin II (Fedorova et al., 2009; Steinberg, 2013). A proteomic study demonstrated differences in Drp1 protein isoforms in ventralized and dorsalized embryos (Gong et al., 2004). The authors also showed that Transferrin1 and transferrin 2 light chain homolog are reduced in ventral cells. This protein regulates redox activities in cells (Gong et al., 2004). A gradient of mitochondrial membrane potential was observed using JC1 dye (Schiffmann, 1997). This suggests a possibility of metabolic differences between ventral and lateral cells. Immune system T cell receptor activation depends on and leads to production of mitochondrial ROS (Dröge, 2002; Kamiński et al., 2012). Transcription of immune response targets is achieved by Nuclear factor-kappaB (NF-κB), a mammalian homologue of Dorsal (Smith-Garvin et al., 2009). NF-κB is activated by a Activating post-translational modification and mitochondrial localization of Drp1 leads to ROS production which is necessary for the function of NF-κB (Röth et al., 2014). It would be interesting to find similar interaction in the case of Toll-Dorsal pathway at *Drosophila* mesoderm.

Taken together, mitochondrial activity and localization is essential for formation of precise ventral furrow during gastrulation. Toll-Dorsal pathway likely regulates mitochondrial localization and activity in the furrow. The mechanistic relation between mitochondrial localization and activity remains to be elucidated. We are studying these interactions in more details by increasing ROS levels in the background of $drp1^{SG}$ by using SOD down-regulation or mutants. We will also attempt to obtain a rescue of phenotypes by combining hyperactive Toll-Dorsal pathway components with *drp1* mutation.

8 Thesis Summary and Future perspectives

Since the discovery of mitochondrial fission and fusion proteins, great progress has been made in understanding of mitochondrial functionality. Mitochondrial dynamics has been studied in details and even more constituents regulating mitochondrial shape regulation are being discovered. Involvement of mitochondria in regulation of signalling has come to light recently and a network of mitochondrial interactors, based on dynamics, metabolism and diseases is being established. Different mitochondrial architecture is also associated with differences in metabolic output and the regulation is cell type specific (Kuznetsov et al., 2009). Early embryos, oocytes and have nascent mitochondrial architecture and metabolism compared to a differentiated cell (Birket et al., 2011; Van Blerkom, 2011; Wang et al., 2012; Xu et al., 2013). Notable studies demonstrate the interaction of mitochondrial architecture with differentiation and growth regulating pathways such as EGFR, Hippo/Yorkie, Notch and cyclin E during cell division (Mandal et al., 2010; Mitra et al., 2012; Nagaraj et al., 2012; Parker et al., 2015; Tomer et al., 2018). Most of the studies related to mitochondrial function are related to their metabolic capacity and fertilization competence of oocytes and pose a clinical relevance. Few studies point out to mitochondrial morphology and localization in various model systems such as preimplantation mammalian, ascidian and *Xenopus* oocytes and embryos (Bavister and Squirrell, 2000; Van Blerkom, 2011; Dumollard et al., 2007; Mtango et al., 2008; Weakley, 1966; Yost et al., 1995). Mitochondrial localization has been suggested using reagents such as mitochondrially derived long ribosomal RNA (mtlr-RNA), germ plasm dyes and redox dyes like JC1 (Van Blerkom, 2011; Van Blerkom et al., 2002; Dumollard et al., 2007; Yost et al., 1995). A systematic characterization of mitochondrial morphology, localization and function in early metazoan embryos had not been done so far.

Various modes of interaction of mitochondria with cellular signalling pathways are upcoming. They largely consists of production and release of small molecules like calcium, ROS, acetyl CoA and cytochrome C (Chandel, 2014). Acetyl-CoA and other mitochondrial enzymes can participate in chromatin modifications (Liao et al., 2006; Nagaraj et al., 2016) and post translational modification of proteins (Shi and Tu, 2015). Other body of evidence suggests localization of signalling molecules on the mitochondria, possibly regulated by the

mitochondrial membrane potential (Parker et al., 2015; Tomer et al., 2018). But the functional significance of mitochondrial architecture and their precise mechanistic roles in signalling and development are not very clearly established yet.

We systematically analysed mitochondrial shape, distribution and function in the *Drosophila* embryo. We studied the importance of mitochondrial shape regulation in the embryo and we propose an interaction of mitochondria with dorso-ventral axis determination.

8.1 Regulation of mitochondrial distribution during *Drosophila* embryogenesis

We characterized mitochondria in the preblastoderm, syncytial blastoderm, cellularization and ventral furrow invagination using live imaging of mitochondrially localized GFP tag (Mito-GFP) expressed using maternally driven *nanos*-Gal4. We were able to potentially mark individual mitochondrial puncta based on fluorescence and measure their sizes using threshold based quantification. The mitochondrial size remained small from preblastoderm to gastrulation and the measured sizes were similar to previously estimated mitochondrial area using EMs. We also successfully engineered and standardized the photoactivation methods to visualize mitochondria in the embryo. We were able to specifically light a few mitochondria using the Mito-PAGFP tag and follow their localization and dynamics in a better analytic way.

Majority of mitochondria locate near the cortex and a fraction of them surround the preblastoderm nuclei deep inside the embryo. Cortical mitochondria are captured around nuclei arriving at the cortex during NC10 and the surround the nuclei. Mitochondria are scarce in the apical regions and mostly localize below the nuclei in the syncytial blastoderm stage (Fig 8.1 A) by binding to microtubules and trafficking by plus ended Kinesin motors. Mitochondria display negligible mobility around nuclei and similar to Golgi complex and endoplasmic reticulum (ER), mitochondria are restricted to one nuclear-cytoplasmic region or “syncytial cell” and are distributed equally in daughter cells. This suggests lineage specific inheritance of mitochondria in the syncytial cells. It has been previously shown that daughter nuclei remain at the same location as mother nuclei. Plasma membrane associated molecules also equally distribute between daughter nuclei (Mavrakis et al., 2009). In addition to equal distribution to daughter nuclei, we found that mitochondria were

stationary within each syncytial cell also. This is likely to be significant for local activities such as energy requirement regulated by mitochondria.

Progressive relocalization of mitochondria from basal regions to the apical regions takes place during cellularization based on their transport on dynein motors (Fig. 8.1 B). The mitochondrial migration occurs synchronously in time with ingression of membranes. Whereas, apical migration during cellularization takes place globally, the apical migration is very specifically enhanced in the ventral furrow cells post cellularization (Fig 8.1 C). This is similar to previous observations made in *Xenopus* embryos using mtlr-RNA (Yost et al., 1995). The apical migration of mitochondria during ventral furrow formation occurred simultaneous with apical constriction of the mesoderm cells.

MZT is characterized by beginning of zygotic RNA expression and degradation of maternal mRNA. The zygotic RNA transcription is regulated by maternal components such as Zelda (*zld*). Majority of zygotic gene transcription initiates around the time of cellularization in *Drosophila* embryo (Harrison et al., 2011). It is essential to note that mitochondrial apical transport takes place during the time of MZT. Mitochondrial basal localization is mediated by Khc during syncytial stages. *khc* is highly expressed in the 0-2 hour old embryo and the transcript levels reduce post 2hrs (modENCODE). At the same time the levels of Dynein light chain 90F (*dlc90f*) increase. Dlc90F is essential for linking of motors and adapters to their cargos. It is possible that regulation of microtubule motor transcription during this stage reverts the mitochondrial and Golgi complex (Papoulas et al., 2005; Sisson et al., 2000) localization. There could also exist a possibility of regulation of MZT itself by organelle relocalization.

Mitochondrial are transported over long distances in neurons on microtubules (Chen and Chan, 2009). It has been shown that mitochondria with higher membrane potential selectively are transported rapidly in anterograde way to the growth cones (Miller and Sheetz, 2004). Although mitochondrial shape in apico-basal axis in *Drosophila* cellularization and gastrulation are similar, we do not know whether there are metabolic differences in mitochondria within a cell. This would be an exciting aspect to follow.

8.2 Role of mitochondrial shape and function during embryogenesis

Maintenance of mitochondrial morphology is essential for embryonic development and survival (Chen et al., 2000; Ishihara et al., 2009; Moore et al., 2010; Rahn et al., 2013; Wakabayashi et al., 2009). Also, early embryo development requires ATP obtained from aerobic respiration (Van Blerkom et al., 1995; Dumollard et al., 2007; Wilding et al., 2009; Zhao et al., 2015).

We studied the impact of ATP inhibition in the syncytial blastoderm stages. By using pAMPK as energy sensor and through acute and genetic inhibition of mitochondrial ETC components, we found that the ETC is active and is the source of energy for early embryos. Similar results were obtained from direct measurement of ATP and staining for mitochondria potential dye CMXRos. Reduction in ATP content in the embryos affected ingression of metaphase furrows. We propose that small mitochondria restricted in space traffic efficiently in the syncytial embryos and are required to locally provide ATP to rapidly growing metaphase furrows.

Next, we attempted to modify mitochondrial morphology using fission and fusion protein mutants and knockdown using an RNAi based approach. Knockdown of fusion did not significantly change the mitochondria morphology, most likely because mitochondria are already at their smallest possible size. Knockdown and mutations in *drp1* significantly increased the mitochondrial clustering. These large mitochondria failed to travel apically, as the microtubule motors may be inefficient in carrying an increased load. We did not observe any changes in the ATP levels, based on the pAMPK staining. This could possibly be because mitochondrial ETC is still intact and/or the effective ATP content remains the same due to a large number of mitochondria present in the embryo. Recent report from the lab shows that the fused mitochondria in drp1 mutant follicle cells shows a higher mitochondrial membrane potential consistent with the explanation that mitochondria are functional (Tomer et al., 2018). ROS on the other hand was reduced in the cellularizing $drp1^{SG}$ embryos.

Shorter cells with wider contractile furrows were formed during cellularization in $drp1^{SG}$ embryos. Cause of lack of ring constriction could be physical barrier presented by clustered immobile mitochondria at the basal regions. Levels of membrane localized Myosin regulatory light chain (MRLC, *sqh*) were significantly low in $drp1^{SG}$ embryos. Tuning of

Myosin levels is controlled by ROS and mitochondrial morphology in constricting amnioserosa cells in *Drosophila* embryo dorsal closure (Muliyil and Narasimha, 2014). A similar mechanism may exist in this situation as well. Thus, lack of membrane extension and less contractility of the actomyosin rings possibly attribute to decrease in the Myosin levels as observed our experiments and previous studies (Wenzl et al., 2010; Xue and Sokac, 2016) done using Myosin mutants .

Myosin II is an essential component during apical constriction and invagination of ventral mesoderm cells. Myosin activity is reduced from the basal region of mesoderm cells and pulsed activation initiates at the apical surfaces (Martin et al., 2009). Levels of myosin are reduced in *drp1*^{SG} embryos. Ventral furrow is misaligned and flattened compared to the WT, similar to phenotypes observed in *rhogef2* and *fog* mutants which fail to localize Myosin at the apical regions of the ventral cells (Barmchi et al., 2005; Dawes-Hoang, 2005; Nikolaidou and Barrett, 2004). An interaction between Fog signalling and Drp1 has been previously established (Ratnaparkhi, 2013) and metabolic differences between ventral mesoderm and ectoderm cells has also been suggested (Gong et al., 2004; Schiffmann, 1997). We would like to further address if gastrulation phenotypes observed in *drp1* mutant embryos is due to their interaction with Toll-Dorsal pathway. Also since ROS levels are reduced in the *drp1*^{SG} embryos, it would be worth analysing if alterations in ROS levels affect Toll-Dorsal pathway components.

8.3 Regulation of mitochondria by Toll-Dorsal pathway

Toll-Dorsal pathway regulates the ventral fate by transcriptional control of the genes *snail*, *twist* and *fog* which in turn activates the ROK, Rho-GEF2 cascade to initiate and maintain Myosin II activity at the ventral furrow (Barmchi et al., 2005; Dawes-Hoang, 2005; Fuse et al., 2013; Leptin, 1991; Leptin and Grunewald, 1990; Martin et al., 2009; Morisato, 2001). Since we observed a very specific enhancement in mitochondrial transport in the ventral mesoderm cells, we wondered if this is regulated by the mentioned pathway. Over-expression of the pathway using *dl*^{1},UAS-*dl*^{WT} expanded the pathway activity in the entire embryo. We found that mitochondrial apical transport occurred in a large number of cells or in the entire embryo when *dorsal* was over-expressed, most-likely in the cells with active Dorsal. The transport reduced when *fog* was knocked down. Mitochondria localized to the

furrow when amounts of Myosin II regulators, Rho-GEF2 and MBS were reduced. These data indicate that mitochondria are likely to function downstream of *fog* and upstream of Rho-GEF2 cascade. We need more experiments to achieve a stronger inhibition of mitochondrial transport in the ventral cells. These are described later in this section.

drp1 mutant embryos render shallow and asymmetric furrows with lowered activity of Myosin. Also, ROS is reduced in these embryos. Fog pathway regulates Drp1 to fragment mitochondria by an unknown mechanism (Ratnaparkhi, 2013). Myosin II functions downstream of Fog. Fog may be responsible for mitochondrial fragmentation, which we are not able to detect with the image resolution we have, leading to the apical enhanced transport. It is also highly likely that the Fog signalling pathway regulates the microtubule based transport in the mesoderm cells. We observed reduction in ROS levels in $drp1^{SG}$ embryos. On the contrary, Fog mediated mitochondrial fission can aid ROS production in the mesoderm. The mitochondrial ROS is likely to be locally delivered at the site of apical constriction, leading to activation of kinases to regulate Myosin II activity. Additionally, it is possible that Fog signalling regulates the transcription of SOD in the mesoderm cells to maintain ROS levels. It would be worth pursuing further how the interaction of Drp1 with Fog signalling controls myosin activity in the ventral furrow in future.

Taken together, we successfully characterized the mitochondrial localization and dynamics in the early *Drosophila* embryogenesis with the help of existing and better visualization tool of Mito-PAGFP. We demonstrated the effect of mitochondrial shape and metabolism modification on the embryogenesis. The work was also able to reveal regulation of mitochondria by the Toll-Dorsal pathway in the *Drosophila* embryo, further analysis will shed more light on the mechanistic details of this interaction.

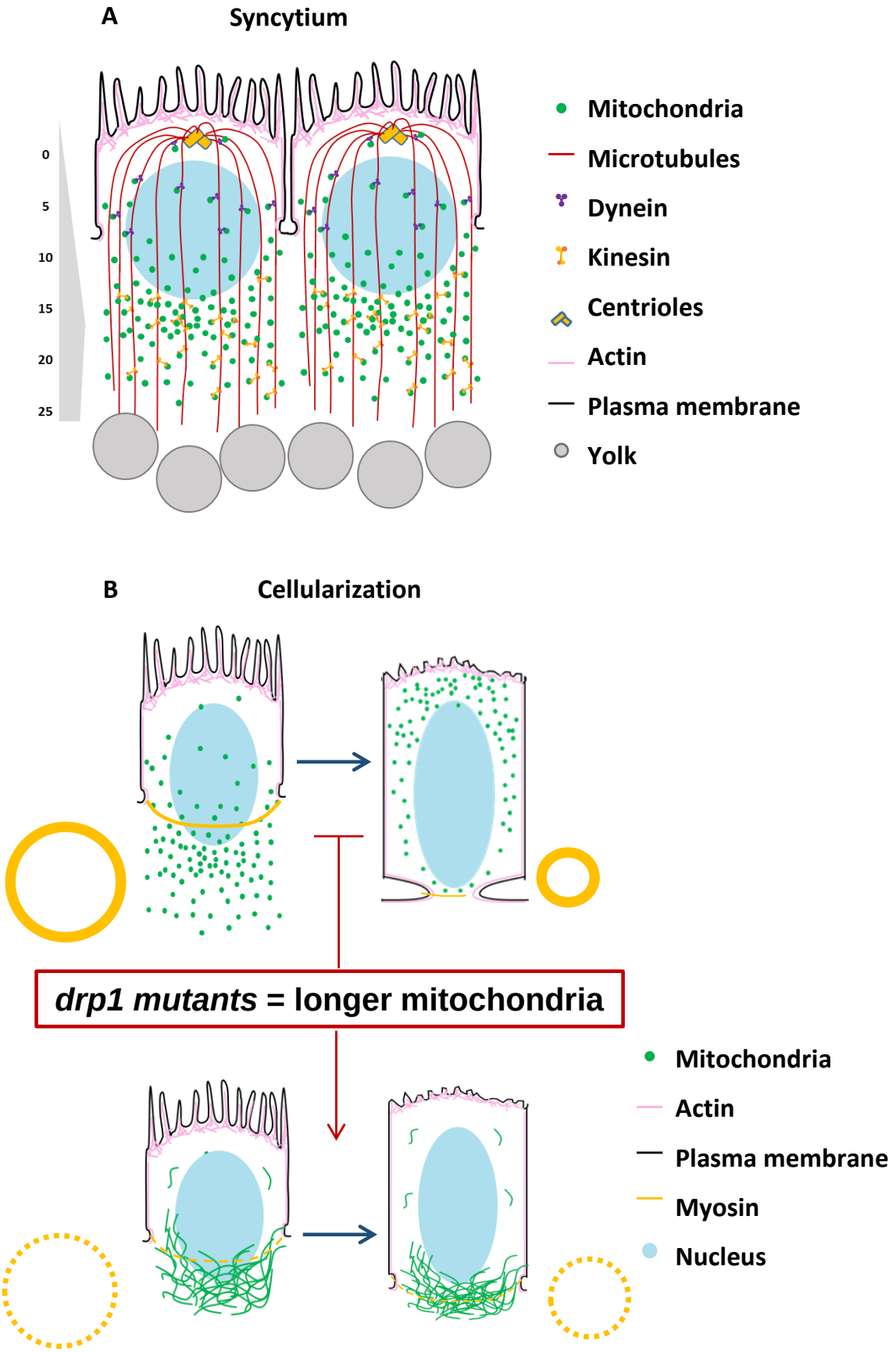
A
Syncytium
0
5
10
15
20
25
Mitochondria
Microtubules
Dynein
Kinesin
Centrioles
Actin
Plasma membrane
Yolk
B
Cellularization
drp1 mutants = longer mitochondria
Mitochondria
Actin
Plasma membrane
Myosin
Nucleus

C

Gastrulation

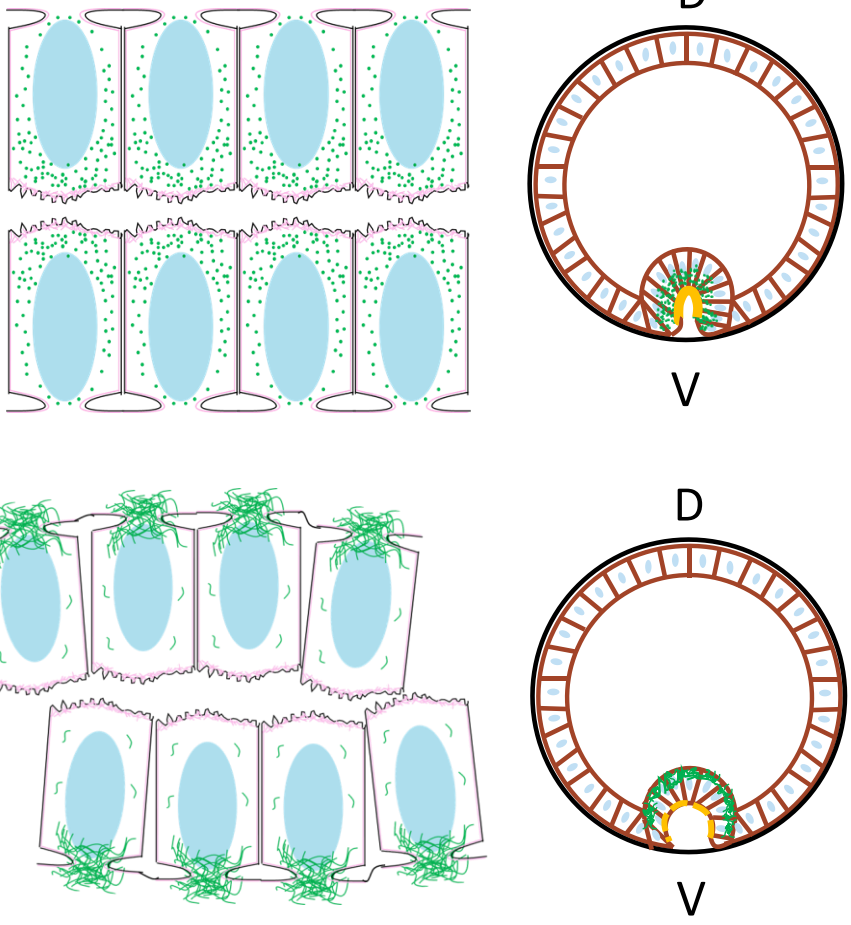

- Mitochondria
- Actin
- Plasma membrane
- Myosin
- Nucleus

Figure 8: Summary of results. Mitochondria (green) are small and basally distributed in the syncytial cells of the *Drosophila* embryo and essential for locally delivering ATP to the dynamic membranes. The mitochondrial distribution regulated is by microtubules (**A**). Reproduced from (Chowdhary et al., 2017) (**A**). Mitochondria (green) migrate apically during cellularization using dynein based transport (**B**). Clustered mitochondria (green) in *drp1* mutant embryos fail to migrate apically (**B**) *drp1* embryos have shorter cells and wider contractile rings with decreased Myosin levels (yellow dotted lines) (**B**). Mitochondrial apical migration is enhanced in the ventral furrow cells (**C**). The ventral furrow is misaligned and shallow in *drp1* mutant embryos. Apical activity of Myosin is reduced in these embryos (**C**).

8.4 Experimental limitations

8.4.1 Knockdown of essential maternal genes led to oocyte developmental defects.

We used RNAi based approach to knockdown transcripts in the embryo. The RNAis were expressed using maternally derived *nanos*-Gal4 and *mat*-Gal4. Mitochondrial proteins regulate *Drosophila* oogenesis (Mitra et al., 2012; Tomer et al., 2018). Optimum knockdown of *marf, opa1 and drp1* using *nanos*-Gal4 led to complete embryonic lethality and oocyte dysfunction. We attempted for stronger *dynein* knockdown using a different RNAi line. The flies obtained from crossing it with *nanos*-Gal4 did not lay any eggs. Mitochondria are clustered to the basal side in $drp1^{SG}$ embryos. We combined $drp1^{SG}$ with khc^{i} in an attempt to stop mitochondrial basal transport and enhance apical transport to rescue mitochondrial localization. The ovaries obtained from this combination were completely deformed. Since proteins are dumped in huge amounts in the embryo, injecting the dsRNA may not be the best option to overcome this limitation. One needs to test different combinations of Gal4 expression lines possibly with the addition of Gal4 suppressors such as Gal80ts to modulate the expression at different incubation temperatures in order to optimise the knockdown in order to obtain embryos with sustained defects at the desired developmental stage.

8.4.2 Knockdown of zygotic genes using maternally expressed Gal4 was not optimal.

Maternal knockdown of genes is a very effective way to reduce amounts of proteins in the early embryo. Majority of zygotic transcription starts at cellularization and effects of maternal driver may dilute out till that time (Staller et al., 2013). We used *nanos*-Gal4 to express *fog*^{i} in the embryo and observed a weak phenotype. We either need to use a stronger RNAi and a more temporal specific Gal4 expression for *fog* knockdown.

8.4.3 Analysis of cellular metabolism using chemical reagents.

A large variety of reagents is now available to analyse mitochondrial metabolism and function. In this thesis, the results obtained using Mitotracker-CMXRos; a mitochondrially localizing membrane potential dye and DHE; a dye to measure cellular ROS. We also tried using Mito-SOX to visualize mitochondria ROS. Mitotacker-CMXRos is a fixable dye whereas the other two can only be used in live samples. It is essential that the samples to be stained are alive at the time of incubation with dyes. The same applies for treatment of the embryos with inhibitor drugs. We tried using different protocols to permeabilize the vitelline membrane to incorporate dyes and drugs in the embryo. We have tested methods using Limonene-heptane combination (Schulman et al., 2013), iso-Propanol-Hexane combination (Strecker et al., 1994) and octane (Limbourg and Zalokar, 1973). This protocols are seemingly effective in the permeabilization of late embryos. In all the methods, the embryos did not survive post treatment and had to be fixed. We could not capture live dynamics of the embryos after dye or drug addition. Method with Limonene and heptane worked when we fixed embryos post drug treatment.

We are standardizing a method to quantify ROS using the expression based and redox sensitive mitochondrially localizing GFP imaging (Vevea et al., 2013) in the embryos and hope to observe dynamics changes in the ROS activity with development.

8.5 Future perspectives

We have put forth our observations and speculations regarding mitochondrial regulation during *Drosophila* embryogenesis and leads to pertinent questions to be addressed in future.

8.5.1 Interaction of Toll-Dorsal pathway and mitochondria

Our work demonstrates distinct regulation of mitochondria at the ventral mesoderm cells. Primary results suggest that mitochondrial localization and activity may be downstream of the Toll-Dorsal pathway and helps regulating Myosin II required for ventral furrow formation. We have not been able to find out the mechanistic role of mitochondrial presence at the apical regions of these cells. ROS and Myosin II activity is reduced in *drp1*^{SG} embryos. It is possible that apical mitochondria regulate Myosin II at apical regions by tuning their ROS production, especially with the help of Fog signalling which has already been shown to regulate mitochondrial morphology (Ratnaparkhi, 2013). Metabolic differences have been suggested between ventral and lateral regions of *Drosophila* embryo. It makes us pose an interesting possibility of regulation of mitochondrial metabolism by the Toll-Dorsal pathway.

A comparative analysis of mitochondrial localization during gastrulation in different species will be able to highlight the similarities between regulation of mitochondria between species.

8.5.2 Regulation of microtubule based transport during embryogenesis.

We reported regulated mitochondrial localization at very peculiar stages during embryogenesis. Mitochondrial distribution changes to more apical during cellularization and is enhanced in ventral furrow cells during gastrulation. Mitochondria are transported on both plus and minus ended motors, Kinesin and Dynein respectively, aided by adapter proteins such as Milton and Miro (Cox and Spradling, 2006; Fransson et al., 2006a; Haghnia et al., 2007; López-Doménech et al., 2018). In addition to mitochondria, Myosin II (Martin et al., 2009), RhoGEF2 (Barmchi et al., 2005), adherens junctional proteins (Weng and Wieschaus, 2016), Fog (Dawes-Hoang, 2005) localize from basal regions or are activated at the apical regions of ventral mesoderm cells. Dissociation of RhoGEF-2 from microtubule plus ends is required for its localization of cellular migration fronts (Rogers et al., 2004).

Taken together, a possibility of regulation of microtubular transport by the Toll-Dorsal pathway in the ventral furrow can be predicted. Whether this pathway also interacts with microtubule motors would be worth studying in future.

8.5.3 Regulation of mitochondria in other dynamic cells during embryogenesis

Mitochondrial polarization at cell migration front has been suggested in invasive cancer cells. This is coupled with increased biogenesis and increase ATP production at the leading edge, forming an energy gradient across the tumour cell (Caino and Altieri, 2015; Rivadeneira et al., 2015; Zhao et al., 2013) by AMPK mediated signalling (Cunniff et al., 2016). An involvement of PI3K and mTOR pathway is also suggested in the mitochondrial relocalization (Caino and Altieri, 2015). The migration and ATP production depends mitochondrial morphology (Desai et al., 2013; Zhao et al., 2013) and on Miro and Dynein motors (Morlino et al., 2014; Schuler et al., 2017) in the cells. Our data shows relocalization of mitochondria to the dynamic apical regions of invaginating cells during gastrulation. Myosin based cellular dynamics and migration have been studied in details in the later stages of *Drosophila* development. A characterization of mitochondrial morphology and metabolism in these stages may help to find and highlight commonalities between interactions of mitochondria and Myosin II.

8.5.4 Regulation of ERK

Mitochondria interact with EGFR pathway in *Drosophila* oogenesis. Downregulation of *drp1* leads to activation of the pathway leading to increase accumulation of downstream component activated phosphorylated Erk (dp-Erk) in the *Drosophila* follicle cells (Mitra et al., 2012; Tomer et al., 2018). In the early *Drosophila* embryos, receptor tyrosine kinase, Torso regulates MAPK signalling (Gabay et al., 1997; Li, 2005). During gastrulation, EGFR controlled MAPK signalling flanks the ventral mesoderm (Gabay et al., 1997; Lim et al., 2013, 2015). Regulation of this signalling can be probed in the *drp1* mutant embryos in order to address impact on the gastrulation in more details.

8.5.5 Role of Golgi Complex and ER during embryogenesis.

Mitochondria act in very close proximity with ER and Golgi complexes. Mitochondrial fission occurs at mitochondria-ER contact sites (Friedman et al., 2011; Korobova et al., 2013). Interaction of mitochondria and ER is necessary to maintain cellular calcium homeostasis (Krols et al., 2016) and lipid exchange (Voss et al., 2012). ER, Golgi Complex are mitochondria are maternally inherited together in the form of a structure called fusome

(Cox and Spradling, 2003). Like mitochondria, Golgi complexes localize basally (Chowdhary et al., 2017) and are apically transported during cellularization (Papoulas et al., 2005). Differences in Golgi Complex morphology and distribution has been observed in Zebrafish gastrulation (Sepich and Solnica-Krezel, 2016). Smooth ER is proposed to regulate calcium signalling at blastopore lip of newt embryos (Komazaki, 1995). Detailed analysis of localization and role of these organelles remains to be explored in the field of embryogenesis.

In conclusion, we performed a detailed analysis of mitochondrial dynamics in *Drosophila* early embryogenesis. We initiated the use of *Drosophila* embryogenesis as a model system to examine mitochondrial functions with respect to maternal mutations. The thesis reveals and predicts the signalling pathways involved in mitochondrial regulation in embryos and we hope to uncover more mechanistic insights in the future.

9 Appendices

A1 Comparison of Mitochondria, ER and Golgi Complex localization in the syncytial *Drosophila* embryo

Golgi Complex and ER localize cortically in the syncytial *Drosophila* embryo (Frescas et al., 2006). Similar to mitochondria, these organelles are documented to be compartmentalized in the syncytial *Drosophila* embryo. The proteins associated with ER do not diffuse across syncytial cells. Golgi Complex secretions are also restricted to one nuclear-cytoplasmic domain (Frescas et al., 2006). Mitochondria are small structures in the *Drosophila* embryo (Fig. 3.4). But unlike ER and Golgi, their localization is far more restricted even within an individual syncytial cell (Fig 3.5).

We compared the localization of mitochondria with ER and Golgi complex in the syncytial embryo. We visualized ER using RFP containing ER localization sequence: KDEL (KDEL-RFP) expressed using *nanos*-Gal4 with Mito-GFP. Similar to earlier report (Frescas et al., 2006), we observed a meshwork of ER tubules present around nuclei. Mitochondria are present within this meshwork of ER tubules (Fig. A1.1 A). Mitochondrial fragmentation takes place at ER-mitochondria contact sites (Friedman, 2011). These contact sites are also essential for lipid exchange and calcium signalling (Krols et al., 2016; Voss et al., 2012). Since mitochondria are small in the *Drosophila* embryo, their association with ER might be important in maintaining their shape.

Next, we visualized Golgi Complex using fluorescently tagged galactosyl transferase (GalT-RFP) with Mito-GFP expressed using *nanos*-Gal4. The mitochondria and Golgi Complexes both appeared as distinct punctae and uniformly surround the nuclei (Fig A1.1 B). Similar to mitochondria (Fig. 3.4), Golgi complexes were abundant towards the basal regions in the syncytial cells, but their density was much less compared to the mitochondria (Fig A1.1 B). Like mitochondria (Fig. 5.2), Golgi Complexes are transported apically during cellularization (Papoulas et al., 2005). Therefore it is likely that the apico-basal distribution and transport of these two organelles is regulated in similar manner.

The functional relevance of mitochondrial association with these organelles, ER and Golgi Complex, is yet to be studied in the embryogenesis.

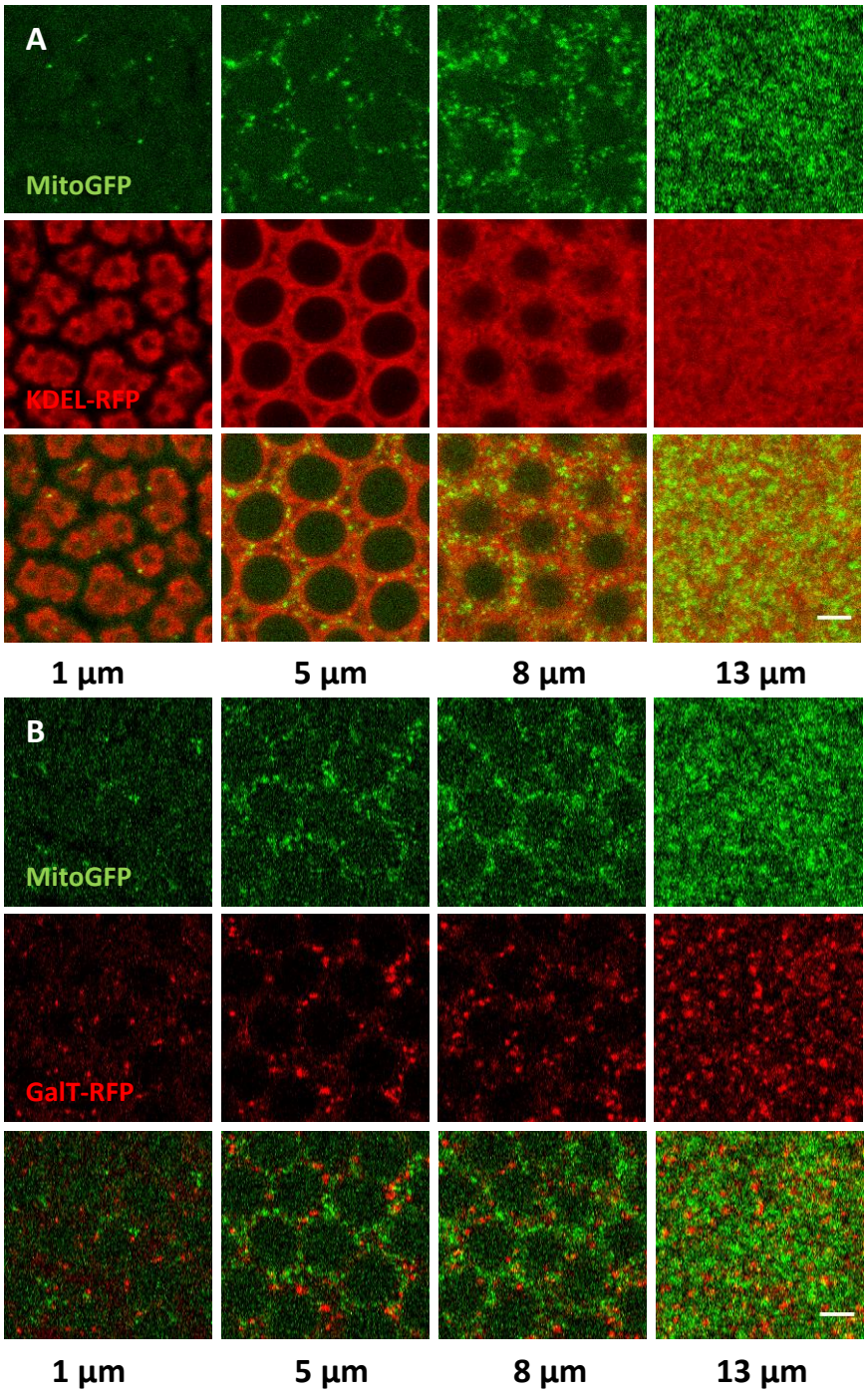

Figure A1.1 Comparison of mitochondria with ER and Golgi Complex distribution. Apical to basal slices show mitochondria (Mito-GFP, green) localized in the ER tubule meshwork (KDEL-RFP, red) (**A**). Distribution of Mitochondria (Mito-GFP, green) and Golgi complexes (GalT-RFP, red) in syncytial cells show their basal abundance (**B**). Adapted from (Chowdhary et al., 2017).

A2 Interaction of mitochondria with ERK signalling in *Drosophila* embryogenesis

Extracellular signal regulated kinases (ERKs) or MAP kinases, or *Drosophila* homolog *rolled* function downstream of Ras signalling. In *Drosophila* embryos, *rolled* signalling operates downstream of Torso pathway at the anterior and posterior ends and is required for terminal structure development (Brunner 1994). During gastrulation, low concentration of Dorsal activates epidermal growth factor receptor (EGFR) pathway via *rhomboid* in the presumptive neuroectoderm region. EGFR pathway functions through activated or phosphorylated Erk (dpErk) in this region (Gabay et al., 1997; Helman et al., 2012; Lim et al., 2013). Erk can activate Drp1 by phosphorylation (Kashatus 2015 ref). EGFR pathway in posterior follicle cells of *Drosophila* ovaries regulated mitochondrial fission and thereby downstream Notch activity (Mitra et al., 2012; Tomer et al., 2018). The study also reports upregulation of EGFR downstream targets, such as dpErk upon *drp1* knockdown in the follicle cells (Tomer et al., 2018). We immunostained $drp1^{SG}$ embryos using dpErk antibody (Chapter 2, 2.3). We observed the reported pattern of dpErk staining at the neuroectoderm regions, flanking the ventral furrow (Fig. A2.1 A). We plotted normalized intensity of dpERK staining across the ventral furrow and observed almost an average of 5 fold increase in the dpERK staining in $drp1^{SG}$ embryos compared to WT (Fig. A2.1 B).

We have observed ventral furrow defects in the $drp1^{SG}$ embryos that are likely due to downregulation of activity of downstream targets of Toll-Dorsal pathway (Chapter 7). dpERK induces the expression of *wnt inhibitor of Dorsal* (*wntD*) in the region between *EGFR* and *dorsal* expression zone. *wntD* restricts the spread of Dorsal signalling and also downregulated Dorsal targets (Helman et al., 2012). We wonder whether ventral furrow defects in the $drp1^{SG}$ embryos are due to additional impact of dpERK upregulation. The interaction of *drp1* with EGFR pathway in the embryos would be a fascinating project to follow in the future.

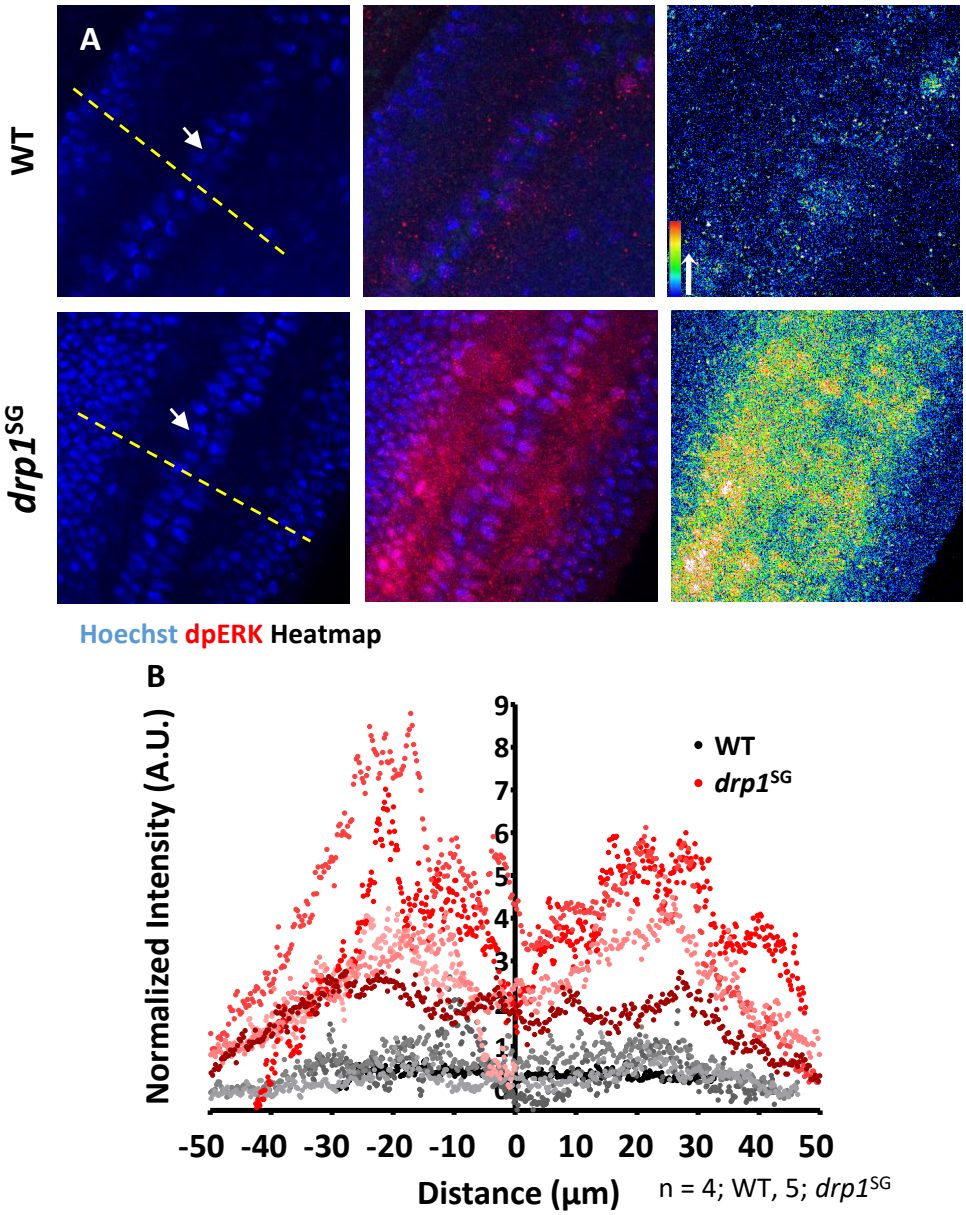

Figure A2.1: Levels of dpERK signal are elevated in *drp1*^{SG} embryos. dpERK (red, heatmap) signal is present in the region flanking the ventral furrow (white arrows) marked by invaginated nuclei (Hoechst, blue) (**A**). The intensity of dpERK (red, heatmap) is increased in *drp1*^{SG} (A, Bottom panel) compared to WT embryos (A, Top panel). Normalized intensity profiles plotted across a line (orientation shown with yellow dashed line) drawn perpendicular to the ventral furrow and covering entire imaging field show bimodal distribution in WT (shades of grey) and *drp1*^{SG} embryo (shades of red) (**B**). Approximately average 5 fold increase is observed in *drp1*^{SG} embryo (shades of red) (**B**). n = 4, 5 embryos for WT and *drp1*^{SG} respectively (**B**) Rainbow scale represents pseudocolour intensities

10 Bibliography

1. Abdelwahid, E., Yokokura, T., Krieser, R.J., Balasundaram, S., Fowle, W.H., and White, K. (2007). Mitochondrial Disruption in *Drosophila* Apoptosis. Dev. Cell *12*, 793–806.
2. Abreu-Blanco, M.T., Verboon, J.M., and Parkhurst, S.M. (2014). Coordination of Rho family GTPase activities to orchestrate cytoskeleton responses during cell wound repair. Curr. Biol. *24*, 144–155.
3. Acton, B.M., Jurisicova, A., Jurisica, I., and Casper, R.F. (2004). Alterations in mitochondrial membrane potential during preimplantation stages of mouse and human embryo development. *10*, 23–32.
4. Afshar, K., Stuart, B., and Wasserman, S.A. (2000). Functional analysis of the *Drosophila* diaphanous FH protein in early embryonic development. Development *127*, 1887–1897.
5. Akiyama, T., and Okada, M. (1992a). Spatial and developmental changes in the respiratory activity of mitochondria in early *Drosophila* embryos. Development *115*, 1175–1182.
6. Akiyama, T., and Okada, M. (1992b). Spatial and developmental changes in the respiratory activity of mitochondria in early *Drosophila* embryos. Development *115*, 1175–1182.
7. Akiyama, T., and Okada, M. (1992c). Spatial and developmental changes in the respiratory activity of mitochondria in early *Drosophila* embryos. Development *1182*, 1175–1182.
8. Amikura, R., Hanyu, K., Kashikawa, M., and Kobayashi, S. (2001a). Tudor protein is essential for the localization of mitochondrial RNAs in polar granules of *Drosophila* embryos. Mech. Dev. *107*, 97–104.
9. Amikura, R., Kashikawa, M., Nakamura, A., and Kobayashi, S. (2001b). Presence of mitochondria-type ribosomes outside mitochondria in germ plasm of *Drosophila* embryos. Proc. Natl. Acad. Sci. *98*, 9133–9138.
10. Amiri, M., and Hollenbeck, P.J. (2008). Mitochondrial biogenesis in the axons of vertebrate peripheral neurons. Dev. Neurobiol. *68*, 1348–1361.
11. Arora, G.K., Tran, S.L., Rizzo, N., Jain, A., and Welte, M.A. (2016). Temporal control of bidirectional lipid-droplet motion in *Drosophila* depends on the ratio of kinesin-1 and

its co-factor Halo. J. Cell Sci. *129*, 1416–1428.

12. Baixauli, F., Martín-Cófreces, N.B., Morlino, G., Carrasco, Y.R., Calabia-Linares, C., Veiga, E., Serrador, J.M., and Sánchez-Madrid, F. (2011). The mitochondrial fission factor dynamin-related protein 1 modulates T-cell receptor signalling at the immune synapse. EMBO J. *30*, 1238–1250.
13. Baqri, R.M., Turner, B.A., Rheuben, M.B., Hammond, B.D., Kaguni, L.S., and Miller, K.E. (2009). Disruption of mitochondrial DNA replication in *Drosophila* increases mitochondrial fast axonal transport in vivo. PLoS One *4*, e7874–e7874.
14. Barmchi, M.P., Rogers, S., and Häcker, U. (2005). DRhoGEF2 regulates actin organization and contractility in the *Drosophila* blastoderm embryo. J. Cell Biol. *168*, 575–585.
15. Barrett, K., Leptin, M., and Settleman, J. (1997). The Rho GTPase and a putative RhoGEF mediate a signaling pathway for the cell shape changes in *Drosophila* gastrulation. Cell *91*, 905–915.
16. Bavister, B.D., and Squirrell, J.M. (2000). Mitochondrial distribution and function in oocytes and early embryos. Hum. Reprod. *15 Suppl 2*, 189–198.
17. Bell, E.L., Klimova, T.A., Eisenbart, J., Moraes, C.T., Murphy, M.P., Budinger, G.R.S., and Chandel, N.S. (2007). The Qo site of the mitochondrial complex III is required for the transduction of hypoxic signaling via reactive oxygen species production. J. Cell Biol. *177*, 1029–1036.
18. Bereiter-Hahn, J., and Vöth, M. (1994). Dynamics of mitochondria in living cells: shape changes, dislocations, fusion, and fission of mitochondria. Microsc. Res. Tech. *27*, 198–219.
19. Birket, M.J., Orr, A.L., Gerencser, A.A., Madden, D.T., Vitelli, C., Swistowski, A., Brand, M.D., and Zeng, X. (2011). A reduction in ATP demand and mitochondrial activity with neural differentiation of human embryonic stem cells. J. Cell Sci. *124*, 348–358.
20. Blerkom, J. Van, and Davis, P. (2007). Mitochondrial signaling and fertilization. *13*, 759–770.
21. Van Blerkom, J. (2004). Mitochondria in human oogenesis and preimplantation embryogenesis: engines of metabolism, ionic regulation and developmental competence. Reproduction *128*, 269–280.
22. Van Blerkom, J. (2011). Mitochondrial function in the human oocyte and embryo and

their role in developmental competence. Mitochondrion *11*, 797–813.

23. Van Blerkom, J., Davis, P.W., and Lee, J. (1995). ATP content of human oocytes and developmental potential and outcome after in-vitro fertilization and embryo transfer. *10*, 415–424.
24. Van Blerkom, J., Davis, P., and Alexander, S. (2000). Differential mitochondrial distribution in human pronuclear embryos leads to disproportionate inheritance between blastomeres: Relationship to microtubular organization, ATP content and competence. Hum. Reprod. *15*, 2621–2633.
25. Van Blerkom, J., Davis, P., Mathwig, V., and Alexander, S. (2002). Domains of high-polarized and low-polarized mitochondria may occur in mouse and human oocytes and early embryos. Hum. Reprod. *17*, 393–406.
26. Van Blerkom, J., Davis, P., and Alexander, S. (2003). Inner mitochondrial membrane potential (¥m), cytoplasmic ATP content and free Ca2+ levels in metaphase II mouse oocytes. Hum. Reprod. *18*, 2429–2440.
27. van der Bliek, A., Shen, Q., and Kawajiri, S. (2013). Mechanisms of mitochondrial fission and fusion. Cold Spring Harb Perspect Biol *5*, 1–16.
28. Boerner, J.L., Demory, M.L., Silva, C., and Parsons, S.J. (2004). Phosphorylation of Y845 on the epidermal growth factor receptor mediates binding to the mitochondrial protein cytochrome c oxidase subunit II. Mol. Cell. Biol. *24*, 7059–7071.
29. Bohovych, I., and Khalimonchuk, O. (2016). Sending Out an SOS: Mitochondria as a Signaling Hub. Front. Cell Dev. Biol. *4*, 109.
30. Boland, M., Chourasia, A., and Macleod, K. (2013). Mitochondrial Dysfunction in Cancer. Front. Oncol. *3*, 292.
31. Brandes, N., Schmitt, S., and Jakob, U. (2009). Thiol-based redox switches in eukaryotic proteins. Antioxid. Redox Signal. *11*, 997–1014.
32. Braschi, E., Zunino, R., and McBride, H.M. (2009). MAPL is a new mitochondrial SUMO E3 ligase that regulates mitochondrial fission. EMBO Rep. *10*, 748–754.
33. Breton, S., Milani, L., Ghiselli, F., Guerra, D., Stewart, D.T., and Passamonti, M. (2014). A resourceful genome: updating the functional repertoire and evolutionary role of animal mitochondrial DNAs. Trends Genet. *30*, 555–564.
34. Burman, J.L., Pickles, S., Wang, C., Sekine, S., Vargas, J.N.S., Zhang, Z., Youle, A.M., Nezich, C.L., Wu, X., Hammer, J.A., et al. (2017). Mitochondrial fission facilitates the

selective mitophagy of protein aggregates. J. Cell Biol. *216*, 3231–3247.

35. Cai, Q., and Sheng, Z. (2009). Moving or Stopping Mitochondria : Miro as a Traffic Cop by Sensing Calcium. Neuron *61*, 493–496.
36. Caino, M.C., and Altieri, D.C. (2015). Cancer cells exploit adaptive mitochondrial dynamics to increase tumor cell invasion. Cell Cycle *14*, 3242–3247.
37. Callen, J.C., Dennebouy, N., and Mounolou, J.C. (1980). Development of the mitochondrial mass and accumlation of mtDNA in previtellogenic stages of *Xenopus* laevis oocytes. J. Cell Sci. *320*, 307–320.
38. Campbell, K., and Swann, K. (2006). Ca2+ oscillations stimulate an ATP increase during fertilization of mouse eggs. Dev. Biol. *298*, 225–233.
39. Cereghetti, G.M., Stangherlin, A., Brito, O.M. De, Chang, C.R., Blackstone, C., and Bernardi, P. (2008). Dephosphorylation by calcineurin regulates translocation of Drp1 to mitochondria. *105*, 15803–15808.
40. Chan, D.C. (2006). Mitochondrial fusion and fission in mammals. Annu. Rev. Cell Dev. Biol. *22*, 79–99.
41. Chandel, N.S. (2014). Mitochondria as signaling organelles. BMC Biol. *12*, 34.
42. Chandel, N.S., Maltepe, E., Goldwasser, E., Mathieu, C.E., Simon, M.C., and Schumacker, P.T. (1998). Mitochondrial reactive oxygen species trigger hypoxia-induced transcription. Proc. Natl. Acad. Sci. U. S. A. *95*, 11715–11720.
43. Chandel, N.S., Schumacker, P.T., and Arch, R.H. (2001). Reactive Oxygen Species Are Downstream Products of TRAF-mediated Signal Transduction. J. Biol. Chem. *276*, 42728–42736.
44. Chanet, S., Sharan, R., Khan, Z., and Martin, A.C. (2017). Myosin 2-Induced Mitotic Rounding Enables Columnar Epithelial Cells to Interpret Cortical Spindle Positioning Cues. Curr. Biol. *27*, 3350–3358.e3.
45. Chang, C.-R., and Blackstone, C. (2007). Cyclic AMP-dependent Protein Kinase Phosphorylation of Drp1 Regulates Its GTPase Activity and Mitochondrial Morphology. J. Biol. Chem. *282*, 21583–21587.
46. Chang, W.-L., Chang, Y.-C., Lin, K.-T., Li, H.-R., Pai, C.-Y., Chen, J.-H., and Su, Y.-H. (2017). Asymmetric distribution of hypoxia-inducible factor α regulates dorsoventral axis establishment in the early sea urchin embryo. Development *144*, 2940 LP-2950.
47. Chaudhari, S.N., and Kipreos, E.T. (2017). Increased mitochondrial fusion allows the

survival of older animals in diverse C. elegans longevity pathways. Nat. Commun. *8*, 182.

48. Che, T.-F., Lin, C.-W., Wu, Y.-Y., Chen, Y.-J., Han, C.-L., Chang, Y., Wu, C.-T., Hsiao, T.-H., Hong, T.-M., and Yang, P.-C. (2015). Mitochondrial translocation of EGFR regulates mitochondria dynamics and promotes metastasis in NSCLC. Oncotarget *6*, 37349–37366.
49. Chen, H., and Chan, D.C. (2005). Emerging functions of mammalian mitochondrial fusion and fission. Hum. Mol. Genet. *14*, 283–289.
50. Chen, H., and Chan, D.C. (2009). Mitochondrial dynamics-fusion, fission, movement, and mitophagy-in neurodegenerative diseases. Hum. Mol. Genet. *18*, 169–176.
51. Chen, S., and Dickman, M.B. (2004). Bcl-2 family members localize to tobacco chloroplasts and inhibit programmed cell death induced by chloroplast-targeted herbicides. J. Exp. Bot. *55*, 2617–2623.
52. Chen, C.T., Hsu, S.H., and Wei, Y.H. (2012). Mitochondrial bioenergetic function and metabolic plasticity in stem cell differentiation and cellular reprogramming. Biochim. Biophys. Acta - Gen. Subj. *1820*, 571–576.
53. Chen, H., Detmer, S.A., Ewald, A.J., Griffin, E.E., Fraser, S.E., and Chan, D.C. (2000). Mitofusins Mfn1 and Mfn2 coordially regualte mitochondria fusion and are essential for embryohnic development. J. Cell Biol. *160*, 189–200.
54. Chen, H., Detmer, S.A., Ewald, A.J., Griffin, E.E., Fraser, S.E., and Chan, D.C. (2003). Mitofusins Mfn1 and Mfn2 coordinately regulate mitochondrial fusion and are essential for embryonic development. J. Cell Biol. *160*, 189–200.
55. Chen, H., Vermulst, M., Wang, Y.E., Chomyn, A., Prolla, T.A., Mccaffery, M., and Chan, D.C. (2010). Mitochondrial fusion is required for mtDNA stability in skeletal muscles and tolerance of mtDNA mutations. Cell *141*, 280–289.
56. Chen, Y., McMillan-Ward, E., Kong, J., Israels, S.J., and Gibson, S.B. (2007). Mitochondrial electron-transport-chain inhibitors of complexes I and II induce autophagic cell death mediated by reactive oxygen species. J. Cell Sci. *120*, 4155–4166.
57. Chhabra, E.S., and Higgs, H.N. (2006). INF2 Is a WASP Homology 2 Motif-containing Formin That Severs Actin Filaments and Accelerates Both Polymerization and Depolymerization. J. Biol. Chem. *281*, 26754–26767.
58. Chiong, M., Cartes-Saavedra, B., Norambuena-Soto, I., Mondaca-Ruff, D., Morales,

P.E., García-Miguel, M., and Mellado, R. (2014). Mitochondrial metabolism and the control of vascular smooth muscle cell proliferation. Front. Cell Dev. Biol. *2*, 72.

59. Cho, S.-G., Du, Q., Huang, S., and Dong, Z. (2010). Drp1 dephosphorylation in ATP depletion-induced mitochondrial injury and tubular cell apoptosis. Am. J. Physiol. Renal Physiol. *299*, F199–F206.
60. Chowdhary, S., Tomer, D., Dubal, D., Sambre, D., and Rikhy, R. (2017). Analysis of mitochondrial organization and function in the *Drosophila* blastoderm embryo. Sci. Rep. *7*, 5502.
61. Coffman, J.A. (2009). Mitochondria and metazoan epigenesis. Semin. Cell Dev. Biol. *20*, 321–329.
62. Coffman, J.A., McCarthy, J.J., Dickey-Sims, C., and Robertson, A.J. (2004). Oral-aboral axis specification in the sea urchin embryo: II. Mitochondrial distribution and redox state contribute to establishing polarity in Strongylocentrotus purpuratus. Dev. Biol. *273*, 160–171.
63. Coffman, J.A., Wessels, A., DeSchiffart, C., and Rydlizky, K. (2014). Oral-aboral axis specification in the sea urchin embryo, IV: Hypoxia radializes embryos by preventing the initial spatialization of nodal activity. Dev. Biol. *386*, 302–307.
64. Cogliati, S., Frezza, C., Soriano, M.E., Varanita, T., Quintana-cabrera, R., Corrado, M., Cipolat, S., Costa, V., Casarin, A., Gomes, L.C., et al. (2013). Mitochondrial Cristae Shape Determines Respiratory Chain Supercomplexes Assembly and Respiratory Efficiency. Cell *155*, 160–171.
65. Cook, M., Bolkan, B.J., and Kretzschmar, D. (2014). Increased actin polymerization and stabilization interferes with neuronal function and survival in the AMPK?? mutant loechrig. PLoS One *9*.
66. Copeland, J.M., Cho, J., Lo, T., Hur, J.H., Bahadorani, S., Arabyan, T., Rabie, J., Soh, J., and Walker, D.W. (2009). Extension of *Drosophila* life span by RNAi of the mitochondrial respiratory chain. Curr. Biol. *19*, 1591–1598.
67. Costa, V., Giacomello, M., Hudec, R., Lopreiato, R., Ermak, G., Lim, D., Malorni, W., Davies, K.J.A., Carafoli, E., and Scorrano, L. (2010). Mitochondrial fission and cristae disruption increase the response of cell models of Huntington's disease to apoptotic stimuli. EMBO Mol. Med. *2*, 490 LP-503.
68. Cotterill, M., Harris, S.E., Collado Fernandez, E., Lu, J., Huntriss, J.D., Campbell, B.K.,

and Picton, H.M. (2013). The activity and copy number of mitochondrial DNA in ovine oocytes throughout oogenesis in vivo and during oocyte maturation in vitro. Mol. Hum. Reprod. *19*, 444–450.

69. Cox, R.T., and Spradling, A.C. (2003). A Balbiani body and the fusome mediate mitochondrial inheritance during *Drosophila* oogenesis. Development *130*, 1579–1590.
70. Cox, R.T., and Spradling, A.C. (2006). Milton controls the early acquisition of mitochondria by *Drosophila* oocytes. Development *133*, 3371–3377.
71. Cox, R.T., Kirkpatrick, C., and Peifer, M. (1996). Armadillo is required for adherens junction assembly, cell polarity, and morphogenesis during *Drosophila* embryogenesis. J. Cell Biol. *134*, 133–148.
72. Cribbs, J.T., and Strack, S. (2007). Reversible phosphorylation of Drp1 by cyclic AMP-dependent protein kinase and calcineurin regulates mitochondrial fission and cell death. EMBO Rep. *8*, 939–944.
73. Csordás, G., Renken, C., Várnai, P., Walter, L., Weaver, D., Buttle, K.F., Balla, T., Mannella, C.A., and Hajnóczky, G. (2006). Structural and functional features and significance of the physical linkage between ER and mitochondria. J. Cell Biol. *174*, 915–921.
74. Csordás, G., Várnai, P., Golenár, T., Roy, S., Purkins, G., Schneider, T.G., Balla, T., and Hajnóczky, G. (2010). Imaging interorganelle contacts and local calcium dynamics at the ER-mitochondrial interface. Mol. Cell *39*, 121–132.
75. Cunniff, B., McKenzie, A.J., Heintz, N.H., Howe, A.K., and Heldin, C.-H. (2016). AMPK activity regulates trafficking of mitochondria to the leading edge during cell migration and matrix invasion. Mol. Biol. Cell *27*, 2662–2674.
76. Dalton, C.M., Szabadkai, G., and Carroll, J. (2013). Dynamic Measurement of ATP in single oocytes: Impact of maturation and cumulus cells on levels and consumption. J. Cell. Physiol. *229*, 353–361.
77. Dawes-Hoang, R.E. (2005). Folded Gastrulation, Cell Shape Change and the Control of Myosin Localization. Development *132*, 4165–4178.
78. Debattisti, V., Gerencser, A.A., Saotome, M., Das, S., and Hajnóczky, G. (2017). ROS Control Mitochondrial Motility through p38 and the Motor Adaptor Miro/Trak. Cell Rep. *21*, 1667–1680.

79. Delettre, C., Lenaers, G., Griffoin, J.M., Gigarel, N., Lorenzo, C., Belenguer, P., Pelloquin, L., Grosgeorge, J., Turc-Carel, C., Perret, E., et al. (2000). Nuclear gene OPA1, encoding a mitochondrial dynamin-related protein, is mutated in dominant optic atrophy. Nat. Genet. *26*, 207–210.

80. Demory, M.L., Boerner, J.L., Davidson, R., Faust, W., Miyake, T., Lee, I., Hüttemann, M., Douglas, R., Haddad, G., and Parsons, S.J. (2009). Epidermal growth factor receptor translocation to the mitochondria: regulation and effect. J. Biol. Chem. *284*, 36592–36604.

81. Desai, S.P., Bhatia, S.N., Toner, M., and Irimia, D. (2013). Mitochondrial localization and the persistent migration of epithelial cancer cells. Biophys. J. *104*, 2077–2088.

82. Dewson, G., and Kluck, R.M. (2009). Mechanisms by which Bak and Bax permeabilise mitochondria during apoptosis. J. Cell Sci. *122*, 2801–2808.

83. DiGregorio, P.J., Ubersax, J.A., and O'Farrell, P.H. (2001). Hypoxia and nitric oxide induce a rapid, reversible cell cycle arrest of the *Drosophila* syncytial divisions. J. Biol. Chem. *276*, 1930–1937.

84. Dorn, G.W., Clark, C.F., Eschenbacher, W.H., Kang, M.-Y., Engelhard, J.T., Warner, S.J., Matkovich, S.J., and Jowdy, C.C. (2011). MARF and Opa1 Control Mitochondrial and Cardiac Function in *Drosophila*. Circ. Res. *108*, 12–17.

85. Dröge, W. (2002). Free Radicals in the Physiological Control of Cell Function. Physiol. Rev. *82*, 47–95.

86. Dumollard, R., Hammar, K., Porterfield, M., Smith, P.J., Cibert, C., Rouvière, C., and Sardet, C. (2003). Mitochondrial respiration and Ca2+ waves are linked during fertilization and meiosis completion. Development *130*, 683–692.

87. Dumollard, R., Marangos, P., Fitzharris, G., Swann, K., Duchen, M., and Carroll, J. (2004). Sperm-triggered [Ca 2 +] oscillations and Ca 2 + homeostasis in the mouse egg have an absolute requirement for mitochondrial ATP production. 3057–3067.

88. Dumollard, R., Duchen, M., and Sardet, C. (2006). Calcium signals and mitochondria at fertilisation. Semin. Cell Dev. Biol. *17*, 314–323.

89. Dumollard, R., Duchen, M., and Carroll, J. (2007). The Role of Mitochondrial Function in the Oocyte and Embryo. Curr. Top. Dev. Biol. *77*, 21–49.

90. Edgar, B.A., O'Dell, G.M., and Schubiger, G. (1987). Cytoarchitecture and the patterning of fushi-tarazu expression in the *Drosophila* blastoderm. Genes Dev. *1*,

1226–1237.

91. Egner, A., Jakobs, S., and Hell, S.W. (2002). Fast 100-nm resolution three-dimensional microscope reveals structural plasticity of mitochondria in live yeast. Proc. Natl. Acad. Sci. *99*, 3370 LP-3375.
92. Ernster, L., and Schatz, G. (1981). Mitochondria: a historical review. J. Cell Biol. *91*, 227s–255s.
93. Estaquier, J., and Arnoult, D. (2007). Inhibiting Drp1-mediated mitochondrial fission selectively prevents the release of cytochrome c during apoptosis. Cell Death Differ. *14*, 1086–1094.
94. Fan, W., Waymire, K.G., Narula, N., Li, P., Rocher, C., Coskun, P.E., Vannan, M.A., Narula, J., Macgregor, G.R., and Wallace, D.C. (2008). A mouse model of mitochondrial disease reveals germline selection against severe mtDNA mutations. Science (80-.). *319*, 958–962.
95. Fedorova, M., Kuleva, N., and Hoffmann, R. (2009). Reversible and irreversible modifications of skeletal muscle proteins in a rat model of acute oxidative stress. Biochim. Biophys. Acta - Mol. Basis Dis. *1792*, 1185–1193.
96. Feng, J., Bussière, F., and Hekimi, S. (2001). Mitochondrial Electron Transport Is a Key Determinant of Life Span in Caenorhabditis elegans. Dev. Cell *1*, 633–644.
97. Fiaschi, T., Cozzi, G., and Chiarugi, P. (2012). Redox Regulation of Nonmuscle Myosin Heavy Chain during Integrin Engagement. J. Signal Transduct. *2012*, 1–9.
98. Field, C.M. (2005). Characterization of anillin mutants reveals essential roles in septin localization and plasma membrane integrity. Development *132*, 2849–2860.
99. Figard, L., Xu, H., Garcia, H., Golding, I., and Sokac, A. (2013). The plasma membrane flattens out to fuel cell-surface growth during *Drosophila* cellularization. Dev. Cell *27*, 648–655.
100. Figard, L., Wang, M., Zheng, L., Golding, I., and Sokac, A.M. (2016). Membrane Supply and Demand Regulates F-Actin in a Cell Surface Reservoir. Dev. Cell *37*, 267–278.
101. Fischer, M.G., Heeger, S., Häcker, U., and Lehner, C.F. (2004). The Mitotic Arrest in Response to Hypoxia and of Polar Bodies during Early Embryogenesis Requires *Drosophila* Mps1. Curr. Biol. *14*, 2019–2024.
102. Foe, V.E., and Alberts, B.M. (1983). Studies of nuclear and cytoplasmic behaviour during the five mitotic cycles that precede gastrulation in *Drosophila* embryogenesis. J.

Cell Sci. *61*, 31–70.

103. Foe, V.E., Field, C.M., Odell, G.M., Adams, R.R., Tavares, A.A., Salzberg, A., Bellen, H.J., Glover, D.M., Afshar, K., Gish, B., et al. (2000). Microtubules and mitotic cycle phase modulate spatiotemporal distributions of F-actin and myosin II in *Drosophila* syncytial blastoderm embryos. Development *127*, 1767–1787.
104. Frank, S., Gaume, B., Bergmann-Leitner, E.S., Leitner, W.W., Robert, E.G., Catez, F., Smith, C.L., and Youle, R.J. (2001). The Role of Dynamin-Related Protein 1, a Mediator of Mitochondrial Fission, in Apoptosis. Dev. Cell *1*, 515–525.
105. Fransson, Å., Ruusala, A., and Aspenström, P. (2003). Atypical Rho GTPases have roles in mitochondrial homeostasis and apoptosis. J. Biol. Chem. *278*, 6495–6502.
106. Fransson, Å., Ruusala, A., and Aspenström, P. (2006a). The atypical Rho GTPases Miro-1 and Miro-2 have essential roles in mitochondrial trafficking. Biochem. Biophys. Res. Commun. *344*, 500–510.
107. Fransson, S., Ruusala, A., and Aspenström, P. (2006b). The atypical Rho GTPases Miro-1 and Miro-2 have essential roles in mitochondrial trafficking. Biochem. Biophys. Res. Community *344*, 500–510.
108. Frescas, D., Mavrakis, M., Lorenz, H., DeLotto, R., and Lippincott-Schwartz, J. (2006). The secretory membrane system in the *Drosophila* syncytial blastoderm embryo exists as functionally compartmentalized units around individual nuclei. J. Cell Biol. *173*, 219–230.
109. Friedman, J.R. (2011). ER Tubules Mark Sites of Mitochondrial Division. *358*.
110. Friedman, J.R., Lackner, L.L., West, M., DiBenedetto, J.R., Nunnari, J., and Voeltz, G.K. (2011). ER tubules mark sites of mitochondrial division. Science (80-.). *334*, 358–362.
111. Fuse, N., Yu, F., and Hirose, S. (2013a). Gprk2 adjusts Fog signaling to organize cell movements in *Drosophila* gastrulation. Development *140*, 4246–4255.
112. Fuse, N., Yu, F., and Hirose, S. (2013b). Gprk2 adjusts Fog signaling to organize cell movements in *Drosophila* gastrulation. Development *140*, 4246–4255.
113. Gabay, L., Seger, R., and Shilo, B.-Z. (1997). MAP kinase in situ activaiton atlas during *Drosophila* embryogenesis. Development *124*, 3535–3541.
114. Gielisch, I., and Meierhofer, D. (2015). Metabolome and proteome profiling of complex i deficiency induced by rotenone. J. Proteome Res. *14*, 224–235.
115. Giles, R.E., Blanc, H., Cann, H.M., and Wallace, D.C. (1980). Maternal inheritance of

human mitochondrial DNA. Proc. Natl. Acad. Sci. U. S. A. *77*, 6715–6719.

116. Glater, E.E., Megeath, L.J., Stowers, R.S., and Schwarz, T.L. (2006). Axonal transport of mitochondria requires milton to recruit kinesin heavy chain and is light chain independent. J. Cell Biol. *173*, 545–557.
117. Goff, D.J., Nilson, L.A., and Morisato, D. (2001). Establishment of dorsal-ventral polarity of the Goff, D. J., Nilson, L. A. and Morisato, D. (2001). Establishment of dorsal-ventral polarity of the *Drosophila* egg requires capicua action in ovarian follicle cells. Development *128*, 4553 LP-4562.
118. Gomez, O., Sanchez-Rodriguez, A., Le, M.Q.U., Sanchez-Caro, C., Molina-Holgado, F., and Molina-Holgado, E. (2011). Cannabinoid receptor agonists modulate oligodendrocyte differentiation by activating PI3K/Akt and the mammalian target of rapamycin (mTOR) pathways. Br. J. Pharmacol. *163*, 1520–1532.
119. Gong, L., Puri, M., Unlü, M., Young, M., Robertson, K., Viswanathan, S., Krishnaswamy, A., Dowd, S.R., and Minden, J.S. (2004). *Drosophila* ventral furrow morphogenesis: a proteomic analysis. Development *131*, 643–656.
120. Górska-Andrzejak, J., Stowers, R.S., Borycz, J., Kostyleva, R., Schwarz, T.L., and Meinertzhagen, I.A. (2003). Mitochondria are redistributed in *Drosophila* photoreceptors lacking Milton, a kinesin-associated protein. J. Comp. Neurol. *463*, 372–388.
121. Goto, Y., Hayashi, R., Kang, D., and Yoshida, K. (2006). Acute Loss of Transcription Factor E2F1 Induces Mitochondrial Biogenesis in HeLa Cells. J. Cell. Physiol. *934*, 923–934.
122. Greer, E.L., Oskoui, P.R., Banko, M.R., Maniar, J.M., Gygi, M.P., Gygi, S.P., and Brunet, A. (2007). The energy sensor AMP-activated protein kinase directly regulates the mammalian FOXO3 transcription factor. J. Biol. Chem. *282*, 30107–30119.
123. Griffin, E.E., Graumann, J., and Chan, D.C. (2005). The WD40 protein Caf4p is a component of the mitochondrial fission machinery and recruits Dnm1p to mitochondria. J. Cell Biol. *170*, 237–248.
124. Grimm, S. (2012). The ER – mitochondria interface : The social network of cell death ARCosome. BBA - Mol. Cell Res. *1823*, 327–334.
125. Grosshans, J. (2005). RhoGEF2 and the formin Dia control the formation of the furrow

canal by directed actin assembly during *Drosophila* cellularisation. Development *132*, 1009–1020.

126. Guo, X., Macleod, G.G.T., Wellington, A., Hu, F., Panchumarthi, S., Schoenfield, M., Marin, L., Charlton, M.M.P., Atwood, H.L.H., and Zinsmaier, K.K.E. (2005). The GTPase dMiro is required for axonal transport of mitochondria to *Drosophila* synapses. Neuron *47*, 379–393.
127. Gusarova, G.A., Trejo, H.E., Dada, L.A., Briva, A., Welch, L.C., Hamanaka, R.B., Mutlu, G.M., Chandel, N.S., Prakriya, M., and Sznajder, J.I. (2011). Hypoxia leads to Na,K-ATPase downregulation via Ca(2+) release-activated Ca(2+) channels and AMPK activation. Mol. Cell. Biol. *31*, 3546–3556.
128. Haghnia, M., Cavalli, V., Shah, S.B., Schimmelpfeng, K., Brusch, R., Yang, G., Herrera, C., Pilling, A., and Goldstein, L.S.B. (2007). Dynactin Is Required for Coordinated Bidirectional Motility, but Not for Dynein Membrane Attachment. Mol. Biol. Cell *18*, 2081–2089.
129. Hales, K.G., and Fuller, M.T. (1997). Developmentally regulated mitochondrial fusion mediated by a conserved, novel, predicted GTPase. Cell *90*, 121–129.
130. Han, Y.H., Kim, S.H., Kim, S.Z., and Park, W.H. (2008). Antimycin A as a mitochondrial electron transport inhibitor prevents the growth of human lung cancer A549 cells. Oncol. Rep. *20*, 689–693.
131. Harada, H., Becknell, B., Wilm, M., Mann, M., Huang, L.J., Taylor, S.S., Scott, J.D., and Korsmeyer, S.J. (1999). Phosphorylation and inactivation of BAD by mitochondria-anchored protein kinase A. Mol. Cell *3*, 413–422.
132. Hardie, D.G., Hawley, S.A., and Scott, J.W. (2006). AMP-activated protein kinase--development of the energy sensor concept. J. Physiol. *574*, 7–15.
133. Harrison, M.M., Li, X.-Y., Kaplan, T., Botchan, M.R., and Eisen, M.B. (2011). Zelda Binding in the Early Drosophila melanogaster Embryo Marks Regions Subsequently Activated at the Maternal-to-Zygotic Transition. PLOS Genet. *7*, e1002266.
134. Haruta, T., Warrior, R., Yonemura, S., and Oda, H. (2010). The proximal half of the *Drosophila* E-cadherin extracellular region is dispensable for many cadherin-dependent events but required for ventral furrow formation. Genes to Cells *15*, 193–208.
135. Hayashi, Y., Otsuka, K., Ebina, M., Igarashi, K., Takehara, A., Matsumoto, M., Kanai, A.,

Igarashi, K., Soga, T., and Matsui, Y. (2017). Distinct requirements for energy metabolism in mouse primordial germ cells and their reprogramming to embryonic germ cells. Proc. Natl. Acad. Sci. U. S. A. *114*, 8289–8294.

136. He, B., Martin, A., and Wieschaus, E. (2016). Flow-dependent myosin recruitment during *Drosophila* cellularization requires zygotic *dunk* activity. Development *143*, 2417–2430.
137. Helman, A., Lim, B., Andreu, M.J., Kim, Y., Shestkin, T., Lu, H., Jimenez, G., Shvartsman, S.Y., and Paroush, Z. (2012). RTK signaling modulates the Dorsal gradient. Development *139*, 3032–3039.
138. Hemavathy, K., Meng, X., and Ip, Y.T. (1997). Differential regulation of gastrulation and neuroectodermal gene expression by Snail in the *Drosophila* embryo. Development *124*, 3683–3691.
139. Hemavathy, K., Hu, X., Ashraf, S.I., Small, S.J., and Ip, Y.T. (2004). The repressor function of Snail is required for *Drosophila* gastrulation and is not replaceable by Escargot or Worniu. Dev. Biol. *269*, 411–420.
140. Hermann, G.J., Thatcher, J.W., Mills, J.P., Hales, K.G., Fuller, M.T., Nunnari, J., and Shaw, J.M. (1998). Mitochondrial Fusion in Yeast Requires the Transmembrane GTPase Fzo1p. *143*, 359–373.
141. Hertig, A.T. (2018). The primary human oocyte: Some observations on the fine structure of Balbiani's vitelline body and the origin of the annulate lamellae. Am. J. Anat. *122*, 107–137.
142. Hill, J.H., Chen, Z., and Xu, H. (2014). Selective propagation of functional mitochondrial DNA during oogenesis restricts the transmission of a deleterious mitochondrial variant. Nat. Genet. *46*, 389–392.
143. Hirusaki, K., Yokoyama, K., Cho, K., and Ohta, Y. (2017). Temporal depolarization of mitochondria during M phase. Sci. Rep. *7*, 3–10.
144. Hoffmann, H.-P., and Avers, C.J. (1973). Mitochondrion of Yeast: Ultrastructural Evidence for One Giant, Branched Organelle per Cell. Science (80-.). *181*, 749 LP-751.
145. Hollinshead, M., Sanderson, J., and Vaux, D.J. (1997). Anti-biotin antibodies offer superior organelle-specific labeling of mitochondria over avidin or streptavidin. J. Histochem. Cytochem. *45*, 1053–1057.
146. Hom, J., Yu, T., Yoon, Y., Porter, G., and Sheu, S.S. (2010). Regulation of mitochondrial

fission by intracellular Ca2+ in rat ventricular myocytes. Biochim. Biophys. Acta - Bioenerg. *1797*, 913–921.

147. Hom, J.R., Quintanilla, R.A., Hoffman, D.L., de Mesy Bentley, K.L., Molkentin, J.D., Sheu, S.-S., and Porter, G.A. (2011). The permeability transition pore controls cardiac mitochondrial maturation and myocyte differentiation. Dev. Cell *21*, 469–478.
148. Hu, C., Huang, Y., and Li, L. (2017). Drp1-dependent mitochondrial fission plays critical roles in physiological and pathological progresses in mammals. Int. J. Mol. Sci. *18*.
149. Hurd, T.R., Herrmann, B., Sauerwald, J., Sanny, J., Grosch, M., and Lehmann, R. (2016). Long Oskar Controls Mitochondrial Inheritance in *Drosophila* melanogaster. Dev. Cell *39*, 560–571.
150. Iida, T., and Kobayashi, S. (1998). Essential role of mitochondrially encoded large rRNA for germ-line formation in *Drosophila* embryos. Proc. Natl. Acad. Sci. U. S. A. *95*, 11274–11278.
151. Illmensee, K., Mahowald, A.P., and Loomis, M.R. (1976). The ontogeny of germ plasm during oogenesis in *Drosophila*. Dev. Biol. *49*, 40–65.
152. Ingerman, E., Perkins, E.M., Marino, M., Mears, J.A., McCaffery, J.M., Hinshaw, J.E., and Nunnari, J. (2005). Dnm1 forms spirals that are structurally tailored to fit mitochondria. J. Cell Biol. *170*, 1021–1027.
153. Ip, Y.T., Park, R.E., Kosman, D., Yazdanbakhsh, K., and Levine, M. (1992). \emph{dorsal-twist} interactions establish \emph{snail} expression in the presumptive mesoderm of the \emph{*Drosophila*} embryo. Genes Dev. *6*, 1518–1530.
154. Ip, Y.T., Maggert, K., and Levine, M. (1994). Uncoupling gastrulation and mesoderm differentiation in the *Drosophila* embryo. EMBO J. *13*, 5826–5834.
155. Ishihara, N., Jofuku, A., Eura, Y., and Mihara, K. (2003). Regulation of mitochondrial morphology by membrane potential, and DRP1-dependent division and FZO1-dependent fusion reaction in mammalian cells. Biochem. Biophys. Res. Commun. *301*, 891–898.
156. Ishihara, N., Nomura, M., Jofuku, A., Kato, H., Suzuki, S.O., Masuda, K., Otera, H., Nakanishi, Y., Nonaka, I., Goto, Y., et al. (2009). Mitochondrial fission factor Drp1 is essential for embryonic development and synapse formation in mice. Nat. Publ. Gr. *11*, 958–966.
157. Jackson, S.M., and Blochlinger, K. (1997). cut interacts with Notch and protein kinase A

to regulate egg chamber formation and to maintain germline cyst integrity during *Drosophila* oogenesis. Development *124*, 3663–3672.

158. Jakobs, S., Martini, N., Schauss, A.C., Egner, A., Westermann, B., and Hell, S.W. (2003). Spatial and temporal dynamics of budding yeast mitochondria lacking the division component Fis1p. J. Cell Sci. *116*, 2005 LP-2014.
159. Ji, A.-R., Ku, S.-Y., Cho, M.S., Kim, Y.Y., Kim, Y.J., Oh, S.K., Kim, S.H., Moon, S.Y., and Choi, Y.M. (2010). Reactive oxygen species enhance differentiation of human embryonic stem cells into mesendodermal lineage. Exp. Mol. Med. *42*, 175.
160. Jiang, J., Kosman, D., Ip, Y.T., and Levine, M. (1991). The dorsal morphogen gradient regulates the mesoderm determinant twist in early *Drosophila* embryos. Genes Dev. *5*, 1881–1891.
161. Jodoin, J.N., Coravos, J.S., Chanet, S., Vasquez, C.G., Tworoger, M., Kingston, E.R., Perkins, L.A., Perrimon, N., and Martin, A.C. (2015). Stable Force Balance between Epithelial Cells Arises from F-Actin Turnover. Dev. Cell *35*, 685–697.
162. St. John, J.C., Ramalho-Santos, J., Gray, H.L., Petrosko, P., Rawe, V.Y., Navara, C.S., Simerly, C.R., and Schatten, G.P. (2005). The Expression of Mitochondrial DNA Transcription Factors during Early Cardiomyocyte In Vitro Differentiation from Human Embryonic Stem Cells. Cloning Stem Cells *7*, 141–153.
163. Jones, B.A., and Fangman, W.L. (1992). Mitochondrial DNA maintenance in yeast requires a protein containing a region related to the GTP-binding domain of dynamin. Genes Dev. *6*, 380–389.
164. Kamata, H., Honda, S., Maeda, S., Chang, L., Hirata, H., and Karin, M. (2005). Reactive Oxygen Species Promote TNFα-Induced Death and Sustained JNK Activation by Inhibiting MAP Kinase Phosphatases. Cell *120*, 649–661.
165. Kamiński, M.M., Sauer, S.W., Kamiński, M., Opp, S., Ruppert, T., Grigaravičius, P., Grudnik, P., Gröne, H.-J., Krammer, P.H., and Gülow, K. (2012). T cell Activation Is Driven by an ADP-Dependent Glucokinase Linking Enhanced Glycolysis with Mitochondrial Reactive Oxygen Species Generation. Cell Rep. *2*, 1300–1315.
166. Kanfer, G., and Kornmann, B. (2016). Dynamics of the mitochondrial network during mitosis. Biochem. Soc. Trans. *44*, 510 LP-516.
167. Karbowski, M., Lee, Y.-J., Gaume, B., Jeong, S.-Y., Frank, S., Nechushtan, A., Santel, A., Fuller, M., Smith, C.L., and Youle, R.J. (2002). Spatial and temporal association of Bax

with mitochondrial fission sites, Drp1, and Mfn2 during apoptosis. J. Cell Biol. *159*, 931–938.

168. Karbowski, M., Jeong, S.Y., and Youle, R.J. (2004). Endophilin B1 is required for the maintenance of mitochondrial morphology. J. Cell Biol. *166*, 1027–1039.
169. Karbowski, M., Neutzner, A., and Youle, R.J. (2007). The mitochondrial E3 ubiquitin ligase MARCH5 is required for Drp1 dependent mitochondrial division. J. Cell Biol. *178*, 71–84.
170. Karr, T.L., and Alberts, B.M. (1986a). Organization of the cytoskeleton in early {{\em {D}rosophila}} embryos. J. Cell Biol. *102*, 1494–1509.
171. Karr, T.L., and Alberts, B.M. (1986b). Organization of the cytoskeleton in early *Drosophila* embryos. J. Cell Biol. *102*, 1494–1509.
172. Kashatus, D.F., Lim, K.H., Brady, D.C., Pershing, N.L.K., Cox, A.D., and Counter, C.M. (2011). RALA and RALBP1 regulate mitochondrial fission at mitosis. Nat. Cell Biol. *13*, 1108–1117.
173. Katayama, M., Zhong, Z., and Lai, L. (2006). Mitochondrial distribution and microtubule organization in fertilized and cloned porcine embryos: implications for developmental potential. Dev. … *299*, 206–220.
174. Keane, P.C., Kurzawa, M., Blain, P.G., and Morris, C.M. (2011). Mitochondrial dysfunction in Parkinson's disease. Parkinsons. Dis. *2011*, 716871.
175. Kelly, R.D.W., Mahmud, A., McKenzie, M., Trounce, I.A., and St John, J.C. (2012). Mitochondrial DNA copy number is regulated in a tissue specific manner by DNA methylation of the nuclear-encoded DNA polymerase gamma A. Nucleic Acids Res. *40*, 10124–10138.
176. Khacho, M., Clark, A., Svoboda, D.S., Azzi, J., MacLaurin, J.G., Meghaizel, C., Sesaki, H., Lagace, D.C., Germain, M., Harper, M.E., et al. (2016). Mitochondrial Dynamics Impacts Stem Cell Identity and Fate Decisions by Regulating a Nuclear Transcriptional Program. Cell Stem Cell *19*, 232–247.
177. Kidd, T., Abu-Shumays, R., Katzen, A., Sisson, J.C., Jiménez, G., Pinchin, S., Sullivan, W., and Ish-Horowicz, D. (2005). The ε-subunit of mitochondrial ATP synthase is required for normal spindle orientation during the *Drosophila* embryonic divisions. Genetics *170*, 697–708.
178. Kim, H.J., Shaker, M.R., Cho, B., Cho, H.M., Kim, H., Kim, J.Y., and Sun, W. (2015).

Dynamin-related protein 1 controls the migration and neuronal differentiation of subventricular zone-derived neural progenitor cells. Sci. Rep. *5*, 1–13.

179. Kim, Y.-M., Youn, S.-W., Sudhahar, V., Das, A., Chandhri, R., Cuervo Grajal, H., Kweon, J., Leanhart, S., He, L., Toth, P.T., et al. (2018). Redox Regulation of Mitochondrial Fission Protein Drp1 by Protein Disulfide Isomerase Limits Endothelial Senescence. Cell Rep. *23*, 3565–3578.
180. Kloc, M., and Etkin, L.D. (1995). Two distinct pathways for the localization of RNAs at the vegetal cortex in *Xenopus* oocytes. Development *121*, 287 LP-297.
181. Kloc, M., Larabell, C., and Etkin, L.D. (1996). Elaboration of the Messenger Transport Organizer Pathway for Localization of RNA to the Vegetal Cortex of *Xenopus* Oocytes. Dev. Biol. *180*, 119–130.
182. Kluck, R.M., and Newmeyer, D.D. (2013). The Release of Cytochrome c from Mitochondria : A Primary Site for Bcl-2 Regulation of Apoptosis The Release of Cytochrome c from Mitochondria : A Primary Site for Bcl-2 Regulation of Apoptosis. *1132*.
183. Kobayashi, S., Amikura, R., and Mukai, M. (1998). Localization of mitochondrial large ribosomal RNA in germ plasm of *Xenopus* embryos. Curr. Biol. *8*, 1117–1120.
184. Koh, H.-J., Brandauer, J., and Goodyear, L.J. (2008). LKB1 and AMPK and the regulation of the skeletal muscle metabolism. Curr. Opin. Clin. Nutr. Metab. Care *11*, 227–232.
185. Koirala, S., Bui, H.T., Schubert, H.L., Eckert, D.M., Hill, C.P., Kay, M.S., and Shaw, J.M. (2010). Molecular architecture of a dynamin adaptor: Implications for assembly of mitochondrial fission complexes. J. Cell Biol. *191*, 1127–1139.
186. Kolsch, V., Seher, T., Fernandez-Ballester, G.J., Serrano, L., and Leptin, M. (2007). Control of *Drosophila* Gastrulation by Apical Localization of Adherens Junctions and RhoGEF2. Science (80-.). *315*, 384–386.
187. Kölsch, V., Seher, T., Fernandez-Ballester, G.J., Serrano, L., and Leptin, M. (2007). Control of *Drosophila* Gastrulation by Apical Localization of Adherens Junctions and RhoGEF2. Science (80-.). *315*, 384 LP-386.
188. Komazaki, S. (1995). Calcium-containing, smooth-surfaced endoplasmic reticulum and vacuoles in cells of the blastopore-forming region during gastrulation of the newt, Cynops pyrrhogaster. Anat. Embryol. (Berl). *191*, 369–376.
189. Kops, G.J.P.L., Dansen, T.B., Polderman, P.E., Saarloos, I., Wirtz, K.W.A., Coffer, P.J.,

Huang, T.-T., Bos, J.L., Medema, R.H., and Burgering, B.M.T. (2002). Forkhead transcription factor FOXO3a protects quiescent cells from oxidative stress. Nature *419*, 316.

190. Korobova, F., Ramabhadran, V., and Higgs, H. (2013). An actin-dependent step in mitochondrial fission mediated by the ER-associated formin INF2. Science (80-.). *339*, 464–467.
191. Koutsopoulos, O.S.O., Laine, D., Osellame, L., Chudakov, D.M., Parton, R.G.R., Frazier, A.A.E., and Ryan, M.T.M. (2010). Human Miltons associate with mitochondria and induce microtubule-dependent remodeling of mitochondrial networks. Biochim. Biophys. Acta - Bioenerg. *1803*, 564–574.
192. Kreitzer, G., Marmorstein, A., Okamoto, P., Vallee, R., and Rodriguez-Boulan, E. (2000). Kinesin and dynamin are required for post-Golgi transport of a plasma-membraneprotein. Nat. Cell Biol. *2*, 125–127.
193. Krols, M., Bultynck, G., and Janssens, S. (2016). ER-Mitochondria contact sites: A new regulator of cellular calcium flux comes into play. J. Cell Biol. *214*, 367–370.
194. Krueger, D., Tardivo, P., Nguyen, C., and De Renzis, S. (2018). Downregulation of basal myosin-II is required for cell shape changes and tissue invagination. EMBO J. e100170.
195. Kuhlmann, C.R.W., Tamaki, R., Gamerdinger, M., Lessmann, V., Behl, C., Kempski, O.S., and Luhmann, H.J. (2007). Inhibition of the myosin light chain kinase prevents hypoxia-induced blood-brain barrier disruption. J. Neurochem. *102*, 501–507.
196. Kuznetsov, A. V., Hermann, M., Saks, V., Hengster, P., and Margreiter, R. (2009). The cell-type specificity of mitochondrial dynamics. Int. J. Biochem. Cell Biol. *41*, 1928–1939.
197. Kuznetsov, A. V, Hermann, M., Troppmair, J., Margreiter, R., and Hengster, P. (2010). Complex patterns of mitochondrial dynamics in human pancreatic cells revealed by fluorescent confocal imaging. J. Cell. Mol. Med. *14*, 417–425.
198. Kwon, J., Lee, S.-R., Yang, K.-S., Ahn, Y., Kim, Y.J., Stadtman, E.R., and Rhee, S.G. (2004). Reversible oxidation and inactivation of the tumor suppressor PTEN in cells stimulated with peptide growth factors. Proc. Natl. Acad. Sci. U. S. A. *101*, 16419–16424.
199. Labrousse, A.M., Zappaterra, M.D., Rube, D.A., Bliek, A.M. van der, van der Bliek, A.M., and Bliek, A.M. van der (1999). C. elegans Dynamin-Related Protein DRP-1 Controls

Severing of the Mitochondrial Outer Membrane. Mol. Cell *4*, 815–826.

200. Laforge, M., Rodrigues, V., Silvestre, R., Gautier, C., Weil, R., Corti, O., and Estaquier, J. (2016). NF-κB pathway controls mitochondrial dynamics. Cell Death Differ. *23*, 89–98.
201. Lapuente-brun, E., Moreno-loshuertos, R., Acín-pérez, R., Latorre-pellicer, A., Colás, C., Balsa, E., Perales-clemente, E., Quirós, P.M., Calvo, E., Navas, P., et al. (2013). Supercomplex Assembly Determines Electron Transport Chain. Science (80-.). *340*, 1567–1570.
202. Lawrence, E.J., and Mandato, C.A. (2013). Mitochondria Localize to the Cleavage Furrow in Mammalian Cytokinesis. *8*.
203. Lawrence, E.J., Boucher, E., and Mandato, C.A. (2016). Mitochondria-cytoskeleton associations in mammalian cytokinesis. Cell Div. *11*.
204. Lecuit, T., and Lenne, P.F. (2007). Cell surface mechanics and the control of cell shape, tissue patterns and morphogenesis. Nat. Rev. Mol. Cell Biol. *8*, 633–644.
205. Lecuit, T., and Wieschaus, E. (2000). Polarized insertion of new membrane from a cytoplasmic reservoir during cleavage of the *Drosophila* embryo. J. Cell Biol. *150*, 849–860.
206. Lee, J.H., Koh, H., Kim, M., Kim, Y., Lee, S.Y., Karess, R.E., Lee, S.-H., Shong, M., Kim, J.-M., Kim, J., et al. (2007). Energy-dependent regulation of cell structure by AMP-activated protein kinase. Nature *447*, 1017–1020.
207. Lee, S.S., Lee, R.Y.N., Fraser, A.G., Kamath, R.S., Ahringer, J., and Ruvkun, G. (2002). A systematic RNAi screen identifies a critical role for mitochondria in C. elegans longevity. Nat. Genet. *33*, 40.
208. Lee, Y., Jeong, S., Karbowski, M., Smith, C.L., and Youle, R.J. (2004). Roles of the Mammalian Mitochondrial Fission and Fusion Mediators Fis1 , Drp1 , and Opa1 in Apoptosis. Mol. Biol. Cell *15*, 5001–5011.
209. Lees, J.G., Gardner, D.K., and Harvey, A.J. (2017). Pluripotent Stem Cell Metabolism and Mitochondria: Beyond ATP. Stem Cells Int. *2017*, 1–17.
210. Leese, H.J., and Barton, A.M. (1984). Pyruvate and glucose uptake by mouse ova and preimplantation embryos. Reproduction *72*, 9–13.
211. Leff, T. (2003). AMP-activated protein kinase regulates gene expression by direct phosphorylation of nuclear proteins. Biochem. Soc. Trans. *31*, 224–227.
212. Legros, F., and Lombès, A. (2002). Mitochondrial fusion in human cells is efficient,

requires the inner membrane potential, and is mediated by mitofusins. Mol. Biol. … *13*, 4343–4354.

213. Leonard, A.P., Cameron, R.B., Speiser, J.L., Wolf, B.J., Peterson, Y.K., Schnellmann, R.G., Beeson, C.C., and Rohrer, B. (2015). Quantitative analysis of mitochondrial morphology and membrane potential in living cells using high-content imaging, machine learning, and morphological binning. Biochim. Biophys. Acta - Mol. Cell Res. *1853*, 348–360.
214. Leptin, M. (1991). twist and snail as positive and negiative regulators during Drosphila mesoderm development. Genes Dev. *5*, 1568–1576.
215. Leptin, M. (1995). *Drosophila* Gastrulation: From Pattern Formation to Morphogenesis. Annu. Rev. Cell Dev. Biol. *11*, 189–212.
216. Leptin, M. (1999). Gastrulation in *Drosophila*: the logic and the cellular mechanisms. EMBO J. *18*, 3187–3192.
217. Leptin, M., and Grunewald, B. (1990). Cell shape changes during gastrulation in *Drosophila*. Development *110*, 73–84.
218. Levinthal, D.J., and DeFranco, D.B. (2005). Reversible Oxidation of ERK-directed Protein Phosphatases Drives Oxidative Toxicity in Neurons. J. Biol. Chem. *280*, 5875–5883.
219. Lewis, M.R., and Lewis, W.H. (1915). Mitochondria (and other cytoplasmic structures) in tissue cultures. Am. J. Anat. *17*, 339–401.
220. Li, W.X. (2005). Functions and mechanisms of receptor tyrosine kinase Torso signaling: Lessons from*Drosophila* embryonic terminal development. Dev. Dyn. *232*, 656–672.
221. Li, Q., Gao, Z., Chen, Y., and Guan, M.-X. (2017). The role of mitochondria in osteogenic, adipogenic and chondrogenic differentiation of mesenchymal stem cells. Protein Cell *8*, 439–445.
222. Li, Y., Lim, S., Hoffman, D., Aspenstrom, P., Federoff, H.J., and Rempe, D.A. (2009). HUMMR, a hypoxia- and HIF-1α–inducible protein, alters mitochondrial distribution and transport. J. Cell Biol. *185*, 1065 LP-1081.
223. Li, Z., Okamoto, K.-I., Hayashi, Y., and Sheng, M. (2004). The importance of dendritic mitochondria in the morphogenesis and plasticity of spines and synapses. Cell *119*, 873–887.
224. Liao, T.S.V., Call, G.B., Guptan, P., Cespedes, A., Marshall, J., Yackle, K., Owusu-Ansah,

E., Mandal, S., Fang, Q.A., Goodstein, G.L., et al. (2006). An efficient genetic screen in *Drosophila* to identify nuclear-encoded genes with mitochondrial function. Genetics *174*, 525–533.

225. Ligoxygakis, P., Roth, S., and Reichhart, J.-M. (2003). A serpin regulates dorsal-ventral axis formation in the *Drosophila* embryo. Curr. Biol. *13*, 2097–2102.
226. Lim, B., Samper, N., Lu, H., Rushlow, C., Jiménez, G., and Shvartsman, S.Y. (2013). Kinetics of gene derepression by ERK signaling. Proc. Natl. Acad. Sci. U. S. A. *110*, 10330–10335.
227. Lim, B., Dsilva, C.J., Levario, T.J., Lu, H., Schüpbach, T., Kevrekidis, I.G., and Shvartsman, S.Y. (2015). Dynamics of Inductive ERK Signaling in the *Drosophila* Embryo. Curr. Biol. *25*, 1784–1790.
228. Lim, B., Levine, M., and Yamakazi, Y. (2017). Transcriptional Pre-patterning of *Drosophila* Gastrulation. Curr. Biol. *27*, 286–290.
229. Limbourg, B., and Zalokar, M. (1973). Permeabilization of *Drosophila* eggs. Dev. Biol. *35*, 382–387.
230. Liu, X., Kim, C.N., Yang, J., Jemmerson, R., and Wang, X. (1996). Induction of apoptotic program in cell-free extracts: requirement for dATP and cytochrome c. Cell *86*, 147–157.
231. Liu, Y., Fiskum, G., and Schubert, D. (2002). Generation of reactive oxygen species by the mitochondrial electron transport chain. J Neurochem *80*, 780–787.
232. López-Doménech, G., Covill-Cooke, C., Ivankovic, D., Halff, E.F., Sheehan, D.F., Norkett, R., Birsa, N., and Kittler, J.T. (2018). Miro proteins coordinate microtubule- and actin-dependent mitochondrial transport and distribution. EMBO J. *37*, e96380.
233. Loson, O.C., Song, Z., Chen, H., and Chan, D.C. (2013). Fis1, Mff, MiD49, and MiD51 mediate Drp1 recruitment in mitochondrial fission. Mol. Biol. Cell *24*, 659–667.
234. Lovas, J.R., and Wang, X. (2013). The meaning of mitochondrial movement to a neuron's life. Biochim. Biophys. Acta *1833*, 184–194.
235. Macchi, M., El Fissi, N., Tufi, R., Bentobji, M., Liévens, J.-C., Martins, L.M., Royet, J., and Rival, T. (2013). The *Drosophila* inner-membrane protein PMI controls crista biogenesis and mitochondrial diameter. J. Cell Sci. *126*, 814 LP-824.
236. Magie, C.R., and Parkhurst, S.M. (2005). Rho1 regulates signaling events required for proper *Drosophila* embryonic development. Dev. Biol. *278*, 144–154.

237. Mahowald, A.P. (2001). Assembly of the *Drosophila* Germ Plasm. Int. Rev. Cytol. *203*, 187–213.

238. Mandal, S., Guptan, P., Owusu-Ansah, E., and Banerjee, U. (2005). Mitochondrial regulation of cell cycle progression during development as revealed by the tenured mutation in *Drosophila*. Dev. Cell *9*, 843–854.

239. Mandal, S., Freije, W.A., Guptan, P., and Banerjee, U. (2010). Metabolic control of G1–S transition: cyclin E degradation by p53-induced activation of the ubiquitin–proteasome system. J. Cell Biol. *188*, 473 LP-479.

240. Mandal, S., Lindgren, A.G., Srivastava, A.S., Clark, A.T., and Banerjee, U. (2011). Mitochondrial function controls proliferation and early differentiation potential of embryonic stem cells. Stem Cells *29*, 486–495.

241. Marti, M., Frei, C., Baltzer, C., and Tiefenbo, S.K. (2009). Nutrition Controls Mitochondrial Biogenesis in the *Drosophila* Adipose Tissue through Delg and Cyclin D / Cdk4. *4*.

242. Martin, A.C., Kaschube, M., and Wieschaus, E.F. (2009). Pulsed contractions of an actin–myosin network drive apical constriction. Nature *457*, 495–499.

243. Martin, A.C., Gelbart, M., Fernandez-Gonzalez, R., Kaschube, M., and Wieschaus, E.F. (2010). Integration of contractile forces during tissue invagination. J. Cell Biol. *188*, 735–749.

244. Martin, M., Iyadurai, S.J., Gassman, A., Gindhart, J.G., Hays, T.S., and Saxton, W.M. (1999). Cytoplasmic Dynein, the Dynactin Complex, and Kinesin Are Interdependent and Essential for Fast Axonal Transport. Mol. Biol. Cell *10*, 3717–3728.

245. Martínez-Reyes, I., Diebold, L.P., Kong, H., Schieber, M., Huang, H., Hensley, C.T., Mehta, M.M., Wang, T., Santos, J.H., Woychik, R., et al. (2016). TCA Cycle and Mitochondrial Membrane Potential Are Necessary for Diverse Biological Functions. Mol. Cell *61*, 199–209.

246. Mason, F.M., Xie, S., Vasquez, C.G., Tworoger, M., and Martin, A.C. (2016). RhoA GTPase inhibition organizes contraction during epithelial morphogenesis. J. Cell Biol. *214*, 603–617.

247. Mavrakis, M., Rikhy, R., Lilly, M., and Lippincott-Schwartz, J. (2008). Fluorescence Imaging Techniques for Studying *Drosophila* Embryo Development. Curr. Protoc. Cell Biol. *39*, 4.18.1-4.18.43.

248. Mavrakis, M., Rikhy, R., and Lippincott-Schwartz, J. (2009). Plasma Membrane Polarity and Compartmentalization Are Established before Cellularization in the Fly Embryo. Dev. Cell *16*, 93–104.
249. Mavrakis, M., Azou-Gros, Y., Tsai, F.C., Alvarado, J., Bertin, A., Iv, F., Kress, A., Brasselet, S., Koenderink, G.H., and Lecuit, T. (2014). Septins promote F-actin ring formation by crosslinking actin filaments into curved bundles. Nat. Cell Biol. *16*, 322–334.
250. May-Panloup, P., Boucret, L., Chao de la Barca, J.-M., Desquiret-Dumas, V., Ferré-L'Hotellier, V., Morinière, C., Descamps, P., Procaccio, V., and Reynier, P. (2016). Ovarian ageing: the role of mitochondria in oocytes and follicles. Hum. Reprod. Update *22*, 725–743.
251. Mazumdar, A., and Mazumdar, M. (2002). How one becomes many: Blastoderm cellularization in *Drosophila* melanogaster. BioEssays *24*, 1012–1022.
252. McKenney, R.J., Huynh, W., Tanenbaum, M.E., Bhabha, G., and Vale, R.D. (2014). Activation of cytoplasmic dynein motility by dynactin-cargo adapter complexes. Science (80-.). *345*, 337 LP-341.
253. Meeusen, S., McCaffery, J.M., and Nunnari, J. (2004). Mitochondrial Fusion Intermediates Revealed in Vitro. Science (80-.). *305*, 1747 LP-1752.
254. Mehta, K., Chug, M.K., Jhunjhunwala, S., and Ananthanarayanan, V. (2017). Microtubule dynamics regulates mitochondrial fission. BioRxiv.
255. Melkov, A., Baskar, R., Alcalay, Y., and Abdu, U. (2016). A new mode of mitochondrial transport and polarized sorting regulated by Dynein, Milton and Miro. Development *143*, 4203–4213.
256. Merz, S., and Westermann, B. (2009). Genome-wide deletion mutant analysis reveals genes required for respiratory growth, mitochondrial genome maintenance and mitochondrial protein synthesis in Saccharomyces cerevisiae. Genome Biol. *10*, R95–R95.
257. Miller, K.E., and Sheetz, M.P. (2004). Axonal mitochondrial transport and potential are correlated. J. Cell Sci. *117*, 2791–2804.
258. Mironov, S.L. (2006). Spontaneous and evoked neuronal activities regulate movements of single neuronal mitochondria. Synapse *59*, 403–411.
259. Mishra, P., and Chan, D.C. (2016). Metabolic regulation of mitochondrial dynamics. J.

Cell Biol. *212*, 379–387.

260. Misko, A., Sasaki, Y., Tuck, E., Milbrandt, J., and Baloh, R.H. (2012). Mitofusin2 mutations disrupt axonal mitochondrial positioning and promote axon degeneration. J. Neurosci. *32*, 4145–4155.
261. Mitra, K., Wunder, C., and Roysam, B. (2009). A hyperfused mitochondrial state achieved at G1–S regulates cyclin E buildup and entry into S phase. Proc. … *106*.
262. Mitra, K., Rikhy, R., Lilly, M., and Lippincott-Schwartz, J. (2012). DRP1-dependent mitochondrial fission initiates follicle cell differentiation during *Drosophila* oogenesis. J. Cell Biol. *197*, 487–497.
263. Monick, M.M., Powers, L.S., Barrett, C.W., Hinde, S., Ashare, A., Groskreutz, D.J., Nyunoya, T., Coleman, M., Spitz, D.R., and Hunninghake, G.W. (2008). Constitutive ERK MAPK Activity Regulates Macrophage ATP Production and Mitochondrial Integrity. J. Immunol. *180*, 7485 LP-7496.
264. Moore, B.A., Gonzalez, G.D., and Caspary, T. (2010). Mitochondrial retention of Opa1 is required for mouse embryogenesis. Mamm. Genome *21*, 350–360.
265. Morisato, D. (2001). Spätzle regulates the shape of the Dorsal gradient in the *Drosophila* embryo. Development *128*, 2309–2319.
266. Morlino, G., Barreiro, O., Baixauli, F., Robles-Valero, J., González-Granado, J.M., Villa-Bellosta, R., Cuenca, J., Sánchez-Sorzano, C.O., Veiga, E., Martín-Cófreces, N.B., et al. (2014). Miro-1 links mitochondria and microtubule Dynein motors to control lymphocyte migration and polarity. Mol. Cell. Biol. *34*, 1412–1426.
267. Morris, R.L., and Hollenbeck, P.J. (1993). The regulation of bidirectional mitochondrial transport is coordinated with axonal outgrowth. *927*, 917–927.
268. Morris, R.L., and Hollenbeck, P.J. (1995). Axonal transport of mitochondria along microtubules and F-actin in living vertebrate neurons. J. Cell Biol. *131*, 1315–1326.
269. Mostov, K.E., Verges, M., and Altschuler, Y. (2000). Membrane traffic in polarized epithelial cells. Curr. Opin. Cell Biol. *12*, 483–490.
270. Motta, P.M., Nottola, S.A., Makabe, S., and Heyn, R. (2000). Mitochondrial morphology in human fetal and adult female germ cells. *15*, 129–147.
271. Mozdy, A.D., Mccaffery, J.M., and Shaw, J.M. (2000). Dnm1p GTPase-mediated Mitochondrial Fission Is a Multi-step Process Requiring the Novel Integral Membrane Component Fis1p. 367–379.

272. Mtango, N.R., Harvey, A.J., Latham, K.E., and Brenner, C.A. (2008). Molecular control of mitochondrial function in developing rhesus monkey oocytes and preimplantation-stage embryos. Reprod Fertil Dev *20*, 846–859.
273. Muliyil, S., and Narasimha, M. (2014). Mitochondrial ROS Regulates Cytoskeletal and Mitochondrial Remodeling to Tune Cell and Tissue Dynamics in a Model for Wound Healing. Dev. Cell *28*, 239–252.
274. Muller, F. (2000). The nature and mechanism of superoxide production by the electron transport chain: Its relevance to aging. Age (Omaha). *23*, 227–253.
275. Munjal, A., and Lecuit, T. (2014). Actomyosin networks and tissue morphogenesis. Development *141*, 1789 LP-1793.
276. Müsch, A. (2004). Microtubule organization and function in epithelial cells. Traffic *5*, 1–9.
277. Nagai, S., Mabuchi, T., Hirata, S., Shoda, T., Kasai, T., Yokota, S., Shitara, H., Yonekawa, H., and Hoshi, K. (2008). Oocyte Mitochondria: Strategies to Improve Embrbryogenesis. Hum. Cell *17*, 195–202.
278. Nagaraj, R., Gururaja-rao, S., Jones, K.T., Slattery, M., Negre, N., Braas, D., Christofk, H., White, K.P., and Mann, R. (2012). Control of mitochondrial structure and function by the Yorkie / YAP oncogenic pathway. Genes Dev. *26*, 2027–2037.
279. Nagaraj, R., Sharpley, M.S., Chi, F., Kim, R., Clark, A.T., Banerjee, U., Nagaraj, R., Sharpley, M.S., Chi, F., Braas, D., et al. (2016). Nuclear Localization of Mitochondrial TCA Cycle Enzymes as a Critical Step in Mammalian Zygotic Article Nuclear Localization of Mitochondrial TCA Cycle Enzymes as a Critical Step in Mammalian Zygotic Genome Activation. Cell *168*, 210–223.e11.
280. Nauseef, W.M. (2008). Biological Roles for the NOX Family NADPH Oxidases. J. Biol. Chem. *283*, 16961–16965.
281. Nelson, W.J., and Yeaman, C. (2001). Protein trafficking in the exocytic pathway of polarized epithelial cells. Trends Cell Biol. *11*, 483–486.
282. Nemoto, S., and Finkel, T. (2002). Redox Regulation of Forkhead Proteins Through a p66shc-Dependent Signaling Pathway. Science (80-.). *295*, 2450 LP-2452.
283. Newhall, K.J., Criniti, A.R., Cheah, C.S., Smith, K.C., Kafer, K.E., Burkart, A.D., and McKnight, G.S. (2006). Dynamic anchoring of PKA is essential during oocyte

maturation. Curr. Biol. *16*, 321–327.

284. Nikolaidou, K.K., and Barrett, K. (2004). A Rho GTPase signaling pathway is used reiteratively in epithelial folding and potentially selects the outcome of Rho activation. Curr. Biol. *14*, 1822–1826.
285. Nishi, Y., Takeshita, T., Sato, K., and Araki, T. (2003). Change of the Mitochondrial Distribution in Mouse OoplasmDuring In Vitro Maturation. J. Nippon Med. Sch. *70*, 408–415.
286. Niwa, R., Nagata-Ohashi, K., Takeichi, M., Mizuno, K., and Uemura, T. (2002). Control of actin reorganization by Slingshot, a family of phosphatases that dephosphorylate ADF/cofilin. Cell *108*, 233–246.
287. Nogueira, V., Park, Y., Chen, C.-C., Xu, P.-Z., Chen, M.-L., Tonic, I., Unterman, T., and Hay, N. (2008). Akt determines replicative senescence and oxidative or oncogenic premature senescence and sensitizes cells to oxidative apoptosis. Cancer Cell *14*, 458–470.
288. Oakes, S.A., Scorrano, L., Opferman, J.T., Bassik, M.C., Nishino, M., Pozzan, T., and Korsmeyer, S.J. (2005). Proapoptotic BAX and BAK regulate the type 1 inositol trisphosphate receptor and calcium leak from the endoplasmic reticulum. Proc. Natl. Acad. Sci. U. S. A. *102*, 105–110.
289. Ohsawa, S., Sato, Y., Enomoto, M., Nakamura, M., Betsumiya, A., and Igaki, T. (2012). Mitochondrial defect drives non-autonomous tumour progression through Hippo signalling in *Drosophila*. Nature *490*, 547.
290. Okada, M., Kleinman, I.A., and Schneiderman, H.A. (1974). Restoration of fertility in sterilized *Drosophila* eggs by transplantation of polar cytoplasm. Dev. Biol. *37*, 43–54.
291. Ong, S.-B., and Hausenloy, D.J. (2010). Mitochondrial morphology and cardiovascular disease. Cardiovasc. Res. *88*, 16–29.
292. Otera, H., Wang, C., Cleland, M.M., Setoguchi, K., Yokota, S., Youle, R.J., and Mihara, K. (2010). Mff is an essential factor for mitochondrial recruitment of Drp1 during mitochondrial fission in mammalian cells. J. Cell Biol. *191*, 1141–1158.
293. Otsuga, D., Keegan, B.R., Brisch, E., Thatcher, J.W., Hermann, G.J., Bleazard, W., and Shaw, J.M. (1998). The dynamin-related GTPase, Dnm1p, controls mitochondrial morphology in yeast. J. Cell Biol. *143*, 333–349.
294. Ottosen, L.D.M., Hindkjaer, J., Lindenberg, S., and Ingerslev, H.J. (2007). Murine pre-

embryo oxygen consumption and developmental competence. J. Assist. Reprod. Genet. *24*, 359–365.

295. Owusu-Ansah, E., and Banerjee, U. (2009). Reactive oxygen species prime *Drosophila* haematopoietic progenitors for differentiation. Nature *461*, 537–541.
296. Owusu-Ansah, E., Yavari, A., Mandal, S., and Banerjee, U. (2008a). Distinct mitochondrial retrograde signals control the G1-S cell cycle checkpoint. Nat. Genet. *40*, 356–361.
297. Owusu-Ansah, E., Yavari, A., and Banerjee, U. (2008b). A protocol for in vivo detection of reactive oxygen species. Protoc. Exch. 1–8.
298. Pandey, R., Heeger, S., and Lehner, C.F. (2007). Rapid effects of acute anoxia on spindle kinetochore interactions activate the mitotic spindle checkpoint. J. Cell Sci. *120*, 2807–2818.
299. Papoulas, O., Hays, T.S., and Sisson, J.C. (2005). The golgin Lava lamp mediates dynein-based Golgi movements during *Drosophila* cellularization. *7*, 1–8.
300. Park, K.-S., Jo, I., Pak, Y., Bae, S.-W., Rhim, H., Suh, S.-H., Park, S., Zhu, M., So, I., and Kim, K. (2002). FCCP depolarizes plasma membrane potential by activating proton and Na+ currents in bovine aortic endothelial cells. Pflügers Arch. - Eur. J. Physiol. *443*, 344–352.
301. Parker, D.J., Iyer, A., Shah, S., Moran, A., Hjelmeland, A.B., Basu, M.K., Liu, R., and Mitra, K. (2015). A new mitochondrial pool of cyclin E, regulated by Drp1, is linked to cell-density-dependent cell proliferation. J. Cell Sci. *128*, 4171 LP-4182.
302. Parkhurst, S.M., and Ish-Horowicz, D. (1991). wimp, a dominant maternal-effect mutation, reduces transcription of a specific subset of segmentation genes in *Drosophila*. Genes Dev. *5*, 341–357.
303. Parone, P.A., Da, S., Tondera, D., Mattenberger, Y., James, D.I., and Martinou, J. (2008). Preventing Mitochondrial Fission Impairs Mitochondrial Function and Leads to Loss of Mitochondrial DNA. *3*, 1–9.
304. Pelissier, A., Chauvin, J.-P., and Lecuit, T. (2003). Trafficking through Rab11 endosomes is required for cellularization during *Drosophila* embryogenesis. Curr. Biol. *13*, 1848–1857.
305. Penefsky, H.S. (1985). Mechanism of inhibition of mitochondrial adenosine triphosphatase by dicyclohexylcarbodiimide and oligomycin: relationship to ATP

synthesis. Proc. Natl. Acad. Sci. U. S. A. *82*, 1589–1593.

306. Pepling, M.E., and Spradling, A.C. (2001). Mouse Ovarian Germ Cell Cysts Undergo Programmed Breakdown to Form Primordial Follicles. Dev. Biol. *234*, 339–351.
307. Pepling, M.E., Wilhelm, J.E., O'Hara, A.L., Gephardt, G.W., and Spradling, A.C. (2007). Mouse oocytes within germ cell cysts and primordial follicles contain a Balbiani body. Proc. Natl. Acad. Sci. U. S. A. *104*, 187–192.
308. Perumalsamy, L.R., Nagala, M., and Sarin, A. (2010). Notch-activated signaling cascade interacts with mitochondrial remodeling proteins to regulate cell survival. Proc. Natl. Acad. Sci. U. S. A. *107*, 6882–6887.
309. Pinho, B.R., Santos, M.M., Fonseca-Silva, A., Valentão, P., Andrade, P.B., and Oliveira, J.M.A. (2013). How mitochondrial dysfunction affects zebrafish development and cardiovascular function: An in vivo model for testing mitochondria-targeted drugs. Br. J. Pharmacol. *169*, 1072–1090.
310. Pinton, P., Ferrari, D., Magalhães, P., Schulze-Osthoff, K., Di Virgilio, F., Pozzan, T., and Rizzuto, R. (2000). Reduced loading of intracellular Ca(2+) stores and downregulation of capacitative Ca(2+) influx in Bcl-2-overexpressing cells. J. Cell Biol. *148*, 857–862.
311. Prudent, J., Popgeorgiev, N., Gadet, R., Deygas, M., Rimokh, R., and Gillet, G. (2016). Mitochondrial Ca2+ uptake controls actin cytoskeleton dynamics during cell migration. Sci. Rep. *6*, 36570.
312. Qian, W., Choi, S., Gibson, G.A., Watkins, S.C., Bakkenist, C.J., and Van Houten, B. (2012). Mitochondrial hyperfusion induced by loss of the fission protein Drp1 causes ATM-dependent G2/M arrest and aneuploidy through DNA replication stress. J. Cell Sci. *125*, 5745–5757.
313. Rahn, J.J., Stackley, K.D., and Chan, S.S.L. (2013). Opa1 Is Required for Proper Mitochondrial Metabolism in Early Development. *8*.
314. Rambold, A.S., Kostelecky, B., Elia, N., and Lippincott-Schwartz, J. (2011). Tubular network formation protects mitochondria from autophagosomal degradation during nutrient starvation. Proc. Natl. Acad. Sci. *108*, 10190 LP-10195.
315. Rapaport, D., Brunner, M., and Westermann, B. (1998). Fzo1p is a mitochondrial outer membrane protein essential for the biogenesis of functional mitochondria in Saccaromyces cerevisiae. Biochemistry *273*, 20150–20155.
316. Ratnaparkhi, A. (2013). Signaling by Folded gastrulation is modulated by mitochondrial

fusion and fission. J. Cell Sci. *126*, 5369–5376.

317. Ratnaparkhi, A., and Zinn, K. (2007). The secreted cell signal Folded Gastrulation regulates glial morphogenesis and axon guidance in *Drosophila*. Dev. Biol. *308*, 158–168.
318. Rawson, R.L., Yam, L., Weimer, R.M., Bend, E.G., Hartwieg, E., Horvitz, H.R., Clark, S.G., and Jorgensen, E.M. (2014). Axons Degenerate in the Absence of Mitochondria in C. elegans. Curr. Biol. *24*, 760–765.
319. Ray, P.D., Huang, B.-W., and Tsuji, Y. (2012). Reactive oxygen species (ROS) homeostasis and redox regulation in cellular signaling. Cell. Signal. *24*, 981–990.
320. Rea, S.L., Ventura, N., and Johnson, T.E. (2007). Relationship between mitochondrial electron transport chain dysfunction, development, and life extension in Caenorhabditis elegans. PLoS Biol. *5*, e259–e259.
321. Reynier, P., May-Panloup, P., Chrétien, M.-F., Morgan, C.J., Jean, M., Savagner, F., Barrière, P., and Malthièry, Y. (2001). Mitochondrial DNA content affects the fertilizability of human oocytes. MHR Basic Sci. Reprod. Med. *7*, 425–429.
322. Rikhy, R., Kamat, S., Ramagiri, S., Sriram, V., and Krishnan, K.S. (2007). Mutations in dynamin-related protein result in gross changes in mitochondrial morphology and affect synaptic vesicle recycling at the *Drosophila* neuromuscular junction. Genes. Brain. Behav. *6*, 42–53.
323. Rikhy, R., Mavrakis, M., and Lippincott-Schwartz, J. (2015). Dynamin regulates metaphase furrow formation and plasma membrane compartmentalization in the syncytial *Drosophila* embryo. Biol. Open *4*, 301–311.
324. Rintoul, G.L., and Reynolds, I.J. (2010). Mitochondrial trafficking and morphology in neuronal injury. Biochim. Biophys. Acta - Mol. Basis Dis. *1802*, 143–150.
325. Rivadeneira, D.B., Caino, M.C., Seo, J.H., Angelin, A., Wallace, D.C., Languino, L.R., and Altieri, D.C. (2015). Survivin promotes oxidative phosphorylation, subcellular mitochondrial repositioning, and tumor cell invasion. Sci. Signal. *8*, ra80 LP-ra80.
326. Roegiers, F., McDougall, A., and Sardet, C. (1995). The sperm entry point defines the orientation of the calcium-induced contraction wave that directs the first phase of cytoplasmic reorganization in the ascidian egg. Development *121*, 3457–3466.
327. Rogers, S.L., Wiedemann, U., Häcker, U., Turck, C., and Vale, R.D. (2004). *Drosophila* RhoGEF2 associates with microtubule plus ends in an EB1-dependent manner. Curr.

Biol. *14*, 1827–1833.

328. Rohn, J.L., Patel, J. V., Neumann, B., Bulkescher, J., McHedlishvili, N., McMullan, R.C., Quintero, O.A., Ellenberg, J., and Baum, B. (2014). Myo19 ensures symmetric partitioning of mitochondria and coupling of mitochondrial segregation to cell division. Curr. Biol. *24*, 2598–2605.
329. Romek, M., Gajda, B., Rolka, M., and Smorag, Z. (2011). Mitochondrial activity and morphology in developing porcine oocytes and pre-implantation non-cultured and cultured embryos. Reprod. Domest. Anim. *46*, 471–480.
330. Röth, D., Krammer, P.H., and Gülow, K. (2014). Dynamin related protein 1-dependent mitochondrial fission regulates oxidative signalling in T cells. FEBS Lett. *588*, 1749–1754.
331. Rowland, A.A., and Voeltz, G.K. (2012). Endoplasmic reticulum–mitochondria contacts : function of the junction. Nat. Rev. Mol. Cell Biol. *13*, 607–625.
332. Royou, A., Field, C., Sisson, J.C., Sullivan, W., and Karess, R. (2004). Reassessing the Role and Dynamics of Nonmuscle Myosin II during Furrow Formation in Early *Drosophila* Embryos. Mol. Biol. Cell *15*, 838–850.
333. Russo, G.J., Louie, K., Wellington, A., Macleod, G.T., Hu, F., Panchumarthi, S., and Zinsmaier, K.E. (2009). *Drosophila* Miro is required for both anterograde and retrograde axonal mitochondria transport. J Neurosci *29*, 5443–5455.
334. Saddar, S., Dienhart, M.K., and Stuart, R.A. (2008). The F1F0-ATP Synthase Complex Influences the Assembly State of the Cytochrome bc1-Cytochrome Oxidase Supercomplex and Its Association with the TIM23 Machinery. J. Biol. Chem. *283*, 6677–6686.
335. Sakamoto, K. (2006). Deficiency of LKB1 in heart prevents ischemia-mediated activation of AMPK 2 but not AMPK 1. AJP Endocrinol. Metab. *290*, E780–E788.
336. Sakamoto, K., Göransson, O., Hardie, D.G., and Alessi, D.R. (2004). Activity of LKB1 and AMPK-related kinases in skeletal muscle: effects of contraction, phenformin, and AICAR. Am. J. Physiol. Endocrinol. Metab. *287*, E310–E317.
337. Sakamoto, K., McCarthy, A., Smith, D., Green, K.A., Grahame Hardie, D., Ashworth, A., and Alessi, D.R. (2005). Deficiency of LKB1 in skeletal muscle prevents AMPK activation and glucose uptake during contraction. EMBO J. *24*, 1810–1820.
338. Santel, A., and Fuller, M.T. (2000). Control of mitochondrial morphology by a human

mitofusin. J. Cell Sci.

339. Saotome, M., Safiulina, D., Szabadkai, G., Das, S., Fransson, A., Aspenstrom, P., Rizzuto, R., and Hajnóczky, G. (2008). Bidirectional Ca2+-dependent control of mitochondrial dynamics by the Miro GTPase. Proc. Natl. Acad. Sci. U. S. A. *105*, 20728–20733.
340. Sathananthan, A.H., and Trounson, A.O. (2000). Mitochondrial morphology during preimplantational human embryogenesis. Hum. Reprod. *15*, 148–159.
341. Savage, R.M., and Danilchik, M. V. (1993). Dynamics of Germ plasm localization and its inhibition by ultraviolet irradiation in early cleavage *Xenopus* embryos. Dev. Biol. *157*, 317–382.
342. Saxton, W.M., and Hollenbeck, P.J. (2005). The axonal transport of mitochondria. J. Cell Sci. *118*, 5411–5419.
343. Saxton, W.M., and Hollenbeck, P.J. (2012). The axonal transport of mitochondria. J. Cell Sci. *125*, 2095–2104.
344. SchaÈgger, H., and Pfeiffer, K. (2000). Supercomplexes in the respiratory chains of yeast and mammalian mitochondria. EMBO J. *19*, 1997.
345. Schafer, G., Narasimha, M., Vogelsang, E., and Leptin, M. (2014). Cadherin switching during the formation and differentiation of the *Drosophila* mesoderm - implications for epithelial-to-mesenchymal transitions. J. Cell Sci. *127*, 1511–1522.
346. Scheckhuber, C.Q., Erjavec, N., Tinazli, A., Hamann, A., Nyström, T., and Osiewacz, H.D. (2006). Reducing mitochondrial fission results in increased life span and fitness of two fungal ageing models. Nat. Cell Biol. *9*, 99.
347. Scheckhuber, C.Q., Houthoofd, K., Weil, A.C., Werner, A., De Vreese, A., Vanfleteren, J.R., and Osiewacz, H.D. (2011). Alternative Oxidase Dependent Respiration Leads to an Increased Mitochondrial Content in Two Long-Lived Mutants of the Ageing Model Podospora anserina. PLoS One *6*, e16620.
348. Schejter, E.D., and Wieschaus, E. (1993). bottleneck acts as a regulator of the microfilament network governing cellularization of the *Drosophila* embryo. Cell *75*, 373–385.
349. Schiffmann, D.A. (1997). Dorsoventral asymmetry in mitochondria membrane potential in early *Drosophila* embryos. 1997.
350. Schomer, B., and Epel, D. (1998). Redox Changes during Fertilization and Maturation of Marine Invertebrate Eggs. Dev. Biol. *203*, 1–11.

351. Schroeder, C.M., and Vale, R.D. (2016). Assembly and activation of dynein–dynactin by the cargo adaptor protein Hook3. J. Cell Biol. *214*, 309–318.
352. Schuler, M.-H., Lewandowska, A., Caprio, G. Di, Skillern, W., Upadhyayula, S., Kirchhausen, T., Shaw, J.M., Cunniff, B., and Steinberg, G. (2017). Miro1-mediated mitochondrial positioning shapes intracellular energy gradients required for cell migration. Mol. Biol. Cell *28*, 2159–2169.
353. Schulman, V.K., Folker, E.S., and Baylies, M.K. (2013). A method for reversible drug delivery to internal tissues of *Drosophila* embryos. Fly (Austin). *7*, 193–203.
354. Schwarz, T.L. (2013). Mitochondrial Trafficking in Neurons. Cold Spring Harb. Perspect. Biol. *5*, a011304–a011304.
355. Scott, I., and Youle, R.J. (2010). Mitochondrial fission and fusion. Essays Biochem *47*, 85–98.
356. Sepich, D.S., and Solnica-Krezel, L. (2016). Intracellular Golgi Complex organization reveals tissue specific polarity during zebrafish embryogenesis. Dev. Dyn. *245*, 678–691.
357. Sharma, S. V, Bell, D.W., Settleman, J., and Haber, D.A. (2007). Epidermal growth factor receptor mutations in lung cancer. Nat. Rev. Cancer *7*, 169.
358. Shaw, J.M., and Nunnari, J. (2002). Mitochondrial dynamics and division in budding yeast. Trends Cell Biol. *12*, 178–184.
359. Sheffer, R., Douiev, L., Edvardson, S., Shaag, A., Tamimi, K., Soiferman, D., Meiner, V., and Saada, A. (2016). Postnatal microcephaly and pain insensitivity due to a de novo heterozygous DNM1L mutation causing impaired mitochondrial fission and function. Am. J. Med. Genet. Part A *170*, 1603–1607.
360. Shi, L., and Tu, B.P. (2015). Acetyl-CoA and the regulation of metabolism: mechanisms and consequences. Curr. Opin. Cell Biol. *33*, 125–131.
361. Shields, L.Y., Kim, H., Zhu, L., Haddad, D., Berthet, A., Pathak, D., Lam, M., Ponnusamy, R., Diaz-Ramirez, L.G., Gill, T.M., et al. (2015). Dynamin-related protein 1 is required for normal mitochondrial bioenergetic and synaptic function in CA1 hippocampal neurons. Cell Death &Amp; Dis. *6*, e1725.
362. Shim, S.-H., Xia, C., Zhong, G., Babcock, H.P., Vaughan, J.C., Huang, B., Wang, X., Xu, C., Bi, G.-Q., and Zhuang, X. (2012). Super-resolution fluorescence imaging of organelles in live cells with photoswitchable membrane probes. Proc. Natl. Acad. Sci. *109*, 13978

LP-13983.

363. Shiota, T., Traven, A., and Lithgow, T. (2015). Mitochondrial biogenesis: Cell-cycle-dependent investment in making mitochondria. Curr. Biol. *25*, R78-E79.
364. Shirendeb, U.P., Calkins, M.J., Manczak, M., Anekonda, V., Dufour, B., McBride, J.L., Mao, P., and Reddy, P.H. (2012). Mutant Huntingtin's interaction with mitochondrial protein Drp1 impairs mitochondrial biogenesis and causes defective axonal transport and synaptic degeneration in Huntington's disease. Hum. Mol. Genet. *21*, 406–420.
365. Sieber, M.H., Thomsen, M.B., and Spradling, A.C. (2016). Electron Transport Chain Remodeling by GSK3 during Oogenesis Connects Nutrient State to Reproduction. Cell *164*, 420–432.
366. Sisson, J.C., Field, C., Ventura, R., Royou, A., Sullivan, W., National, C., Recherche, D., Moléculaire, C.D.G., and Yvette, G. (2000). Lava Lamp , a Novel Peripheral Golgi Protein , Is Required for *Drosophila* melanogaster Cellularization. *151*.
367. Skulachev, V.P. (2001). Mitochondrial filaments and clusters as intracellular power-transmitting cables. Trends Biochem. Sci. *26*, 23–29.
368. Smirnova, E., Shurland, D., Ryazantsev, S.N., and Bliek, A.M. Van Der (1998a). A Human Dynamin-related Protein Controls the Distribution of Mitochondria. *143*, 351–358.
369. Smirnova, E., Shurland, D.L., Ryazantsev, S.N., and van der Bliek, a M. (1998b). A human dynamin-related protein controls the distribution of mitochondria. J. Cell Biol. *143*, 351–358.
370. Smith-Garvin, J.E., Koretzky, G.A., and Jordan, M.S. (2009). T Cell Activation. Annu. Rev. Immunol. *27*, 591–619.
371. Sokac, A.M., and Wieschaus, E. (2008). Local Actin-Dependent Endocytosis Is Zygotically Controlled to Initiate *Drosophila* Cellularization. Dev. Cell *14*, 775–786.
372. Solnica-Krezel, L., and Sepich, D.S. (2012). Gastrulation: Making and Shaping Germ Layers. Annu. Rev. Cell Dev. Biol. *28*, 687–717.
373. Son, M.J., Kwon, Y., Son, M.-Y., Seol, B., Choi, H.-S., Ryu, S.-W., Choi, C., and Cho, Y.S. (2015). Mitofusins deficiency elicits mitochondrial metabolic reprogramming to pluripotency. Cell Death Differ. *22*, 1957–1969.
374. Squirrell, J.M., Wokosin, D.L., White, J.G., and Bavister, B.D. (1999). Long-term two-photon fluorescence imaging of mammalian embryos without compromising viability. Nat. Biotechnol. *17*, 763.

375. Squirrell, J.M., Schramm, R.D., Paprocki, A.M., Wokosin, D.L., and Bavister, B.D. (2003). Imaging Mitochondrial Organization in Living Primate Oocytes and Embryos using Multiphoton Microscopy. Microsc. Microanal. *9*, 190–201.

376. Staller, M. V, Yan, D., Randklev, S., Bragdon, M.D., Wunderlich, Z.B., Tao, R., Perkins, L.A., De Pace, A.H., and Perrimon, N. (2013). Depleting gene activities in early *Drosophila* embryos with the "maternal-Gal4-shRNA" system. Genetics *193*, 51–61.

377. Steffen, W., Karki, S., Vaughan, K.T., Vallee, R.B., Holzbaur, E.L.F., Weiss, D.G., and Kuznetsov, S.A. (1997). The Involvement of the Intermediate Chain of Cytoplasmic Dynein in Binding the Motor Complex to Membranous Organelles of *Xenopus* Oocytes. Mol. Biol. Cell *8*, 2077–2088.

378. Steinberg, S.F. (2013). Oxidative stress and sarcomeric proteins. Circ. Res. *112*, 393–405.

379. Stern, S., Biggers, J.D., and Anderson, E. (1971). Mitochondria and early development of the mouse. J. Exp. Zool. *176*, 179–191.

380. Stewart, J.B., and Chinnery, P.F. (2015). The dynamics of mitochondrial DNA heteroplasmy: Implications for human health and disease. Nat. Rev. Genet. *16*, 530–542.

381. Stewart, J.B., Freyer, C., Elson, J.L., Wredenberg, A., Cansu, Z., Trifunovic, A., and Larsson, N.-G. (2008). Strong Purifying Selection in Transmission of Mammalian Mitochondrial DNA. PLOS Biol. *6*, e10.

382. Stone, S.J., and Vance, J.E. (2000). Phosphatidylserine synthase-1 and -2 are localized to mitochondria-associated membranes. J. Biol. Chem. *275*, 34534–34540.

383. Stowers, R.S., Megeath, L.J., Górska-Andrzejak, J., Meinertzhagen, I.A., and Schwarz, T.L. (2002). Axonal transport of mitochondria to synapses depends on milton, a novel *Drosophila* protein. Neuron *36*, 1063–1077.

384. Strecker, T.R., Mcghee, S., Shih, S., and Ham, D. (1994). Permeabilization, staining and culture of living *Drosophila* embryos. Biotech. Histochem. *69*, 25–30.

385. Stroud, D.A., and Ryan, M.T. (2013). Mitochondria: Organization of Respiratory Chain Complexes Becomes Cristae-lized. Curr. Biol. *23*, R969–R971.

386. Suhr, S.T., Chang, E.A., Tjong, J., Alcasid, N., Perkins, G.A., Goissis, M.D., Ellisman, M.H., Perez, G.I., and Cibelli, J.B. (2010). Mitochondrial Rejuvenation After Induced Pluripotency. *5*.

387. Taguchi, N., Ishihara, N., Jofuku, A., Oka, T., and Mihara, K. (2007). Mitotic phosphorylation of dynamin-related GTPase Drp1 participates in mitochondrial fission. J. Biol. Chem. *282*, 11521–11529.

388. Tao, K., Matsuki, N., and Koyama, R. (2014). AMP-activated protein kinase mediates activity-dependent axon branching by recruiting mitochondria to axon. Dev. Neurobiol. *74*, 557–573.

389. Teixeira, F.K., Sanchez, C.G., Hurd, T.R., Seifert, J.R.K., Czech, B., Preall, J.B., Hannon, G.J., and Lehmann, R. (2015). ATP synthase promotes germ cell differentiation independent of oxidative phosphorylation. Nat. Cell Biol. *17*, 689–696.

390. Tennessen, J.M., Baker, K.D., Lam, G., Evans, J., and Thummel, C.S. (2011). The *Drosophila* Estrogen-Related Receptor Directs a Metabolic Switch that Supports Developmental Growth. Cell Metab. *13*, 139–148.

391. Tennessen, J.M., Bertagnolli, N.M., Evans, J., Sieber, M.H., Cox, J., and Thummel, C.S. (2014). Coordinated Metabolic Transitions During *Drosophila* Embryogenesis and the Onset of Aerobic Glycolysis. *4*, 839–850.

392. Thomson, T., and Lasko, P. (2005). Tudor and its domains: Germ cell formation from a Tudor perspective. Cell Res. *15*, 281–291.

393. Thomson, T., Liu, N., Arkov, A., Lehmann, R., and Lasko, P. (2008). Isolation of new polar granule components in *Drosophila* reveals P body and ER associated proteins. Mech. Dev. *125*, 865–873.

394. Thuy An, P.N. guyen, Yamaguchi, M., Bamba, T., and Fukusaki, E. (2014). Metabolome analysis of *Drosophila* melanogaster during embryogenesis. PLoS One *9*, e99519.

395. Tomer, D., Chippalkatti, R., Mitra, K., and Rikhy, R. (2018). ERK regulates mitochondrial membrane potential in fission deficient *Drosophila* follicle cells during differentiation. Dev. Biol. *434*, 48–62.

396. Tondera, D., Grandemange, S., Jourdain, A., Karbowski, M., Mattenberger, Y., Herzig, S., Da Cruz, S., Clerc, P., Raschke, I., Merkwirth, C., et al. (2009). SLP-2 is required for stress-induced mitochondrial hyperfusion. EMBO J. *28*, 1589 LP-1600.

397. Toomre, D., Keller, P., White, J., Olivo, J.C., and Simons, K. (1999). Dual-color visualization of trans-Golgi network to plasma membrane traffic along microtubules in living cells. J. Cell Sci. *112*, 21 LP-33.

398. Tothova, Z., Kollipara, R., Huntly, B.J., Lee, B.H., Castrillon, D.H., Cullen, D.E.,

McDowell, E.P., Lazo-Kallanian, S., Williams, I.R., Sears, C., et al. (2007). FoxOs are critical mediators of hematopoietic stem cell resistance to physiologic oxidative stress. Cell *128*, 325–339.

399. Toyama, E.Q., Herzig, S., Courchet, J., Lewis, T.L., Losón, O.C., Hellberg, K., Young, N.P., Chen, H., Polleux, F., Chan, D.C., et al. (2016). Metabolism: AMP-activated protein kinase mediates mitochondrial fission in response to energy stress. Science (80-.). *351*, 275–281.
400. Trimarchi, J.R., Liu, L., Porterfield, D.M., Smith, P.J.S., and Keefe, D.L. (2000). Oxidative Phosphorylation-Dependent and -Independent Oxygen Consumption by Individual Preimplantation Mouse Embryos. *1874*, 1866–1874.
401. Twig, G., Elorza, A., Molina, A.J.A., Mohamed, H., Wikstrom, J.D., Walzer, G., Stiles, L., Haigh, S.E., Katz, S., Las, G., et al. (2008). Fission and selective fusion govern mitochondrial segregation and elimination by autophagy. EMBO J. *27*, 433–446.
402. Ukeshima, A., and Fujimoto, T. (2018). A fine morphological study of germ cells in asymmetrically developing right and left ovaries of the chick. Anat. Rec. *230*, 378–386.
403. Vaarmann, A., Mandel, M., Zeb, A., Wareski, P., Liiv, J., Kuum, M., Antsov, E., Liiv, M., Cagalinec, M., Choubey, V., et al. (2016). Mitochondrial biogenesis is required for axonal growth. Development *143*, 1981 LP-1992.
404. Vance, E. (1990). Phospholipid Mitochondria * Synthesis in a Membrane Fraction Associated identified. J. Biol. Chem. *265*, 7248–7257.
405. Varadi, A., Johnson-Cadwell, L.I., Cirulli, V., Yoon, Y., Allan, V.J., and Rutter, G.A. (2004). Cytoplasmic dynein regulates the subcellular distribution of mitochondria by controlling the recruitment of the fission factor dynamin-related protein-1. J. Cell Sci. *117*, 4389–4400.
406. Vasquez, C.G., Tworoger, M., and Martin, A.C. (2014). Dynamic myosin phosphorylation regulates contractile pulses and tissue integrity during epithelial morphogenesis. J. Cell Biol. *206*, 435–450.
407. Verburg, J., and Hollenbeck, P.J. (2009). Mitochondrial Membrane Potential in Axons Increases with Local NGF or Semaphorin Signaling. J Neurosci *28*, 8306–8315.
408. Verstreken, P., Ly, C. V, Venken, K.J.T., Koh, T.-W., Zhou, Y., and Bellen, H.J. (2005). Synaptic mitochondria are critical for mobilization of reserve pool vesicles at *Drosophila* neuromuscular junctions. Neuron *47*, 365–378.

409. Vevea, J.D., Alessi Wolken, D.M., Swayne, T.C., White, A.B., and Pon, L.A. (2013). Ratiometric Biosensors that Measure Mitochondrial Redox State and ATP in Living Yeast Cells. J. Vis. Exp. 1–12.

410. Voss, C., Lahiri, S., Young, B.P., Loewen, C.J., and Prinz, W.A. (2012). ER-shaping proteins facilitate lipid exchange between the ER and mitochondria in S. cerevisiae. J. Cell Sci. *125*, 4791–4799.

411. Vrailas-Mortimer, A., del Rivero, T., Mukherjee, S., Nag, S., Gaitanidis, A., Kadas, D., Consoulas, C., Duttaroy, A., and Sanyal, S. (2011). A muscle-specific p38 MAPK/Mef2/MnSOD pathway regulates stress, motor function, and life span in *Drosophila*. Dev. Cell *21*, 783–795.

412. Wai, T., Ao, A., Zhang, X., Cyr, D., Dufort, D., and Shoubridge, E.A. (2010). The role of mitochondrial DNA copy number in mammalian fertility. Biol. Reprod. *83*, 52–62.

413. Wakabayashi, J., Zhang, Z., Wakabayashi, N., Tamura, Y., Fukaya, M., Kensler, T.W., Iijima, M., and Sesaki, H. (2009). The dynamin-related GTPase Drp1 is required for embryonic and brain development in mice. J. Cell Biol. *186*, 805–816.

414. Walensky, L.D., and Gavathiotis, E. (2011). BAX unleashed: the biochemical transformation of an inactive cytosolic monomer into a toxic mitochondrial pore. Trends Biochem. Sci. *36*, 642–652.

415. Wallace, R.A., and Selman, K. (2018). Ultrastructural aspects of oogenesis and oocyte growth in fish and amphibians. J. Electron Microsc. Tech. *16*, 175–201.

416. Wang, X., and Schwarz, T.L. (2009). The Mechanism of Kinesin Regulation by Ca(++) for Control of Mitochondrial Motility. Cell *136*, 163–174.

417. Wang, F., Dumstrei, K., Haag, T., and Hartenstein, V. (2004). The role of DE-cadherin during cellularization, germ layer formation and early neurogenesis in the *Drosophila* embryo. Dev. Biol. *270*, 350–363.

418. Wang, X., Winter, D., Ashrafi, G., Schlehe, J., Wong, Y.L., Selkoe, D., Rice, S., Steen, J., Lavoie, M.J., and Schwarz, T.L. (2011). PINK1 and Parkin target miro for phosphorylation and degradation to arrest mitochondrial motility. Cell *147*, 893–906.

419. Wang, Z.A.Z.Z. a, Huang, J., and Kalderon, D. (2012). *Drosophila* follicle stem cells are regulated by proliferation and niche adhesion as well as mitochondria and ROS. Nat. Commun. *3*, 769.

420. Warn, R.M., and Robert-Nicoud, M. (1990). F-actin organization during the

cellularization of the *Drosophila* embryo as revealed with a confocal laser scanning microscope. J. Cell Sci. *96 (Pt 1)*, 35–42.

421. Warren, G., and Wickner, W. (1996). Organelle inheritance. Cell *84*, 395–400.
422. Wasiak, S., Zunino, R., and McBride, H.M. (2007). Bax/Bak promote sumoylation of DRP1 and its stable association with mitochondria during apoptotic cell death. J. Cell Biol. *177*, 439–450.
423. Weakley, B.S. (1966). Electron microscopy of the oocyte and granulosa cells in the developing ovarian follicles of the golden hamster (Mesocricetus auratus). J. Anat. *100*, 503–534.
424. Weaver, A.K., Liu, X., and Sontheimer, H. (2004). Role for calcium-activated potassium channels (BK) in growth control of human malignant glioma cells. J. Neurosci. Res. *78*, 224–234.
425. Weidemann, A., Bernhardt, W.M., Klanke, B., Daniel, C., Buchholz, B., Câmpean, V., Amann, K., Warnecke, C., Wiesener, M.S., Eckardt, K.-U., et al. (2008). HIF Activation Protects From Acute Kidney Injury. J. Am. Soc. Nephrol. *19*, 486 LP-494.
426. Welte, M. a, Welte, M. a, Gross, S.P., Gross, S.P., Postner, M., Postner, M., Block, S.M., Block, S.M., Wieschaus, E.F., and Wieschaus, E.F. (1998). Developmental Regulation of Vesicle Transport in. Cell *92*, 547–557.
427. Weng, M., and Wieschaus, E. (2016). Myosin-dependent remodeling of adherens junctions protects junctions from Snail-dependent disassembly. J. Cell Biol. *212*, 219–229.
428. Wenzl, C., Yan, S., Laupsien, P., and Großhans, J. (2010). Localization of RhoGEF2 during *Drosophila* cellularization is developmentally controlled by slam. Mech. Dev. *127*, 371–384.
429. Westermann, B. (2012). Bioenergetic role of mitochondrial fusion and fission. Biochim. Biophys. Acta - Bioenerg. *1817*, 1833–1838.
430. Wheaton, W.W., Weinberg, S.E., Hamanaka, R.B., Soberanes, S., Sullivan, L.B., Anso, E., Glasauer, A., Dufour, E., Mutlu, G.M., Budigner, G.R.S., et al. (2014). Metformin inhibits mitochondrial complex I of cancer cells to reduce tumorigenesis. Elife *3*, e02242.
431. West, A.P., Brodsky, I.E., Rahner, C., Woo, D.K., Erdjument-Bromage, H., Tempst, P., Walsh, M.C., Choi, Y., Shadel, G.S., and Ghosh, S. (2011). TLR signalling augments

macrophage bactericidal activity through mitochondrial ROS. Nature *472*, 476–480.

432. White, C., Li, C., Yang, J., Petrenko, N.B., Madesh, M., Thompson, C.B., and Foskett, J.K. (2005). The endoplasmic reticulum gateway to apoptosis by Bcl-X(L) modulation of the InsP3R. Nat. Cell Biol. *7*, 1021–1028.
433. Wilding, M., Carotenuto, R., Infante, V., Dale, B., Marino, M., Di Matteo, L., and Campanella, C. (2001a). Confocal microscopy analysis of the activity of mitochondria contained within the 'mitochondrial cloud' during oogenesis in *Xenopus laevis*. Zygote *9*, 347–352.
434. Wilding, M., Dale, B., Marino, M., di Matteo, L., Alviggi, C., Pisaturo, M.L., Lombardi, L., and De Placido, G. (2001b). Mitochondrial aggregation patterns and activity in human oocytes and preimplantation embryos. Hum. Reprod. *16*, 909–917.
435. Wilding, M., Coppola, G., Dale, B., and Di Matteo, L. (2009). Mitochondria and human preimplantation embryo development. Reproduction *137*, 619–624.
436. Williams, M.J., Habayeb, M.S., Hultmark, D., Verdier, V., Guang-Chao-Chen, Settleman, J., Romanello, V., Sandri, M., Pagliuso, A., Tham, T.N., et al. (2016). Mitochondrial bioenergetic function and metabolic plasticity in stem cell differentiation and cellular reprogramming. Biochim. Biophys. Acta - Gen. Subj. *1820*, 571–576.
437. Wilsch-Bräuninger, M., Schwarz, H., and Nüsslein-Volhard, C. (1997). A Sponge-like Structure Involved in the Association and Transport of Maternal Products during *Drosophila* Oogenesis. J. Cell Biol. *139*, 817–829.
438. Witzberger, M.M., Fitzpatrick, J.A.J., Crowley, J.C., and Minden, J.S. (2008). End-on imaging: A new perspective on dorsoventral development in *Drosophila* embryos. Dev. Dyn. *237*, 3252–3259.
439. Wong, E.D., Wagner, J.A., Gorsich, S.W., Mccaffery, J.M., Shaw, J.M., and Nunnari, J. (2000). The Dynamin-related GTPase , Mgm1p , Is an Intermembrane Space Protein Required for Maintenance of Fusion Competent Mitochondria. *151*, 341–352.
440. Xie, S., and Martin, A.C. (2015). Intracellular signalling and intercellular coupling coordinate heterogeneous contractile events to facilitate tissue folding. Nat. Commun. *6*, 7161.
441. Xu, X., Duan, S., Yi, F., Ocampo, A., Liu, G.-H., and Izpisua Belmonte, J.C. (2013). Mitochondrial Regulation in Pluripotent Stem Cells. Cell Metab. *18*, 325–332.
442. Xue, Z., and Sokac, A.M. (2016). Back-to-back mechanisms drive actomyosin ring

closure during *Drosophila* embryo cleavage. J. Cell Biol. *215*, 335–344.

443. Yaffe, M.P., Harata, D., Verde, F., Eddison, M., Toda, T., and Nurse, P. (1996). Microtubules mediate mitochondrial distribution in fission yeast. Proc. Natl. Acad. Sci. *93*, 11664–11668.
444. Yaffe, M.P., Stuurman, N., and Vale, R.D. (2003). Mitochondrial positioning in fission yeast is driven by association with dynamic microtubules and mitotic spindle poles. Proc. Natl. Acad. Sci. U. S. A. *100*, 11424–11428.
445. Yang, Y., Song, Y., and Loscalzo, J. (2007). Regulation of the protein disulfide proteome by mitochondria in mammalian cells. Proc. Natl. Acad. Sci. *104*, 10813 LP-10817.
446. Yonashiro, R., Sugiura, A., Miyachi, M., Fukuda, T., Matsushita, N., Inatome, R., Ogata, Y., Suzuki, T., Dohmae, N., Yanagi, S., et al. (2009). Mitochondrial Ubiquitin Ligase MITOL Ubiquitinates Mutant SOD1 and Attenuates Mutant SOD1-induced Reactive Oxygen Species Generation. Mol. Biol. Cell *20*, 4524–4530.
447. Yost, H.J., Phillips, C.R., Boore, J.L., Bertman, J., Whalon, B., and Danilchik, M. V. (1995). Relocation of mitochondria to the prospective dorsal marginal zone during *Xenopus* embryogenesis. Dev. Biol. *170*, 83–90.
448. Youle, R.J., and Strasser, A. (2008). The BCL-2 protein family: opposing activities that mediate cell death. Nat. Rev. Mol. Cell Biol. *9*, 47.
449. Young, P.E., Pesacreta, T.C., and Kiehart, D.P. (1991). Dynamic changes in the distribution of cytoplasmic myosin during *Drosophila* embryogenesis. Development *111*, 1–14.
450. Yu, T., Robotham, J.L., and Yoon, Y. (2006). Increased production of reactive oxygen species in hyperglycemic conditions requires dynamic change of mitochondrial morphology. Proc. Natl. Acad. Sci. *103*, 2653–2658.
451. Yung, H.W., Wyttenbach, A., and Tolkovsky, A.M. (2004). Aggravation of necrotic death of glucose-deprived cells by the MEK1 inhibitors U0126 and PD184161 through depletion of ATP. Biochem. Pharmacol. *68*, 351–360.
452. Zaja, I., Bai, X., Liu, Y., Kikuchi, C., Dosenovic, S., Yan, Y., Canfield, S.G., and Bosnjak, Z.J. (2014). Cdk1, PKCδ and calcineurin-mediated Drp1 pathway contributes to mitochondrial fission-induced cardiomyocyte death. Biochem. Biophys. Res. Commun. *453*, 710–721.
453. Zhan, L., Cao, H., Wang, G., Lyu, Y., Sun, X., An, J., Wu, Z., Huang, Q., Liu, B., and Xing, J.

(2016). Drp1-mediated mitochondrial fission promotes cell proliferation through crosstalk of p53 and NF-κB pathways in hepatocellular carcinoma. Oncotarget *7*, 65001–65011.

454. Zhang, Y., and Chan, D.C. (2007). Structural basis for recruitment of mitochondrial fission complexes by Fis1. Proc. Natl. Acad. Sci. *104*, 18526–18530.
455. Zhang, B., Srirangam, A., Potter, D.A., and Roman, A. (2005). HPV16 E5 protein disrupts the c-Cbl-EGFR interaction and EGFR ubiquitination in human foreskin keratinocytes. Oncogene *24*, 2585–2588.
456. Zhang, D., Lu, C., Whiteman, M., Chance, B., and Armstrong, J.S. (2008a). The mitochondrial permeability transition regulates cytochrome c release for apoptosis during endoplasmic reticulum stress by remodeling the cristae junction. J. Biol. Chem. *283*, 3476–3486.
457. Zhang, J., Khvorostov, I., Hong, J.S., Oktay, Y., Vergnes, L., Nuebel, E., Wahjudi, P.N., Setoguchi, K., Wang, G., Do, A., et al. (2011). UCP2 regulates energy metabolism and differentiation potential of human pluripotent stem cells. EMBO J. *30*, 4860–4873.
458. Zhang, Y.-Z., Ouyang, Y.-C., Hou, Y., Schatten, H., Chen, D.-Y., and Sun, Q.-Y. (2008b). Mitochondrial behavior during oogenesis in zebrafish: A confocal microscopy analysis. Dev. Growth Differ. *50*, 189–201.
459. Zhao, N., Zhang, Y., Liu, Q., and Xiang, W. (2015). Mfn2 affects embryo development via mitochondrial dysfunction and apoptosis. PLoS One *10*, 1–12.
460. Zhao, Y., Butler, E.B., and Tan, M. (2013). Targeting cellular metabolism to improve cancer therapeutics. Cell Death Dis. *4*, e532–e532.
461. Zunino, R., Schauss, A., Rippstein, P., Andrade-Navarro, M., and McBride, H.M. (2007). The SUMO protease SENP5 is required to maintain mitochondrial morphology and function. J. Cell Sci. *120*, 1178–1188.
462. Zhou, R., Yazdi, A.S., Menu, P., and Tschopp, J. (2010). A role for mitochondria in NLRP3 inflammasome activation. Nature *469*, 221.